Theory and Application of Autoproducts

by

Brian M. Worthmann

A dissertation submitted in partial fulfillment
of the requirements for the degree of
Doctor of Philosophy
(Applied Physics)
in the University of Michigan
2018

Doctoral Committee:

Professor David R. Dowling, Chair
Professor Karl Grosh
Associate Professor Oliver D. Kripfgans
Assistant Professor Bogdan I. Popa
Professor Kamal Sarabandi

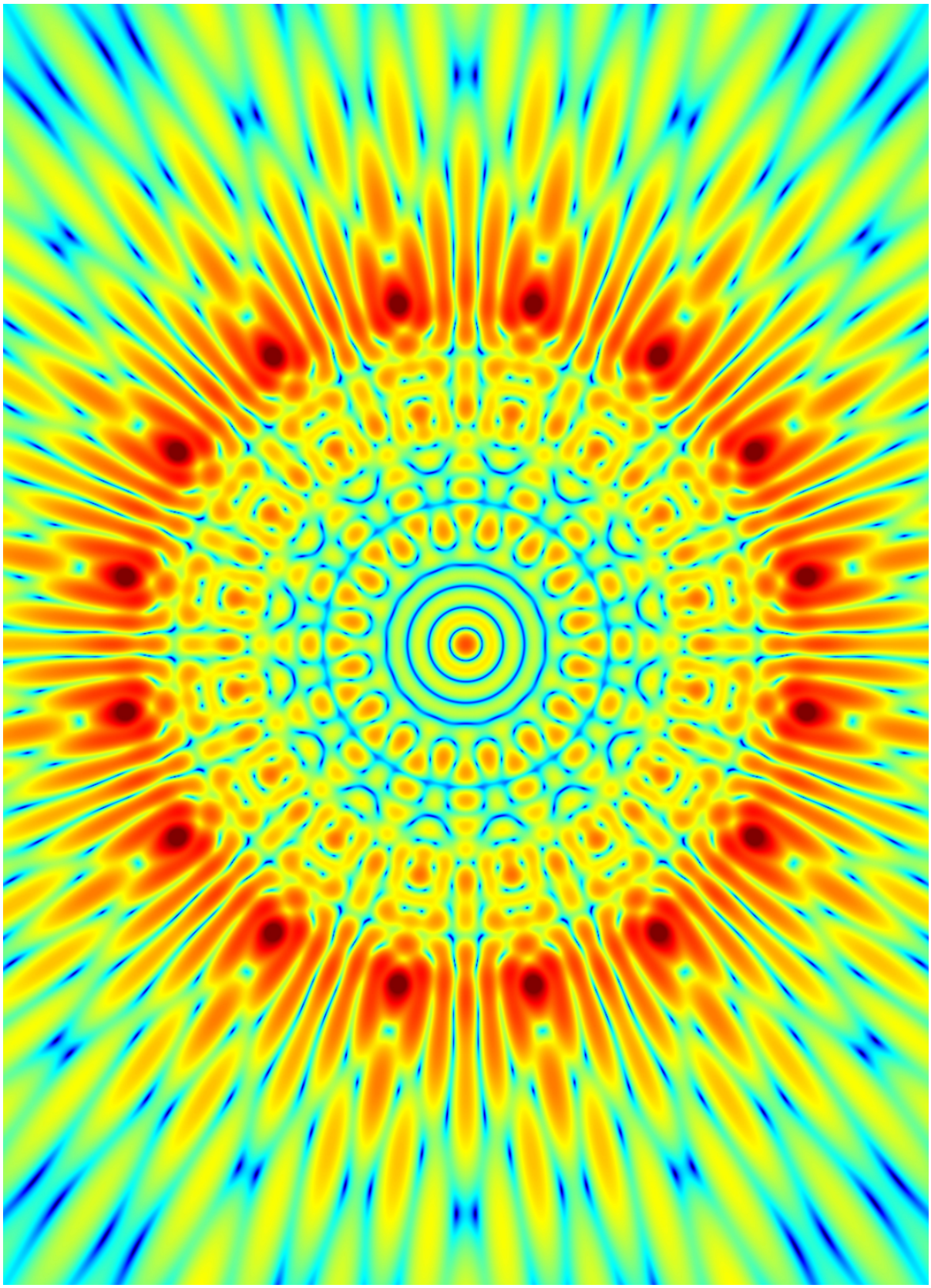

Brian M. Worthmann
bworthma@umich.edu
ORCID iD: 0000-0003-2437-9038

DEDICATION

To A.

ACKNOWLEDGMENTS

I would like to begin by sincerely thanking my research advisor, Prof. David R. Dowling, without whom none of this work would have been possible. Thanks to his mentorship, I feel that I have flourished in graduate school, due in no small part to the level of flexibility, availability, and freedom he has provided me over the last five years.

I would also like to thank my committee members, Professors Karl Grosh, Oliver Kripfgans, Bogdan Popa, and Kamal Sarabandi. I really appreciate their willingness to serve on my committee, and for providing valuable input on my thesis.

I would like to thank Dr. Heechun Song of the Scripps Institution of Oceanography for his collaborations during my thesis, including sharing valuable data taken from at-sea experiments, and even more valuable suggestions and thought-provoking conversations. I would also like to thank Jessica Lipa, without whom an entire chapter of this thesis would never have been possible. She is easily one of the hardest working individuals I have had to pleasure to work with, and her physical intuition and laboratory skills are impeccable. Thank you Heechun and Jessica!

I would be remiss if I did not thank my funding sources, including: the National Science Foundation for their Graduate Research Fellows Program (Grant Fund No. DGE 1256260), the Office of Naval Research (Award No. N00014-11-1-0047 and Award No. N00014-16-1-2975), the University of Michigan Applied Physics program, Rackham Graduate School for their unparalleled yearly travel grant, and finally to the Acoustical Society of America for travel grants as well.

I also need to thank my mother, Cindy, my father Ronald, my brother Mathew, my sister Leslie, and my grandparents Mutti and Papi. Without them, I would've never made it to college, let alone graduate school. They have been an endless source of encouragement and inspiration for me.

Over my time here at the University of Michigan, I've had the great pleasure of getting to know dozens of people who I happily call my friend. I do not have the time now to give a special shout out to each and every one of you, but before the final version of this document is submitted, I'll be sure to thank each of you individually.

And finally, above everyone else, the one person that truly made all of this possible, is my best friend and loving wife, Alicia Welden. I cannot put into words the level of gratitude I have for having her in my life. And so, I dedicate my PhD thesis to the love of my life, Alicia.

TABLE OF CONTENTS

Dedication ii
Acknowledgments iii
List of Figures viii
List of Tables xx
List of Appendices xxi
Abstract xxii

1 Introduction 1
1.1 Background 1
1.1.1 Remote Sensing 1
1.1.2 Shallow Ocean Wave Propagation 2
1.1.3 Array Signal Processing for Localization 5
1.2 Thesis Overview 7
1.2.1 Autoproduct Idea 7
1.2.2 Thesis Objectives 9
1.2.3 Thesis Organization 9
2 High Frequency Source Localization in a Shallow Ocean Sound Channel Using Frequency Difference Matched Field Processing 13
2.1 Introduction 14
2.2 Mathematical Formulation 17
2.2.1 Single and Bi-frequency MFP Formulations 17
2.2.2 Interpretations of the Autoproduct 20
2.2.3 Broadband MFP 23
2.2.4 Source Waveform Dependence 25
2.2.5 Consequences of Nonlinearity 27
2.3 Simulation Results 30
2.4 Experimental Results 38
2.5 Summary and Conclusions 46
3 Adaptive Frequency-Difference Matched Field Processing for High Frequency Source Localization in a Noisy Shallow Ocean 51
3.1 Introduction 52
3.2 Matched Field Processing Schemes 55
3.2.1 In-band and Δf Implementations of Conventional MFP . . 55
3.2.2 Source Waveform Dependence 60
3.2.3 Adaptive Frequency Difference MFP Techniques 61
3.2.4 Δf-MFP Theory 66

3.2.5 Frequency Difference Replica Calculation . . . 68
3.3 Source Localization Results Using Experimental Data . . . 70
3.3.1 KAM11 Experiment . . . 70
3.3.2 Signal to Noise Ratio Analysis . . . 71
3.4 Results . . . 74
3.4.1 Adaptive MFP and SNR Results . . . 74
3.4.2 Dynamic Range Discussion . . . 81
3.5 Summary and Conclusions . . . 83
4 Nonlinear Signal Processing Techniques for Active Sonar Localization in the Shallow Ocean with Significant Environmental Uncertainty and Reverberation 87
4.1 Introduction . . . 88
4.2 Signal Processing Algorithms . . . 90
4.2.1 Matched Filter . . . 90
4.2.2 Conventional MFP . . . 91
4.2.3 Frequency Difference MFP . . . 93
4.2.4 Incoherent Frequency Difference MFP . . . 94
4.2.5 Coherent Frequency Difference MFP . . . 95
4.2.6 Difference Frequency Bandwidth . . . 96
4.3 Simulation Parameters . . . 96
4.4 Results . . . 99
4.5 Conclusions . . . 101
5 The Frequency-Difference and Frequency-Sum Acoustic-Field Autoproducts 104
5.1 Introduction . . . 105
5.2 Autoproduct Definitions and Field Equations . . . 109
5.3 Plane- and Spherical-wave Autoproduct Fields . . . 114
5.4 Autoproduct Fields in the Ray Approximation . . . 117
5.5 Autoproducts Near Reflecting Boundaries . . . 123
5.5.1 Frequency-Independent Reflection Coefficients . . . 124
5.5.2 Frequency-Dependent Reflection Coefficients . . . 128
5.6 Autoproduct Fields in a Lloyd's Mirror Environment . . . 130
5.7 Summary and Conclusions . . . 138
6 Measurement of Autoproduct Fields in a Lloyd's Mirror Environment . . . 140
6.1 Introduction . . . 141
6.2 Theoretical Fields and Comparison Metrics . . . 143
6.2.1 Autoproduct Definitions . . . 143
6.2.2 Lloyd's Mirror Environment . . . 146
6.3 Experiment . . . 148
6.3.1 Acoustic-Field Measurements . . . 148
6.3.2 Source Characterization . . . 149
6.3.3 Environmental Characterization . . . 152
6.4 Results and Comparisons . . . 154
6.5 Summary and Conclusions . . . 161
7 Autoproducts In and Near Acoustic Shadow Zones Created by Barriers . . . 163
7.1 Introduction . . . 164
7.2 Autoproduct Definitions . . . 166

7.3 Sommerfeld Half-Plane Problem . . . 171
7.4 Mie Scattering from a Sphere . . . 179
7.5 Summary and Conclusions . . . 191
8 The Effects of Refraction and Caustics on Autoproducts . . . 193
8.1 Introduction . . . 194
8.2 Autoproduct Definitions . . . 198
8.3 n^2-Quadratic . . . 200
8.4 n^2-Linear . . . 208
8.5 Summary and Conclusion . . . 216
9 Cross Term Analysis for Dynamic Range Expansion . . . 219
9.1 Introduction . . . 220
9.2 Autoproducts and Δ f-MFP Overview . . . 222
9.2.1 Definitions . . . 222
9.2.2 Replica Calculation Modifications . . . 224
9.2.3 Robustness to Environmental Uncertainties . . . 225
9.2.4 Cross Terms . . . 226
9.3 Cross Term Analysis . . . 227
9.3.1 Simulation Parameters . . . 227
9.3.2 Self and Cross Term Analysis . . . 230
9.4 Cross Term Subtraction . . . 239
9.4.1 Monte Carlo Cross Term Subtraction . . . 240
9.4.2 N-Path Estimates of Cross Terms . . . 242
9.4.3 Diagonal Zeroing . . . 245
9.4.4 Comparison of Techniques . . . 246
9.4.5 Positive Semi-Definiteness . . . 247
9.5 Δf-MFP Results with Cross Term Mitigation . . . 248
9.6 Summary and Conclusion . . . 251
10 Summary, Conclusions, and Future Work . . . 253
10.1 Summary . . . 253
10.2 Conclusions . . . 255
10.2.1 Theory . . . 256
10.2.2 Applications . . . 258
10.3 Future Work . . . 259
Appendices . . . 262
Bibliography . . . 290

LIST OF FIGURES

1.1 Amplitude plots of a nominally shallow ocean (panel a) and deep ocean (panel b). The color scale is logarithmic (in dB), with red (blue) corresponding to louder (quieter) regions of the acoustic field. The source is located along the left hand side, where a finite angle fan of rays is launched from the source. Note the aspect ratio, as elsewhere in this thesis, is horizontally compressed. This plot was created with the ray code BELLHOP (Porter and Reiss 1983). 3

1.2 Organizational schematic of this thesis. Solid black lines indicate some of the types of results given in *this* thesis. The black lines do not indicate these topics are solved, just that some progress has been made. Dotted lines indicate topics that have been excluded from this thesis, have been given to other PhD students. The chapter and appendix labels are meant as a rough guide, not as a definitive statement of applicability. Additionally, the topics listed here are not meant to be an exhaustive list; many more applications of autoproducts are possible, just as there are other methods of understanding the theoretical nature of autoproducts. 12

2.1 Acoustic Moire patterns. The top two-thirds of this figure have 101 evenly spaced vertical bars, and the bottom two-thirds of the figure have 99 evenly spaced vertical bars. The middle one-third of this figure shows the overlap of these two patterns, where a low frequency pattern emerges, the spacing of which is related to the difference in the number of bars. This is analogous to the operating principle of frequency difference MFP in that two slightly different high frequency signals are combined in such a way to produce a result that behaves like the much lower difference frequency. 21

2.2 Phasor representation of frequency difference MFP. The high frequency component of the autoproduct is represented by the phasor ranging from arrow A and spirally inward to arrow B. The slightly lower frequency component of the autoproduct, with its complex conjugate, spirals outward from arrow B to arrow C. Then, the difference frequency replica, which introduces the environmental mismatch, is calculated to continue from arrow C back to the real axis near arrow A. Without mismatch, the combination of the autoproduct and replica will always land perfectly on the real axis, meaning the phases across the receivers will add coherently and produce a peak in the ambiguity surface. 22

2.3 Geometry, source, and array parameters intended to mimic the KAM11 experiment. A 16-element vertical array of hydrophones spaced 3.75 m apart (half-wavelength spacing at 200 Hz), for a total array aperture of 56.25 m, is centered at 69.3 m below the surface in this 106-m-deep sound channel. At a range of 3 km, an omnidirectional source located 67.7 m below the surface broadcasts a 100-ms linear-frequency-modulated pulse from 11.2 kHz to 32.8 kHz. The bottom of the sound channel is idealized to be perfectly rigid with no absorption. The sound speed profile is downward refracting with an approximate change in sound speed of 5.1 m/s over the depth of the channel, and is taken from observed KAM11 data. 32
2.4 Sound speed profiles (SSPs) used in this investigation. The solid curve represents a measured sound speed profile from the KAM11 experiment. The dashed curve is a best-fit arctangent curve to the KAM11 data. The dotted line represents a best fit line to the KAM11 data. The shaded region shows the range of sound speeds observed over three days (JD183JD185) of the KAM11 experiment, and indicates the environmental variability at the site of the experiment. The solid, measured profile is used for simulation of recorded pressure fields. The dotted and dashed curves are used in MFP replica calculations. 33
2.5 Eigenray plot simulated using Bellhop. The source at a range of 3 km and depth of 67.7 m broadcasts high frequency sound, illustrated above with rays, to the receiving array on the left at a range of 0 m. The figure above shows the eigenrays connecting the source to the center of the receiving array at a depth of 69.3 m. The measured sound speed profile from KAM11 was used in this calculation, shown as the solid line in Fig. 2.4. It can be seen from this diagram that the environments vertical sound speed produces a multipath downward-refracting environment. Only rays arriving within the first 10 ms are shown, as this is intended to mimic time delay spreads found in the KAM11 experimental data. Additionally, the rays amplitude information is represented in the line thickness, meaning thicker lines refer to stronger amplitudes, while thinner lines refer to weaker amplitudes. The importance of refraction and bottom-reflections in this environment is made evident here. 34
2.6 Plot of the mode shapes used in the calculation of replicas for frequency difference MFP. These are the three lowest-order modes calculated at four difference frequencies which are evenly spaced in the frequency difference bandwidth from 50 Hz to 500 Hz. The arctangent sound speed profile, shown as a dashed curve in Fig. 2.4, is used for this mode calculation. It can be seen in the mode shapes near the surface that the modified boundary conditions are used, where both the top and bottom surfaces are treated as perfectly rigid boundaries, leading to unexpected mode shapes. 35

2.7 Spectrograms of two different recorded pressure profiles. The source is at a depth of 67.7m and range of 3km, and the receiver is at a depth of 67.4m. Fig 7a) shows the recorded pressure profile when the source waveform used is the 100-ms LFM pulse from 11.2kHz to 32.8kHz. Fig. 2.7b) shows the result of scrambling the source waveforms phase by multiplying each frequency bin with a random complex phase factor. The result has the same spectral power, but the randomized phases lead to a loss of the time-frequency structure. The relative phases between any two hydrophones is still the same, and therefore processing these waveforms with MFP yields the same result, as given in Fig. 2.8. 36
2.8 Comparison of simulations of conventional (Bartlett) MFP (Fig. 2.8a) and frequency difference MFP (Fig. 2.8b) for the KAM11 geometry, with a source depth of 67.7 m. In this range-depth cross section of the ocean waveguide, the black circles along the left indicate the location of the 16 array elements, and the filled white circle in the center indicates the correct location of the source. The peak in the ambiguity surface is provided by a white $\bigotimes$ symbol. The 5 dB color scale refers to the output of MFP, the ambiguity surface, where the most likely source locations are found at the top of the color scale. The recorded pressure data are simulated using Bellhop through the measured KAM11 sound speed profile. Conventional MFP calculates replicas using Bellhop through the arctangent sound speed profile, and averages across the signal bandwidth of 11.2 kHz to 32.8 kHz. Frequency difference MFP calculates replicas using the first three modes at difference frequencies between 50 Hz and 500 Hz, averaging first through the signal bandwidth and then a second iteration of averaging across the difference frequency bandwidth to produce the ambiguity surface shown above. 37
2.9 Frequency difference MFP ambiguity surface for a source at 4km range, simulated with Bellhop. The peaks in the ambiguity surface are now located at 1km, 4km, and 7km in range. These peaks have the same spacing as Fig. 2.8b), but because they are shifted, it would suggest that the 3km pattern is a result of the sound speed profile and geometry, and is not necessarily a function of source range. . . 39
2.10 Conventional MFP ambiguity surface for a source at 3 km range, 67.7 m depth, and signal frequencies from 50 Hz to 500 Hz. Had the source truly broadcast 50 Hz to 500 Hz, the resulting ambiguity surface also contains the same 0 km, 3 km, and 6 km peaks, as did Fig. 2.8b). Qualitatively, the features in the ambiguity surfaces are comparable to Fig. 2.8b). Conventional MFP at a low frequency still performs much better in terms of localization as compared to frequency difference MFP at the same frequency, which can likely be attributed to the production of undesired cross terms in the frequency difference formulation. 40
2.11 Spectrogram of KAM11 data. The 100-ms linear-frequency-modulated (LFM) pulse from 11.2 kHz to 32.8 kHz is illustrated above. Specifically, this is the spectrogram of the recording from the hydrophone at a depth of 67.4 m (nearest to the center of the array) for the bottom-moored source at a depth of 67.7 m. The horizontal axis shows the relative time over the 300-ms recording, and the vertical axis shows the constituent frequencies around a particular time. The logarithmic color scale is normalized such that the strongest time-frequency bin has a magnitude of unity. 41

2.12 A sample measurement of the channel impulse response for the KAM11 environment. The vertical axis displays the depths of the hydrophones, and the horizontal axis shows the relative arrival times for a bottom-moored source at a depth of 67.7 m. The multipath structure of the experimental data is clearly illustrated above, with an approximate time delay spread of 10 ms. 42
2.13 Ambiguity surfaces for the KAM11 data using conventional and frequency difference MFP. The horizontal and vertical axes, dynamic range of the color scale, and source and receiving array labels are the same as Fig. 2.8. Fig. 2.11a) illustrates conventional matched field processing. Here, the source localization effort is largely unsuccessful, with many ambiguous peaks. Fig. 2.11b) shows the same data processed using frequency difference MFP, showing a more successful source localization. The dominant ray cycle distance in this environment is approximately 3 km, as seen in Fig. 2.5, and this leads to the strong side-lobes, approximately 3 km up and down range from the true source location. 43
2.14 Spectrograms and ambiguity surfaces analyzing the dependence of the frequency difference MFP technique on the source waveform. All three spectrograms have a horizontal axis ranging from 0 to 300 ms, a vertical axis spanning 0 to 48 kHz and 40 dB of dynamic range. All three ambiguity surfaces have a horizontal axis showing range from 0 to 6 km, a vertical axis showing 0 to 106 m of depth, and 5 dB of dynamic range. All experimental parameters were held the same as in Fig. 2.13. The horizontal white lines in the spectrograms denote the nominal 11.2kHz to 32.8kHz bandwidth. Fig. 2.14a) shows the spectrogram of a time-windowed version of Fig. 2.11, but focusing on the LFM pulse only. When such a time series is processed with frequency difference MFP, the ambiguity surface is shown at right. Similarly, Fig. 2.14b) also has a time-window, but focuses only on the last 24 ms of data, which contains part of a communications signal. It can be seen that this signal, with clearly no time-frequency structure, has very comparable results as its LFM pulse counterpart in Fig 2.14a). Fig. 2.14c) shows a time window that subtracts the time components of Figs. 2.14a) and 2.14b) from the full recorded data in Fig. 2.11, the result of which is expected to be purely noise or reverberation. By processing just this, one would not expect any clear localization result, which is confirmed as shown in the accompanying ambiguity surface. This plot is included as a confirmation that frequency difference MFP does not always produce the same ambiguity surface, as one might be led to believe considering the similarities between the other frequency difference MFP ambiguity surfaces shown here. 44
2.15 Examples of frequency difference MFP for four different trials. Panel a) is the trial with the best localization result, specifically a bottom-moored source at a depth of 60.2 m, with a range error of 50 m and depth error of 1.3 m. Panel b) is the worst localization result, with a ship-mounted source at a depth of 61.5 m, with a range error of 525 m and depth error of 13.9 m. Panel c) shows the shallowest source, a ship-mounted source at a depth of 31.5 m, resulting in a range error of 125 m and a depth error of 20.0 m. Panel d) shows the deepest source, a bottom-moored source at a depth of 90.2 m, resulting in a range error of 150 m and depth error of 7.2 m. 46

3.1 KAM11 geometry and sound speed profile. A schematic of the geometry of the nominal KAM11 geometry is shown, with a rigid bottom and a pressure release surface. The 16 element vertical line array is shown on the left, and the bottom-moored source is illustrated 3 km away and at a depth of 67.7 m. A measured sound speed profile is given on the right, and can be seen to be downward refracting, with a difference in sound speed between the top and bottom of 5.1 m/s. 71
3.2 KAM11 spectrogram. The spectrogram (averaged through all 16 hydrophones) is shown for a source depth of 67.7m. The gray scale spans 30 dB. The horizontal dashed lines show the bandwidth of the KAM11 signal. Region a) shows a pure noise sample. Region b) shows the recorded LFM pulse, with the characteristic linear shape, along with some reverberation occurring after the main linear stripe. Region c) shows reverberation, and region d) shows the beginning of a KAM11 communications signal. For this study, only region a) and the first 75ms of region b) are used. 72
3.3 Truncated KAM11 spectrograms for varying SNR. The gray scales in all three spectrograms are held fixed at 30dB. Panel a) shows the 20dB *SNR* result, which is essentially the same as the first 75ms of Region b) in Figure 3.2. Panel b) shows the 0 dB *SNR* spectrogram, and the signal is clearly degraded by the noise. Panel c) shows the 10dB *SNR* spectrogram, and the presence of the signal is almost completely obscured by the noise. 74
3.4 Sample in-band Bartlett MFP ambiguity surface. This range-depth cross section of the ocean shows the most likely source locations on a logarithmic color scale, with a dynamic range of 5 dB. The true source location is shown with a white O, located at 3 km range and 67.7m depth. The highest peak in the field is shown with a white X. The localization result here is ambiguous, with numerous possible source locations, roughly constrained to the bottom half of the sound channel. This poor localization result is expected due to the strong detrimental effects of environmental mismatch in the signal band (11.2 kHz to 26.2 kHz). . . 76
3.5 Sample frequency difference MFP ambiguity surface plots at $SNR = +20$ and 0 dB. All ten plots show the same range-depth cross section of the ocean, and the color scales each span 5dB, with the true source location shown with a white O, and the peak in the ambiguity surface shown is shown with a white X. The left column (panels a, c, e, g, i) is for 20 dB *SNR* data, while the right column (panels b, d, f, h, j) is for 0 dB *SNR* data. The first row shows Bartlett Δf-MFP results (panels a and b). The second row shows MVDR Δf-MFP results (panels c and d). The third row shows MCM Δf-MFP results (panels e and f). The fourth row shows MUSIC Δf-MFP results (panels g and h). The final row shows MMP Δf-MFP results (panels i and j). 78

3.6 Frequency difference MFP performance as a function of SNR. The same six performance metrics as given in Table 1 are plotted here as a function of SNR between ± 20dB. The mean across all 16 trials is plotted; the variability in that data is omitted here for clarity, but is comparable to the variability specified in Table 1. The solid (black) lines refer to Bartlett, the dotted (red) lines refer to MVDR, the dash-dotted (green) lines refer to MCM, the dash-double-dotted (blue) lines refer to MUSIC, and the dashed (magenta) lines refer to MMP. . . 82

4.1 Simulation geometry and simulated hydrophone measurements 97
4.2 Target localization performance for conventional and Δf-MFP techniques . . . 100
4.3 Comparison of localization techniques for weaker target 102

5.1 Frequencies for the in-band (true acoustic) and out-of-band (autoproduct) fields. The in-band field has frequencies ω between Ω_L and Ω_H. The frequency-difference autoproduct field, AP_Δ, uses this in-band field information to create out-of-band field information at lower frequencies between 0 and $\Omega_H - \Omega_L$. Similarly, the frequency-sum autoproduct field, AP_Σ, uses this in-band field information to create out-of-band field information at higher frequencies between $2\Omega_L$ and $2\Omega_H$. The vertical axis indicates the relative number of possible frequency pairs over which the autoproduct fields may be averaged when the entire signal bandwidth is used. The arrows indicate where the below-band and above-band field information originates. 111
5.2 Coordinates and wave orientations for an acoustic plane-wave P_I incident at angle θ_I on a two-fluid interface at $y = 0$ (see Kinsler *et al.* 2000). The reflected plane wave is $P_R = RP_I$, where R is the surface reflection coefficient. The total field near the surface is the sum of P_I and P_R. The near-surface interference layer where the autoproducts will not mimic acoustic fields at the sum and difference frequencies nominally exists for $y < h_{\Delta,\Sigma}$. 125
5.3 Schematic for the Lloyd's mirror environment, a homogeneous half-space with a pressure-release surface. The source is 100 m below the surface and broadcasts a known 1 - 2 kHz pulse. The fields are then sampled in one of two sampling windows, depending on the frequency. Low frequency fields (100 Hz) are sampled in the larger 20-m-wide-by-200-m-deep window (solid line). High frequency fields (kHz range) are sampled in the smaller 7.5-m-wide-by-7.5-m-deep window (dashed line). The figure is not to scale. 131

5.4 The real part of true acoustic fields in the Fig. 5.3 environment normalized according to (5.5) at a source-to-window-center range of 1.0 km when the sample window's upper edge coincides with the reflecting surface. White indicates a null, while red and blue indicate positive and negative values. The color scale ranges between ± 2. Part a) shows a below-band 100 Hz field in the 20-m-by-200-m sample window with a pressure release surface (R = -1). Part b) shows a below-band 100 Hz field in the 20-m-by-200-m sample window with a rigid surface (R = +1). Parts c), d) and e) show in-band 1.0 kHz, 1.1 kHz, and 2.0 kHz fields, respectively, in the 7.5-m-by-75-m sample window with a pressure release surface (R = -1). Part f) shows an above-band 3.0 kHz field in the 7.5-m-by-75-m sample window with a hard surface (R = +1). These true acoustic fields provide the constituent elements and comparison data for the autoproduct field results shown in Figs. 5.5 and 5.6. 133

5.5 Frequency-difference autoproduct field results at Δf = 100Hz in the Fig. 5.3 environment normalized according to (5.5) in the 20-m-by-200-m sample window for a 1.0 kHz to 2.0 kHz in-band field. The color scale is the same as Fig. 5.4. Panel a) shows $\mathrm{Re}\,[AP_{\Delta}^{norm}]$ at a center frequency of 1.05 kHz. Panel b) shows $\mathrm{Re}\,[AP_{\Delta}^{norm}]$ at a center frequency of 1.95 kHz. Panel c) show the signal-bandwidth-averaged $\mathrm{Re}\,[\langle AP_{\Delta}\rangle_{\omega}^{norm}]$ and is nearly identical to Fig. 5.4b) away from the surface. Panel d) shows the difference between Fig. 5.4b) and Fig. 5.5c), and the dashed line is at the depth h_{Δ} specified by (5.41). 134

5.6 Frequency-sum autoproduct field results at Σf = 3.0kHz in the Fig. 5.3 environment normalized according to (5.5) in the 7.5-m-by-75-m sample window for a 1.0 kHz to 2.0 kHz in-band field. The color scale is the same as Fig. 5.4. Panel a) shows $Re\,[AP_{\Sigma}^{norm}]$ at Δf = 100Hz. Panel b) shows $\mathrm{Re}\,[AP_{\Sigma}^{norm}]$ at Δf = 1.01.0 kHz. Panel c) shows the difference-frequency-averaged $\mathrm{Re}\,[\langle AP_{\Sigma}\rangle_{\Delta\omega}^{norm}]$ and is nearly identical to Fig. 5.4f) away from the surface. Panel d) shows the difference between Fig. 5.4f) and Fig. 5.6c), and the dashed line is at the depth h_{Σ} specified by (5.44). 135

5.7 Difference between the cross correlation coefficient from (5.6) and unity in dB, $10\log_{10}(1-\chi_{\Delta,\Sigma})$, between normalized true out-of-band acoustic fields and normalized averaged autoproduct fields as a function of normalization-window center range, r_c, and center depth, z_c, using the 20m-in-range-by-200m-in-depth sample window. The color scale varies from −30 dB, or χ = 0.999 (dark blue) to 0 dB, or χ = 0 (dark red). Panel a) shows results for the Δf autoproduct with Δf = 100Hz. Panel b) shows results for the Σf autoproduct with Σf = 3.0kHz. In both cases, frequency-averaged autoproduct fields mimic out-of-band acoustic fields away from the source and the reflecting surface. The white regions around the edges of both figures are a result of the fixed size of the normalization window. 136

6.1 Schematic and photograph of the experimental setup. Panel a) illustrates the location of the broadcast transducer and the various locations of the receiving transducer relative to the walls of the water tank and the water surface, shown with the dashed lines around the edges. The receiver was positioned in 1-mm increments in the top 100mm of depth and in 5-mm increments in the next 300mm of depth, providing 400mm of depth sampled nonuniformly. Pressure waveforms were recorded at three source-to-receiver ranges: 175, 325, and 475mm. Panel b) shows the broadcast and receiving transducers, along with the tank's horizontal spanning bars, which allowed the height gauge (the base of which can be seen at the top right in dark gray) to translate in range. 150

6.2 Measured direct-path waveforms in the time domain (upper panel) and frequency domain (lower panel). The nominal source waveform is shown with the dashed curves. The red semitransparent curves show the 291 signal samples used for characterization of the actual source waveform, scaled for spherical spreading and shifted in time to maximize their temporal cross-correlations with the nominal source waveform. The coherent-average direct-path waveform, shown with the solid black curves, is taken to be the experimentally determined source waveform, and is scaled vertically to contain the same total signal energy as the nominal source waveform. 151

6.3 In-band field plots. The measured in-band Green's functions are shown with red "'×"'s. The theoretical in-band Green's functions are shown with the black curves. All five panels have the same horizontal axes (depth from 0 to 400 mm) and vertical axes (normalized units from –4 to +4). The range and frequency for each panel is indicated in the lower right corner, with ranges from 175 to 475 mm, and frequencies from 40 to 110 kHz. 155

6.4 Autoproduct and out-of-band field plots. The measured bandwidth-averaged autoproducts are shown with red × 's. The theoretical autoproducts, calculated using the optimized values for the environmental parameters, are shown with the black solid curves. Theoretical out-of-band fields at the given difference or sum frequency, with modified (+1) reflection coefficient, are shown with the blue dotted curves. All ten panels have the same horizontal axes (depth from 0 to 400 mm) and vertical axes (normalized units from –4 to +4). The depth of the interference layer for each plot is given by the vertical dashed line, labeled as $h_{\Delta,\Sigma}$. The range and difference or sum frequency for each panel is indicated in the lower right corner, with ranges from 175 to 475mm, difference frequencies from 5 to 60kHz (of the possible 0 to 70kHz), and sum frequencies from 115 to 185kHz (of the possible 80 to 220kHz). 157

6.5 Cross-correlation vs. in-band or out-of-band frequency. Cross-correlations for the frequency-difference autoproduct, in-band field, and frequency-sum autoproduct are shown from left to right in blue, black, and red, respectively. The solid curves show the cross-correlation between measured fields and genuine acoustic fields. The dashed curves show the cross-correlation between theoretical fields and genuine acoustic fields, and serve as an upper bound for the solid curves. The dotted curves show the cross-correlation between measured fields and genuine acoustic fields using the unoptimized environmental parameters. The genuine acoustic fields use the unmodified (-1) surface reflection coefficient for the in-band fields and the modified $(+1)$ surface reflection coefficient for the out-of-band fields. 159

7.1 Schematic for the Sommerfeld half-plane problem, showing a plane wave incident from the left onto a rigid barrier of negligible thickness at the origin. The circular domain of interest, of radius R, is subdivided into smaller normalization regions that are roughly one wavelength squared in area, where $kR = 40$ for the grid shown here. 172

7.2 Acoustic field plots for the Sommerfeld half-plane problem for $kR = 40$ (magnitude and phase in panels a and b, respectively), and for $kR = 400$ (magnitude and phase in panels c and d, respectively). 174

7.3 Frequency-difference autoproduct field plots for the Sommerfeld half-plane problem, with magnitude and phase in panels a and b, respectively. The plots shown are for parameters $k_c R = 400$, $k_\Delta = 40$, and $k_{BW}^\Delta R = 40$. 175

7.4 Cross correlations between the frequency-difference autoproduct ($k_c R = 400$, $k_\Delta R = 40$, $k_{BW}^\Delta = 40$) and an out-of-band acoustic field at $kR = 40$. Panel a) shows the magnitude of χ_Δ on a logarithmic color scale, and panel b) shows the phase of χ_Δ. 176

7.5 Cross correlations between the frequency-sum autoproduct ($k_c R = 400$, $k_\Sigma R = 800$, $k_{BW}^\Sigma = 40$) and an out-of-band acoustic field at $kR = 800$. Panel a shows the magnitude of χ_Σ on a logarithmic color scale, and panel b shows the phase of χ_Σ. 179

7.6 Schematic for Mie scattering from a sphere, showing a plane wave incident from the left onto a hard (soft) sphere as shown in the upper (lower) half of the plot. The circular domain of interest has radius R, which is 10 times the radius of the sphere a, and is subdivided into smaller normalization regions that are roughly one wavelength-squared in area, where $kR = 40$ and $ka = 4$ for the grid shown here. 182

7.7 Acoustic field plots for the Mie scattering from a sphere problem, with $ka = 4; kR = 40$ shown in panel a (magnitude) and panel b (phase), and $ka = 40; kR = 400$ shown in panel c (magnitude) and panel d (phase). 183

7.8 Acoustic field magnitude plots of Mie scattering from a sphere in the ray approximation for $ka = 4; kR = 40$ and $ka = 40; kR = 400$ in panels a and b, respectively. 187

7.9 Frequency-difference autoproduct field plots for the Mie scattering from a sphere environment, with $k_c a = 40$, $k_\Delta a = 4$, and $k_{BW}^{\Delta} a = 4$. Magnitude and phase shown in panels a and b, respectively 188
7.10 Cross correlations between the frequency-difference autoproduct and out-of-band fields in the Mie scattering from a sphere environment. Magnitude of χ_Δ given in panel a on a logarithmic scale; phase of χ_Δ given in panel b. 188
7.11 Cross correlations of frequency-sum autoproducts and out-of-band fields in the Mie scattering from a sphere environment, with parameters $k_c a = 40$, $k_\Sigma a = 80$, and $k_{BW}^{\Sigma} a = 4$. Magnitude and phase of χ_Σ is shown in panels a and b, respectively. 189
7.12 Magnitude of the cross correlations for χ_Δ (panel a) and χ_Σ (panel b) when the autoproducts and out-of-band fields are evaluated in the ray approximation. Fields in a given normalization region that are identically zero (*i.e.* in the shadow zone) are defined to be a perfect match ($\chi = 1$). 190
7.13 Point-wise phase differences between frequency-difference (frequency-sum) autoproducts and out-of-band fields are shown in panel a (panel b). 190

8.1 Sound speed profiles for the two range-independent but depth-dependent waveguides in this study: the n^2-quadratic (solid line) and the n^2-linear (dotted line) profile. These waveguides are symmetric and infinite in extent, though the inhomogeneous portion of the sound speed profile has a finite depth of 100 m, and has a sound speed minimum of 1450 m/s. 198
8.2 Plots of the ray trace (upper) and the acoustic amplitude (lower) for a 5 kHz source at the origin of the n^2-quadratic profile. 202
8.3 Plots of the transmission loss for the out-of-band field (upper) and frequency-difference autoproduct field (lower), for a difference frequency of 500 Hz, derived from in-band frequencies of 1 to 5 kHz. Note the dynamic range in the lower plot is twice that of the upper plot. 203
8.4 Cross correlation magnitude (upper) and phase (lower) for the frequency-difference autoproduct in the n^2-quadratic sound speed profile. 204
8.5 Transmission loss plot for the out-of-band (upper) and frequency-sum autoproduct (lower) field for a sum frequency of 6 kHz, derived from a bandwidth of 1 to 5 kHz. Note the dynamic range in the lower plot is double that of the upper plot. 206
8.6 Frequency-sum autoproduct cross-correlations for a sum frequency of 6 kHz in the n^2-quadratic sound speed profile. 207
8.7 Plots of the ray trace (upper) and the transmission loss (lower) for a 5 kHz source at the origin of the n^2-linear sound speed profile. 209
8.8 Transmission loss plots of the out-of-band field (upper) and frequency-difference autoproduct at a difference frequency of 1 kHz, derived from in-band fields between 4 and 6 kHz. Note that the dynamic range of the lower plot is double that of the upper plot. 210
8.9 Cross correlation magnitude (upper) and phase (lower) between the frequency-difference autoproduct and an out-of-band field for a difference frequency of 1 kHz and a bandwidth of 4 to 6 kHz. 211

8.10 Transmission loss plots of the out-of-band field (upper) and frequency-difference autoproduct at a difference frequency of 5 kHz, derived from in-band fields between 1 and 9 kHz. Note that the dynamic range of the lower plot is double that of the upper plot. 213
8.11 Cross correlation magnitude (upper) and phase (lower) between the frequency-difference autoproduct and an out-of-band field for a difference frequency of 5 kHz and a bandwidth of 1 to 9 kHz. 214

9.1 Schematic of the Lloyd's mirror environment, where a vertical line array with 34 elements, spanning 100 meters, receives a 24 – 26 kHz broadcast from a source at a range and depth of 500 meters and 50 meters, respectively. 228
9.2 Ambiguity surfaces for a Lloyd's mirror environment. Panel *a*) shows the ambiguity surface for conventional MFP, performed between 24 and 26 kHz. Panel *b*) shows the ambiguity surface for conventional MFP at a lower frequency of 250 Hz. Panel *c*) shows the ambiguity surface for Δf-MFP, where 24 – 26 kHz is shifted down to 250 Hz. 229
9.3 Real part of cross spectral density matrices. Panel *a*) shows the normalized and bandwidth averaged autoproduct CSDM, including environmental uncertainties. Panel *b*) shows the normalized out-of-band CSDM at the difference frequency, and excludes environmental uncertainties. The color scale in both plots is $\pm 0.9\sqrt{N}$, where N is the number of receivers, with red corresponding to positive values. 235
9.4 Real part of the autoproduct CSDM constituents: self-self terms (panels *a* and *d*), self-cross terms (panels *b* and *e*) and cross-cross terms (panels *c* and *f*). The upper row gives the CSDMs without environmental uncertainty; the lower row includes environmental mismatch. The color scale here, as before varies between $\pm 0.9\sqrt{N}$, where N is the number of receivers. 236
9.5 Frequency difference ambiguity surfaces for the self-self terms (a), self-cross terms (b), and cross-cross terms (c). The spatial and color axes span the same values as in Fig. 9.2. 238
9.6 Cross-term CSDMs showing no mismatch (panel *a*), one realization with mismatch (panel *b*), and an average over 100 realizations with mismatch (panel *c*). The color scale is the same as in Figs. 9.3 and 9.4. 243
9.7 Ambiguity surfaces for $B_{AP}(\boldsymbol{r})$ (panel *a*), $B_{AP}^{MCCTS}(\boldsymbol{r})$ (panel *b*), and $B_{AP}^{DZ}(\boldsymbol{r})$ (panel *c*) in a Lloyd's mirror environment. 249
9.8 Ambiguity surfaces for $B_{AP}(\boldsymbol{r})$ (panel *a*), $B_{AP}^{MCCTS}(\boldsymbol{r})$ (panel *b*), and $B_{AP}^{DZ}(\boldsymbol{r})$ (panel *c*) in a method-of-images environment which includes 10 arrivals. 249
9.9 Ambiguity surfaces for $B_{AP}(\boldsymbol{r})$ (panel *a*) and $B_{AP}^{DZ}(\boldsymbol{r})$ (panel *b*) for the experimental KAM11 data, using a source at a depth of 60.2 m. The maximum in the field was scaled to 0 dB, and the color scale spans 5 dB. 250

A.1 Fourier transform relationships between various bilinear time-frequency analysis functions, and the frequency domain autoproduct. 267

A.2 Cross-correlations of measured and modeled KAM 11 impulse responses. All panels show all 16 hydrophone depths, from 41m (top) to 97m (bottom). The first plot has a horizontal axis spanning 100 ms, and the subsequent eight plots have horizontal axes spanning 20 ms. The red curves in the lower six plots correspond to autocorrelations. 270

B.1 Plots of the real and imaginary parts of the leaky mode eigenvalues (poles) for a variety of frequencies. 283

B.2 Side by side comparison of Airy modes (upper half) and RAM, a parabolic equation solver (lower half). The plots show 5 km range and ± 100 m depth. The frequency evaluated is 5 kHz, with c_∞ =1500 m/s, $n_0 = \frac{1500}{1450}$, and $L = 100$ m. The color scale spans -150 to -50 dB. 284

LIST OF TABLES

2.1 Summary of the performance of frequency difference MFP for two different sound speed profiles using the experimental KAM11 data for all sixteen source depths. The first eight rows correspond to sources mounted to the ship, and the last eight rows corresponding to sources moored to the ocean bottom. The range and depth error are defined as the absolute distance between the maximum in the ambiguity surface and the nominal source location. The peak-to-side-lobe ratio (PSR) is provided as well, and it should be noted that the peak and side-lobe locations were chosen between ranges of 1 km and 5 km to avoid the peaks generated by the approximately 3-km ray-cycle distance. The average range and depth errors using the arctangent profile are approximately 6% of the nominal range and 9% of the sound channel depth, respectively. Additionally, when moving to the linear sound speed profile, which is a worse match to the measured sound speed profile, depth estimates were approximately the same, but range estimation is degraded, with an average error of 19% of the nominal 3-km range. 47

3.1 Localization performance for Δf-MFP and in-band MFP for all 16 KAM11 trials. Here, IQR is the inter-quartile range, and is the difference in value between the 75^{th} percentile and 25^{th} percentile of the data, and is a measure of its variability. Six different performance metrics: range error, depth error, peak range extent (peak width), peak depth extent (peak height), peak-to-sidelobe ratio, and dynamic range are given in the table, as a function of SNR. Additionally, a composite score gives a simple metric by which to compare each of the five Δf-MFP techniques. 80

LIST OF APPENDICES

A Relationships to Signal Processing Techniques 263
B n^2-Quadratic and n^2-Linear Modal Decomposition Derivations 273
C Comparisons to Delta-K Radar 285

ABSTRACT

Acoustics is a branch of physics largely governed by linear field equations. Linearity carries with it the implication that only the frequencies broadcast by acoustic sources can be measured in the surrounding acoustic medium. However, nonlinearities introduced not in the physical world, but in the mathematical and signal processing realm, have the potential to change frequency content. In this dissertation, nonlinear mathematical constructions termed autoproducts are created which have the potential to shift frequencies from the measured, in-band frequencies to other higher or lower frequencies which may no longer be in-band. These out-of-band autoproduct fields did not physically propagate in the environment, and yet, this research has found that autoproducts can nonetheless mimic genuine out-of-band fields in a number of different acoustic environments.

Approximately half of this dissertation addresses the theory of autoproducts. More specifically, mathematical analyses and simple acoustic models are used to uncover the reasons for how this frequency-shifting behavior works, and what its limitations are. It is found that there are no inherent limitations on the frequencies considered, and that in single-path environments, like plane or spherical waves, autoproducts mimic out-of-band fields in all or nearly all circumstances, respectively. However, in multipath environments, the mimicry of out-of-band fields by autoproducts is no longer so complete. Though, with bandwidth averaging techniques, it is found that the difference in time-of-arrivals of multiple paths is an important parameter: if it is larger than the inverse of the bandwidth available for averaging, then

autoproducts can succeed in mimicking out-of-band fields. Other theoretical considerations include the effects of diffraction behind barriers and the effects of strong refraction. Strengths and limitations of autoproducts are assessed with a variety of simple acoustic models, and conclusions are drawn as to the predicted capabilities of autoproduct-based techniques.

The other half of this dissertation covers applications of autoproducts. More specifically, it focuses on the use of autoproducts to perform physics-based source localization, especially for applications in the shallow ocean. Existing techniques are well-known to be very sensitive to uncertainties in the acoustic environment (e.g. the sound speed), especially at high frequencies (nominally greater than 1 kHz in the shallow ocean). Through the use of autoproducts, measured fields at high frequency can be shifted to much lower frequencies, where they can be processed with much more robustness to environmental uncertainties. In one of the main results of this dissertation, it is shown that a remote acoustic source broadcasting sound between 11 and 33 kHz in a 106-meter-deep, downward refracting sound channel could be localized using measurements from a sparse array located 3 km away. The data from the method suggest that autoproduct-based source localization can make physics-based array signal processing robust at arbitrarily high frequencies a novel and important contribution to existing literature.

Overall, by developing the theory for, and exploring applications of, these nonlinear mathematical constructions, the extent to which autoproducts are fundamentally limited is assessed, and new signal processing techniques are developed which have the potential to significantly improve the robustness of source localization algorithms for uncertain multipath environments. Through this study, significant portions of the necessary theoretical foundation have been laid, which will aid in the further development of robust, autoproduct-based signal processing techniques.

CHAPTER 1

Introduction

This thesis touches on the intersection of many disciplines, including remote sensing, acoustic wave propagation, and array signal processing. Thus, to begin, there is short review of some of the relevant background information, followed by an overview of this thesis main ideas, objectives, and organization.

1.1 Background

1.1.1 Remote Sensing

Remote sensing is the general term given to the task of obtaining information about an object or environment from a distance (Dowling and Sabra 2015). This definition is very vague, and could technically include a wide variety of phenomenon. The scope here is limited to remote sensing of physical phenomena that satisfy the wave equation, which could include electromagnetic waves (*i.e.* light), elastic waves (*e.g.* seismic waves), or acoustic waves (*i.e.* sound). The latter of these waves will dominate the discussion in this thesis, though many of the principles discussed here could also be applied to other types of waves. The acoustic wave equation discussed here may include spatially varying sound speeds, but the sound speed are non-dispersive (*i.e.* independent of frequency) and scalar (*i.e.* only one wave type,

compressional, with only one polarization, longitudinal)

Remote sensing collectively comprises four different tasks, typically evaluated serially, as defined here (Dowling and Sabra 2015). The examples provided here are inspired by Naval applications, but this restriction is not necessary. The first task in remote sensing is *detection* or the determination of whether the received signal is purely ambient noise (*e.g.* wind noise), or if it contains anything else that might be of interest. After a detection is made, then the next task is *classification*, which is a determination that the detected signal is something that requires further attention or decision making (*e.g.* a submarine) or if it is just some other source of sound deemed uninteresting (*e.g.* snapping shrimp). If the detection is determined to require further attention, then *localization* is performed, where signal processing techniques attempt to determine where the source is (*e.g.* miles away, or right behind you). A related task, which is combined with localization for the purposes of this thesis, is that of *tracking*, which asks for the sources position as a function of time. The fourth and final task is *identification*, which asks who or what, specifically, is the source of sound (*e.g.* what type of vessel is it, and what entity is likely operating it). Most of this thesis pertains to *localization*; in other words, detection and classification are assumed to be complete, and the primary question is "'where did the sound originate?"' Tracking can in principle be done as well, but the sources given in this thesis are, without exception, assumed to be stationary. Before the details of source localization can be discussed, a brief overview of acoustic wave propagation is important.

1.1.2 Shallow Ocean Wave Propagation

Acoustic waves, like many other waves, feature a variety of propagation phenomena. Transmission, reflection, refraction, absorption, dispersion, diffraction, scattering, interference, and advection can play important roles in sound propagation, depending on the acoustic regime (Morse and Ingard 1970). In this thesis, shallow ocean wave propagation plays a

central role. Shallow oceans are defined to be on the order of 100 meters deep, with ranges of interest on the order of 1 to 10 kilometers, and the wave propagation features significant reflections from the ocean surface and/or bottom (Kuperman and Roux 2007). This contrasts with the deep ocean, which is typically a few kilometers deep, with ranges on the order of hundreds to thousands of kilometers, and features more significant refraction than reflection (Urick 1975). See 1.1 for a side-by-side comparison of shallow and deep ocean wave propagation.

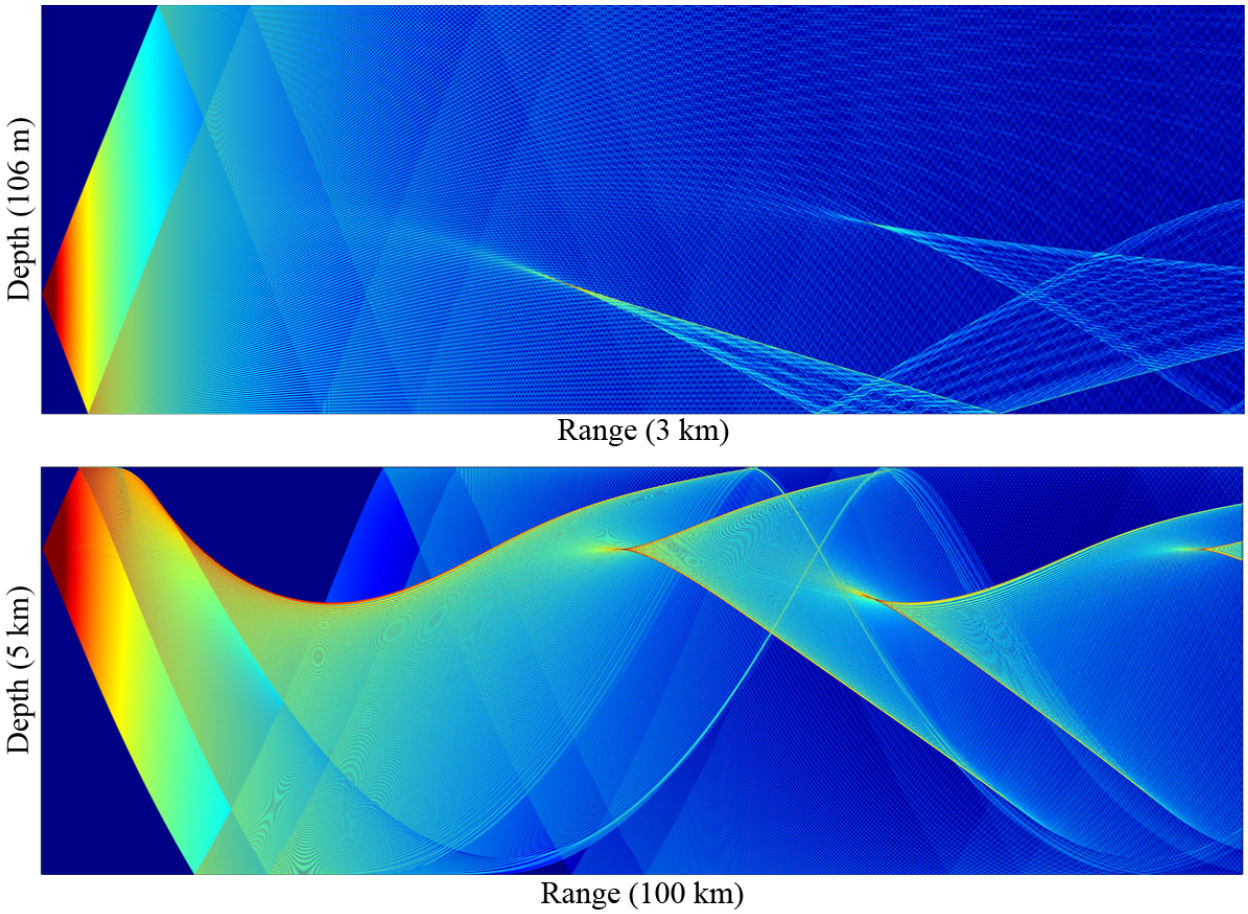

Figure 1.1: Amplitude plots of a nominally shallow ocean (panel a) and deep ocean (panel b). The color scale is logarithmic (in dB), with red (blue) corresponding to louder (quieter) regions of the acoustic field. The source is located along the left hand side, where a finite angle fan of rays is launched from the source. Note the aspect ratio, as elsewhere in this thesis, is horizontally compressed. This plot was created with the ray code BELLHOP (Porter and Reiss 1983).

In the shallow ocean, refraction effects can still be important, as the temperature and salinity

of the ocean vary spatially (especially in depth, less significantly in range) and temporally (typically on the scale of hours, days or months) (Urick 1975). Reflection off a rough surface or multi-layered bottom can also be important, and introduces a frequency-dependence to the sound propagation (Jackson and Richardson 2007). Absorption can be introduced by a poroelastic or viscoelastic bottom (Bonomo 2015), or by volume attenuation of seawater (Kinsler 2006). Typically, sound speeds are relatively constant as a function of frequency, so dispersion is less important (Urick 1975), though modal dispersion due to geometrical constraints does frequently occur (Ewing 1957). Effects from diffraction, which are strongly frequency dependent, can occur for sound propagation around bathymetric obstacles (such as a sea mount (Buckingham 1986) or canyon (Chiu 2011)), as well as the focusing of sound by refraction (leading to caustics and convergence zones (Chapman 2004)). Scattering effects can be important at and near the surface (water waves, entrained air bubbles (Medwin 1970)), near the bottom (ocean floor roughness, seagrass (Lee 2017), shell hash (Stanic 1989), or methane vents (Leifer 2007)) or in the water column (fish swim bladders (Love 1978)). Interference is pervasive in the ocean due to multi-path propagation. Advection due to ocean currents is typically negligible (as they are vanishingly small fractions of the bulk sound speed (Brumley 1991)). While moving sources/targets with respect to stationary receivers could introduce Doppler shifting (Chitre 2008), this phenomenon is neglected here.

To numerically simulate wave propagation, there are many techniques available. Ray-based methods (*e.g.* BELLHOP (Porter and Bucker 1987)) efficiently capture the effects of reflection, refraction, and some types of scattering, but are only accurate in the high frequency limit, where the wavelength is much smaller than any features in the environment. Thus, ray methods neglect most of the effects of diffraction (Jensen 2011). Mode-based methods (*e.g.* KRAKEN (Porter and Reiss 1984)) exactly satisfy the wave equation in range-independent waveguides (Jensen 2011) (and approximately satisfy range-dependent waveguides (Evans 1983)), but these tend to be computationally expensive for high frequencies where hundreds or thousands of modes could be important for propagation (Jensen 2011). Methods exist

that offer intermediate speed and accuracy, as compared to rays and modes. Parabolic equation solvers (*e.g.* RAM (Collins 1996)), are one type of solver which capture some diffraction effects and naturally handle range-dependence, but due to their range-marching scheme, they cannot handle backpropagation (Tappert 1974), nor are they well suited to handle propagations over wide angles (Thomson and Chapman 1983). Other techniques, not used in this thesis, include wavenumber integration (*e.g.* OASES (Schmidt and Jensen 1985)), finite element methods (*e.g.* COMSOL (Isakson and Chotiros 2011)), and finite-difference methods (*e.g.* TDFD (Mori 2006) and FDFD (Hustedt 2004)), all of which can become computationally unwieldy in shallow ocean environments at high frequencies (Porter 1993, Jensen 2011). Numerical methods for wave propagation are important for creating simulated wave-field data (which is easier and cheaper than running experiments), but they also play an important role in some types of array signal processing.

1.1.3 Array Signal Processing for Localization

Acoustic remote sensing for localization, broadly speaking, can take on two forms: active and passive. *Active* remote sensing for *target* localization uses an acoustic transducer (a *projector*) to broadcast a known sound into the environment, and then an array of transducers to listen for echoes from the relevant target; time-of-flight is then typically used to estimate target distances. Examples of this include echolocation by bats and dolphins, as well as the popular conception of sonar. *Passive* remote sensing for *source* localization is similar, except that instead of broadcasting a known sound, one instead quietly listens to sound intentionally or unintentionally broadcasted by distant acoustic sources, and then uses the received signals to determine the source location. Not having time-of-flight information may seem like a significant problem, but your ears deal with this problem every time someone is talking to you: youre able to, even with your eyes closed, determine with reasonable accuracy where the person speaking is, thanks to the signal processing your ears and brain

perform (Cheng and Wakefield 1999)). For both active and passive acoustic remote sensing, simple acoustic environments permit simple array signal processing algorithms. However, generalizing these localization techniques to more complex environments is non-trivial.

One signal processing technique for passive source localization in arbitrary environments is called matched field processing, or MFP (Baggeroer 1993). Originally developed in the mid-1970s by Homer Bucker (Bucker 1976), MFP methods became quite popular through the 1980s and early 1990s (Katsnelson 2012, Doolittle 1993). MFP can be thought of as a generalization of the well-known array signal processing technique of *beamforming* (Jensen 2011), which like MFP, requires more than one recording element, relies upon accurately captured amplitude and phase differences between array elements, and does *not* require knowledge of the source waveform. Beamforming determines the sounds direction-of-arrival by comparing measured array data to modeled array data created from plane waves impinging on the array from a variety of possible arrival angles. MFP generalizes this technique by replacing *plane waves* from a variety of *arrival angles* with a more general *acoustic field calculation* from a variety of possible *source locations*. Thus, MFP requires significant environmental information for accurate source localization, whereas the only environmental information that beamforming requires is the local sound speed (Jensen 2011). With the additional environmental information, MFP can provide not just arrival angle estimates, but also source range and depth estimates as well. If the acoustic environment is *perfectly* known, then MFP is formulated to be the optimal localization scheme for signals in the presence of noise (Baggeroer 1988). Said differently, multi-path propagation, as is common in underwater acoustics, could be viewed from a beamforming perspective to be a signal interferer or contaminant, whereas for MFP, these additional arrivals are explicitly leveraged for more accurate source localization. Additionally, MFP, in general, does not have ranges or depths of complete insensitivity; however, depending on the environment, some dimensions can be less sensitive than others (*e.g.* MFP performed in free space is generally more sensitive to arrival angle than source range, particularly when the source range is larger than the array

aperture).

However, even in the absence of noise, an *imperfectly* known environment can create problems for MFP (Fizell 1987, Hamson and Heitmeyer 1989, Baggeror 1993). The term *environmental mismatch* is used to describe this imperfect match between the real-life environment through which sound actually propagated, and the fictional, modeled environment through which sound propagation was only simulated. Since MFP relies upon accurately capturing phase differences across the array, any environmental uncertainties or variabilities that distort these phases too significantly cause MFP techniques to not just struggle, but to catastrophically fail. Typically, for a certain level of environmental mismatch, there is some frequency below which localization with MFP is possible, and above which MFP is effectively impossible. In the shallow ocean, a nominal value for this frequency is 1 kHz (Worthmann 2015). There are techniques available in the literature that can localize sounds above this frequency, but they are typically for short propagation distances (tens or hundreds of wavelengths, rather than thousands or tens of thousands) (Baggeroer 1993) or a known source waveform (Hursky 2004), or are computationally expensive techniques that only marginally improve this frequency limitation (Collins 1991, Soares 2001, Michalopoulou and Porter 2006). Developing a physics-based source localization technique that is *fundamentally* robust to environmental mismatch is the objective of this thesis research, as one does not otherwise exist in the literature.

1.2 Thesis Overview

1.2.1 Autoproduct Idea

What if it were possible to take recorded array measurements and create a new set of quantities that appear to be at a much lower or much higher frequency? This is the central

motivating idea for the *frequency-difference autoproduct* (AP_Δ) and *frequency-sum autoproduct* (AP_Σ), respectively. These terms are not standard nomenclature in the field they were in fact coined during this thesis research. The two autoproducts are defined below:

$$AP_\Delta\left(\boldsymbol{r},\omega,\Delta\omega\right) \equiv P\left(\boldsymbol{r},\omega+\frac{\Delta\omega}{2}\right)P^*\left(\boldsymbol{r},\omega-\frac{\Delta\omega}{2}\right) \leftrightarrow \widetilde{P}\left(\boldsymbol{r},\Delta\omega\right)$$

$$AP_\Sigma\left(\boldsymbol{r},\omega,\Delta\omega\right) \equiv P\left(\boldsymbol{r},\omega+\frac{\Delta\omega}{2}\right)P\left(\boldsymbol{r},\omega-\frac{\Delta\omega}{2}\right) \leftrightarrow \widetilde{P}\left(\boldsymbol{r},\Sigma\omega\right)$$

As defined here and throughout this thesis, $\boldsymbol{r}$ is the spatial coordinate, P is the measured or modeled acoustic field, ω is the in-band frequency (contained in the nominal bandwidth $\Omega_L \leq \omega \leq \Omega_H$, $\Delta\omega$ and $\Sigma\omega$ are the difference and sum frequency respectively (and are collectively referred to as *out-of-band* frequencies). Note that the right-most double-arrow correspondences turn into equalities when $P\left(\mathbf{r},\omega\right) = \exp\left(i\omega\frac{\hat{\mathbf{n}}}{c}\cdot\boldsymbol{r}\right)$, a plane wave with unity amplitude. The tildes on the right hand side indicate the fact that these fields do not genuinely propagate or exist in the physical environment.

The quantities in (Worthmann and Dowling 2017) are called *autoproducts* because they are products of complex field amplitudes drawn from the same acoustic field, evaluated at the same spatial position, but at different frequencies. Generalizations of these quantities to higher order (*e.g.* cubic or quartic products) or evaluations at different spatial positions instead of (or in addition to) different frequencies are possible but are beyond the scope of this thesis.

Autoproducts were originally utilized by a prior PhD student to determine direction-of-arrivals with a sparse array for synthetic blind deconvolution (Abadi 2012). The success observed in so-called frequency-difference beamforming was the motivation behind this thesis.

1.2.2 Thesis Objectives

The objective of this thesis is effectively two-fold: (1) explore the utility of autoproducts for shallow ocean source/target localization using realistic simulations and experimental ocean data, and (2) explore the theoretical limitations of autoproducts to mimic genuine out-of-band fields using simple acoustic environments and experiments, combined with mathematical analyses.

In exploring a new technique, it may be more intuitive to begin with the theory, and then apply it to an application. However, chronologically, the research actually began with an application, the success of which led to theoretical questions of how it worked, and under what limitations. This newly-found theory was then used to improve source localization results, thus closing the circle of theory and application.

1.2.3 Thesis Organization

This chapter serves as an introduction, providing the relevant background information as well as a high-level description of the research projects main ideas and objectives. Chapters 2 – 9 are effectively reproductions of existing journal articles, or soon-to-be-submitted manuscripts. As such, they each contain their own title, abstract, introduction, and conclusion. There may be intellectual overlap between the various chapters introductions, but the objective of each chapter/manuscript is distinct, as summarized below.

Chapter 2 introduces the frequency-difference matched field processing technique, and applies the technique to realistic shallow ocean environments using simulated as well as experimental propagation data. This paper was intended as a proof-of-concept for the utility of autoproducts in the task of source localization. The content from this chapter has been published in the Journal of the Acoustical of America (Worthmann 2015).

Chapter 3 presents a follow up study to the previous chapter, and presents the sensitivity of the technique to noise, as well as develops extensions of existing MFP algorithms to their frequency-difference autoproduct-based analogues, and provides those techniques performance with experimental data taken from the ocean. The content from this chapter has also been published in the Journal of the Acoustical Society of America (Worthmann, Song and Dowling 2017).

Chapter 4 presents an application of frequency-difference autoproducts to active sonar, which differs from passive sonar in that source waveforms and time-of-flight techniques are possible for target ranging, but the effects of reverberation are significant. A coherently-averaged version of frequency difference matched field processing is developed which outperforms the more conventional matched filtering technique in the simulated shallow ocean environment provided. The content from this chapter was originally submitted as a conference proceeding for the International Congress on Acoustics meeting in Buenos Aires in 2016; the Proceedings on the Meetings of Acoustics journal now hosts this article (Worthmann and Dowling 2016). Note that this publication was not subject to peer review.

Chapter 5 acknowledges the successes of autoproducts for localization, and poses the question of what theoretical justifications are there for shifting frequencies around in this manner. Helmholtz equation analyses, particularly in the ray acoustics approximation, are provided here, and analytical and simulated of autoproduct fields are compared to genuine out-of-band analytical and simulated acoustic fields. This paper describes some of the theoretical limitations of autoproducts to mimic out-of-band fields. The content from this chapter has been published in the Journal of the Acoustical Society of America (Worthmann and Dowling 2017).

Chapter 6 is a follow up study to Chapter 5, and presents laboratory-scale experimental measurements obtained in collaboration with mechanical engineering undergraduate student Ms. Jessica Lipa. These experimental results validated the theoretical predictions and claims

presented in Chapter 5, and showed that even under the imperfect conditions, autoproducts could be shown to successfully mimic out-of-band fields in a simple two-path environment. The content from this chapter has also been published in the Journal of the Acoustical Society of America (Lipa *et al.* 2018).

Chapter 7 presents analyses of the effect that diffraction has on the ability of autoproducts to mimic out-of-band fields. Particularly of interest are acoustic shadow zones where the previous ray-based theory is unable to make any predictions of, since no rays propagate into shadow zones. In this chapter, the shadow zones are created by barriers placed in a homogeneous medium, and ensonified with a plane wave. The barriers considered are a semi-infinite rigid plane, and acoustically hard and soft spheres.

Chapter 8 is closely related to the previous chapter; however, instead of considering diffraction behind barriers, an inhomogeneous sound speed leading to refraction is used. In other words, diffractive effects that are created as a result of refraction are presented, with specific attention paid to the effect of caustics and refraction-created shadow zones on autoproducts. In such media, the ray acoustics is generally valid, except in and near caustics. Interestingly, it is found that the ray-acoustic breakdown at caustics causes autoproducts to partially lose their ability to mimic genuine fields.

Chapter 9 utilizes the theory developed over the previous chapters, especially Chapter 5, and to improve source localization performance. Here, the cross-terms from the quadratic nonlinearity (which arise in multipath autoproducts) are shown to lead to degradation of the dynamic range of MFP ambiguity surfaces. Techniques are proposed which can improve dynamic range by mitigating the effects of these cross-terms.

Chapter 10 summarizes the results of this thesis, and presents the overall conclusions that can be drawn from it.

There are multiple appendices, which each provide auxiliary information not included else-

where in the chapters. Appendix A considers the similarity of autoproducts to standard signal processing techniques, including Wigner transforms and other bilinear time-frequency formulations. Appendix B provides some intermediate results that are part of a modal decomposition derivation that is utilized in Chapter 8. Appendix C compares autoproduct techniques to the related Δk -radar technique, and highlights some of the main similarities and differences.

A graphical representation of the outline of, and the topical connections made within, this thesis is shown in 1.2.

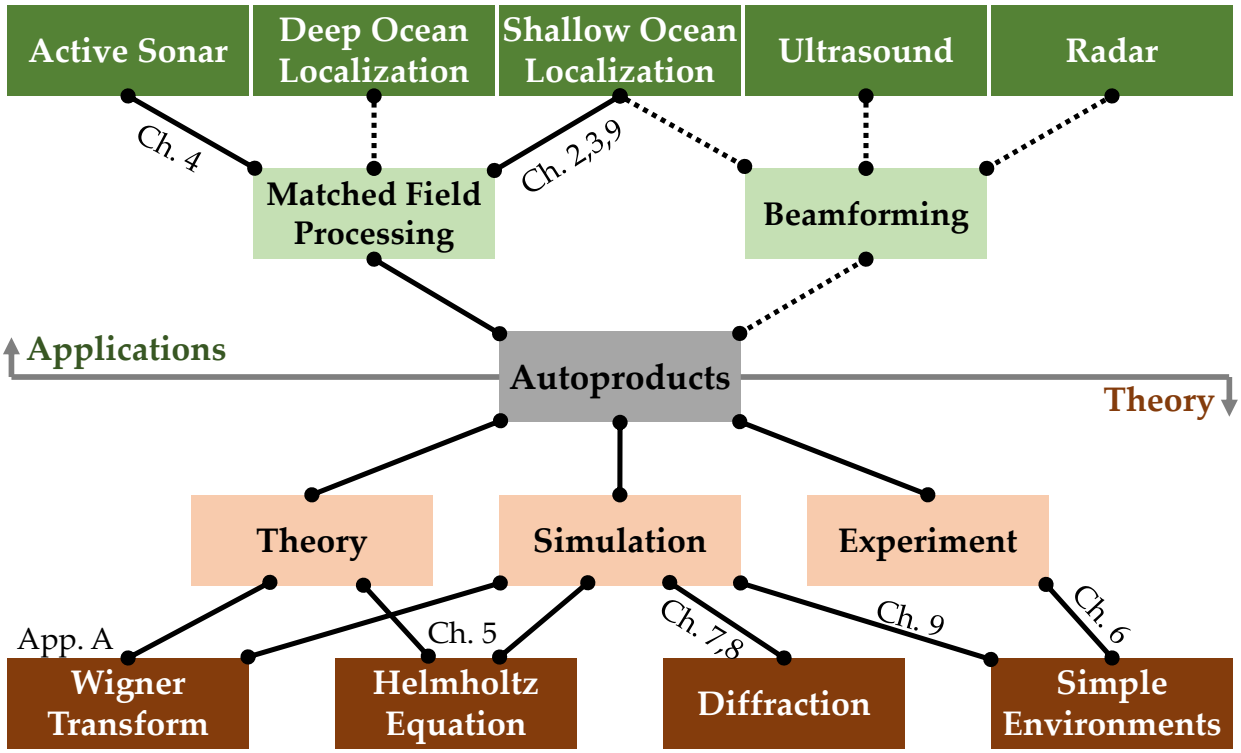

Figure 1.2: Organizational schematic of this thesis. Solid black lines indicate some of the types of results given in *this* thesis. The black lines do not indicate these topics are solved, just that some progress has been made. Dotted lines indicate topics that have been excluded from this thesis, have been given to other PhD students. The chapter and appendix labels are meant as a rough guide, not as a definitive statement of applicability. Additionally, the topics listed here are not meant to be an exhaustive list; many more applications of autoproducts are possible, just as there are other methods of understanding the theoretical nature of autoproducts.

CHAPTER 2

High Frequency Source Localization in a Shallow Ocean Sound Channel Using Frequency Difference Matched Field Processing

Abstract

Matched field processing (MFP) is an established technique for source localization in known multipath acoustic environments. Unfortunately, in many situations, particularly those involving high frequency signals, imperfect knowledge of the actual propagation environment prevents accurate propagation modeling and source localization via MFP fails. For beamforming applications, this actual-to-model mismatch problem was mitigated through a frequency downshift, made possible by a nonlinear array-signal-processing technique called frequency difference beamforming (Abadi *et. al.* 2012). Here, this technique is extended to conventional (Bartlett) MFP using simulations, and measurements from the 2011 Kauai Acoustic Communications MURI experiment (KAM11), to produce ambiguity surfaces at frequencies well below the signal bandwidth, where the detrimental effects of mismatch are reduced. Both the simulation and experimental results suggest that frequency difference

MFP can be more robust against environmental mismatch than conventional MFP. In particular, signals of frequency 11.2 kHz to 32.8 kHz were broadcast 3 km through a 106-m-deep shallow-ocean sound channel to a sparse 16-element vertical receiving array. Frequency difference MFP unambiguously localized the source in an assortment of experimental data sets with average peak-to-side-lobe ratio of 0.9 dB, average absolute-value range error of 170 m, and average absolute-value depth error of 10 m.

2.1 Introduction

Source localization is the task of determining the location of a remote sound source based on recordings from one or more transducers. While this task has applications in many areas of acoustics (see Dowling and Sabra 2015), the focus here is on source localization in an imperfectly known shallow ocean environment where a vertical array of hydrophones passively records sound broadcast from the remote source. In this circumstance, reflection, refraction, and scattering of the sound propagating away from the source will lead to multipath propagation that cannot be perfectly predicted because the requisite environmental knowledge is not available. The phase errors between predicted and actual acoustic propagation grow monotonically with increasing range and signal frequency. However, when the range and signal frequency are low enough, acoustic propagation predictions and measurements may possess some coherence, and array-signal-processing techniques, such as beamforming or matched field processing (MFP), may be used to deduce the array-to-source direction, the array-to-source range, and the source depth. The purpose of this article is to describe a novel type of MFP that uses nearby frequency components within a recorded high frequency signal to recover low frequency propagation information that can be used for source localization via conventional (Bartlett) MFP incoherently averaged over the various signal bandwidths.

Matched field processing (MFP) was first proposed for source localization in ocean sound

channels approximately four decades ago (Bucker 1976). It is a mature area of array signal processing that involves a number of different schemes (Baggeroer et al. 1993, Jensen et al. 2011). MFP is usually formulated as a frequency domain spatial filtering of array-recorded complex field values where the complex filter weights, known as replicas, for each array element and presumed source location are based on computational point-source solutions of the Helmholtz equation obtained with a model of the ocean environment. The output of MFP, known as an ambiguity surface, depends on the signal frequency and presumed source coordinates. When there is one source and MFP is successful, the global maximum in the MFP ambiguity surface indicates the source location.

Conventional (or Bartlett) MFP is the simplest scheme. In the frequency domain, it provides a normalized measure of the coherence or correlation of the measured and computed complex fields. In the time-domain, conventional MFP can be thought of as a two-step process. First, the source sends its waveform *forward* through the true environment to the recording array. Then, field information at the array is propagated *backward* through a computational model of the environment (note that acoustic reciprocity allows this forward- and backward-propagation interpretation to be reversed). Comparisons between the measured fields and modeled fields allow the formation of an acoustic map (the ambiguity surface) of possible source locations. The intent is to determine the location where the recorded multipath signals would recombine. Conventional MFP commonly serves as a benchmark for more advanced techniques, and is quantitatively described in the next section. In ideal circumstances, the resolution of conventional MFP increases with increasing frequency. For broadband signals, conventional MFP ambiguity surfaces from different frequencies may be incoherently combined. In the present research effort, an extension of conventional broadband MFP was implemented to spatially filter a quadratic product of recorded complex field amplitudes created from two nearby frequencies, with the Helmholtz equation computation for the complex weights performed at the difference of the two frequencies.

The primary limitation of MFP arises from mismatch between the simulated acoustic field computed in the model environment and the actual acoustic field measured in the physical environment. This environmental mismatch problem leads to a lack of robustness in MFP source location estimates and increases in severity with increasing frequency and array-to-source range. It is caused by the same sensitivity to the acoustic field phase that leads to beneficial increased MFP source location resolution at higher frequencies. An actual ocean environment is dynamic and cannot be known to arbitrary precision, and thus, in practice, 1 kHz is an approximate nominal upper frequency limit for successful application of conventional MFP in shallow ocean environments. In enclosed reverberant environments, the advantages of MFP are lost when the random mismatch exceeds more than approximately 1/3 of an acoustic wavelength (Williamson *et. al.* 2014). Yet, the technique described here, frequency difference MFP, can be successful at higher frequencies by sacrificing the resolution possible from a high-frequency signal in favor of greater robustness to mismatch.

There are MFP techniques that provide higher resolution source localization results than conventional MFP. For example, adaptive techniques such as Minimum Variance Distortionless Response (MVDR) (Johnson 1982, Baggeroer 1988), and Matched Mode Processing (MMP) (Shang 1985) both offer better source localization resolution than conventional MFP at low frequencies. However, these techniques all suffer similarly at higher frequencies because of the environmental mismatch problem, and all are based on the direct use of the complex field, not a quadratic field product as is the case for frequency difference MFP. At high underwater sound frequencies, techniques involving a modal decomposition become difficult to use, both due to the computational cost associated with high frequency mode calculations, and due to the fact that mode shapes and wavenumbers which may be used to localize a source become strongly dependent on the modeled sound speed profile, which may not be known sufficiently well at high frequency another incarnation of the mismatch problem. An alternative high-frequency source localization technique (Hursky *et. al.* 2004) utilizes the multipath arrival-time structure in the shallow ocean. By knowing the source waveform, and

having several independent trials (snapshots) to average over, this model-based technique was able to localize high frequency sources. For comparison, the frequency difference MFP technique described here does not require high frequency mode calculations, knowledge of the source waveform, or multiple independent trials for averaging. Additionally, it can be successful with very sparse arrays.

In previous work, the frequency difference concept was used for beamforming with a sparse array for blind deconvolution of a remote source signal (Abadi *et. al.* 2012). The present work extends this beamforming technique to MFP to create a source localization technique that is inherently robust to environmental mismatch, and thus offers new possibilities for source localization at frequencies previously inaccessible for MFP.

The remainder of this manuscript is organized into four sections. The next section describes the mathematical formulation of the frequency difference MFP technique in comparison to conventional MFP. The third section presents simulation results for frequency difference MFP. The fourth section documents the results of this technique with experimental data recorded during the Kauai Acoustic Communications Multiple University Research Initiative (MURI) experiment of 2011 (KAM11). The final section summarizes the results of this research and provides the conclusions drawn from it.

2.2 Mathematical Formulation

2.2.1 Single and Bi-frequency MFP Formulations

Acoustic pressure fluctuations from a simple point source in a shallow-ocean sound channel with a spatially varying sound speed satisfy the inhomogeneous Helmholtz equation

$$\left[\nabla^2 + \frac{\omega^2}{c^2(\boldsymbol{r})}\right] P(\boldsymbol{r},\omega) = -S(\omega)\,\delta(\boldsymbol{r}-\boldsymbol{r}_s) \tag{2.1}$$

where $P(\boldsymbol{r},\omega)$ is the complex acoustic pressure at radian frequency $\omega = 2\pi f$, $c(\boldsymbol{r})$ is the actual, spatially-varying sound speed in the environment, $S(\omega)$ is the Fourier-transform of the sources pressure signal, and $\boldsymbol{r}_s$ is the point sources location.

Conventional MFP, as discussed in the last section, correlates measured and modeled complex field amplitudes to localize the source. For a harmonic signal, the conventional MFP ambiguity surface $B_c(\boldsymbol{r},\omega)$ is defined by:

$$B_c(\boldsymbol{r},\omega) = \frac{\left|\sum_j P_j(\omega)\, w_j^*(\boldsymbol{r},\omega)\right|^2}{\sum_j |P_j(\omega)|^2 \sum_j |w_j(\boldsymbol{r},\omega)|^2} \tag{2.2}$$

where $P_j(\omega) = P(\boldsymbol{r},\omega)$ is the field measured by the jth hydrophone at frequency ω. Additionally, the replica field, $w_j(\boldsymbol{r},\omega)$, is the simulated field from a point source at the test location $\boldsymbol{r}$ that reaches the jth hydrophone at frequency ω, and the asterisk denotes a complex conjugate. The denominator is a normalization factor chosen to guarantee that $0 \leq B_c(\boldsymbol{r},\omega) \leq 1$, where zero denotes no correlation of $P_j(\omega)$ and $w_j^*(\boldsymbol{r},\omega)$, while unity denotes perfect correlation of $P_j(\omega)$ and $w_j^*(\boldsymbol{r},\omega)$. In (2.2), the replica field is the Greens function in the modeled environment, $w_j(\boldsymbol{r},\omega) = G_c(r_j,\boldsymbol{r},\omega)$, where

$$\left[\nabla^2 + \frac{\omega^2}{c_m^2(\boldsymbol{r})}\right] G_c(\boldsymbol{r},\boldsymbol{r}',\omega) = -\delta(\boldsymbol{r}-\boldsymbol{r}') \tag{2.3}$$

$c_m(\boldsymbol{r})$ is the speed of sound in the modeled environment, and $\delta(\boldsymbol{r})$ is the Dirac-delta function. Ideally, $c_m(\boldsymbol{r})$ is the same as $c(\boldsymbol{r})$, so any differences between c and c_m contribute to the environmental mismatch problem.

Now consider a signal with only two frequency components, ω_1 and ω_2, which can be ex-

pressed equivalently as $\omega \pm \frac{\Delta\omega}{2}$, where for most problems of interest, $\Delta\omega$ is much less than ω. For simplicity here, assume the source broadcasts just these two frequency components. The more practically relevant broadband formulation is presented in 2.2.3. One may define a new quantity, termed the frequency-difference autoproduct, or $AP_{\Delta,j}$, which is a quadratic product of the measured field P_j at these two frequencies:

$$AP_{\Delta,j}\left(\omega, \Delta\omega\right) = P_j\left(\omega + \frac{\Delta\omega}{2}\right) P_j^*\left(\omega - \frac{\Delta\omega}{2}\right) \tag{2.4}$$

The frequency-difference MFP ambiguity surface, $B_{\Delta f}\left(\boldsymbol{r}, \omega, \Delta\omega\right)$ is formulated using (2.4) in place of $P_j\left(\omega\right)$ in (2.2) with w_j evaluated at $\Delta\omega$:

$$B_{\Delta f}\left(\boldsymbol{r}, \omega, \Delta\omega\right) = \frac{\left|\sum_j AP_{\Delta,j}\left(\omega, \Delta\omega\right) w_j^*\left(\boldsymbol{r}, \Delta\omega\right)\right|^2}{\sum_j \left|AP_{\Delta,j}\left(\omega, \Delta\omega\right)\right|^2 \sum_j \left|w_j\left(\boldsymbol{r}, \Delta\omega\right)\right|^2} \tag{2.5}$$

In spite of their similar formulation, (2.2) and (2.5) are different in two important ways. First, the numerator summand in (2.5) is a triple product of fields (two measured and one computed) as opposed to the numerator summand in (2.2) which is a quadratic product of fields (one measured and one computed). And second, the replica $w_j\left(\boldsymbol{r}, \omega\right)$ in (2.2) is calculated from (2.3) at the signal frequency ω whereas the replica $w_j\left(\boldsymbol{r}, \Delta\omega\right)$ in (2.5) is calculated at the difference-frequency $\Delta\omega$:

$$\left[\nabla^2 + \left(\frac{\Delta\omega}{c_m\left(\boldsymbol{r}\right)}\right)^2\right] G_{\Delta f}\left(\boldsymbol{r}, \boldsymbol{r}', \Delta\omega\right) = -\delta\left(\boldsymbol{r} - \boldsymbol{r}'\right) \tag{2.6}$$

where $w_j\left(\boldsymbol{r}, \Delta\omega\right) = G_{\Delta f}\left(r_j, \boldsymbol{r}, \Delta\omega\right)$. Additionally, the boundary conditions used in (2.3) are different from those used in (2.6). The reasons for this are provided in 2.2.5.

2.2.2 Interpretations of the Autoproduct

The autoproduct can be interpreted as an acoustic Moir pattern. Consider Figure 2.1, where two nearby high frequencies plane-waves are represented schematically with two sets of vertical bars with slightly different spacings. Here for unity amplitude, unity sound speed, and unity spatial extent, let the upper set of bars correspond to the real part of the complex plane wave $\exp[2\pi i(101)]$, and let the lower set bars correspond to the real part of the complex plane wave $\exp[-2\pi i(99)]$, so that there are two more cycles ($101 = 99 + 2$ bars) in the upper set compared to the lower set (99 bars). When the product of the two plane waves is formed the phases add, $\exp[2\pi i(101)] \times \exp[-2\pi i(99)] = \exp[2\pi i(2)]$, and this addition is displayed in the central overlapping region of the figure which represents the autoproduct and clearly shows a two cycle visual pattern (a Moir pattern) having a much lower spatial frequency. In this visual example, the wavefront kinematics require two low-frequency cycles because of the two extra high frequency cycles in the upper set of bars. Even though the visual-acoustic analogy described here may be imperfect, the autoproduct can be interpreted as a mathematical construction that provides low-frequency information in a manner similar to that of a visual Moir pattern.

Another analogy involves a phasor description of the complex signal from a single receiver and is shown in Figure 2.2. First consider how conventional MFP relates to this figure in a single-path acoustic environment. Start with an acoustic wave, given by $P(\omega) = A(s)\exp(i\omega s/c)$ where the amplitude A is real and s the distance along the propagation path. The phase of this wave, $\omega s/c$, can represent numerous phase-wraps, particularly for high frequency signals. And for illustration purposes, assume $A(s)$ decreases smoothly as s increases because of wave spreading. The two-factor summand in conventional MFP, see (2.2), is $P(\omega)\, w^*(\omega)$, where the hydrophone index j and dependence on the test coordinate $\boldsymbol{r}$ have been omitted for simplicity. The first term, $P(\omega)$, can be represented as the phasor that starts as the arrow A and spirals inward along the solid line, shown in Fig. 2.2, to become arrow B when

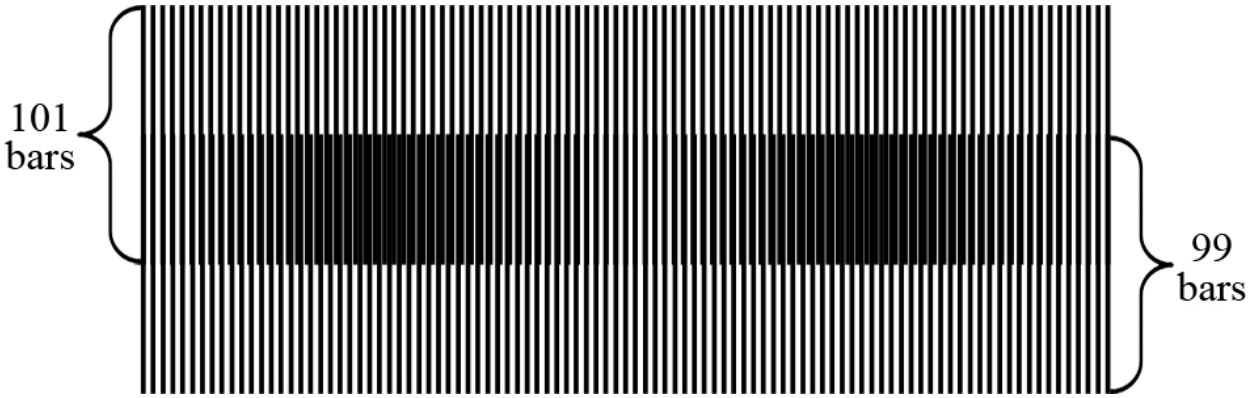

Figure 2.1: Acoustic Moire patterns. The top two-thirds of this figure have 101 evenly spaced vertical bars, and the bottom two-thirds of the figure have 99 evenly spaced vertical bars. The middle one-third of this figure shows the overlap of these two patterns, where a low frequency pattern emerges, the spacing of which is related to the difference in the number of bars. This is analogous to the operating principle of frequency difference MFP in that two slightly different high frequency signals are combined in such a way to produce a result that behaves like the much lower difference frequency.

the signal reaches the receiver. Thus, $P(\omega)$ represents the forward propagation step from source to receiver and it takes place in the actual environment. Then, multiplication of $P(\omega)$ with $w^*(\omega)$ causes the phase of $w^*(\omega)$ to be added to $P(\omega)$, which in the absence of environmental mismatch, would be equal and opposite to the phase of $P(\omega)$. The phase of this ideal replica is shown as the combination of the dashed and dotted lines spiraling outward from arrow B to arrow A, and because of the complex conjugate. Thus, $w^*(\omega)$ can be viewed as a back-propagation from receiver to source, and it takes place with the model environment. Unfortunately, environmental mismatch commonly causes the replicas phase to not perfectly match the recorded signal phase, meaning that $P(\omega)\, w^*(\omega)$ may not return perfectly to where the signal started (the real axis in this case). If the phase error is $\phi_e = \omega\delta/c$, then δ is an unknown propagation difference distance between the true and modeled propagation paths, and is a measure of the environmental mismatch. When the size of such path length fluctuations are on the order of the wavelength, conventional MFP is unable to accurately estimate the source location. Other types of uncertainty, such as geometric uncertainty associated with unknown array tilt, could also be characterized in terms of an effective path length variation, δ.

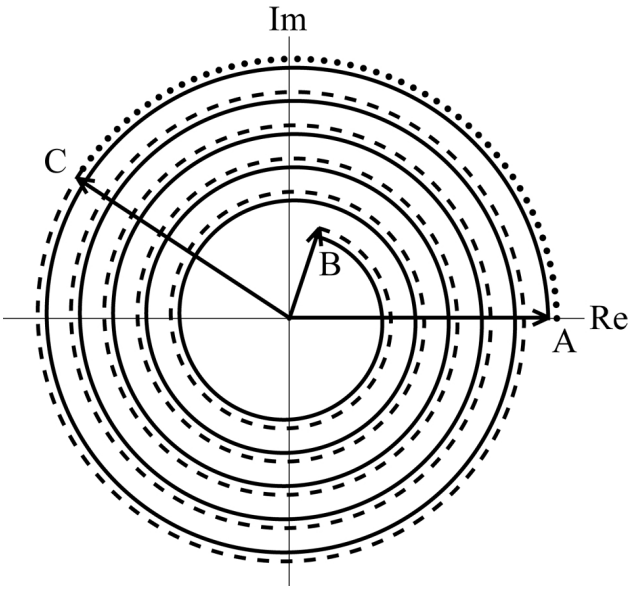

Figure 2.2: Phasor representation of frequency difference MFP. The high frequency component of the autoproduct is represented by the phasor ranging from arrow A and spirally inward to arrow B. The slightly lower frequency component of the autoproduct, with its complex conjugate, spirals outward from arrow B to arrow C. Then, the difference frequency replica, which introduces the environmental mismatch, is calculated to continue from arrow C back to the real axis near arrow A. Without mismatch, the combination of the autoproduct and replica will always land perfectly on the real axis, meaning the phases across the receivers will add coherently and produce a peak in the ambiguity surface.

Now consider the three-factor summand of frequency difference MFP from (2.5), $P\left(\omega+\frac{\Delta\omega}{2}\right)P^*\left(\omega-\frac{\Delta\omega}{2}\right)w^*\left(\Delta\omega\right)$ and again use Fig. 2.2 to interpret each factor. First, $P\left(\omega+\frac{\Delta\omega}{2}\right)$ is the forward propagation step in the actual environment, and is shown as the solid line spiraling inward from arrow A to arrow B. Second, the $P^*\left(\omega-\frac{\Delta\omega}{2}\right)$ factor is a backward propagation step in the actual environment, and is shown as the dashed line spiraling outward from arrow B to arrow C. This back-propagation step reaches the source, but at a slightly lower frequency so it involves fewer phase rotations that the forward propagation step, $P\left(\omega+\frac{\Delta\omega}{2}\right)$. Finally, the replica factor $w^*\left(\Delta\omega\right)$ completes the backward propagation step in the model environment, and is shown as the dotted line spiraling outward from arrow C back to arrow A. For a perfect match in this situation, both conventional MFP and frequency difference MFP must return to the real axis. When this occurs, contributions from individual receivers will add coherently across the array to produce a peak in the ambiguity

surface at the source location. However, when considering environmental mismatch, the phase error associated with frequency difference MFP is $(\Delta\omega)\,\delta/c$. Thus, when $\Delta\omega \ll \omega$, any such phase errors may be much less important than the equivalent phase errors in conventional MFP, $\omega\delta/c$. Therefore, improved robustness to environmental mismatch can be expected with frequency difference MFP. Also, it is possible that values for $\Delta\omega$ can be estimated if the degree of environmental variability or uncertainty is known – estimates can be performed that relate those environmental variations with corresponding path length variations, δ. Alternatively, for a desired $\Delta\omega$, the amount of environmental uncertainty that can be tolerated can be determined, again by relating environmental variations with path length variations.

2.2.3 Broadband MFP

The previous sections described how conventional and frequency difference MFP techniques are defined for single frequency and bi-frequency signals, respectively. However, most signals, and particularly high frequency signals in the shallow ocean, may have sufficient bandwidth for MFP to be conducted over a range of frequencies. In this case, combining the ambiguity surfaces from multiple frequencies is possible, and may improve the source location estimate.

While there are many ways to create a broadband MFP technique, the simplest is to incoherently average the single-frequency ambiguity surface defined by (2.2) over frequencies in the signals bandwidth:

$$B_{c,avg}\left(\boldsymbol{r}\right) = \frac{1}{M}\sum_{m=1}^{M} B_c\left(\boldsymbol{r},\omega_m\right). \tag{2.7}$$

Here m is the frequency index, $1 \le m \le M$, and $\omega_m = \Omega_L + \left[\frac{m-1}{M-1}\right](\Omega_U - \Omega_L)$ are sample frequencies uniformly spaced between the lower (Ω_L) and upper (Ω_U) frequency bounds of

the signals bandwidth.

Broadband frequency difference MFP has two sets of frequencies, ω and $\Delta\omega$, and both may be averaged over incoherently, so (2.5) becomes:

$$B_{\Delta f,avg}\left(\boldsymbol{r}\right) = \frac{1}{N'}\sum_{n=1}^{N'}\left(\frac{1}{M'}\sum_{m=1}^{M'} B_{\Delta f}\left(\boldsymbol{r},\omega_m,\Delta\omega_n\right)\right) \tag{2.8}$$

Here, m is again the frequency index, $1 \leq m \leq M'$, but $\omega_m = \left(\Omega_L + \frac{\Delta\omega}{2}\right) + \left[\frac{m-1}{M'-1}\right]\left(\Omega_U - \Omega_L - \Delta\omega\right)$ so that the difference frequency is accommodated within in the signal bandwidth at the lower and upper frequency limits of the sum where $m = 1$ and M', respectively. The inner sum in (2.8) includes all possible pairs of frequencies separated by a given $\Delta\omega_n$. In (2.8), difference frequencies, $\Delta\omega$, are constrained to lie in the signal bandwidth, $0 < \Delta\omega_n \leq \Omega_U - \Omega_L$, but otherwise may be selected by the user. In the present study, N' difference frequencies were uniformly spaced between lower ($\Delta\Omega_L$) and upper ($\Delta\Omega_U$) difference-frequency bounds of 50 Hz and 500 Hz, respectively. Thus, with n as the difference-frequency index, $1 \leq n \leq N'$, the difference frequencies in (2.8) are given by$\Delta\omega_n = \Delta\Omega_L + \left[\frac{n-1}{N'-1}\right]\left(\Delta\Omega_U - \Delta\Omega_L\right)$.

Interestingly, the first averaging step in (2.8) may be considered analogous to the additional averaging step that multiple signal snapshots would bring to (2.7). Notably however, (2.8) does not need multiple snapshots, and so it is possible that the statistical reliability associated with multiple snapshots may be achievable with just a single snapshot when the signal bandwidth is large enough. Additionally, it can be noted that the Wiener-Khintchine Theorem (Pierce, 1994) does not apply to this autoproduct formulation because there is no ensemble average, nor is there a bandwidth average over the autoproduct itself.

2.2.4 Source Waveform Dependence

By using signal frequencies in pairs, intuition may suggest that some degree of coherence in the phases across the different frequency pairs is necessary for success. However, this is not the case, the formulation of frequency difference MFP provided by (2.8) is independent of the source signal to the same extent as the formulation of conventional MFP provided in (2.7).

This independence can be seen as follows. In a time invariant environment, $P_j(\omega) = S(\omega) G_j(\omega)$, where $S(\omega)$ is the source spectrum and $G_j(\omega)$ is the solution of (2.1) at the location of the jth receiver when $S(\omega) = 1$. Additionally, consider $S(\omega)$ in magnitude and phase form: $S(\omega) = |S(\omega)| \, exp(i\phi_s(\omega))$, where $\phi_s(\omega)$ is the signal phase. Therefore, from (2.4), the autoproduct is:

$$AP_{\Delta,j}(\omega, \Delta\omega) = |S_+| \, |S_-| \, e^{i\phi_s\left(\omega+\frac{\Delta\omega}{2}\right)-i\phi_s\left(\omega+\frac{\Delta\omega}{2}\right)} G_j\left(\omega + \frac{\Delta\omega}{2}\right) G_j^*\left(\omega - \frac{\Delta\omega}{2}\right) \tag{2.9}$$

where the $\pm$ subscripts refer to evaluations at the frequencies $\omega \pm \frac{\Delta\omega}{2}$. When normalized as is shown in (2.5), the dependence on the sources amplitude is removed, but the phase dependence remains.

$$\frac{AP_{\Delta,j}(\omega, \Delta\omega)}{\sqrt{\sum_j |AP_{\Delta,j}(\omega, \Delta\omega)|^2}} = e^{i\phi_s\left(\omega+\frac{\Delta\omega}{2}\right)-i\phi_s\left(\omega-\frac{\Delta\omega}{2}\right)} \frac{G_j\left(\omega + \frac{\Delta\omega}{2}\right) G_j^*\left(\omega - \frac{\Delta\omega}{2}\right)}{\sqrt{\sum_j |G_j\left(\omega + \frac{\Delta\omega}{2}\right) G_j^*\left(\omega - \frac{\Delta\omega}{2}\right)|^2}} \tag{2.10}$$

Continuing with the frequency difference MFP technique as defined in (2.5), one must multiply (2.10) with the normalized replica vector $w_j^*(\boldsymbol{r}, \Delta\omega) \,/\, \left[\sum_j |w_j(\boldsymbol{r}, \Delta\omega)|^2\right]^{1/2}$ and sum over array elements. At this point, the sources phase information is still present, as shown in (2.11). However, the source-phase factors are independent of the receiver index (j), and may

pass through the summation over receivers:

$$b_{\Delta f}\left(\boldsymbol{r},\omega,\Delta\omega\right)=e^{i\phi_s\left(\omega+\frac{\Delta\omega}{2}\right)-i\phi_s\left(\omega-\frac{\Delta\omega}{2}\right)}\frac{\sum_j G_j\left(\omega+\frac{\Delta\omega}{2}\right)G_j^*\left(\omega-\frac{\Delta\omega}{2}\right)w_j^*\left(\boldsymbol{r},\Delta\omega\right)}{\sqrt{\sum_j\left|G_j\left(\omega+\frac{\Delta\omega}{2}\right)G_j^*\left(\omega-\frac{\Delta\omega}{2}\right)\right|^2}\sqrt{\sum_j\left|w_j^*\left(\boldsymbol{r},\Delta\omega\right)\right|^2}} \tag{2.11}$$

Equation (2.11) only contains source waveform dependence in the form of a complex phase factor. The quantity shown in (2.11) may be used in a blind deconvolution scheme to recover the source phase, as described in Abadi *et. al.* (2012) for frequency difference beamforming. However, in the present formulation, the objective is source localization, which does not require the source phase information. Taking the magnitude-squared of (2.11) recovers frequency-difference MFP formulation as defined by (2.5), but with all information about the sources waveform removed.

$$\left|b_{\Delta f}\left(\boldsymbol{r},\omega,\Delta\omega\right)\right|^2=B_{\Delta f}\left(\boldsymbol{r},\omega,\Delta\omega\right)=\frac{\left|\sum_j G_j\left(\omega+\frac{\Delta\omega}{2}\right)G_j^*\left(\omega-\frac{\Delta\omega}{2}\right)w_j^*\left(\boldsymbol{r},\Delta\omega\right)\right|^2}{\sum_j\left|G_j\left(\omega+\frac{\Delta\omega}{2}\right)G_j^*\left(\omega-\frac{\Delta\omega}{2}\right)\right|^2\sum_j\left|w_j^*\left(\boldsymbol{r},\Delta\omega\right)\right|^2} \tag{2.12}$$

Intuitively, this independence on the source waveform may be expected, since the MFP formulation seeks only relative phase differences between receivers, not absolute phases. Even though the autoproduct has source waveform information embedded in it, as shown in (2.9), with the appropriate normalizations, the source waveforms contributions appear only as a phase factor in front of the summations, which disappears upon taking the magnitude. An analogous procedure can be used to show that conventional MFP is independent of the source waveform, too. Therefore, no restrictions on the source waveform are necessary, particularly those involving any kind of phase structure or symmetry.

2.2.5 Consequences of Nonlinearity

Several features of frequency difference MFP do not have conventional analogues, such as the users ability to choose the frequency difference bandwidth (see above), the need to be concerned with the production of unintentional cross-terms, and the requirement for calculating the replicas in an environment with unnatural boundary conditions. The second two features are consequences of the quadratic nonlinearity of the autoproduct.

In a multipath environment, the nonlinearity of the autoproduct causes both desired and unintentional path-product terms to arise. Consider a sum-of-rays form for the recorded complex pressure at frequencyω in the vicinity of the jth receiver:

$$P_j(\omega) = \sum_n A_{jn} \exp(i\omega\tau_{jn}), \tag{2.13}$$

Here A_{jn} and τ_{jn} are the normalized complex amplitude and relative arrival time of the nth ray at the jth hydrophone, respectively. The dependence of A_{jn}on frequency may come in the form of the source waveform (discussed in the previous section as unnecessary for MFP), and may include frequency dependent propagation effects (neglected). Therefore, within this approximation, A_{jn}may be considered frequency independent. When $\Delta\omega$ is small enough so that τ_{jn} may also be considered frequency independent, then the un-normalized autoproduct is:

$$P_j\left(\omega + \frac{\Delta\omega}{2}\right) P_j^*\left(\omega - \frac{\Delta\omega}{2}\right) = \underbrace{\sum_n |A_{jn}|^2 \exp(i\Delta\omega\tau_{jn})}_{desired}$$
$$+ \underbrace{\sum_{n>m} \sum_m 2\,|A_{jn}|\,|A_{jm}| \exp\left(\frac{i\Delta\omega(\tau_{jn}+\tau_{jm})}{2}\right) \cos\left(\omega(\tau_{jn}-\tau_{jm}) + \phi_{nm}^j\right)}_{unintentional} \tag{2.14}$$

where $\phi^j_{nm} = arg\,(A_{jn}) - arg\,(A_{jm})$. For Q total wave front arrivals, the desired sum in (2.5) includes the Q diagonal terms ($m = n$) and its phase is independent of ω. Moreover, its appearance is essentially identical to (2.13) except that the phase factor depends on the frequency difference $\Delta\omega$, which is much lower than ω. The unintentional sum in (2.5) is comprised of the $(Q^2 - Q)$ off-diagonal terms ($m \neq n$) which occur in pairs and lead to the cosine factor that explicitly depends on ω. Thus, when $\tau_{jm} \neq \tau_{jn}$, averaging (2.5) through the signal bandwidth should not affect the desired sum but it should suppress the contribution of the unintentional sum since the cosine factor may rapidly change sign as ω varies, provided ω is large enough.

In addition, since the desired sum has the same character as a sound field at $\Delta\omega$ it may be well correlated with the replica evaluated at $\Delta\omega$, which can be put in the form of (2.13) as $w_j = \sum_n A'_{jn} \exp\left(i\Delta\omega\tau'_{jn}\right)$, where the primes denote computed values for the modeled environment. When this is true, the desired sum will yield terms that should add coherently across receivers due to their spatially correlated phases and it should therefore support accurate source localization. Meanwhile, the unintentional sum might not display any special correlation with w^*_j, so its influence might not be dominant even though it represents more terms than the desired sum when there are more than two wave front arrivals. Here, we note in passing that the unintentional sum is absent in single-path environments.

Thus, for successful frequency difference MFP, a sufficiently large signal bandwidth $\Omega_U - \Omega_L$ is desired. It provides a greater opportunity for the unintentional terms to cancel within the signal bandwidth averaging specified in (2.8). An additional averaging across the difference frequency bandwidth further limits the effect of the unintentional cross terms. A large signal bandwidth also permits a larger range of $\Delta\omega$ since $0 < \Delta\omega \leq \Omega_U - \Omega_L$.

Another interesting feature the frequency-difference approach is the handling of boundary conditions for replica calculations using (2.6). As a model problem, consider a simple shallow ocean waveguide with a flat pressure-release surface and a flat rigid bottom. In such an envi-

ronment, the ocean surface and bottom reflection coefficients would be1and+1, respectively. As can be seen from (2.5), the autoproduct creates the desired terms with amplitudes that depend on the magnitude squared of the original amplitudes. This implies that the replicas used in (2.5) should be computed in an ocean sound channel with reflection coefficients for both the upper and lower boundaries that are the magnitude squared of the actual reflection coefficients, or for the simple ocean waveguide,+1for both surfaces. In other words, the replica should be evaluated in the modeled environment, but with rigid bottom and *rigid* surface boundary conditions, despite the original signal having propagated through an environment with more natural boundary conditions. While this explanation may not be mathematically rigorous, using rigid boundary conditions was sufficient for source localization in the KAM 11 geometry, as discussed in Sections 2.3 and 2.4.

In more realistic shallow ocean situations, frequency-dependent interactions with the bottom may be significant. Typically, high frequency sounds do not penetrate into the bottom very significantly, whereas low frequencies may penetrate much farther. If such frequency dependence is significant, the frequency difference technique as described here may not work. However, it is possible that there is a more consistent way to modify the bottom boundary conditions in the replica calculation for a more general ocean bottom, but answering this question is beyond the scope of the present research. Yet, it should be noted that satisfactory results were obtained with this rigid surface and rigid bottom approximation when using experimental data (see Section 2.4).

Interestingly, another advantage afforded by frequency difference MFP, besides improved robustness to mismatch, is reduced computational cost. Conventional MFP requires the use of propagation calculations on grid resolutions suitable for the signal frequency ω, which can be computationally expensive at high frequency. However, frequency difference MFP merely requires the use of a propagation calculation (with the modified boundary conditions) and grid resolutions suitable for the difference frequency $\Delta\omega$, which may be significantly lower

than$\omega$and therefore less computationally expensive. The frequency difference bandwidth over which the replicas must be evaluated can be chosen to be as large as the signal bandwidth or as small as desired. Admittedly, there is an additional averaging step in frequency difference MFP, specifically an average over the difference frequency bandwidth, and performing this step will add to the techniques computational cost. Nevertheless, in the present work, frequency difference MFP was found to be approximately three to four orders of magnitude less computationally expensive than conventional MFP, even when calculated with the same search grid resolution. Further optimization of both algorithms is undoubtedly possible, but such an effort is beyond the scope of the present research.

2.3 Simulation Results

Using the formulations (2.7) and (2.8), the source localization performance of the two MFP techniques were simulated and compared in the presence of known environmental mismatch. The ocean sound channel environment and geometry used in these simulations are illustrated in Figure 2.3, and were chosen to mimic the experimental conditions of the KAM11 experiment (Hodgkiss *et. al.* 2011). The sound channel was 106 m deep, and will be modeled with a flat rigid bottom and a flat pressure-release surface. An omnidirectional source at a depth of 67.7 m broadcasted a 100-ms linear-frequency-modulated (LFM) pulse from 11.2 kHz to 32.8 kHz. This signal was recorded by a 16-element vertical line array centered 69.3 m below the ocean surface 3 km from the source. The spacing between array elements was 3.75 m for a total aperture of 56.3 m. At the signal center frequency of 22 kHz, this element spacing is more than 50 center-frequency wavelengths, making this a very sparse array. The recorded signals were sampled at a rate of 96 kHz for a duration of 300 ms. The range-independent but depth dependent sound speed profile$c\,(z)$is shown in Figure 2.4 as a solid curve. Here $c\,(z)$ is mildly downward refracting with a 5.1-m/s difference in the surface and bottom water-column sound speeds. This sound speed profile was measured near the propagation plane of

the KAM11 measurements close to the time of the propagation measurements. During the KAM11 experiment, thermistor strings were used to monitor ocean temperature variations. These variations were converted into sound speed fluctuations, and the total range of the sound speeds observed in a three-day span (JD183 JD185) during the KAM11 experiment are shown in the gray area in Fig. 2.4. Given the existence of such fluctuations, significant environmental mismatch is to be expected in the KAM11 environment, and one means of introducing such mismatch within simulation is to use a slightly different sound speed profile for the replica calculation than was used for the forward propagation. The dashed curve on Fig. 2.4 is a best-fit arctangent profile for the measured $c(z)$. The dotted curve in Fig. 2.4 is a best-fit straight-line for the measured $c(z)$. The best fit sound speeds, in m/s, are shown below as function of depth z, in meters, defined for $0 \leq z \leq 106$m.

$$c_{arctan}(z) = 1.923 \arctan(4.683 - 0.0893z) + 1534.15 \tag{2.15}$$

$$c_{linear} = 1537.61 - 0.0657z \tag{2.16}$$

These two profiles provide different amounts of environmental mismatch compared to the measured $c(z)$ and were used to test the robustness of frequency difference MFP while still capturing the wave-propagation physics of the measured sound speed profile (*i.e.* its downward refracting character).

The propagation simulations leading to the recorded pressure time series were performed with the ray-trace code BELLHOP (available from HLS Research, Inc.). For the forward propagation step, the measured sound speed profile was used. The eigenrays connecting the source to the center of the receiving array are shown in Figure 2.5 with thicker lines indicating ray paths having larger amplitudes. Notably, due to the downward refracting sound speed profile, the two water-borne-only rays (which do not reflect off the surface or bottom) have little contribution to the overall received signal; rather, the strongest contributions come from bottom-reflected rays. Only the rays arriving in the first 10 ms are shown and only

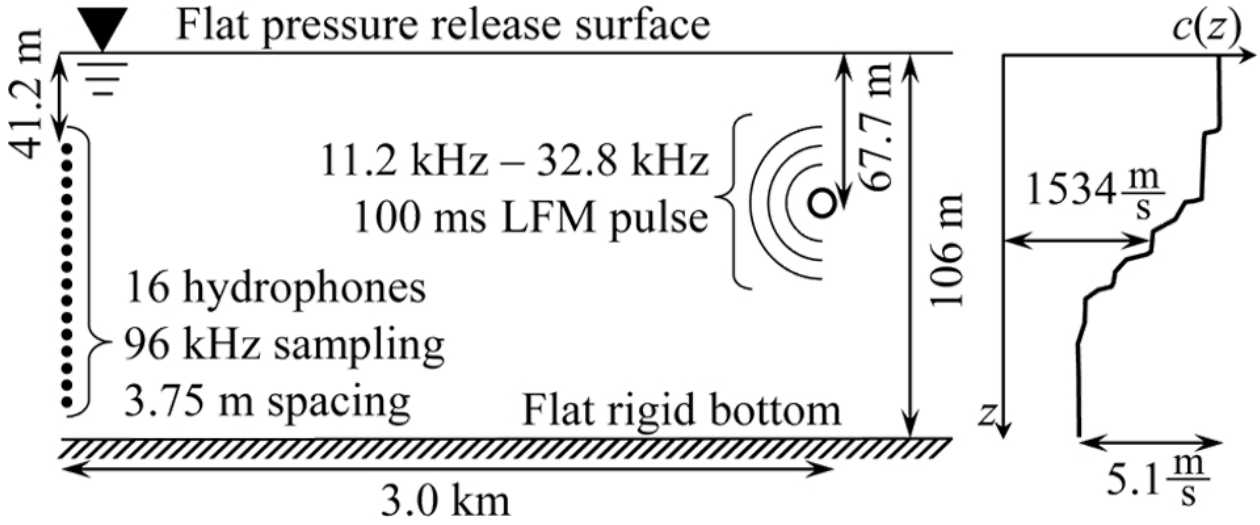

Figure 2.3: Geometry, source, and array parameters intended to mimic the KAM11 experiment. A 16-element vertical array of hydrophones spaced 3.75 m apart (half-wavelength spacing at 200 Hz), for a total array aperture of 56.25 m, is centered at 69.3 m below the surface in this 106-m-deep sound channel. At a range of 3 km, an omnidirectional source located 67.7 m below the surface broadcasts a 100-ms linear-frequency-modulated pulse from 11.2 kHz to 32.8 kHz. The bottom of the sound channel is idealized to be perfectly rigid with no absorption. The sound speed profile is downward refracting with an approximate change in sound speed of 5.1 m/s over the depth of the channel, and is taken from observed KAM11 data.

these were retained in the simulations. Later arrivals were suppressed. This 10 ms duration was chosen to mimic the approximate time delay spread observed in the KAM11 experiments. Surface scattering and bottom attenuation in the KAM 11 experimental data limited the importance of later arriving rays so that 92% of the impulse-response signal energy arrived within the first 10 ms.

The backward propagation step in the simulations was completed with some intentionally introduced mismatch. The replicas were computed using the best-fit arctangent sound speed profile, shown as the dashed curve in Fig. 2.4, and not the measured one. Otherwise, all other parameters were held at their forward-propagation-step values. For conventional MFP at the higher frequency ω, the replicas were computed using Bellhop. For frequency difference MFP at the lower frequency $\Delta\omega$, the replicas were calculated with a modal decomposition using rigid surface and bottom boundary conditions, a necessary consequence of performing

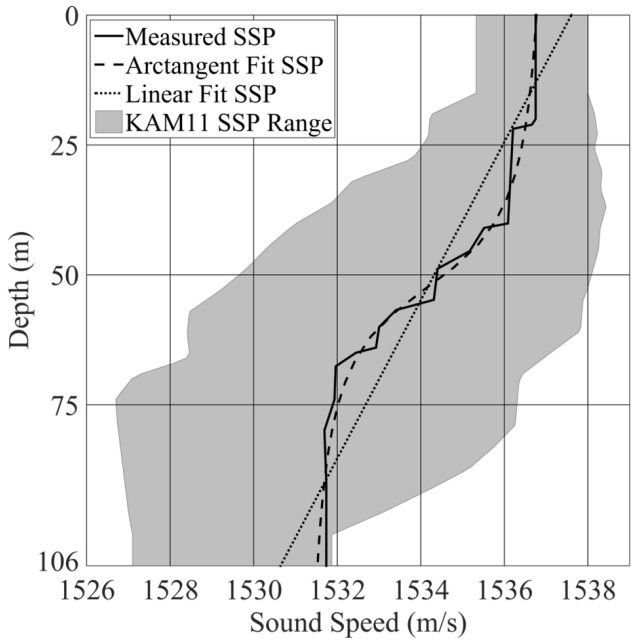

Figure 2.4: Sound speed profiles (SSPs) used in this investigation. The solid curve represents a measured sound speed profile from the KAM11 experiment. The dashed curve is a best-fit arctangent curve to the KAM11 data. The dotted line represents a best fit line to the KAM11 data. The shaded region shows the range of sound speeds observed over three days (JD183JD185) of the KAM11 experiment, and indicates the environmental variability at the site of the experiment. The solid, measured profile is used for simulation of recorded pressure fields. The dotted and dashed curves are used in MFP replica calculations.

MFP with the nonlinear autoproduct (see Section 2.2.5). The mode code used for this was created using a shooting method, where low frequency mode shapes nearly satisfying the ideal sound channel were used as the initialization, and slowly increased in frequency until arriving at the desired frequency. The MATLAB function bvp4c was utilized for this purpose, and the results were benchmarked against the mode shapes and eigenvalues calculated by Kraken, a mode code developed by HLS Research. For these simulations, the signal frequency range was 11.2kHz $\leq \omega/2\pi \leq$ 32.8kHz with $M = 6480$ and M' between 6465 and 6330, depending on the difference frequency. In order to best suit this environment, the frequency difference bandwidth was chosen to be 50Hz $\leq \Delta\omega/2\pi \leq$ 500Hz with $N' = 91$, and the replica calculation from (2.6) included only the three lowest-order modes at each difference frequency. Higher order modes were neglected because they are not as strongly orthogonal across the partial water-column spanning array and because they are more sensitive to sound

speed profile mismatch. The three modes used in these simulations are shown in 2.6 for four difference frequencies (50, 200, 350, and 500 Hz), and were calculated using the arctangent sound speed profile. For both conventional and frequency difference MFP, the search grid covered from 0 to 6 km in range and 0 to 106 m in depth, sampling every 50 m in range, and 50 cm in depth. This is a very course grid considering the signal center-frequency wavelength is $\sim$ 7cm.

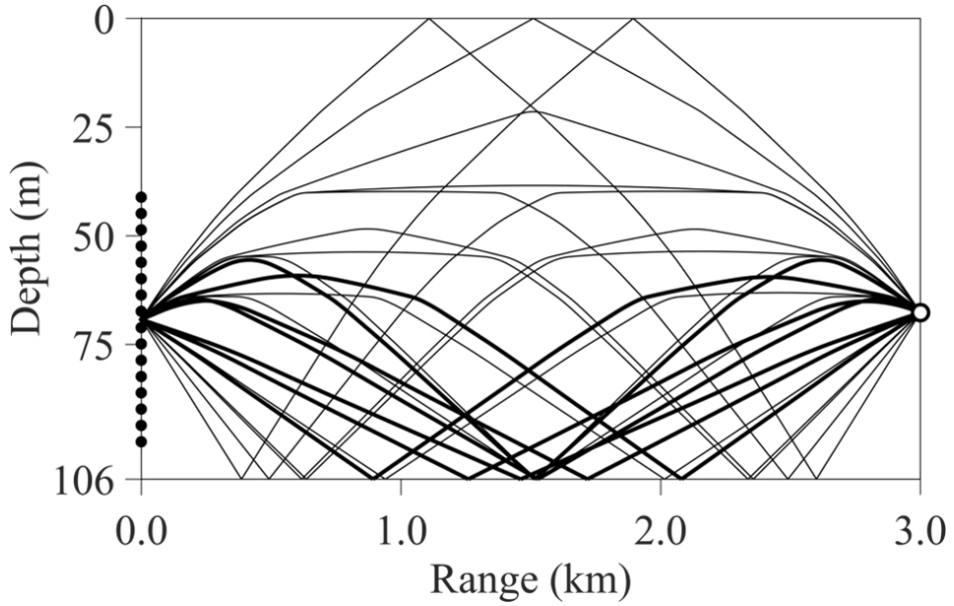

Figure 2.5: Eigenray plot simulated using Bellhop. The source at a range of 3 km and depth of 67.7 m broadcasts high frequency sound, illustrated above with rays, to the receiving array on the left at a range of 0 m. The figure above shows the eigenrays connecting the source to the center of the receiving array at a depth of 69.3 m. The measured sound speed profile from KAM11 was used in this calculation, shown as the solid line in Fig. 2.4. It can be seen from this diagram that the environments vertical sound speed produces a multipath downward-refracting environment. Only rays arriving within the first 10 ms are shown, as this is intended to mimic time delay spreads found in the KAM11 experimental data. Additionally, the rays amplitude information is represented in the line thickness, meaning thicker lines refer to stronger amplitudes, while thinner lines refer to weaker amplitudes. The importance of refraction and bottom-reflections in this environment is made evident here.

Figure 2.7 shows signal spectrograms for two different simulated pressure waveforms for a source depth of 67.7m, a receiver depth of 67.4m, and a source-array range of 3 km. Both were calculated using Bellhop for the forward-propagation. Figure 2.7a) shows results for the previously mentioned 11.2 kHz to 32.8 kHz frequency sweep signal, while Figure 2.7b)

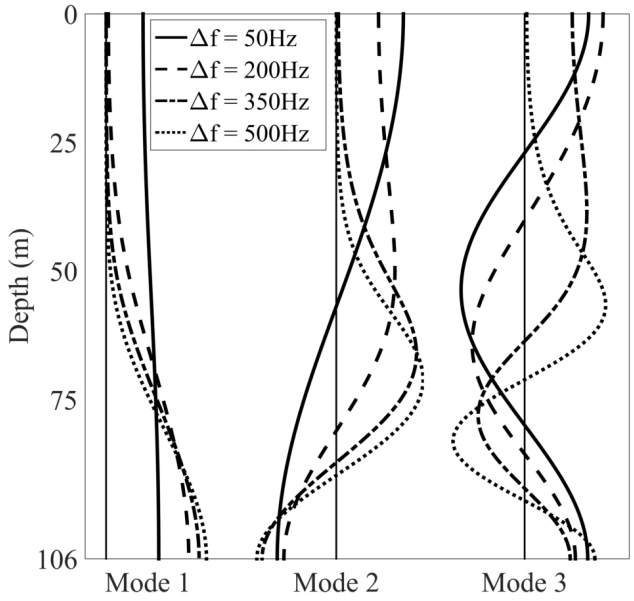

Figure 2.6: Plot of the mode shapes used in the calculation of replicas for frequency difference MFP. These are the three lowest-order modes calculated at four difference frequencies which are evenly spaced in the frequency difference bandwidth from 50 Hz to 500 Hz. The arctangent sound speed profile, shown as a dashed curve in Fig. 2.4, is used for this mode calculation. It can be seen in the mode shapes near the surface that the modified boundary conditions are used, where both the top and bottom surfaces are treated as perfectly rigid boundaries, leading to unexpected mode shapes.

shows results for a signal with same amplitude and bandwidth but with random phase at each frequency. As a result, the spectrogram in Fig. 2.7b) no longer contains any clear structure.

Sample simulated range-depth ambiguity surfaces for conventional and frequency difference MFP are shown in Figure 2.8 with a 5-dB dynamic range using the Fig. 2.7 signals. A round white dot marks the actual source location in both panels, and the largest peak in the ambiguity surface between the ranges of 1 km and 5 km is marked with a white $\otimes$ symbol. As can be seen in Fig. 2.8a), conventional MFP fails to unambiguously localize the source under these conditions, producing an speckled ambiguity surface with numerous possible source locations in the lower half of the sound channel. In contrast, as seen in Fig. 2.8b), frequency difference MFP produces a large, unambiguous peak near the source depth and range (within 4.8 m in depth and 350 m in range). In addition, the results shown in both

panels of Fig. 2.8 are independent of which signal from Fig. 2.7 was used. There is perfect pixel-to-pixel matching when comparing ambiguity surface results from the same technique for the two different signals. Thus, as mentioned and shown in Section **??**, both localization schemes, (2.7) and (2.8), are independent of the phase of the broadcast signal.

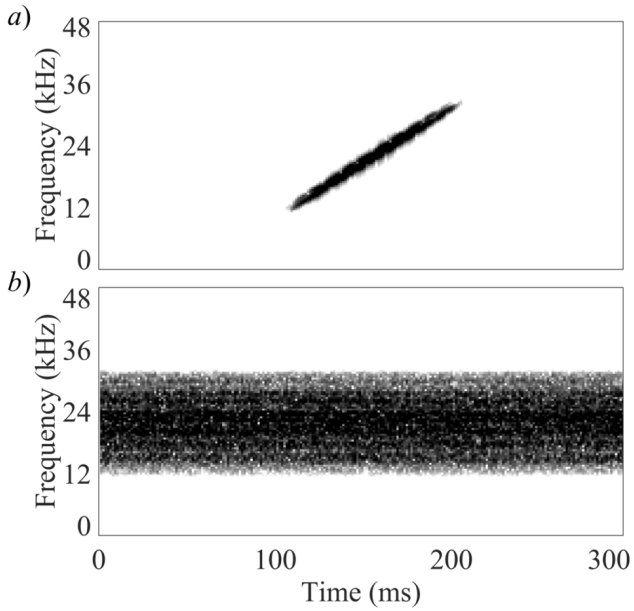

Figure 2.7: Spectrograms of two different recorded pressure profiles. The source is at a depth of 67.7m and range of 3km, and the receiver is at a depth of 67.4m. Fig 7a) shows the recorded pressure profile when the source waveform used is the 100-ms LFM pulse from 11.2kHz to 32.8kHz. Fig. 2.7b) shows the result of scrambling the source waveforms phase by multiplying each frequency bin with a random complex phase factor. The result has the same spectral power, but the randomized phases lead to a loss of the time-frequency structure. The relative phases between any two hydrophones is still the same, and therefore processing these waveforms with MFP yields the same result, as given in Fig. 2.8.

Although the source is approximately localized in Fig. 2.8b), there are other peaks in the ambiguity surface: one at zero range, and another at approximately twice the source range. The spacing between these peaks was found to depend on the sound speed profile, channel depth, vertical array depth, and difference frequency bandwidth (50 to 500 Hz). It is an artifact of the environment and the geometry. In particular, the 3 km spacing between peaks is the ray-cycle distance in the lower half of the sound channel. In this environment, a shallow angle ray launched near the bottom would travel $\sim$ 3 km before returning to the bottom as a result of downward refraction. This can be observed in Fig. 2.5, where a few

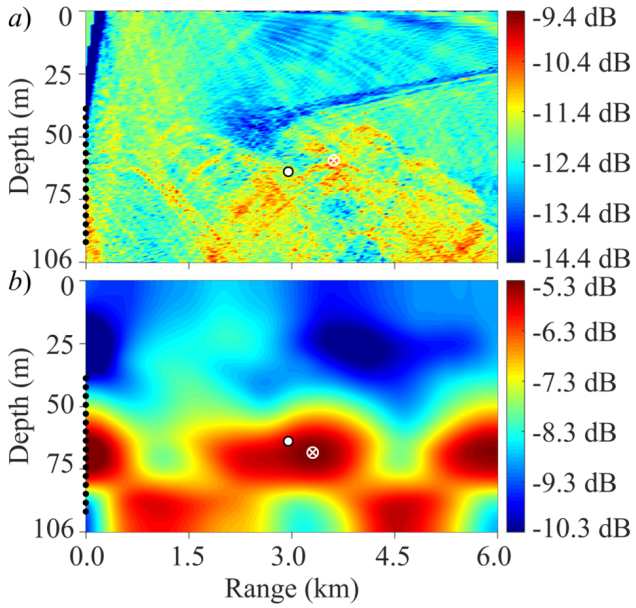

Figure 2.8: Comparison of simulations of conventional (Bartlett) MFP (Fig. 2.8a) and frequency difference MFP (Fig. 2.8b) for the KAM11 geometry, with a source depth of 67.7 m. In this range-depth cross section of the ocean waveguide, the black circles along the left indicate the location of the 16 array elements, and the filled white circle in the center indicates the correct location of the source. The peak in the ambiguity surface is provided by a white $\otimes$ symbol. The 5 dB color scale refers to the output of MFP, the ambiguity surface, where the most likely source locations are found at the top of the color scale. The recorded pressure data are simulated using Bellhop through the measured KAM11 sound speed profile. Conventional MFP calculates replicas using Bellhop through the arctangent sound speed profile, and averages across the signal bandwidth of 11.2 kHz to 32.8 kHz. Frequency difference MFP calculates replicas using the first three modes at difference frequencies between 50 Hz and 500 Hz, averaging first through the signal bandwidth and then a second iteration of averaging across the difference frequency bandwidth to produce the ambiguity surface shown above.

dominant bottom-interacting rays, shown with thick lines, have a half-ray-cycle distance of 1.5km. Therefore, there exists a periodic ambiguity in the source range estimation, which coincidentally aligns with the source-to-array distance, leading to peaks near 0 km and 6 km in addition to the desired ambiguity surface peak at 3 km.

Figures 2.9 and 2.10 further elaborate further on this 3km cycle-distance in the ambiguity surface. Both figures depict the same simulation conditions as Fig. 2.8b). However, for Fig. 2.9, the source range was moved to 4 km (instead of 3 km), and the ambiguity surface peaks occur at 1km, 4km, and 7km, and notably not 0km, 4km, and 8km. This pattern

suggests that the periodicity observed in the ambiguity surface in Fig. 2.8b) is a function of the geometry and environment, and not of the source range. In Fig. 2.10, the geometry is unchanged from Fig. 2.8b), but the source signal is a 50-500Hz frequency sweep broadcast through a hypothetical sound channel having rigid upper and lower surfaces. Here, the major side lobes occur at the source depth at ranges of 0 and 6 km, with lesser side lobes near the bottom at 1.5 km and 4.5 km. Qualitatively, this same structure with 3km repetition in the ambiguity peaks exists in Fig. 2.8b). This correspondence suggests that the frequency difference MFP technique is actually creating out-of-band signal propagation information for a slightly modified environment. Furthermore, the effect of the undesired cross terms discussed in Section 2.2.5 is evident in the comparison of Fig. 2.10 to Fig. 2.8b. Both simulations have the same amount of mismatch, but the result in Fig. 2.10 is much more successful because of the lack of cross-terms. Overall, Figs. 2.9 and 2.10 both show that the side lobe structure seen in the frequency difference MFP ambiguity surface, Fig. 2.8b), is consistent with a low frequency source in a similar environment. Additionally, other simulations, omitted here, suggest that the absence of environmental mismatch does not qualitatively change the ambiguity surface, meaning the features of the ambiguity surface here are associated with the Δf-MFP algorithm, not the amount of environmental mismatch.

2.4 Experimental Results

Given these promising simulation results, the next research step was the determination of frequency difference MFPs localization performance with experimental data. The data sets used to determine the localization performance of frequency difference MFP were collected during the KAM11 experiment (Hodgkiss *et. al.* 2011). This experiment was performed off the western coast of Kauai during the summer of 2011, and had the goal of investigating the coupling of oceanography, acoustics, and underwater communications. It was not a source localization experiment, so its utility for this MFP study was unexpected.

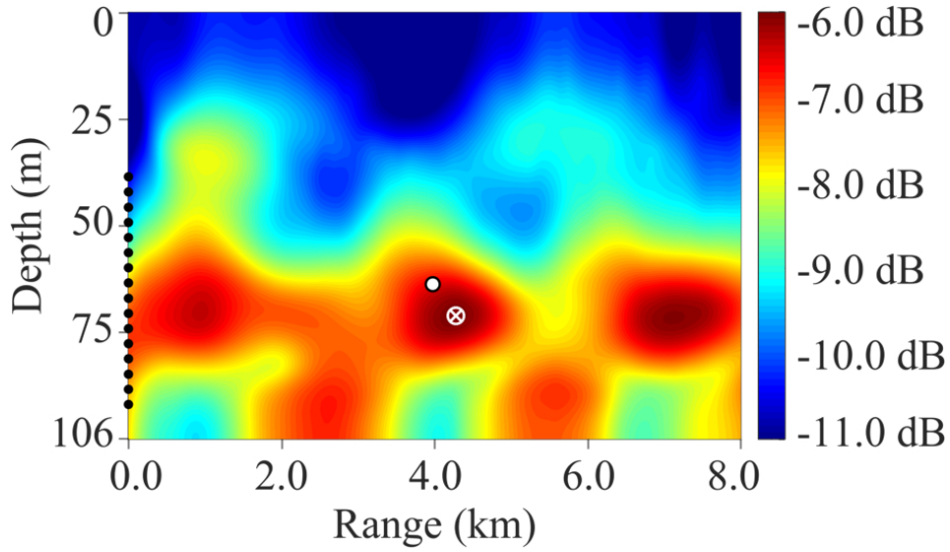

Figure 2.9: Frequency difference MFP ambiguity surface for a source at 4km range, simulated with Bellhop. The peaks in the ambiguity surface are now located at 1km, 4km, and 7km in range. These peaks have the same spacing as Fig. 2.8b), but because they are shifted, it would suggest that the 3km pattern is a result of the sound speed profile and geometry, and is not necessarily a function of source range.

The KAM11 recordings employed in this study were collected using the experimental geometry shown in Fig. 2.3 with one exception; sixteen different source depths were considered, and are listed in Table 2.1. The first eight depths correspond to a ship-mounted source array (JD183). The next eight depths correspond to data taken approximately a day later (JD184), and the source array in this case was moored to the bottom of the ocean. As a result, more stable transmission was expected in this data set. A sample KAM11 spectrogram is provided in Figure 2.11. Most distinctly, there is a diagonal ridge in the center of the figure that sweeps upward in frequency from slightly less than 12 kHz to more than 30 kHz; this is the frequency sweep signal. Also noteworthy is the lower amplitudes of the signal at higher frequencies, which is likely a result of frequency-dependent volume attenuation in the ocean. The average signal-to-noise ratio (SNR) of the sixteen data sets was found to be about 7.5 dB, with higher SNR found at the lower frequencies in the bandwidth. As suggested by the normalization of (2.5), all frequencies within the 11.2 kHz to 32.8 kHz frequency range are treated with equal weight, even though high frequency components may have a lower

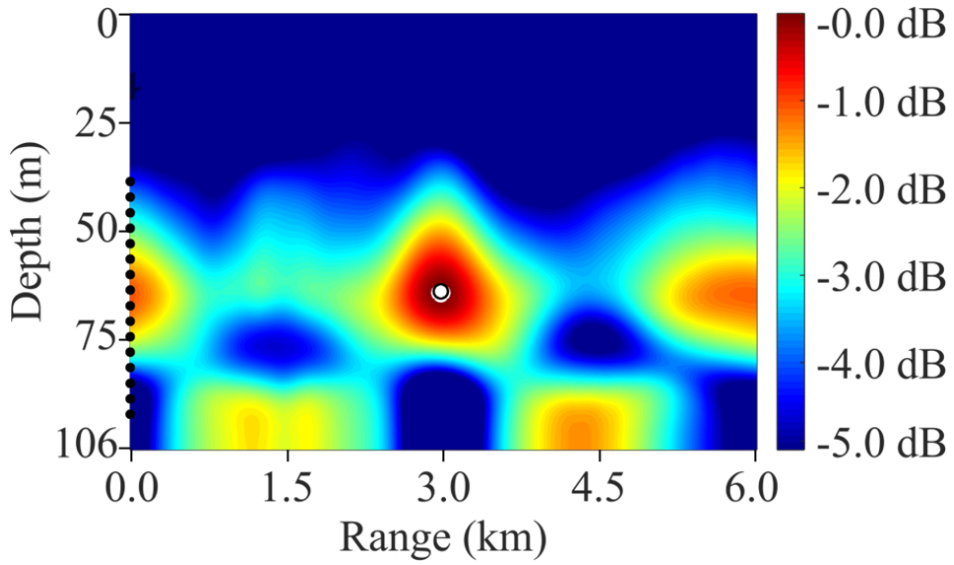

Figure 2.10: Conventional MFP ambiguity surface for a source at 3 km range, 67.7 m depth, and signal frequencies from 50 Hz to 500 Hz. Had the source truly broadcast 50 Hz to 500 Hz, the resulting ambiguity surface also contains the same 0 km, 3 km, and 6 km peaks, as did Fig. 2.8b). Qualitatively, the features in the ambiguity surfaces are comparable to Fig. 2.8b). Conventional MFP at a low frequency still performs much better in terms of localization as compared to frequency difference MFP at the same frequency, which can likely be attributed to the production of undesired cross terms in the frequency difference formulation.

SNR. Separate investigations suggest that the full 21.6-kHz signal bandwidth is not required for localization, and that narrower bandwidths as small as 0.5 kHz can provide comparable performance, particularly when they contain the high SNR signal frequencies.

A sample set of KAM11 impulse responses is shown in Figure 2.12. Here, the various time-series are arranged in order with the shallowest array elements recording at the top and the deepest array elements recording at the bottom of this figure. The arrival structure shown on this figure clearly indicates complicated multipath propagation with a time delay spread of approximately 10 ms, corresponding to 92% of the total impulse-response energy. The apparent arrival angle at the array is within 5 degrees of horizontal, in accordance with expectations for this environment.

Sample range-depth KAM11 MFP ambiguity surfaces for the conventional and frequency difference MFP techniques are shown in Figure 2.13 with a dynamic range of 5 dB. The

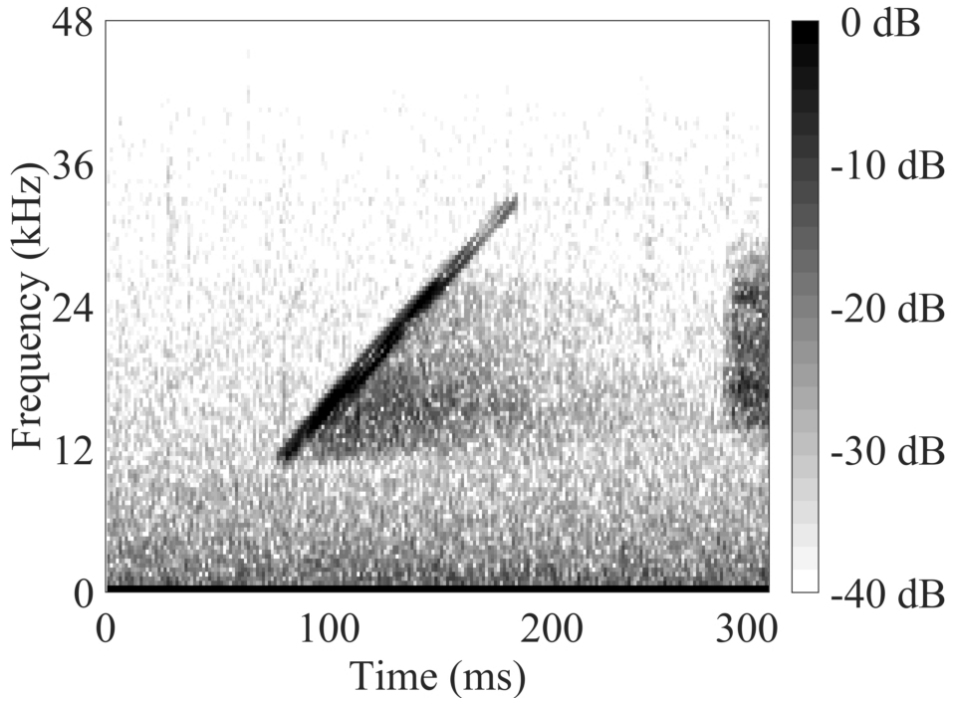

Figure 2.11: Spectrogram of KAM11 data. The 100-ms linear-frequency-modulated (LFM) pulse from 11.2 kHz to 32.8 kHz is illustrated above. Specifically, this is the spectrogram of the recording from the hydrophone at a depth of 67.4 m (nearest to the center of the array) for the bottom-moored source at a depth of 67.7 m. The horizontal axis shows the relative time over the 300-ms recording, and the vertical axis shows the constituent frequencies around a particular time. The logarithmic color scale is normalized such that the strongest time-frequency bin has a magnitude of unity.

processing parameters here are identical to those used for Fig. 2.8. In both cases, the forward propagation data is taken from a bottom-moored source at a depth of 67.7 m, and the replicas are computed with the arctangent sound speed profile. As might be expected, the conventional MFP result shown in Fig. 2.13a) does not uniquely or clearly localize the source. The frequency difference MFP results shown in Fig. 2.13b), on the other hand, does uniquely identify the source, with range and depth errors of 50 m and 9.1 m, respectively. The 3-km ambiguity-surface peak-repetition distance is found in simulation, is also present here with side lobe peaks arising at 0 km and 6 km.

Interestingly, the signal shown in Fig. 2.11 allows a final inquiry into the effect of the source waveform on the frequency-difference MFP ambiguity surface. Figure 2.14 shows, three sets

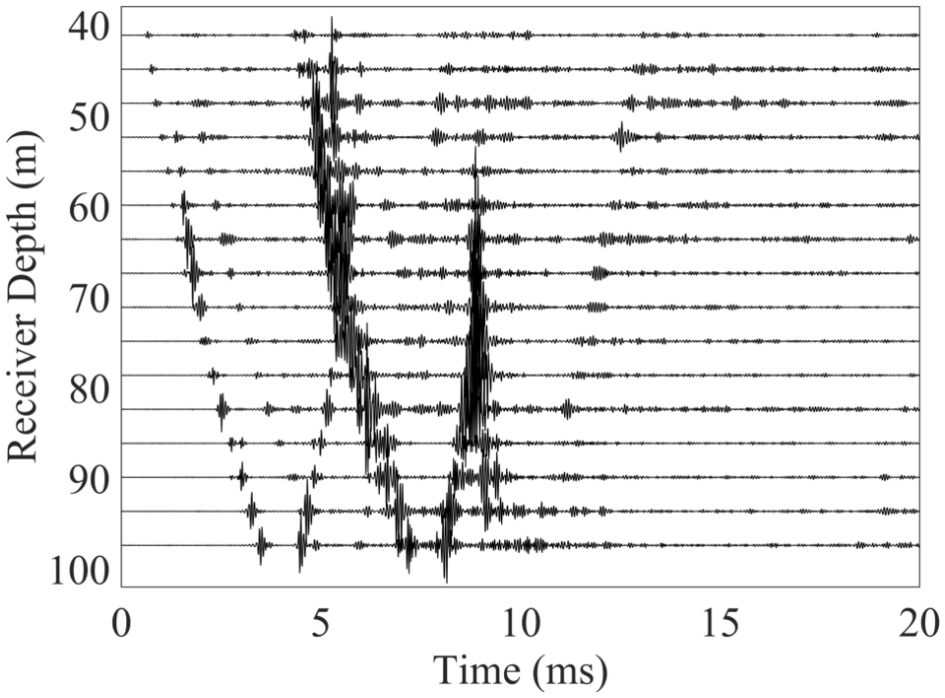

Figure 2.12: A sample measurement of the channel impulse response for the KAM11 environment. The vertical axis displays the depths of the hydrophones, and the horizontal axis shows the relative arrival times for a bottom-moored source at a depth of 67.7 m. The multipath structure of the experimental data is clearly illustrated above, with an approximate time delay spread of 10 ms.

of spectrograms paired with three ambiguity surfaces. Each spectrogram ranges from 0 to 300 ms on the horizontal axis, 0 to 48 kHz on the vertical axis, and spans 30 dB on the color scale. Similarly, the ambiguity surfaces each span 6km in range, 106m in depth, and the color scale spans 5 dB. Figure 2.14a) shows the results of isolating (in time) the LFM pulse from Fig. 2.9. The white horizontal bars in the spectrogram identify the 11.2 kHz to 32.8 kHz bandwidth that was used for processing (signal content outside of this frequency range was neglected). The ambiguity surface for this situation is essentially identical to Fig. 2.13b). More interestingly, consider Fig 14b), which shows the original spectrum truncated to just the last 24 ms that contains the beginning of a KAM11 communications signal. By processing just this 24 ms span, the ambiguity surface results are very similar to Fig. 2.14a) and Fig. 2.13b), This is further confirmation that frequency difference MFP results are not dependent on the source waveform. Plus, this results shows that single time windows

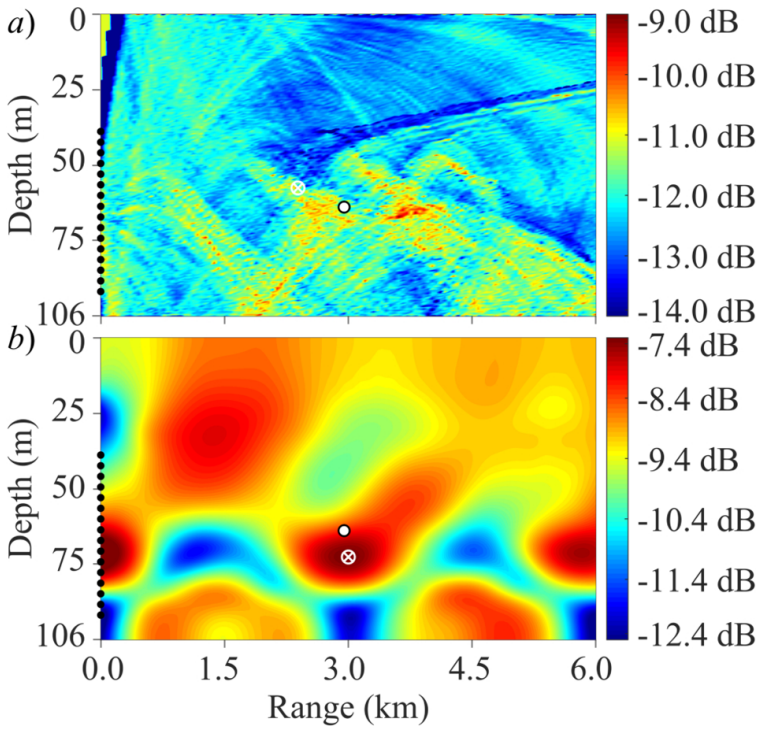

Figure 2.13: Ambiguity surfaces for the KAM11 data using conventional and frequency difference MFP. The horizontal and vertical axes, dynamic range of the color scale, and source and receiving array labels are the same as Fig. 2.8. Fig. 2.11a) illustrates conventional matched field processing. Here, the source localization effort is largely unsuccessful, with many ambiguous peaks. Fig. 2.11b) shows the same data processed using frequency difference MFP, showing a more successful source localization. The dominant ray cycle distance in this environment is approximately 3 km, as seen in Fig. 2.5, and this leads to the strong side-lobes, approximately 3 km up and down range from the true source location.

(snapshots) as short as $\sim$ 20 ms may produce acceptable results. Investigation of even shorter windows suggest that 10 ms is the lower limit for the KAM11 scenario. And finally, to rule out the possibility that all of these results have been coincidence, frequency difference MFP was performed on just the noise components of the recorded pulse. These results are shown in Fig. 2.14c) and the ambiguity surface in this case has almost no structure and lack distinct peaks, but the 3km-repetition pattern still emerges, which is again likely a result of the ray-cycle distance as previously discussed.

Figure 2.15 provides examples of frequency-difference MFP ambiguity surface results for the 16 different source depths. Fig. 2.15a) is the most accurate localization result, with range

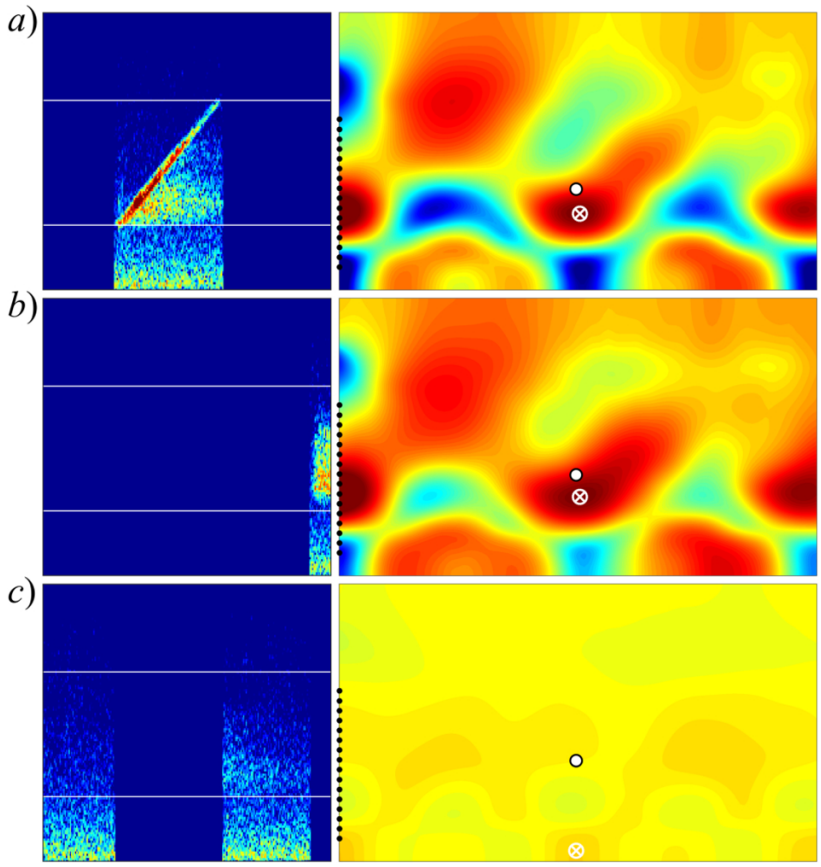

Figure 2.14: Spectrograms and ambiguity surfaces analyzing the dependence of the frequency difference MFP technique on the source waveform. All three spectrograms have a horizontal axis ranging from 0 to 300 ms, a vertical axis spanning 0 to 48 kHz and 40 dB of dynamic range. All three ambiguity surfaces have a horizontal axis showing range from 0 to 6 km, a vertical axis showing 0 to 106 m of depth, and 5 dB of dynamic range. All experimental parameters were held the same as in Fig. 2.13. The horizontal white lines in the spectrograms denote the nominal 11.2kHz to 32.8kHz bandwidth. Fig. 2.14a) shows the spectrogram of a time-windowed version of Fig. 2.11, but focusing on the LFM pulse only. When such a time series is processed with frequency difference MFP, the ambiguity surface is shown at right. Similarly, Fig. 2.14b) also has a time-window, but focuses only on the last 24 ms of data, which contains part of a communications signal. It can be seen that this signal, with clearly no time-frequency structure, has very comparable results as its LFM pulse counterpart in Fig 2.14a). Fig. 2.14c) shows a time window that subtracts the time components of Figs. 2.14a) and 2.14b) from the full recorded data in Fig. 2.11, the result of which is expected to be purely noise or reverberation. By processing just this, one would not expect any clear localization result, which is confirmed as shown in the accompanying ambiguity surface. This plot is included as a confirmation that frequency difference MFP does not always produce the same ambiguity surface, as one might be led to believe considering the similarities between the other frequency difference MFP ambiguity surfaces shown here.

and depth errors of 50 m and 1.3 m, respectively. Fig. 2.15b) is the least accurate localization result, with range and depth errors of 525 m and 13.9 m, respectively. The final two panels of Fig. 2.13 show MFP results for the shallowest (Fig. 2.15c) and deepest (Fig. 2.15d) sources. Quantitative results for all sixteen experimental source depths are provided in Table 2.1. Here, the peak-to-side-lobe ratio (PSR) is determined by examining the ambiguity surfaces throughout the water column between the ranges of 1 km and 5 km, so as to avoid including the 0 km and 6 km peaks in this calculation. The average depth error was found to be 9.8 m, or about 9% of the nominally 106-m deep sound channel. The average range error was found to be 170 m, or about 6% of the nominal 3-km range. Ambiguity surface peaks were on average were about 1 km wide in range, and about 20 m tall in depth. The average peak-to-side-lobe ratio was just 0.85 dB. For conventional MFP, such a small peak-to-side-lobe ratio would likely indicate a weak and uncertain localization result. However, frequency-difference MFP is a nonlinear technique that involves a substantial amount of incoherent averaging, so the conventional (linear) MFP expectations may not apply here.

In fact, frequency-difference MFP was found to be reasonably robust with respect to changes in the environment. To elaborate, consider the impact of using the best-fit linear sound speed profile, shown as the dotted line in Fig. 2.4, in the field model used to compute the replicas. As can be seen, the environmental mismatch is more significant with this sound speed profile than the fitted arctangent profile used to create all the ambiguity surfaces shown here. Despite this added mismatch, the resulting KAM11 frequency-difference ambiguity surface results (see Table 2.1) using the best-fit linear profile are not significantly worse than those using the fitted arctangent profile. The average range and depth errors here were found to be 560 m and 8.1 m, with an average peak-to-side-lobe ratio of 1.01 dB. This level of robustness to sound speed profile mismatch is typically not found in conventional MFP, and especially not at a signal center frequency of 22 kHz. These linear-profile results suggest that frequency-difference MFP is more robust to environmental mismatch than its relatively low peak-to-side-lobe ratio would suggest.

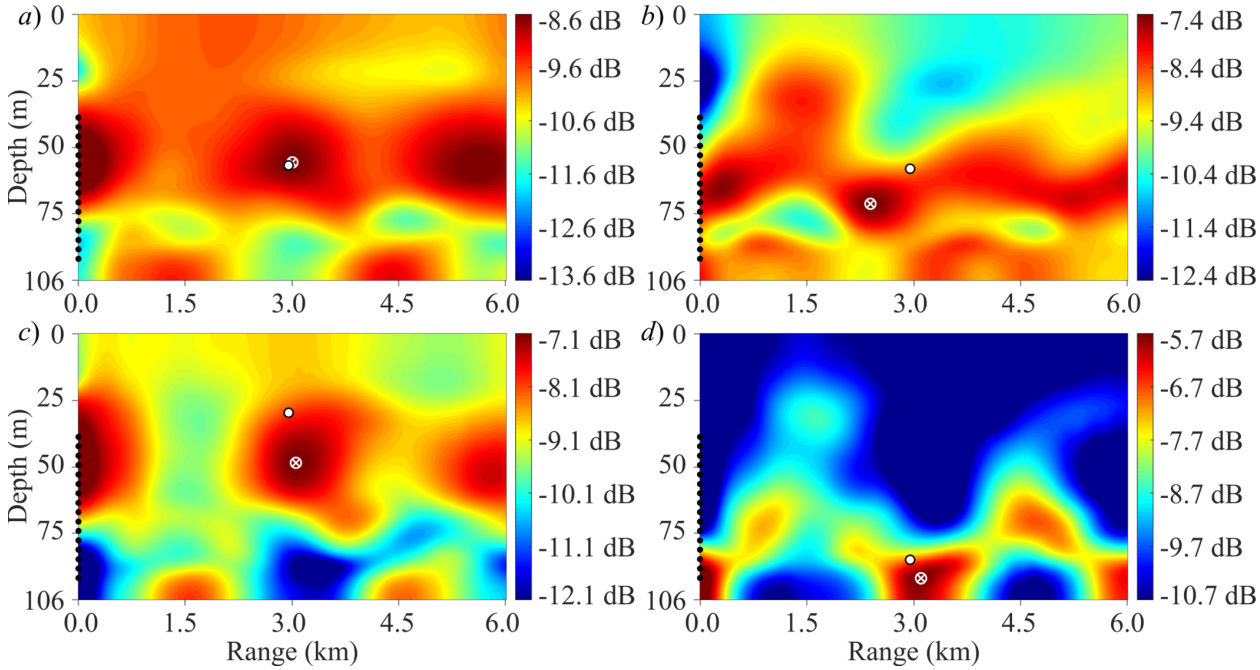

Figure 2.15: Examples of frequency difference MFP for four different trials. Panel a) is the trial with the best localization result, specifically a bottom-moored source at a depth of 60.2 m, with a range error of 50 m and depth error of 1.3 m. Panel b) is the worst localization result, with a ship-mounted source at a depth of 61.5 m, with a range error of 525 m and depth error of 13.9 m. Panel c) shows the shallowest source, a ship-mounted source at a depth of 31.5 m, resulting in a range error of 125 m and a depth error of 20.0 m. Panel d) shows the deepest source, a bottom-moored source at a depth of 90.2 m, resulting in a range error of 150 m and depth error of 7.2 m.

Frequency-difference MFP ambiguity surfaces for all sixteen trials, processed with both the arctangent sound speed profile and the linear sound speed profile, are available online as supplemental material for this article.

2.5 Summary and Conclusions

A novel nonlinear array signal processing technique based on conventional matched field processing (MFP) of a quadratic field product at a significantly downshifted frequency has been developed. This technique, frequency difference MFP, is an extension of frequency-difference beamforming (Abadi *et. al.* 2012) to MFP. Its performance has been investigated for source

Source Depths (m)	Best-Fit Arctangent SSP			Best-Fit Linear SSP		
	Range Error (m)	Depth Error (m)	PSR (dB)	Range Error (m)	Depth Error (m)	PSR (dB)
84.0	275	11.2	0.62	600	4.4	0.43
76.5	225	6.2	0.46	675	5.3	0.48
69.0	50	17.2	0.63	100	16.3	0.16
61.5	525	13.9	0.78	1300	7.6	0.38
54.0	75	3.6	0.57	475	4.0	1.19
46.5	475	17.6	0.61	525	21.1	1.53
39.0	150	9.6	1.66	1100	0.0	1.84
31.5	125	20.0	0.92	550	20.8	1.46
90.2	150	7.2	1.05	525	0.4	0.63
82.7	200	10.1	0.59	250	8.2	0.65
75.2	75	11.1	0.18	150	9.2	0.59
67.7	25	9.1	0.53	300	8.4	0.04
60.2	50	1.3	0.52	400	0.6	0.84
52.7	125	2.1	0.68	675	5.2	1.53
45.2	100	6.4	1.60	675	8.4	1.75
37.7	75	10.5	1.82	650	9.9	1.96
Average	170 m	9.8 m	0.85 dB	560 m	8.1 m	1.01 dB

Table 2.1: Summary of the performance of frequency difference MFP for two different sound speed profiles using the experimental KAM11 data for all sixteen source depths. The first eight rows correspond to sources mounted to the ship, and the last eight rows corresponding to sources moored to the ocean bottom. The range and depth error are defined as the absolute distance between the maximum in the ambiguity surface and the nominal source location. The peak-to-side-lobe ratio (PSR) is provided as well, and it should be noted that the peak and side-lobe locations were chosen between ranges of 1 km and 5 km to avoid the peaks generated by the approximately 3-km ray-cycle distance. The average range and depth errors using the arctangent profile are approximately 6% of the nominal range and 9% of the sound channel depth, respectively. Additionally, when moving to the linear sound speed profile, which is a worse match to the measured sound speed profile, depth estimates were approximately the same, but range estimation is degraded, with an average error of 19% of the nominal 3-km range.

localization in a 106-m-deep shallow ocean sound channel at an array-to-source range of 3-km with both simulated and measured signals in the 11.2-kHz to 32.8-kHz frequency range.

The following five conclusions can be drawn from this research effort. (1) Frequency differ-

ence MFP can be successful at localizing high frequency sound sources in a shallow ocean environment with environmental mismatch. Using measurements from the KAM11 experiment, the techniques source range and depth estimates were unambiguous with average absolute-value range and depth errors of 6% and 9% , respectively. (2) The frequency difference MFP technique has several unexpected features that have no conventional analogues. First, the replicas are calculated at a user-defined difference frequency that may be smaller than the signal frequencies that actually propagated through the ocean environment. Second, the environment for the replica calculation must have unnatural rigid surface and bottom boundary conditions. And third, the nonlinear product creates unintentional cross-terms in a multipath environment, which can be suppressed by averaging over the signal- and the difference-frequency bandwidths to successfully localize the source. (3) The source localization results from frequency difference MFP, although imperfect, are robust to environmental mismatch, changes in the signals phase at each frequency, and the reduction of the available signal bandwidth. Furthermore, the low peak-to-side-lobe ratios found in this study may be characteristic of the non-linearity and the extensive averaging, and do not necessarily indicate weak or uncertain localization results. (4) The source localization performance this technique offers is unique. No technique known to the authors offers comparable shallow-ocean source-localization results at high frequencies with a sparse array in the presence of environmental mismatch using just a single snapshot of an unknown source waveform. Additionally, no additional or specialized hardware is required, nor any changes to data collection with the exception of skipping a low-pass filter step, such that the high frequency data is not removed before the MFP step. And finally, (5) frequency difference MFP is computationally less expensive than comparable conventional MFP calculations.

While these five conclusions are positive, the results they are based on were obtained after some adjustment of the signal processing parameters that must be chosen by the user. For example, the difference frequency bandwidth (50 to 500 Hz) and the number of modes to include in the replica calculation (3) are examples of such parameters, and for this study,

those values were chosen through a trial-and-error process using the ambiguity surfaces as visual feedback for the suitability of various parameters. This parameter search did not select specific frequency pairs, instead all possible frequency pairs for a given difference frequency were included. Less localization success was found, even within simulation, for alternative choices of these parameters. However, the fact that this technique still yielded potentially useful results with the more strongly mismatched linear sound speed profile suggests that some robustness against environmental mismatch is retained in frequency difference MFP, despite its sensitivity to difference frequency bandwidth and mode number in the replica calculations.

A final note concerns the choice of the back-propagation model, which for conventional MFP, a ray-based code is utilized, whereas for Δf-MFP, a mode-based code is used. It may appear that the autoproduct artificially manufactures low frequency field information, since it is based on high frequency measurements or ray-code simulations. Therefore, one might expect, given the desired terms in (), that the ideal calculation for the replicas would be a high-frequency ray code, evaluated at the lower difference frequency. However, this approach resulted in poor source localization performance. Acceptable results were only obtained when the replicas were legitimate Helmholtz equation solutions (a truncated modal sum) at the difference frequency with modified boundary conditions. The fact that the replicas must be calculated with rigid-surface-and-bottom low-frequency modes even though no such modes *actually* propagated in the true environment, suggests that the autoproduct may actually contain low-frequency wave-propagation information, despite its high frequency origins.

Overall, the main result of this research is a new source localization technique, termed frequency difference MFP, which extends MFP for undersea sound sources into a frequency range that was previously inaccessible. While, the performance of the technique with multiple sources and in noisy environments is not known, it may nonetheless prove useful for locating and tracking untethered remotely-operated underwater vehicles. Additionally, if its

performance can be scaled based on acoustic wavelength, frequency difference MFP may also be effective for deep-ocean source localization at lower signal frequencies and longer ranges. Additionally, this technique may carry relevance for radar and ultrasound applications, where there may be fewer multipath propagation effects.

CHAPTER 3

Adaptive Frequency-Difference Matched Field Processing for High Frequency Source Localization in a Noisy Shallow Ocean

Abstract

Remote source localization in the shallow ocean at frequencies significantly above 1 kHz is virtually impossible for conventional array signal processing techniques due to environmental mismatch. A recently proposed technique called frequency-difference matched field processing (Δf-MFP) (Worthmann *et al.* 2015) overcomes imperfect environmental knowledge by shifting the signal processing to frequencies below the signals band through the use of a quadratic product of frequency-domain signal amplitudes called the autoproduct. This paper extends these prior Δf-MFP results to various adaptive MFP processors found in the literature, with particular emphasis on minimum variance distortionless response, multiple constraint method, multiple signal classification, and matched mode processing at signal-to-noise ratios (SNRs) from 20 to +20 dB. Using measurements from the 2011 Kauai Acoustic Communications Multiple University Research Initiative experiment (KAM11), the localization performance of these techniques is analyzed and compared to Bartlett Δf-MFP. The results show that a source broadcasting a frequency sweep from 11.2 kHz to 26.2 kHz

through a 106-m-deep sound channel over a distance of 3 km and recorded on a 16 element sparse vertical array can be localized using Δf-MFP techniques within average range and depth errors of 200 m and 10 m, respectively, at SNRs down to 0 dB.

3.1 Introduction

There are many passive acoustic source localization techniques (see Dowling & Sabra, 2015). One of the most common techniques, Matched Field Processing (MFP), can be successful at low signal-to-noise ratios when the propagation environment is well-known. However, if the propagation environment is not known perfectly, then there is an upper limit on the source signal-frequencies that allow localization with this technique. In practice, this limit is nominally 1 kHz in the shallow ocean. A previous study (Worthmann *et al.* 2015) proposed a frequency-difference (Δf) MFP technique that was able to successfully localize sources using ocean-recorded data with signal frequencies between 11 and 33 kHz, well above the nominal 1 kHz limit. The Δf-MFP technique is based on a nonlinear construction, termed the autoproduct, that effectively creates low-frequency field information from high-frequency measurements. In this paper, the Δf-MFP technique is expanded to include adaptive MFP techniques in an effort to improve source localization performance, and the effects of increased noise on each of these techniques is also presented. It is found that some adaptive Δf-MFP techniques are able to improve source localization performance (*i.e.* reduce localization errors to 200 m in range and 10 m in depth), but the improvements were not as significant as originally expected. Additionally, acceptable localization performance was consistently found for signal-to-noise ratios as low as 0 dB, and as low as 10 dB in some cases. Although imperfect, these results are encouraging because of the dearth of passive source localization techniques for sources at arbitrarily high frequencies, and even fewer techniques that are successful with recordings from sparse arrays in imperfectly known acoustic environments using only a single signal sample (*i.e.* one snapshot).

MFP was developed in the mid 1970s (Bucker 1976), and remained a popular source localization technique through to the 1990s. MFP correlates acoustic measurements recorded on an array with simulated acoustic fields developed from a model of the environment, and is a mature area of research (Baggeroer 1993, Jensen *et al.* 2011). For the purposes of this study, only shallow ocean environments are considered, although it is noted that MFP can in general be applied to any acoustic domain. In shallow ocean environments with source-to-array ranges on the order of kilometers, MFP has been successful with source-signal frequencies below 1 kHz in shallow ocean waveguides at signal-to-noise ratios (SNRs) as low as 5 dB (Porter & Tolstoy 1994). Above this frequency, imperfect knowledge of the acoustic environment leads to a severe degradation in localization performance, a problem known as environmental mismatch that is well-documented (Baggeroer 1993). A lack of robustness to environmental mismatch has plagued MFP techniques since their inception.

Alternative signal processing schemes exist for localizing high frequency sources in the shallow ocean, but each has its own limitations. One high-frequency passive source localization technique (Hursky *et al.* 2004), uses either matched filtering with a known source waveform or a cross correlation between array elements with an unknown source waveform to determine the arrival time structure of the multipath environment. Here, using numerous snapshots to create a robust estimate of the arrival time structure, comparisons can be made with a modeled environment to obtain range and depth estimates. By comparison, the Δf-MFP technique outlined in this paper only requires a single snapshot and does not require knowledge of the source waveform. Another technique, called focalization (Collins & Kuperman 1991, Michalopoulou & Porter 1996, and Soares 2001), sought to overcome environmental mismatch by including environmental parameters in the MFP search. This allowed for the localization of 1.5 kHz signals, higher than the nominal 1 kHz limit. However, the expanded parameter search required by this technique makes it computationally expensive, and it does not readily scale to arbitrarily high frequencies.

More recently, a nonlinear frequency-difference (Δf) beamforming technique (Abadi *et al.* 2012) was extended to MFP (Worthmann *et al.* 2015). The resulting Δf-MFP technique provided robustness to environmental mismatch at source-signal frequencies well above 1 kHz, from a single signal snapshot, without knowledge of the source waveform, without a computationally expensive environmental parameter search, and with a sparse array. Plus, it scales in principle to arbitrarily high frequencies. The Δf-MFP technique is a form of out-of-band signal processing based on auto-heterodyning within the signal band. It works by using a quadratic product of complex frequency-domain signal amplitudes referred to herein as the *autoproduct* to shift the signal processing bandwidth down to frequencies, which may be well below the signal band, where MFP techniques are more reliable. The increased robustness from the frequency downshifting is achieved at the expense of reduced spatial resolution. However, utilizing the frequency-difference approach with MFP significantly raises the upper signal-frequency limit where MFP can be successful in the shallow ocean (Worthmann *et al.* 2015).

Frequency-difference MFP successfully localized a source with signal bandwidth from 11 and 33kHz and placed at 16 different depths in a 106-m deep shallow ocean over a source-to-array range of 3 km, both within simulation and experiment. From an MFP perspective, that study can be considered a proof-of-concept; it used only the simplest signal processing scheme to process measured data with high SNR. The focus of this study is to investigate Δf-MFP with more sophisticated adaptive signal processing schemes, and to simultaneously investigate the impact of less favorable SNR. The adaptive schemes considered here are: minimum variance distortionless response (MVDR), multiple constraint method (MCM), multiple signal classification (MUSIC), and matched mode processing (MMP). Results from these processors are compared with conventional (Bartlett) in-band MFP and Δf-MFP results at signal-to-noise ratios (SNRs) from -20 to $+20$ dB. To facilitate comparisons of all the results, the modifier in-band will be used whenever a signal processing scheme has been evaluated using acoustic field values in the frequency band of the source signal, and the

modifier Δf will be used whenever a signal processing scheme has been evaluated using the autoproduct in a lower (user-defined) frequency band. The mathematical details associated with the in-band and Δf implementations of the various algorithms are provided in 3.2.

The remainder of this paper is divided into four sections. The next section contains a summary of in-band and Δf-MFP techniques, as well as descriptions of the signal processing algorithms utilized in this study, and an explanation of the theoretical foundations for these techniques. Section 3.3 discusses the KAM11 experiment and the post-processing used to artificially lower the signal-to-noise ratio. Section 3.4 provides the results obtained by applying the various in-band- and Δf-MFP techniques to the experimental data. Here comparisons are provided detailing the effect of each signal processing algorithm on source localization performance, as well as the effect of increased noise on this performance. The final section summarizes this study, and presents its conclusions and the impact they may have.

3.2 Matched Field Processing Schemes

3.2.1 In-band and Δf Implementations of Conventional MFP

Both the in-band and the Δf (or out-of-band) MFP processing schemes can be applied to the same measurements. Here, $p_j(t)$ is the measured time-domain pressure signal from the jth element of a hydrophone array, where j varies from 1 to N, the total number of elements in the array, and t is discretely sampled at sampling rate f_s for a total time of T. With a discrete Fourier transform, $p_j(t)$ can be converted to $P_j(\omega)$, where ω is the discretely sampled radian frequency ranging between 0 (the DC component) and πf_s, half the sampling rate. Let $\mathbf{P}(\omega)$ be the column vector of length N, with jth component equal to $P_j(\omega)$. To perform MFP, the relative phase and amplitude differences between the recordings of each pair of hydrophones is required. This information is stored in the cross-spectral density matrix $\mathbf{R}_P$,

or CSDM, defined here for in-band MFP.

$$\underline{\mathbf{R}}_P(\omega) = \frac{\mathbf{P}(\omega)\,\mathbf{P}^{\dagger}(\omega)}{\mathbf{P}^{\dagger}(\omega)\,\mathbf{P}(\omega)} \tag{3.1}$$

The † symbol denotes a conjugate transpose. Due to the column vector nature of $\mathbf{P}$, the numerator represents an outer-product, and yields a Hermitian matrix. The denominator represents an inner-product, and normalizes the CSDM so that its trace is unity. When there are multiple independent signal samples (commonly referred to as snapshots), $\underline{\mathbf{R}}_P(\omega)$ from (3.1) is commonly averaged over these snapshots to increase its robustness and suppress noise. MFP requires the calculation of complex weight vectors, $\mathbf{w}$, which are column vectors of length N. These weights, also called replicas, are created from a model of the acoustic environment. Consider the Greens function solution to the Helmholtz equation:

$$\left(\nabla^2 + \frac{\omega^2}{c^2(\boldsymbol{r})}\right) G(\boldsymbol{r}, \boldsymbol{r}', \omega) = -\delta(\boldsymbol{r} - \boldsymbol{r}'), \tag{3.2}$$

where $c(\boldsymbol{r})$ is the spatially inhomogeneous (but temporally constant) sound speed, and $\delta(\boldsymbol{r})$ is the 3D Dirac delta function. The jth component of the conventional replica vector, $\mathbf{w}$, is simply the normalized Greens function connecting a test source location, $\boldsymbol{r}$, to the jth hydrophone location, $\boldsymbol{r}_j$,

$$w_j(\boldsymbol{r}, \omega) = \frac{G(\boldsymbol{r}, \boldsymbol{r}_j, \omega)}{\sqrt{\sum_j |G(\boldsymbol{r}, \boldsymbol{r}_j, \omega)|^2}}, \tag{3.3}$$

where the normalization guarantees that $\mathbf{w}^{\dagger}\mathbf{w} = 1$. In-band Bartlett MFP is a frequency-domain spatial correlation between the measured signals and the modeled signals. It takes the following mathematical form:

$$B_{IB,Bart}\left(\boldsymbol{r},\omega\right)=\mathbf{w}^{\dagger}\left(\boldsymbol{r},\omega\right)\underline{\mathbf{R}}_{P}\left(\omega\right)\mathbf{w}\left(\boldsymbol{r},\omega\right). \tag{3.4}$$

$B_{IB,Bart}$ is the in-band Bartlett MFP ambiguity surface, and is a function of the test coordinate $\boldsymbol{r}$ and the in-band frequency of interest ω. Together, the normalizations of $\mathbf{w}$ and $\underline{\mathbf{R}}_{P}$ require that $0 \leq B_{IB,Bart} \leq 1$, with B near unity (or zero) indicating a likely (or unlikely) source location, since this implies a strong (or weak) correlation between measured and modeled signals. For broadband signals, (3.4) can be incoherently averaged through the signal bandwidth (Booth *et al.*, 1996)

$$B_{IB,Bart,avg}\left(\boldsymbol{r}\right)=\frac{1}{M}\sum_{m=1}^{M}B_{IB,Bart}\left(\boldsymbol{r},\omega_{m}\right)=\frac{1}{M}\sum_{m=1}^{M}\mathbf{w}^{\dagger}\left(\boldsymbol{r},\omega_{m}\right)\underline{\mathbf{R}}_{P}\left(\omega_{m}\right)\mathbf{w}\left(\boldsymbol{r},\omega_{m}\right), \tag{3.5}$$

where the subscript '*avg*' denotes an average through the signal bandwidth, and M is the number of frequencies used for averaging between Ω_L and Ω_H, the lower and upper bounds of the signals bandwidth, respectively. Typically, the ω_m-frequencies are evenly spaced through the signal bandwidth so that $\omega_m = \Omega_L + (\Omega_H - \Omega_L)\left[\frac{(m-1)}{(M-1)}\right]$ with the minimum frequency spacing being $2\pi/T$.

For Δf-MFP, the formulation given by (3.1)–(3.5) is followed with two primary differences. The first primary difference is the use of a quadratic product (the autoproduct) of measured complex field amplitudes in place of $P_j(\omega)$. The autoproduct for the jth hydrophone is

$$AP_{j}\left(\omega,\Delta\omega\right)=P_{j}\left(\omega+\frac{\Delta\omega}{2}\right)P_{j}^{*}\left(\omega-\frac{\Delta\omega}{2}\right), \tag{3.6}$$

and it contains the user-defined parameter $\Delta\omega$, the difference frequency, which is only constrained by the signal recording duration and the signal bandwidth, $2\pi/T \leq \Delta\omega \leq \Omega_H - \Omega_L$.

The underlying premise of using (3.6) for MFP is that the $AP_j(\omega, \Delta\omega)$ is a pseudo-field similar to an acoustic Moiré pattern (see Worthmann *et al.* 2015) that can be exploited for source localization because its structure mimics the lower-frequency field $P_j(\Delta\omega)$ (see section 3.2.4 for more details). In practice, $\Delta\omega$, is typically chosen to be in the frequency range where conventional MFP is likely to be successful, which means nominally below 1 kHz for a shallow ocean waveguide. An autoproduct column vector, $\mathbf{AP}$, maybe be defined using (3.6) for each of the N hydrophones. And, in analogy with (3.1), an autoproduct cross-spectral density matrix can be assembled.

$$\underline{\mathbf{R}}_{AP}(\omega, \Delta\omega) = \frac{\mathbf{AP}_{\Delta}(\omega, \Delta\omega)\,\mathbf{AP}_{\Delta}^{\dagger}(\omega, \Delta\omega)}{\mathbf{AP}_{\Delta}^{\dagger}(\omega, \Delta\omega)\,\mathbf{AP}_{\Delta}(\omega, \Delta\omega)} \tag{3.7}$$

The second primary difference between in-band and Δf-MFP is the use of complex weights (or replicas) that are normalized Greens function solutions to the Helmholtz equation at the difference frequency.

$$\left(\nabla^2 + \left(\frac{\Delta\omega}{c(\boldsymbol{r})}\right)^2\right) G(\boldsymbol{r}, \boldsymbol{r}', \Delta\omega) = -\delta(\boldsymbol{r} - \boldsymbol{r}') \tag{3.8}$$

For the range of difference frequencies considered in this study, the solution to (3.8) was presumed to be a modal sum truncated to include only the first three propagating modes. Additionally, these three modes were calculated with a rigid surface boundary condition (see 2.2.5). The jth replica for Δf-MFP, in analogy with (3.3) is:

$$w_j(\boldsymbol{r}, \Delta\omega) = \frac{G(\boldsymbol{r}, \boldsymbol{r}_j, \Delta\omega)}{\sqrt{\sum_j |G(\boldsymbol{r}, \boldsymbol{r}_j, \Delta\omega)|^2}}. \tag{3.9}$$

Thus, when w_j from (3.9) is assembled into a column vector, the Bartlett Δf-MFP formulation is:

$$B_{\Delta f,Bart}\left(\boldsymbol{r},\omega,\Delta\omega\right)=\mathbf{w}^{\dagger}\left(\boldsymbol{r},\Delta\omega\right)\mathbf{R}_{AP}\left(\omega,\Delta\omega\right)\mathbf{w}\left(\boldsymbol{r},\Delta\omega\right), \tag{3.10}$$

a direct analogy to (3.4). Equation (3.10) represents the out-of-band signal processing step since the information carried by $\mathbf{w}(\boldsymbol{r},\Delta\omega)$ corresponds to acoustic propagation at frequency $\Delta\omega$, and $\Delta\omega$ may lie below the signal bandwidth, $\Omega_L \leq \omega \leq \Omega_H$. It should be noted that an equivalent representation of (3.10) can be defined, as given below in (3.11).

$$B_{\Delta f,Bart}\left(\boldsymbol{r},\omega,\Delta\omega\right)=\frac{\left|\sum_{j=1}^{N}P_j\left(\omega+\frac{\Delta\omega}{2}\right)P_j^{*}\left(\omega-\frac{\Delta\omega}{2}\right)w_j^{*}\left(\boldsymbol{r},\Delta\omega\right)\right|^2}{\sum_{j=1}^{N}\left|P_j\left(\omega+\frac{\Delta\omega}{2}\right)P_j^{*}\left(\omega-\frac{\Delta\omega}{2}\right)\right|^2\sum_{j=1}^{N}\left|w_j\left(\boldsymbol{r},\Delta\omega\right)\right|^2} \tag{3.11}$$

In this representation, it can be seen more clearly that $B_{\Delta f}$ is close to unity when the net phases of the autoproduct align well with the phase of the replica across the receiving array.

As before, an incoherent average of (3.10) may be taken over bandwidths, but this time there are two bandwidths: the signal bandwidth, and the user-defined difference frequency bandwidth.

$$B_{\Delta f,Bart,avg}\left(\boldsymbol{r}\right)=\frac{1}{N'}\sum_{n=1}^{N'}\left(\frac{1}{M'}\sum_{m=1}^{M'}B_{\Delta f,Bart}\left(\boldsymbol{r},\omega_m,\Delta\omega_n\right)\right) \tag{3.12}$$

Here, M' is the number of signal-band frequencies between $\Omega_L+\Delta\omega/2$ and $\Omega_H-\Delta\omega/2$, $\omega_m=\left(\Omega_L+\frac{\Delta\omega}{2}\right)+\left(\Omega_H-\Omega_L-\Delta\omega\right)\left[\frac{(m-1)}{(M'-1)}\right]$, N' is the number of difference frequencies between the user-defined lower ($\Delta\Omega_L$) and upper ($\Delta\Omega_H$) bounds on $\Delta\omega$, and $\Delta\omega_n=\Delta\Omega_L+\left(\Delta\Omega_H-\Delta\Omega_L\right)\left[\frac{(n-1)}{(N'-1)}\right]$. Equation (3.12) can be simplified by passing the incoherent signal-band average through to the autoproduct cross-spectral density matrix defined by (3.7) to form:

$$\underline{\mathbf{R}}_{AP,avg}(\Delta\omega) = \frac{1}{M'}\sum_{m=1}^{M'} \frac{\mathbf{AP}(\omega_m, \Delta\omega)\,\mathbf{AP}^{\dagger}(\omega_m, \Delta\omega)}{\mathbf{AP}^{\dagger}(\omega_m, \Delta\omega)\,\mathbf{AP}(\omega_m, \Delta\omega)}. \tag{3.13}$$

This signal-bandwidth averaging step increases the robustness of $\mathbf{R}_{AP}$ for use in Δf-MFP just like averaging over multiple signal snapshots increases the robustness of $\mathbf{R}_P$ for use in in-band MFP. However, this averaging is possible for Δf-MFP techniques with only a single signal snapshot. Combining (3.7), (3.10), (3.12), and (3.13) produces an alternative version of (3.12):

$$B_{\Delta f,Bart,avg}(\boldsymbol{r}) = \frac{1}{N'}\sum_{n=1}^{N'} \mathbf{w}^{\dagger}(\boldsymbol{r}, \Delta\omega_n)\,\underline{\mathbf{R}}_{AP,avg}(\Delta\omega_n)\,\mathbf{w}(\boldsymbol{r}, \Delta\omega_n), \tag{3.14}$$

Results from (3.14) are directly compared with those from (3.5) in Section 3.4.

3.2.2 Source Waveform Dependence

Returning to the definition of $B_{\Delta f}$ as given in (3.11), it is clear that the summand is the product of the autoproduct, $P_j(\omega_+)P_j^*(\omega_-)$, and the replica, $w_j^*(\Delta\omega)$, where $\omega_\pm = \omega \pm \Delta\omega/2$. However, an alternate perspective could be considered instead, where the measured field quantity is $P_j(\omega_+)$, and the "'replica"' is $P_j^*(\omega_-)w_j^*(\Delta\omega)$. This representation, while mathematically equivalent, could lead to the conclusion that this new replica depends on the measured field, and even more specifically, on the source waveform. However, this is not the case; thanks to the definition of the cross-spectral density matrices given in (3.7) and (3.13), or equivalently, the normalizations and magnitude-squared operation in (3.11), the source waveform cancels out of the expression.

To see how this is possible, consider defining the recorded waveform $P_j(\omega)$ as the product of the source waveform $S(\omega)$ and the Greens function $G_j(\omega)$. Furthermore, assume $S(\omega_\pm) =$

$|S_\pm| e^{i\phi_\pm}$, where $S_\pm$ and $\phi_\pm$ represent the source waveforms unknown amplitude and phase, respectively, at frequency $\omega_\pm$. Plugging this into (3.11), it is straightforward to show that:

$$B_{\Delta f,Bart}(\boldsymbol{r},\omega,\Delta\omega) = \frac{\left||S_+||S_-|e^{i(\phi_+-\phi_-)}\sum_{j=1}^{N} G_j(\omega_+) G_j^*(\omega_-) w_j^*(\boldsymbol{r},\Delta\omega)\right|^2}{\sum_{j=1}^{N}\left||S_+||S_-|e^{i(\phi_+-\phi_-)}G_j(\omega_+) G_j^*(\omega_-)\right|^2 \sum_{j=1}^{N}|w_j(\boldsymbol{r},\Delta\omega)|^2}, \tag{3.15}$$

In this representation, it is clear that when the magnitude-squared operations in the numerator and denominator are evaluated, the $|S_\pm|$ terms as well as the complex exponentials that contain the source waveforms dependence disappear, since $|e^{i\phi}A| = |A|$. Thus, the source waveform cancels out in this representation, and it is not necessary to know the sources waveform *a priori*. It can be shown that the cross-spectral density matrices, as defined in (3.1) and (3.7), are also independent of the source waveform, thanks to the normalizations and the complex conjugate in the numerator. Therefore, even though it is possible to recast the technique as using measured waveform at ω_- as part of the replica, the source waveform always cancels out and is not needed to perform source localization.

3.2.3 Adaptive Frequency Difference MFP Techniques

Bartlett MFP is the most basic MFP signal processing algorithm, and its application to in-band and Δf-MFP is described in the previous sections. This section briefly presents the formulation of four other MFP signal processing algorithms. Unlike the Bartlett processor where w_j from (3.2) and (3.3) depends only on the acoustic environment and the frequency ω, these four are adaptive processors and their associated w_j depend on the environment, the frequency, and the signal/noise characteristics contained in the recorded signals, $P_j(\omega)$.

The first adaptive processor is minimum variance distortionless response (MVDR), and it is also known as minimum variance (MV), maximum likelihood method (MLM), or the Capon filter. When applied to MFP, MVDR is known for strong side lobe suppression (Jensen *et al.*

2011), resulting in significant improvement in peak-to-side-lobe ratios compared to Bartlett MFP. However, the technique is more sensitive to environmental mismatch than Bartlett. The ambiguity surface for Δf-MFP using MVDR is given by:

$$B_{\Delta f,MVDR,avg}\left(\boldsymbol{r}\right) = \frac{1}{N'}\sum_{n=1}^{N'} \frac{1}{\mathbf{w}^{\dagger}\left(\boldsymbol{r},\Delta\omega_n\right)\underline{\mathbf{R}}_{AP,avg}^{-1}\left(\Delta\omega_n\right)\mathbf{w}\left(\boldsymbol{r},\Delta\omega_n\right)} \tag{3.16}$$

The MVDR technique is further described in Johnson (1982) and Baggeroer (1988). An additional option available for MVDR MFP is the White Noise Constraint, or WNC (Cox *et al.* 1987, Debever & Kuperman 2007) which is intended to prevent numerical instability when the CSDM, $\mathbf{R}$, in the denominator of (3.16) does not have full rank. Depending on the choice of parameters, MVDR with WNC can be made to have localization performance similar to Bartlett or MVDR. Because these two are considered already in this study, for the sake of brevity, further discussion of MVDR with WNC is not included here.

The second adaptive processor considered here is the multiple constraints method (MCM) (Schmidt *et al.*, 1990, Jensen *et al.*, 2011). MCM MFP attempts to retain the robustness of Bartlett MFP to environmental mismatch while simultaneously improving side lobe suppression. To simultaneously accomplish both tasks, the search window of each replica is widened to include information from the replicas of surrounding grid points. In the implementation chosen for this study, the search window is a range-depth cross pattern. For a given test point (r, z), five replicas were calculated: $\mathbf{w}(r,z)$, $\mathbf{w}(r\pm\Delta r,z)$ and $\mathbf{w}(r,z\pm\Delta z)$, where Δr and Δz are chosen to be widths and depths of the MFP search grid for convenience. These replicas are referred to as $\mathbf{w}_1$ through $\mathbf{w}_5$, with $\mathbf{w}_1 = \mathbf{w}(r,z)$, all of which are column vectors of size $N\times 1$, where N is the number of hydrophones. The MCM method was implemented via a $N\times 5$ matrix $\underline{\mathbf{E}}$ composed of $[\mathbf{w}_1,\mathbf{w}_2,\mathbf{w}_3,\mathbf{w}_4,\mathbf{w}_5]$ and a 5×1 vector $\mathbf{d} = \underline{\mathbf{E}}^{\dagger}\mathbf{w}_1$, where the replica normalizations require the first entry of $\mathbf{d}$ to be unity. With these two quantities defined, the ambiguity surface for Δf-MFP using MCM is given by:

$$B_{\Delta f,MCM,avg}\left(\boldsymbol{r}\right)=\frac{1}{N'}\sum_{n=1}^{N'}\left[\frac{\mathbf{d}^{\dagger}\left(\underline{\underline{\mathbf{E}}}^{\dagger}\underline{\underline{\mathbf{R}}}_{AP,avg}^{-1}\underline{\underline{\mathbf{E}}}\right)^{-1}\mathbf{d}}{\mathbf{d}^{\dagger}\left(\underline{\underline{\mathbf{E}}}^{\dagger}\underline{\underline{\mathbf{E}}}\right)^{-1}\mathbf{d}}\right]. \tag{3.17}$$

Here, all of the terms inside the square brackets are dependent on the difference frequency $\Delta\omega_n$, and all the terms other than the CSDM are dependent on the test coordinate $\boldsymbol{r}$, though these dependencies have been suppressed in (3.17) for clarity.

The third adaptive processor that can be used for MFP is multiple signal classification (MUSIC) (Schmidt, 1986). This technique is often employed successfully for direction finding in nearly single-path environments with multiple sources. Application of the MUSIC processor to a single source in a multi-path environment may not be as successful. As part of the algorithm, detailed below, a decision must be made by the user as to how many eigenvectors of the CSDM constitute the signal subspace, implying that the remaining eigenvectors represent the noise subspace. Since the current investigation presumes the presence of a single remote source, only one signal eigenvector (designated by the largest eigenvalue) was selected, and the remaining $N-1$ eigenvectors were presumed to constitute noise. Additionally, in this study, it was found that one eigenvalue was typically much larger than the other $N-1$ eigenvalues. There are other ways to decide which eigenvectors constitute signal or noise, but employing these methods did not substantially change the qualitative behavior of the ambiguity surfaces and the accompanying localization performance, so for the sake of simplicity and brevity, results from alternative signal-space determination schemes are not reported here.

The MUSIC algorithm was implemented as follows. First, an eigenvalue decomposition of $\underline{\underline{\mathbf{R}}}_{AP,avg}$ was performed to yield $\underline{\underline{\mathbf{R}}}_{AP,avg}\mathbf{u}_i=\lambda_i\mathbf{u}_i$ where λ_i and $\mathbf{u}_i$ are the eigenvalues and column eigenvectors, respectively. Next, the eigenvalues λ_i were arranged in ascending order such that λ_N is the largest eigenvalue. Then, the noise projection matrix $\underline{\underline{\mathbf{\Phi}}}$ was computed from the other eigenvectors: $\underline{\underline{\mathbf{\Phi}}}=\sum_{i=1}^{N-1}\mathbf{u}_i\mathbf{u}_i^{\dagger}$. With this matrix, the ambiguity surface for

Δf-MFP using MUSIC is given by:

$$B_{\Delta f,MUSIC,avg}\left(\boldsymbol{r}\right) = \frac{1}{N'}\sum_{n=1}^{N'}\frac{1}{\mathbf{w}^{\dagger}\left(\boldsymbol{r},\Delta\omega_n\right)\underline{\boldsymbol{\Phi}}\left(\Delta\omega_n\right)\mathbf{w}\left(\boldsymbol{r},\Delta\omega_n\right)} \tag{3.18}$$

It is not possible to normalize $B_{\Delta f,MUSIC,avg}$ to guarantee that it falls between 0 and 1. Nonetheless, this quantity is still displayed on a decibel scale in ambiguity surface plots in Section 3.4.

Another adaptive technique considered in this study is called CLEAN (Hgbom 1974, Song *et al.*, 2002). It was developed for radio astronomy and it iteratively employs MVDR with a WNC, particularly in an effort to find multiple sources. However, the localization performance of CLEAN was found to be very comparable to MVDR with WNC, and as such, has been omitted from the remainder of this study due to its lack of unique localization performance compared to the other processors.

The final processor considered is matched mode processing (MMP) (Yang, 1989) which produces an ambiguity surface after the recorded signals are projected onto the propagating modes of the sound channel. If the acoustic field from a remote source is recorded by N hydrophones and there are M propagating modes of interest in the sound channel, then if $M \leq N$, the N measured field amplitudes can be converted into M modal amplitudes by means of a least-squares fit. Because of the environmental mismatch problem, it is expected that higher-order modes are a less reliable means for conveying source location information than lower-order modes. Therefore, by projecting the recorded data onto the lower-order modes, the detrimental effects of environmental mismatch may be limited and computational burden of high-order mode calculations may be relieved more details about the modal decomposition calculation can be found in Section 3.2.5. As described in Section 3.3.1, the modal decomposition for this study was performed in the difference frequency bandwidth (approximately 10^2 to 10^3 Hz), *not* the signal bandwidth (approximately 10^4 Hz

and higher), so only the first few propagating modes were considered.

To apply the MMP algorithm, the N field measurements are assumed to follow $P_j = \sum_{m=1}^{M} a_m \psi_m(z_j)$ where a_m is a mode-weighting coefficient, ψ_m is the shape of the mth propagating mode of the sound channel, z_j is the depth of the jth hydrophone, the array is assumed vertical, and the mode shapes are normalized such that their inner products over the entire sound channel depth are unity. Define an $N \times M$ matrix of mode shapes called $\underline{\mathbf{F}}$, where $F_{jm} = \psi_m(z_j)$. By defining the $M \times N$ projection matrix $\underline{\mathbf{Q}} = \left(\underline{\mathbf{F}}^{\dagger}\underline{\mathbf{F}}\right)^{-1}\underline{\mathbf{F}}^{\dagger}$, one can use this to project a given $N \times 1$ field amplitude vector into a $M \times 1$ modal amplitude vector (see Yang, 1989 for more details). The ambiguity surface for Δf-MFP using MMP is given by:

$$B_{\Delta f,MMP,avg}(\boldsymbol{r}) = \frac{1}{N'} \sum_{n=1}^{N'} \frac{\mathbf{w}^{\dagger}\underline{\mathbf{Q}}\mathbf{R}_{AP,avg}\underline{\mathbf{Q}}^{\dagger}\mathbf{w}}{\mathbf{w}^{\dagger}\underline{\mathbf{Q}}\underline{\mathbf{Q}}^{\dagger}\mathbf{w}} \tag{3.19}$$

In this technique, the replicas are complex modal amplitudes, not field amplitudes, and as such, are $M \times 1$ column vectors calculated from a modal decomposition. In the present study, $M = 3$ modes are chosen, since higher order modes are expected to have an increased sensitivity to the environmental mismatch (see section 3.2.5). All the terms in the summand of (3.19) depend on the difference frequency $\Delta\omega_n$, and the replicas additionally depend on the test coordinate $\boldsymbol{r}$. This technique is not adaptive, but the fitting to a modal basis rather than a depth (hydrophone) basis moves it beyond Bartlett MFP. The MMP technique may also include an eigenvalue decomposition to pick the most relevant combinations of modes while ignoring the less relevant modes. Such variations of MMP were considered, but their performance was not considerably different than the simplest version of MMP outlined here, so for brevity only ambiguity surface results from (3.19) are provided in Section 3.4.

3.2.4 Δf-MFP Theory

The theoretical foundation for the Δf-MFP technique presumes two fundamental steps. The first fundamental step is to construct the autoproduct field from high-frequency acoustic recordings under the assumption that it mimics a genuine acoustic field at the lower difference frequency. The second fundamental step is to use the autoproduct field within established MFP processing techniques as if it were a low-frequency field. In particular, this second step requires the replica vectors $\mathbf{w}$ in (3.14) – (3.19) to be evaluated at the difference frequency.

The justification for first step can be illustrated simply by assuming that the high-frequency recordings are a sum of ray path contributions, here simplified to two paths. The results for N ray paths can also be derived (see Worthmann and Dowling, submitted 2016) and provide a similar result. Here, due to the autoproducts independence of the source waveform, $S(\omega)$ will be treated as unity without loss of generality. Thus, consider the following complex acoustic field $P(\omega)$ at frequency ω,

$$P(\omega) = A_1 e^{i\omega t_1} + A_2 e^{i\omega t_2}, \tag{3.20}$$

where, t_1 and t_2 are ray-path arrival times at the recording location, and A_1 and A_2 are the complex amplitudes of each wave, which for simplicity are assumed independent of frequency. Each of these 4 parameters may vary for different recording locations, but since the autoproduct is defined using two different frequencies recorded at the *same* location, this variation across hydrophones does not present a problem. Using (3.20), the autoproduct definition (3.6) leads to:

$$AP_{\Delta}(\omega, \Delta\omega) = |A_1|^2 e^{i\Delta\omega t_1} + |A_2|^2 e^{i\Delta\omega t_2} + 2|A_1||A_2| e^{i\Delta\omega \frac{t_1+t_2}{2}} \cos(\omega(t_2 - t_1) + \phi_{12}), \tag{3.21}$$

where $\phi_{12} = \arg(A_2 A_1^*)$. The first two terms of (3.21) represent the desired self-terms, and they have the same phase dependence as a genuine low-frequency field at the difference frequency. The second term is the sum of the two undesired cross-terms, which arise from the autoproducts nonlinearity. However, an average through the signals bandwidth may minimize the detrimental effects of the cross terms. For large enough signal bandwidths relative to the difference in arrival times, the signal-bandwidth-average of the cosine factor in (3.21) will approach zero and thereby suppress the cross-terms importance. Thus, for a field that locally behaves as a sum of ray path arrivals, the bandwidth-averaged autoproduct will resemble a field in the same environment at a the lower, out-of-band, user-defined difference frequency, as long as the cross terms are suppressed by bandwidth averaging. A more thorough exposition of the autoproducts mimicry of a genuine low-frequency field is provided in Worthmann *et al.* (submitted 2016).

If the first fundamental step for the Δf-MFP technique is accepted, the second fundamental step is justified by the existing MFP literature. Many MFP techniques, including Bartlett and the adaptive techniques considered herein, were developed for use with measured acoustic fields at sufficiently low frequency where the acoustic environment and array geometry are considered known and environmental mismatch is not a problem. Thus, if the autoproduct is considered to be such a field, the existing literature for the various MFP processors provides the necessary theoretical foundation for their use here.

An alternative perspective is to view Δf-MFP is as a single-step nonlinear signal processing technique that utilizes high frequency field measurements to provide reduced-resolution source localization estimates. From this perspective, the theoretical justification for Δf-MFP must necessarily arise from appropriate statistical signal processing analysis involving constraints and/or optimization. However, such a justification for Δf-MFP is presently not available.

3.2.5 Frequency Difference Replica Calculation

As part of the replica calculation in (3.9), the Greens function shown in (3.8) must be evaluated. Since this is a Helmholtz equation at a low frequency in a bounded shallow ocean, the most convenient means of solving this equation is through a modal decomposition. Assuming loss-less boundaries, there are infinitely many modes, though only finitely many propagating modes, in an ocean sound channel, with the remainder being evanescent. Therefore, it may seem logical to calculate the replica vector using all propagating modes. However, environmental mismatch reduces or negates the utility of including higher-order modes. The wavenumbers and mode shapes of higher-order modes becomes increasingly more dependent on the details of the sound speed profile, which is not known to arbitrary precision. Thus, higher-order modes are not necessarily beneficial for successful source localization. Additionally, since the recording array may not span the full water column, mode orthogonality, as sampled by the array, may be imperfect leading to mis-estimation of received modal amplitudes. Thus, the number of modes included in the replica calculation here is much less than the number of propagating modes.

For the KAM11 recordings (elaborated upon in Section 3.3) considered here, a trial-and-error process led to the use of three modes in the replica calculations. Use of a single mode does not allow for source localization and was not considered. Use of two modes, while successful, produced overly-large ambiguity surface peaks. Use of four modes improved the source localization for some source depths, but was a detriment for others. This indicated the onset of the environmental mismatch problem. When five or more modes were used, the ambiguity surfaces lost their clearly defined peaks, and source localization performance was severely degraded. The limited number of modes also contributes to the roughly 3-km periodicity found in the ambiguity surface results of the KAM11 data. Although use of more modes would prevent this periodicity, the environmental mismatch was too severe for such a remedy.

The spatial resolution of the peaks in the MFP ambiguity surfaces scales with the difference frequency chosen by the user. A very low difference frequency results in broad peaks, which, while unambiguous, may be too large in range and depth to be useful. A higher difference frequency leads to narrower peaks in range and depth, but side lobes, possibly arising from cross-terms, become an issue. Therefore, a difference frequency bandwidth of 50Hz $\leq \Delta f \leq$ 500 Hz was chosen by trial-and-error to avoid these two extremes.

Finally, the replica calculation for frequency difference MFP is performed at the difference frequency, and with a modified boundary condition. Specifically, the ocean surface is treated as a rigid boundary, instead of the natural pressure-release boundary condition. The reason for this can be seen in (3.21). If sound traveling on the second path in (3.20) reflected from a pressure-release surface, then its waveform would be inverted because the reflection coefficient of a pressure-release surface is 1. However, in (3.21), the "'self-term"' representing this surface-interacting path has amplitude $|A_2|^2$ which is always positive. This implies that the autoproduct feels a reflection coefficient of +1 at a pressure release surface. Therefore, the three modes used in the replica vectors were calculated with this modified boundary condition. A more detailed analysis of the autoproduct field near boundaries can be found in Worthmann and Dowling (submitted 2016).

In general, using a pressure-release boundary condition for Δf-MFP in the shallow ocean produces incorrect replica vectors that lead to errors in source location estimates. However, in the downward-refracting KAM11 environment where the first three modes have scant amplitude near the ocean surface, either boundary condition was acceptable for localizing sources in the lower half of the sound channel. But, a source near the surface could only be localized if the +1 surface reflection coefficient were used to calculate modes for the replica vectors. Therefore, the unnatural surface boundary condition is important for accurate source localization with the Δf-MFP technique, at least in the KAM11 environment.

3.3 Source Localization Results Using Experimental Data

3.3.1 KAM11 Experiment

The experimental data used in this study is from the 2011 Kauai Acoustic Communications Multiple University Research Initiative experiment (KAM11) (Hodgkiss & Preisig 2011). This was an underwater acoustic communication experiment, so the utility of KAM11 data for source localization research was unexpected. KAM11 was conducted in the shallow ocean off the coast of Kauai in the summer of 2011. The nominal experimental geometry is shown in Figure 3.1. Here, a vertical 16-element hydrophone array with an array center depth of 69 m and a 3.75 m element spacing (half-wavelength spaced at 200 Hz) recorded signals at a 96 kHz sampling rate in a 106-m-deep sound channel. The source was positioned 3 km away at 16 different depths between 31.5 m and 90.2 m and broadcasted a 100-ms-long 11.2 kHz to 32.8 kHz linear frequency modulated (LFM) pulse. A sample recorded-signal spectrogram is shown in Fig. 3.2. The sound speed profile was downward refracting with a difference in sound speed between the ocean surface and bottom of 5.1 m/s, and was assumed to be range independent. There was substantial variation in the sound speed profile during the KAM11 experiment (Hodgkiss & Preisig 2011, Worthmann *et al.* 2015), and this was presumed to be a primary source of environmental mismatch. A sample measured sound speed profile from near the propagation plane is shown on the right in Fig. $Ch3_1$. The three modes used for this study were calculated in the frequency difference bandwidth using a smoothed version of this sound speed profile (see Worthmann *et al.* 2015). For the example trial used to illustrate the ambiguity surface results, the source was at a depth of 67.7 m. The other tabulations and plots provided here include results from all 16 source locations.

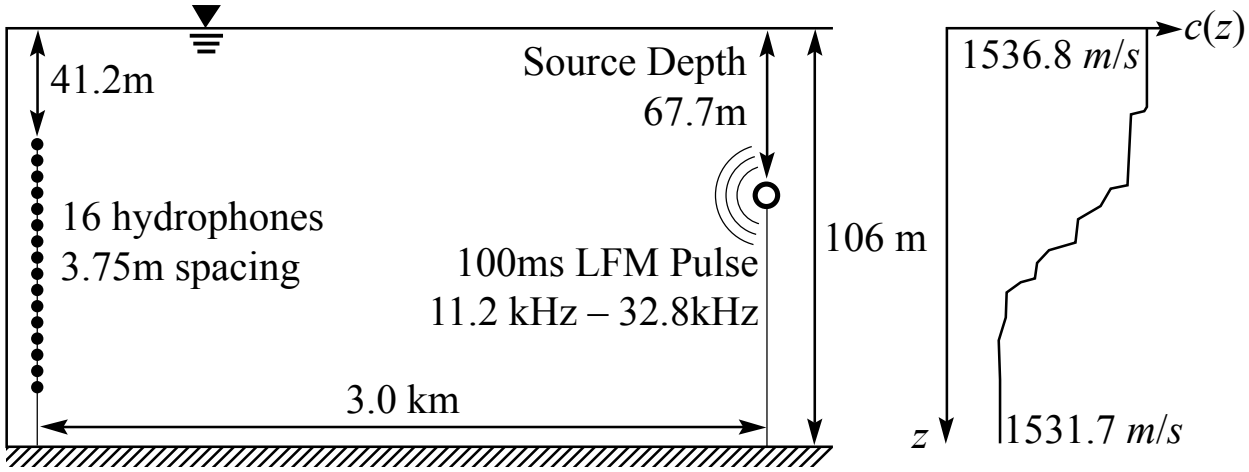

Figure 3.1: KAM11 geometry and sound speed profile. A schematic of the geometry of the nominal KAM11 geometry is shown, with a rigid bottom and a pressure release surface. The 16 element vertical line array is shown on the left, and the bottom-moored source is illustrated 3 km away and at a depth of 67.7 m. A measured sound speed profile is given on the right, and can be seen to be downward refracting, with a difference in sound speed between the top and bottom of 5.1 m/s.

3.3.2 Signal to Noise Ratio Analysis

The quantitative localization results reported here for the various implementations of in-band and Δf-MFP are reported as a function of signal-to-noise ratio (SNR). Here, the noise level was varied by adding an increasing amount of recorded ocean noise to the original measurements. The noise samples were 75 ms in duration and immediately preceded each LFM signal recording. The timing is illustrated in Figure 3.2 which shows a noise sample in region a), the 100-ms LFM signal pulse in region b), a reverberation time window in region c), and the beginning of the KAM11 communication-signal broadcast in region d). To match the durations of the noise and signal recordings so that they could be overlaid in the time domain, the final 25 ms of the signal window was not included. Thus, the results reported here are for the 15 kHz signal bandwidth from 11.2 kHz and 26.2 kHz.

The definition of signal-to-noise ratio used here includes the fact that the original recordings contain some amount of noise, and the specific waveform of this noise is not known. Let $n_j(t)$

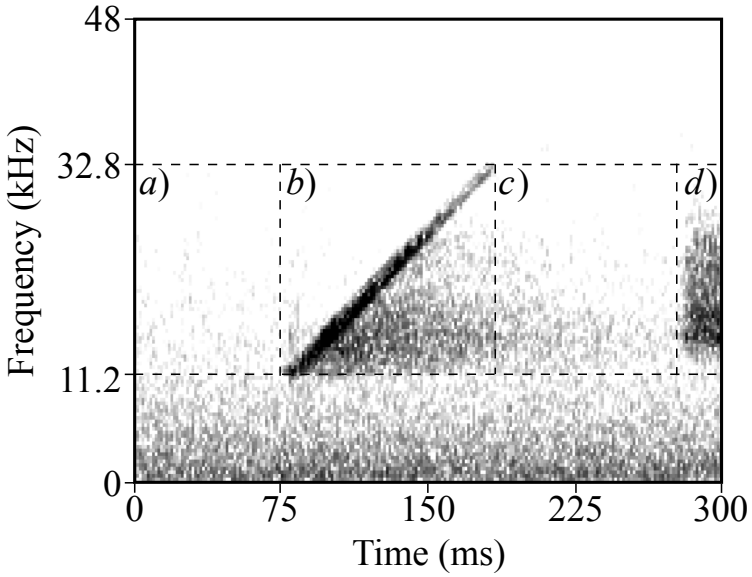

Figure 3.2: KAM11 spectrogram. The spectrogram (averaged through all 16 hydrophones) is shown for a source depth of 67.7m. The gray scale spans 30 dB. The horizontal dashed lines show the bandwidth of the KAM11 signal. Region a) shows a pure noise sample. Region b) shows the recorded LFM pulse, with the characteristic linear shape, along with some reverberation occurring after the main linear stripe. Region c) shows reverberation, and region d) shows the beginning of a KAM11 communications signal. For this study, only region a) and the first 75ms of region b) are used.

and $p_j(t)$ be the measured noise and signal plus noise for the jth hydrophone, corresponding to the a) and b) regions of the spectrogram shown in Fig. 3.2. Let $\mathbf{N}(\omega)$ and $\mathbf{P}(\omega)$ represent the noise and signal plus noise vectors in the frequency domain, where the jth element of these column vectors corresponds to the Fourier transform of $n_j(t)$ and $p_j(t)$, respectively. Before adding any noise to the measurements, the original signal-to-noise ratio (SNR), labeled as SNR_0 and reported in decibels, can be estimated when the noise is stationary as:

$$SNR_0 = 10\log_{10}\left(\frac{\langle \mathbf{P}^\dagger(\omega)\,\mathbf{P}(\omega)\rangle - \langle \mathbf{N}^\dagger(\omega)\,\mathbf{N}(\omega)\rangle}{\langle \mathbf{N}^\dagger(\omega)\,\mathbf{N}(\omega)\rangle}\right), \tag{3.22}$$

where the $\langle\ \rangle$ brackets refer to an average over the signal bandwidth and the numerator of the argument of the logarithm is the estimated signal power. In the KAM11 experimental data, SNR_0 was on average 23 dB. To add more noise to the signal-region measurements,

measured noise was simply added to $\mathbf{P}(\omega)$:

$$\mathbf{P}'(\omega) = \mathbf{P}(\omega) + \alpha \mathbf{N}(\omega). \tag{3.23}$$

Here α is a non-negative constant, and $\mathbf{P}'(\omega)$ is the enhanced-noise measurement vector that is used in the various MFP algorithms outlined in Section 3.2 via (3.1) for in-band MFP, and via (3.6) for Δf-MFP. Using (3.23) and noting that the noise in $\mathbf{P}(\omega)$ was recorded at a different time than $\mathbf{N}(\omega)$, the noise power in $\mathbf{P}'(\omega)$ is $(1+\alpha^2)\langle \mathbf{N}^\dagger(\omega)\mathbf{N}(\omega)\rangle$ since the noise is likely uncorrelated between the noise region (the first 75 ms of Fig. 3.2) and the measurement region (the second 75 ms of Fig. 3.2). Thus, the enhanced-noise SNR may be calculated from:

$$SNR = 10\log_{10}\left(\frac{\langle \mathbf{P}^\dagger(\omega)\mathbf{P}(\omega)\rangle - \langle \mathbf{N}^\dagger(\omega)\mathbf{N}(\omega)\rangle}{(1+\alpha^2)\langle \mathbf{N}^\dagger(\omega)\mathbf{N}(\omega)\rangle}\right) \tag{3.24}$$

This SNR formulation behaves correctly in the appropriate limits: (i) when the measurements approach pure noise, $SNR \to -\infty$; (ii) when no noise is added, $\alpha = 0$ and $SNR = SNR_0$; and (iii) when an overwhelming amount of noise is added, $\alpha \to \infty$, and $SNR \to -\infty$. Figure 3.3 illustrates the effect of increasing α, and shows sample spectrograms of the noise-enhanced measurements when $SNR = 20$ dB (Fig. 3.3a), $SNR = 0$ dB (Fig. 3.3b), and $SNR = 10$ dB (Fig. 3.3c).

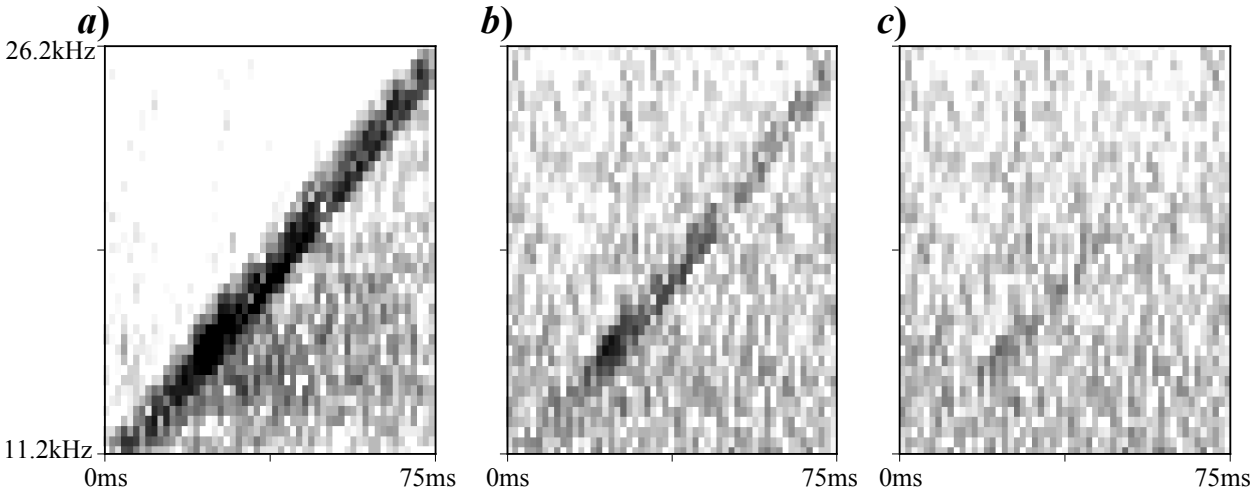

Figure 3.3: Truncated KAM11 spectrograms for varying SNR. The gray scales in all three spectrograms are held fixed at 30dB. Panel a) shows the 20dB *SNR* result, which is essentially the same as the first 75ms of Region b) in Figure 3.2. Panel b) shows the 0 dB *SNR* spectrogram, and the signal is clearly degraded by the noise. Panel c) shows the 10dB *SNR* spectrogram, and the presence of the signal is almost completely obscured by the noise.

3.4 Results

3.4.1 Adaptive MFP and SNR Results

In this section, ambiguity surfaces for five different Δf-MFP techniques (Bartlett, MVDR, MCM, MUSIC, and MMP) are presented for signal-to-noise ratios of 20 dB and 0 dB for one trial of the KAM11 experiment. Additionally, average values from all 16 KAM11 trials for six performance metrics (range error, depth error, peak range extent, peak depth extent, peak-to-side-lobe ratio, and dynamic range) are compared as a function of SNR. Here, range (depth) error is the absolute value of the difference between the true range (depth) and the range (depth) of the peak in the MFP ambiguity surface. To quantify the size of the peaks, a paraboloid is least-squares-fit to the peak and the nearby grid points. The range and depth extent (width and height) of the peak is defined by the distance it takes for the best-fit paraboloid to drop by 0.5 dB from its best-fit maximum. The peak-to-side-lobe ratio compares the height of the largest and second largest local maxima of the ambiguity

surface. Dynamic range is defined as the difference between the maximum and minimum in the ambiguity surface. Due to the periodic nature of the ambiguity surfaces (discussed below), all of the peak-finding algorithms only search between 1 km and 5 km in ranges.

An in-band Bartlett MFP ambiguity surface is shown in Figure 3.4. Here the processing is performed in the signal bandwidth: 11.2 kHz to 26.2 kHz. The horizontal axis is the range from the vertical receiving array and it varies from 0 to 6 km. The vertical axis is the depth below the ocean surface and it varies from 0 and 106 m, the entire depth of the ocean sound channel. The color scale is a logarithmic and spans 5 dB. The colors are chosen so that the maximum in the field (between 1 km and 5 km range) is deep red, and is marked with a white X. The true location of the source (3km range, and for this trial, 67.7m depth) is marked with a white circle. Even though the $SNR = 20$ dB, the ambiguity surface in Fig. 3.4 shows multiple strong peaks in the field scattered in the lower half of the sound channel with no obvious localization result in range and depth. In-band MFP results for the other adaptive processors were significantly worse than that shown in Fig. 3.4, particularly methods that require a matrix inverse of the CSDM, which is poorly conditioned for in-band processing due to a lack of multiple snapshots. Even with multiple snapshots, this failure to localize the source is expected at these in-band frequencies due to the detrimental effects of environmental mismatch, together with the extremely sparse vertical array with elements half-wavelength spaced at 200 Hz.

Ten Δf-MFP ambiguity surfaces are shown in Figure 3.5 in the same format as the in-band Bartlett MFP result shown in Fig. 3.4. The left column of Fig. 3.5 parts a), c), e), g) and i) show results for $SNR = 20$ dB, while the right column for Fig. 3.5 parts b), d), f), h) and j) show results for $SNR = 0$ dB. The rows of Fig. 3.5, from the top down, provide results for the Bartlett, MVDR, MCM, MUSIC, and MMP processors. All ten ambiguity surfaces in this figure involve incoherent averaging through the frequency difference bandwidth, 50 Hz $\leq \Delta f \leq$ 500 Hz, and all show a nearly periodic structure in range, best exemplified by

the peaks at 0km, 3km, and 6km. These peaks arise because the combined effects of the sound speed profile, the depth of the source, and the use of only 3 modes produces a field periodicity of approximately 3km. It was expected that the adaptive techniques would help mitigate the side lobes at 0 km and 6 km, however this was not found to be the case for frequency-difference MFP techniques. However, other considerations, such as reasonable estimates for source level could help differentiate between these peaks (*i.e.* it could be a quiet source at close range, or a loud source at far range). Source level and other absolute amplitude considerations are beyond the scope of MFP as defined here. On the other hand, Fig. 3.5 shows that the addition of a significant amount of noise does not drastically change the localization performance even though peak-to-side-lobe ratios and dynamic range are clearly lower. In general, for all Δf-MFP techniques, increasing noise primarily raises an ambiguity surfaces background level until it swamps the peaks, and this generally occurs at *SNR*s less than 5dB or so in the current study.

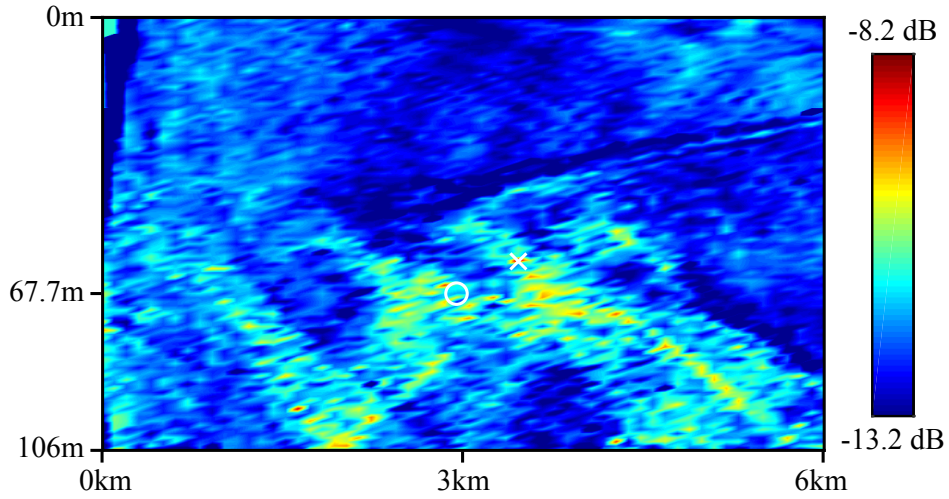

Figure 3.4: Sample in-band Bartlett MFP ambiguity surface. This range-depth cross section of the ocean shows the most likely source locations on a logarithmic color scale, with a dynamic range of 5 dB. The true source location is shown with a white O, located at 3 km range and 67.7m depth. The highest peak in the field is shown with a white X. The localization result here is ambiguous, with numerous possible source locations, roughly constrained to the bottom half of the sound channel. This poor localization result is expected due to the strong detrimental effects of environmental mismatch in the signal band (11.2 kHz to 26.2 kHz).

The results shown in the ten parts of Fig. 3.5 are merely for one of 16 KAM11 source depths. Tabulated results from all 16 trials at $SNR = 20$ dB are provided in Table 3.1 for in-band Bartlett MFP and the five Δf-MFP techniques used to create Figs. 4 and 5. In particular, Table 3.1 provides averages and interquartile ranges (the difference between the 75^{th} and 25^{th} percentile values) for six localization performance metrics (range error, depth error, peak range extent, peak depth extent, peak-to-side-lobe ratio, and dynamic range) for each MFP technique. Here, interquartile range is used as a metric for variability between trials; this was used instead of standard deviation because it is less sensitive to extreme outliers, and is more suitable for values recorded in decibels. For computational convenience, only the data with an *SNR* of 20dB was considered for in-band

Bartlett MFP (due to its high computation time); adding noise is obviously not expected to improve the already very poor localization results offered by in-band Bartlett processing. Additionally, the range and depth extent (width and height) of the in-band Bartlett MFP peaks were found to be much smaller than the replica search grid spacing (100 m in range, 1 m in depth). In principle, the grid could be refined to obtain a better estimate of the range and depth extent, but this too was a computational inconvenience and as such, was omitted. Additionally, the range and depth error, and resulting variations over the 16 source depths available in the experiment are used here as metrics for robustness in the technique. While this localization error metric is imperfect, it is the simplest metric for robustness that is suitable to the limited number of data sets available, and suitable for an experiment where there is limited control of the acoustic environment.

Table 3.1 provides a variety of noteworthy results with respect to Δf-MFP techniques. First, the range and depth errors of Bartlett, MUSIC, and MMP are roughly the same, implying these techniques do not help or hurt Δf-MFP localization efforts. However, MVDR and MCM both show larger localization errors, though the large inter-quartile range suggests this is highly variable, with some trials performing well, and others performing poorly. The

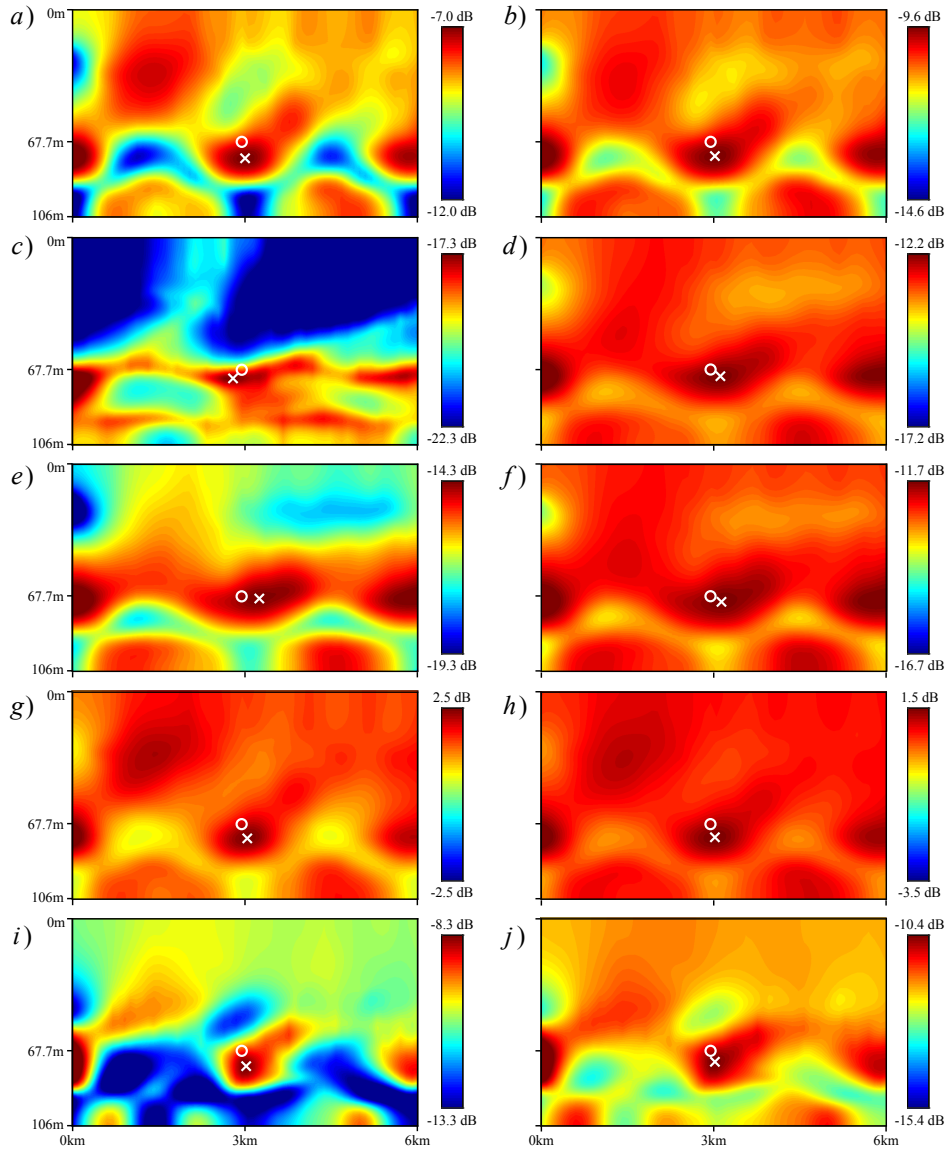

Figure 3.5: Sample frequency difference MFP ambiguity surface plots at $SNR = +20$ and 0 dB. All ten plots show the same range-depth cross section of the ocean, and the color scales each span 5dB, with the true source location shown with a white O, and the peak in the ambiguity surface shown is shown with a white X. The left column (panels a, c, e, g, i) is for 20 dB SNR data, while the right column (panels b, d, f, h, j) is for 0 dB SNR data. The first row shows Bartlett Δf-MFP results (panels a and b). The second row shows MVDR Δf-MFP results (panels c and d). The third row shows MCM Δf-MFP results (panels e and f). The fourth row shows MUSIC Δf-MFP results (panels g and h). The final row shows MMP Δf-MFP results (panels i and j).

range and depth extent numbers document the size (resolution) of the peaks. In range, all the techniques provide roughly the same peak width, with the exception of MCM which

has very wide peaks in range. In depth, the MVDR and MMP techniques offer significantly smaller peaks compared to Bartlett. However, MMP is more consistent in its narrow depth extents, whereas MVDR has more variation. MVDR offered the best peak-to-side-lobe ratios, but surprisingly was the only adaptive technique to out-perform Bartlett. However, the aggressive but hit-or-miss nature of MVDR is well illustrated here: MVDR also has a significantly higher variability in peak-to-side-lobe ratio. MCM, MMP, and MUSIC, on the other hand, did not achieve the peak-to-side-lobe ratio of Bartlett but all were more consistent. Interestingly, the dynamic range results tell a different story. Although MVDR provides large but variable dynamic range, MMP outperforms it and does so very consistently. MUSIC offers the lowest average dynamic range, and also does so the most consistently. And finally, a simple composite performance score for each technique is also given in Table 3.1. Within each of the six performance metrics, the mean values are ranked; the best technique earned 5 points, and the worst technique earned 1 point. For example, at an SNR of 20dB, MMP ranked 2^{nd}, 3^{rd}, 1^{st}, 2^{rd}, 3^{rd}, and 1^{st} in the six metrics to achieve a composite score of 4+3+5+4+3+5=24 points, and is the most successful technique based on this composite score for both SNRs provided in Table 3.1.

The results listed in Table **??** show only two *SNR*s, 20dB and 0dB. Using the noise addition technique described in Section 3.3.2, these were extended down to $SNR = 20$ dB in 1 dB increments, and the results are plotted in the six parts of Fig. 3.6. Here, the average value for each performance metric is plotted as a function of *SNR* between ±20dB. The interquartile range of these metrics as a function of SNR is similar to that given in Table I and is omitted for brevity.

Specific results for each performance metric are as follows. The effect of decreasing SNR on the range and depth errors is illustrated in Figure 3.6a) and b). Bartlett, MUSIC, and MMP have almost exactly the same performance as a function of *SNR* down to about 0 dB. Below that, the errors begin diverging. The variability (not shown here) indicates

Property	SNR (dB)	Frequency Difference										In-Band	
		Bartlett		MVDR		MCM		MUSIC		MMP		Bartlett	
		Mean	IQR	Mean	IQR	Mean	IQR	Mean	IQR	Mean	IQR	Mean	IQR
Range Error (m)	20	168	71	217	146	286	166	149	79	163	72	775	525
	0	155	64	176	190	168	90	148	66	159	76		
Depth Error (m)	20	9.1	4.5	15.4	9.3	14.0	8.7	9.1	4.1	9.8	7.8	15.3	11.4
	0	9.4	5.9	10.9	8.8	10.6	9.3	9.0	4.5	9.9	6.6		
Range Extent (m)	20	351	59	335	150	506	104	352	87	318	101	< 100m	
	0	436	105	453	113	511	152	428	162	408	136		
Depth Extent (m)	20	9.4	4.6	5.4	5.1	11.6	5.6	9.0	4.7	6.1	2.2	< 1m	
	0	11.3	5.3	9.9	4.8	13.7	7.4	10.4	4.4	7.6	3.2		
Peak to Sidelobe Ratio (dB)	20	0.83	0.50	1.13	1.36	0.41	0.48	0.61	0.42	0.77	0.43	0.34	0.33
	0	0.51	0.33	0.58	0.58	0.31	0.25	0.41	0.59	0.44	0.27		
Dynamic Range (dB)	20	6.2	2.3	7.1	3.9	5.5	2.9	2.6	0.8	7.3	1.9	6.7	2.3
	0	3.7	1.4	2.8	1.0	2.7	0.8	2.0	0.7	3.5	1.2		
Composite Score (5 to 30)	20	20 (3rd)		21 (2nd)		8 (5th)		17 (4th)		24 (1st)			
	0	22 (2nd)		16 (4th)		9 (5th)		20 (3rd)		23 (1st)			

Table 3.1: Localization performance for Δf-MFP and in-band MFP for all 16 KAM11 trials. Here, IQR is the inter-quartile range, and is the difference in value between the 75^{th} percentile and 25^{th} percentile of the data, and is a measure of its variability. Six different performance metrics: range error, depth error, peak range extent (peak width), peak depth extent (peak height), peak-to-sidelobe ratio, and dynamic range are given in the table, as a function of SNR. Additionally, a composite score gives a simple metric by which to compare each of the five Δf-MFP techniques.

drastic variations in these errors, and for *SNR*s below 5 dB, the variability is similar to that of uniformly-distributed random source location estimate. The range and depth extents, shown in Fig. 3.6c) and d), illustrate a roughly monotonic increase of the peak size as SNR decreases for all the techniques. Figure 3.6e) shows the expected results that the peak-to-side-lobe ratio generally decreases with decreasing *SNR*. As in Table I, MVDR has the best peak-to-side-lobe ratio, but this advantage is lost below $SNR = 5$ dB. While peak-to-side-lobe ratio is often used as a metric for robustness for in-band MFP, it is not such an indicator for Δf-MFP, as can be seen by MVDRs poor performance in Table 1. A better indicator is dynamic range, which can be thought of as the difference between the best and worst

correlated replicas in the field. Figure 3.6f) illustrates this by showing MMP to be the most robust technique for positive SNR. However, more importantly, all of the techniques show a monotonic decrease in dynamic range with decreasing SNR. Thus, since dynamic range does not require knowledge of the source position, it can actually be used as a likely-effectiveness metric to assess the trustworthiness of any Δf-MFP localization result. In practical cases, the source position is unknown, so if the dynamic range of the resulting Δf-MFP ambiguity surface can be determined to be above a certain threshold (approximately 3dB in the shallow ocean environment considered here), then the localization result can be treated as reliable. But, when the dynamic range is lower, a Δf-MFP localization result is less certain and less trustworthy, but it is still likely to be more reliable than an in-band MFP result.

3.4.2 Dynamic Range Discussion

For high SNR, adaptive MFP techniques are anticipated to have a large dynamic range, or similarly, a large peak-to-side lobe ratio. However, Δf-MFP consistently underperforms with respect to dynamic range, even when considering high SNR trials. This occurs for a number of reasons, all of which originate from the nonlinear nature of the autoproduct.

Suppose a measured field, $P(\omega\ )$, was composed of a signal $s(\omega\ )$, and a noise source $N(\omega\ )$. The signal-to-noise ratio is defined as the ratio of the signal power divided by the noise power, which is simply $\frac{SNR=|s(\omega)|^2}{|n(\omega)|^2}$. However, when calculating the autoproduct, four terms arise: $AP = s_+s_-^* + s_+n_-^* + s_-^*n_+ + n_+n_-^*$, where the $\pm$ subscript indicates an evaluation at frequency $\omega_\pm = \omega \pm \frac{\Delta\omega}{2}$. The first term is the desired term: the autoproduct of the signal. The last three terms all represent noise in the context of the autoproduct, since none of those three should be expected to correlate well with a replica. Therefore, the signal to noise ratio in the autoproduct domain, SNR_{AP}, can be defined as the ratio of $|s_+s_-^*|^2$ to $|s_+n_-^* + s_-^*n_+ + n_+n_-^*|^2$. The denominator here is bounded above by $\left(|s_+n_-^*| + |s_-^*n_+| + |n_+n_-^*|\right)^2$, thanks to the triangle inequality. Therefore, the lower bound on the effective SNR for the

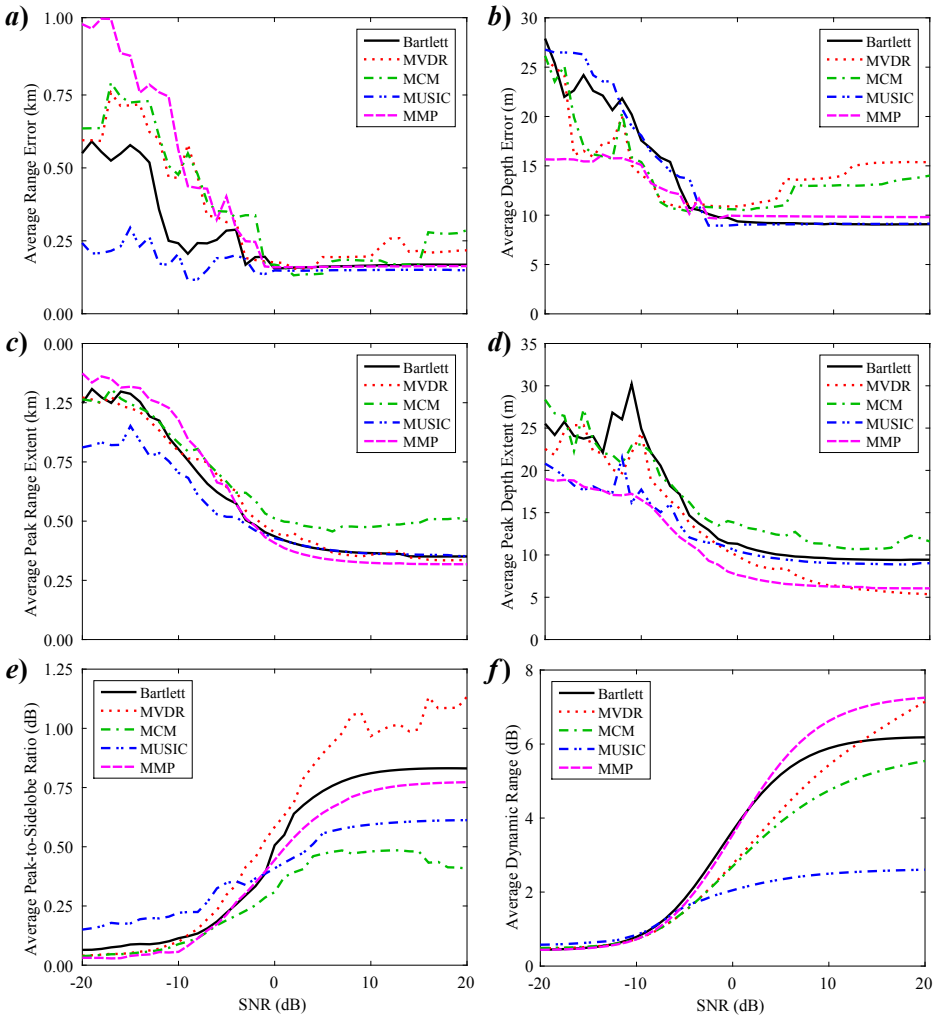

Figure 3.6: Frequency difference MFP performance as a function of SNR. The same six performance metrics as given in Table 1 are plotted here as a function of SNR between ± 20dB. The mean across all 16 trials is plotted; the variability in that data is omitted here for clarity, but is comparable to the variability specified in Table 1. The solid (black) lines refer to Bartlett, the dotted (red) lines refer to MVDR, the dash-dotted (green) lines refer to MCM, the dash-double-dotted (blue) lines refer to MUSIC, and the dashed (magenta) lines refer to MMP.

autoproduct domain can be written as:

$$SNR_{AP} \geq \left(\frac{|s_+ s_-^*|}{|s_+ n_-^*| + |s_-^* n_+| + |n_+ n_-^*|} \right)^2 \approx \left(\frac{SNR}{1 + 2\sqrt{SNR}} \right)^2, \tag{3.25}$$

where the final approximation of (3.25) is made by assuming that the SNR is approximately

constant across the signal bandwidth. The right side of (3.25) is always smaller than *SNR*. More specifically, at a very high *SNR*, the effective SNR_{AP} is smaller by a factor of 4 (6 dB) lower than the standard *SNR*. And at very low *SNR*, the SNR_{AP} is close to SNR^2, or double the number of (negative) decibels. Therefore, adding any amount of noise has the potential to be more detrimental in the autoproduct domain, and particularly so for negative SNR.

The above analysis is valid even for free-space propagation, which contains no cross-terms in the $\left|s_+ s_-^*\right|^2$ term. However, the presence of multiple arrivals implies there will be detrimental cross-terms (see Eq. (3.21)), even before compensating for noise. Therefore, in the presence of both noise and multiple arrivals, Δf-MFP is at a significant handicap compared to its low-frequency conventional MFP analogue. However, since no such low-frequency is truly recorded by the array, only high-frequency conventional MFP exists as the alternative processing scheme, and the effects of environmental mismatch severely degrade its source localization performance in most practical shallow ocean environments. Therefore, the poor dynamic range seen in the Δf-MFP ambiguity surfaces can be explained by the nonlinear construction of the autoproduct both in how it amplifies the effect of any amount of noise, and how it creates detrimental cross terms.

3.5 Summary and Conclusions

Frequency difference (Δf) matched-field processing (MFP) is a new technique for high frequency remote source localization in any imperfectly-known acoustic environment (Worthmann *et al.* 2015). This paper reports the results of applying several well-known adaptive array signal processing techniques to Δf-MFP in a shallow ocean environment. These performance results are quantified through six localization metrics extracted from the various MFP range-depth ambiguity surfaces calculated from recordings from the KAM11 experiment. Here, chirp signals were broadcast 3 km from 16 different source depths to a 56-m-long verti-

cal receiving array through a nominally-range-independent 106-m-deep ocean sound channel. For this study, Δf-MFP was implemented using in-band frequencies of 11.2 kHz to 26.2 kHz but just three modes for the requisite replica calculations in the frequency-difference bandwidth, 50Hz $\leq \Delta f \leq$ 500 Hz. In addition, the effect of noise on the localization results was determined by degrading the 23 dB signal-to-noise ratio (SNR) of the KAM11 measurements downward to 20 dB through the weighted addition of *in-situ* measured noise.

This research supports the following five conclusions. First, for the KAM11 environment and the KAM11 LFM signal pulses, any of the Δf-MFP techniques considered here will provide superior localization performance compared to in-band MFP. The frequency difference approach to MFP (and beamforming) explicitly trades in-band resolution for robustness by exploiting the autoproduct to shift the signal processing out of the signal band down to a frequency range where MFP (or beamforming) techniques can be applied with greater confidence.

Second, Δf-MFP was not significantly improved with adaptive array signal processing techniques. The adaptive techniques considered here (MVDR, MCM, MUSIC, MMP) do not provide the level of side lobe reduction or resolution improvements that are possible when these techniques are applied to in-band and in known environments. The cause of this lack of improvement is associated with the production of unintentional cross-terms generated by the quadratic nature of the autoproduct, which leads to smearing of the ambiguity surface peaks in a multipath environment, as well as the detrimental effects of noise, as described in Section 3.4.2. Another possible explanation that was considered involves the detrimental effects of environmental mismatch at the lower, out-of-band, difference frequency bandwidth. However, this explanation was deemed unlikely based on simulations (not shown here) that indicate no significant changes in localization performance even with perfect environmental agreement.

Third, in the current study, the matched-mode processor (Yang, 1989) was found to perform

the best followed closely by the Bartlett processor. MMP provided the tightest ambiguity surface peaks, largest dynamic range, and relatively low range and depth errors, consistently across all 16 trials. However, its performance was only marginally better that Bartlett processing. As might be expected, the results using MVDR were more variable, with some trials providing excellent localization results while others did not. In this study, the MCM processor mostly provided Bartlett-like localization results but with decreased resolution. The MUSIC processor also provided Bartlett-like results, but its dynamic range was consistently lower. At a fundamental level, it is remarkable that the MMP performs best in this study since the KAM11 acoustic propagation measurements are best understood via rays refracted and reflected in the shallow ocean. However, replicas based on the first three propagating modes of the sound channel computed with an unnatural ocean-surface boundary condition at frequencies well below the KAM11 signal band are found to correlate best with a quadratic product of in-band recorded signal amplitudes, despite noise and environmental mismatch.

Fourth, even though Δf-MFP does not provide ambiguity surfaces with large dynamic range, its performance declines slowly with decreasing SNR and it remains a viable source localization technique at SNR as low as 0 dB, and possibly as low as 5 dB, in the KAM11 environment considered here. Adding noise merely fills in the valleys of a Δf-MFP ambiguity surface, thereby decreasing its dynamic range, until finally the localization peak disappears into the rising noise background.

And fifth, when Δf-MFP does breakdown at low SNR it does so gracefully. All the performance curves in Fig. 3.6 show smooth degradation as the SNR falls. Furthermore, the dynamic range of a Δf-MFP ambiguity surface can be monitored to anticipate when Δf-MFP is likely to be inaccurate or inapplicable. For the current study, this threshold dynamic range for successful Δf-MFP was approximately 3 dB.

Lastly, it is worth reiterating how the Δf-MFP techniques outlined here outperform any other conventional techniques found in the literature. Given the environmental uncertainty

that accompanies shallow oceans, no other techniques known to the authors are able to localize a source broadcasting a high-frequency and unknown waveform using a single signal snapshot and a sparse array. Other potential applications of the frequency-difference approach may exist beyond underwater acoustics in ultrasonics, seismology, or structural acoustics, and potentially in radar, too.

CHAPTER 4

Nonlinear Signal Processing Techniques for Active Sonar Localization in the Shallow Ocean with Significant Environmental Uncertainty and Reverberation

Abstract

Sonar signal processing techniques based on acoustic models of shallow ocean environments are frequently of limited use for the mid- to high-frequency regimes typical for active sonar. To make use of acoustical models of the environment, signal processing algorithms typically require better-than-a-wavelength accuracy in the acoustic path estimates. Given this limitation, and practical knowledge that can be expected for shallow ocean environments, model-based signal processing schemes are often limited to frequencies below approximately 1 kHz. Recently, a new nonlinear signal processing technique (see Worthmann et al., JASA 138, 3549-3562, 2015) was able to localize mid-water-column, high frequency sources in the shallow ocean despite imperfect knowledge of the acoustic environment. The new technique takes advantage of a nonlinear construction called the autoproduct to controllably create difference frequencies to recover out-of-band, low frequency field information from in-band, high

frequency hydrophone measurements. This passive source localization technique is extended to monostatic active sonar target localization, where strongly reverberant environments can obscure a desired target echo. The frequency difference active sonar technique is presented along with comparisons to existing detection and localization algorithms. Additionally, simulations are provided of these algorithms performance in a 200-m deep ideal waveguide with strong reverberation and environmental uncertainties that includes a mid-water-column target at 5-km range, using broadcast frequencies between 2 kHz and 5 kHz. Successful detection and localization of this target using this nonlinear frequency difference scheme is found to be possible at signal-to-reverberation levels as low as 12 dB in this simulation.

4.1 Introduction

Active sonar is a very active research field in signal processing and underwater acoustics research communities. One of the core problems in active sonar signal processing is the challenge presented by reverberation. Given the presence of a target of interest, the desired target echo may be obscured by a comparatively larger background level of reverberation or noise. Additionally, model-based signal processing schemes have conventionally been of limited use, as the imperfect knowledge of the shallow ocean is insufficient for localizing targets using mid-to-high frequencies. The techniques outlined in this paper, which are referred to collectively as frequency difference matched field processing (Δf-MFP), were developed to localize a target echo in the presence of strong reverberation and environmental uncertainties that would typically obscure the target when using other signal processing techniques.

One of the simplest signal processing techniques for target localization is the matched filter (Turin 1960). The cross correlation between recorded waveforms and broadcast waveforms gives a series of peaks, which based on their timing can provide estimates of target ranges.

In contrast to Δf-MFP, the matched filter is unable to obtain a depth estimate, and also relies on the target echo rising sufficiently above the background reverberation. Another technique, originally developed for passive source localization, is matched field processing, or MFP (Jensen 2011). This model-based signal processing scheme correlates measured signals with modeled signals to produce an ambiguity surface showing the most and least likely target locations. However, it is well-known that MFP is very sensitive to imperfect environmental knowledge [3], particularly at frequencies above 1kHz, in a shallow ocean. This problem, termed environmental mismatch, is avoided in Δf-MFP, where the signal processing is performed at a much lower frequency that is more robust to environmental mismatch. Another technique, the matched field depth estimation (MFDE) method, has been developed by Hickman and Krolik (Hickman and Krolik, 2004). Essentially, it is a combination of the matched filter and conventional MFP, and therefore it shares many of the same deficiencies. A probabilistic approach using the back-propagation of rays was developed by Mours *et al.* (Mours 2016), but this technique requires many pings worth of data to estimate the targets depth, and is not fundamentally robust to environmental mismatch.

Recent nonlinear signal processing techniques developed for passive sonar by Abadi *et al.* (Abadi 2012) and Worthmann *et al.* (Worthmann 2015) have demonstrated the possibility of overcoming the problems presented by sparse arrays and environmental mismatch in beamforming and MFP. This is accomplished by using high frequency field measurements to create pseudo-fields that behave as if they were low frequency measurements, and then performing the signal processing at this lower frequency. This paper represents an extension of these techniques to active sonar.

The techniques outlined in this paper also offer a new method to perform clutter discrimination. It is well known that, because of reverberation and various sources of clutter, there is a high false-alarm rate in active sonar systems. Most techniques rely upon using hundreds or

thousands of pings to develop clutter statistics, which can then be compared to known probability distributions for discriminating between clutter and targets (Abraham 2011). One of the techniques described in this study offers the ability to localize reverberation in depth, which may provide a means of reducing the false alarm rate. In this paper, Δf-MFP for active sonar is introduced (Section 4.2), and then a very simple, proof-of-concept simulation is performed (Section 4.3). The localization performance of conventional techniques and frequency difference techniques are compared (Section 4.4), and the conclusions that can be drawn this study are summarized (Section 4.5).

4.2 Signal Processing Algorithms

Suppose the j^{th} element of an N element hydrophone array receives the time series $p_j(t)$, where the time $t=0$ is synchronized with the beginning of the broadcast of waveform $s(t)$. The Fourier transform of these two time-series is provided by $P_j(\omega\ )$ and $S(\omega\ )$, respectively, where ω is the temporal frequency.

4.2.1 Matched Filter

The matched filter, denoted by $y_j(t)$, is given by the cross-correlation of the recorded time series with the broadcast waveform, and then normalized as shown below in (4.1).

$$y_j\left(t\right) = \left[\int_{-\infty}^{\infty} \left|S\left(\omega\right)\right|^2 d\omega\right]^{-1/2} \int_{-\infty}^{\infty} P_j\left(\omega\right) S^*\left(\omega\right) e^{-i\omega t} d\omega \tag{4.1}$$

Where $*$ denotes a complex conjugate. Effectively, $y_j(t)$ is an estimate of the impulse response of the channel. Adaptive normalizations of (4.1) which compensate for the two-way spreading losses are possible (Baldacci 2006), but for simplicity these normalizations are omitted here.

4.2.2 Conventional MFP

Conventional MFP (Jensen 2011) performs a search over possible target locations, and the strength of the correlation between measured signals and modeled signals are plotted as a function of target position, forming what is called an ambiguity surface. The stronger the correlation, the more likely the position of the target. In conventional MFP, there are four main steps. The first, unique to active sonar, is a time-gating procedure. The second is the creation of the cross-spectral density matrix, or CSDM, which contains information about the relative phases of the measured signal between hydrophones. Third, the modeled signal, called a replica, is evaluated for each test point in the search grid. In the fourth step, the replicas and CSDM are combined and bandwidth-averaged to produce one output for each pixel of the ambiguity surface.

A time-gating procedure is necessary for active sonar because of the large amplitude variations as a function of time, which is primarily a result of spreading losses. The procedure chosen for this study (see Section 4.3 for more information about the simulation parameters) is given as follows: given the range r of a certain test position, define τ_0 as the two way travel time, or $\tau_0 = 2r/c$, where c is the mean sound speed. Then the full time-series is cropped between the times $\tau_0 - \tau_1$ and $\tau_0 + \tau_2$, such that only $\tau_1 + \tau_2$ of the full time series is kept. Then this $\tau_1 + \tau_2$ subset is windowed with a half-sine-wave, Fourier-transformed into the frequency domain, and finally stored as $\widetilde{\mathbf{P}}(\omega)$, where the tilde indicates this time gating procedure has been performed, and the boldface denotes a column vector of length N.

Next, the CSDM must be calculated. This is defined as the outer product of the vector $\widetilde{\mathbf{P}}(\omega)$, and then normalized by its inner product, as shown below in (4.2).

$$\underline{\mathbf{R}}_{conv}(\omega) = \frac{\widetilde{\mathbf{P}}(\omega)\,\widetilde{\mathbf{P}}^{\dagger}(\omega)}{\mathbf{P}^{\dagger}(\omega)\,\mathbf{P}(\omega)} \tag{4.2}$$

Here † represents the conjugate transpose, and the underbar indicates a matrix.

Next, a replica is required. A replica is an N element column vector of complex weights, and is calculated by propagating waves from a test location $\boldsymbol{r}$ to the receiver locations $\boldsymbol{r}_j$ in the modeled environment. The jth element of the replica is simply the frequency-domain Greens function, of the modeled environment, evaluated at the frequency ω, as defined below in (Baggeroer 1993).

$$\left(\nabla^2 + \frac{\omega^2}{c_m^2(x)}\right) G_{conv}(\boldsymbol{r}, \boldsymbol{r}', \omega) = -\delta(\boldsymbol{r} - \boldsymbol{r}') \tag{4.3}$$

Where $c_m(\boldsymbol{r})$ is the modeled sound speed (which may in general vary spatially), and $\delta(\boldsymbol{r})$ is the Dirac delta function. Note that in practical cases of interest, the modeled environment will differ slightly from the true environment, a result of environmental uncertainty. The replica is then evaluated as $w_{conv,j}(\boldsymbol{r}, \omega) = G_{conv}(\boldsymbol{r}_j, \boldsymbol{r}, \omega)$, where $\boldsymbol{r}$ is the test coordinate and $\boldsymbol{r}_j$ is the position of the jth hydrophone. Finally, the replica is normalized to have an inner product of unity. It should be noted that while the sound is propagated two-ways (from broadcast transducer to target, then target to each receiver), the replica calculated is only a one-way replica (from target to each receiver). This is because only the Greens function from the target to the receivers contributes to phase *differences* between hydrophones. In other words, for the purposes of conventional MFP, the ensonified target can be treated as mathematically equivalent to a source.

Lastly, the CSDM and replicas are combined and bandwidth averaged to produce the ambiguity surface, as defined in (4.4)

$$B_{conv}(\boldsymbol{r}) = \int_{\omega_L}^{\omega_H} \frac{d\omega}{\omega_H - \omega_L} \left(\mathbf{w}_{conv}^{\dagger}(\boldsymbol{r}, \omega)\, \underline{\mathbf{R}}_{conv}(\omega)\, \mathbf{w}_{conv}(\boldsymbol{r}, \omega)\right) \tag{4.4}$$

Where Ω_H and Ω_L are the upper and lower bounds of the relevant bandwidth, and B is

the ambiguity surface, a positive scalar which is a function of the test position. There are other ways to combine the replica and CSDM, but this formulation, also called Bartlett MFP, is the simplest. As a result of the normalization, B is forced to be between 0 and 1, corresponding to perfectly uncorrelated and correlated matches between measured and modeled signals, respectively. It should also be noted that the broadcast waveform was not used in this formulation, and in fact cancels out when forming the CSDM in (4.2).

4.2.3 Frequency Difference MFP

In contrast to conventional MFP where all the signal processing occurs at the broadcast frequencies between Ω_L andΩ_H, frequency difference MFP performs the signal processing at a much lower, user-defined difference frequency $\Delta\ \omega$, or more specifically, over a range of difference frequencies between $\Delta\Omega_L$ and $\Delta\Omega_H$. In order to move the processing to this lower, difference frequency, a quantity termed the autoproduct is constructed, as defined below in (4.5).

$$\widetilde{\mathbf{AP}}_{\Delta,j}\left(\omega,\Delta\omega\right)=\widetilde{\mathbf{P}}_j\left(\omega+\frac{\Delta\omega}{2}\right)\widetilde{\mathbf{P}}_j^*\left(\omega-\frac{\Delta\omega}{2}\right) \tag{4.5}$$

The tildes here represent the same time-gating procedure as used in conventional MFP. The autoproduct is a quadratic product of complex field amplitudes evaluated at two different, but nearby, frequencies. It can be shown that if P_j is evaluated as a single, broadband plane wave, then the autoproduct has identically the same behavior with respect to frequency as a plane wave at a much lower frequency, even if that lower, difference frequency, $\Delta\omega$, is not present in the original bandwidth. This is no longer identically true for a multi-path environment, but only approximately so. Further discussion of the cross terms that arise may be found in (Worthmann 2015). Frequency difference MFP is performed by using the autoproduct as the measured field, with a few changes.

One required change to frequency difference MFP is in the replica calculation. Instead of being evaluated using (Baggeroer 1993), it must instead be evaluated at the lower difference frequency using (4.6), as shown below.

$$\left(\nabla^2 + \frac{(\Delta\omega)^2}{c_m^2(\boldsymbol{r})}\right) G_{\Delta f}(\boldsymbol{r}, \boldsymbol{r}', \Delta\omega) = -\delta(\boldsymbol{r} - \boldsymbol{r}') \tag{4.6}$$

Equation (4.6) and (Baggeroer 1993) are very similar, differing only by the frequency to be evaluated. Additionally, the surface boundary condition must be modified in (4.6) to be a rigid boundary condition, for reasons that are described more thoroughly in (Worthmann 2015).

The next two sub-sections develop two kinds of frequency difference MFP one where the known broadcast waveform is not needed, and another where this knowledge is leveraged, labeled as incoherent and coherent Δf-MFP, respectively. In the last sub-section, an incoherent average over the frequency difference bandwidth is given.

4.2.4 Incoherent Frequency Difference MFP

The incoherent Δf-MFP CSDM is calculated using the autoproduct as the field, and can be considered as analogous to (4.2), except that there is an additional averaging step performed over all possible frequency pairs in the bandwidth that are separated by the given difference frequency. This formulation is given below in (4.7).

$$\underline{\mathbf{R}}_{\Delta f}^{incoherent}(\Delta\omega) = \int_{\Omega_L + \frac{\Delta\omega}{2}}^{\Omega_H - \frac{\Delta\omega}{2}} \frac{d\omega}{\Omega_H - \Omega_L - \Delta\omega} \left(\frac{\widetilde{\mathbf{AP}}(\omega, \Delta\omega)\, \widetilde{\mathbf{AP}}^{\dagger}(\omega, \Delta\omega)}{\widetilde{\mathbf{AP}}^{\dagger}(\omega, \Delta\omega)\, \widetilde{\mathbf{AP}}(\omega, \Delta\omega)} \right) \tag{4.7}$$

Despite the quadratic nature of the autoproduct, the source waveform cancels out of (4.7) for the same reasons that it cancels out of (4.2).

The replica for incoherent Δf-MFP is calculated using a one-way propagation, or in other words, $w_{\Delta f,j}(\boldsymbol{r}, \Delta\omega) = G_{\Delta f}(\boldsymbol{r}_j, \boldsymbol{r}, \Delta\omega)$ and then $w_{\Delta f}$ is normalized to have unit magnitude.

4.2.5 Coherent Frequency Difference MFP

For coherent Δf-MFP, the broadcast waveform is required. Incoherent Δf-MFP averages the phase differences between hydrophones (contained in the CSDM) across the signal bandwidth. Instead, coherent Δf-MFP *directly* averages the autoproduct field across the signal bandwidth. Said differently, the absolute source-to-array propagation times are unknown for incoherent MFP (where instead only relative arrival times are needed), whereas coherent MFP requires knowledge of the absolute source-to-array propagation times. Note that time-of-arrival changes in the time domain manifest themselves as phase changes in the frequency domain, so absolute phases are needed for coherent MFP, whereas only relative phases across phones are needed for incoherent MFP.

If care is not taken to compensate for the broadcast waveforms phase in this bandwidth average, then the resulting bandwidth-averaged field will be physically meaningless. Therefore it is easiest to first define a bandwidth-averaged autoproduct field, and then second, create the normalized coherent CSDM, as defined in (4.8) and (4.9).

$$AP_{avg}(\Delta\omega) = \int_{\Omega_L+\frac{\Delta\omega}{2}}^{\Omega_H-\frac{\Delta\omega}{2}} d\omega \left(AP(\omega, \Delta\omega) \left[S^*\left(\omega + \frac{\Delta\omega}{2}\right) S\left(\omega - \frac{\Delta\omega}{2}\right) \right] \right) \tag{4.8}$$

$$\underline{\mathbf{R}}_{\Delta f}^{coherent}(\Delta\omega) = \frac{\widetilde{\mathbf{AP}}_{avg}(\Delta\omega)\, \widetilde{\mathbf{AP}}_{avg}^{\dagger}(\Delta\omega)}{\widetilde{\mathbf{AP}}_{avg}^{\dagger}(\Delta\omega)\, \widetilde{\mathbf{AP}}_{avg}(\Delta\omega)} \tag{4.9}$$

Where $S(\omega)$ is the Fourier transform of the broadcast waveform.

Additionally, the replicas for coherent Δf-MFP, $w_{\Delta f}(\boldsymbol{r}, \Delta\omega)$, must be calculated using a

two-way propagation from the broadcast transducer to the test location, and then back to the receivers. In other words, $w_{\Delta f,j}(\boldsymbol{r},\Delta\omega) = G_{\Delta f}(\boldsymbol{r}_b,\boldsymbol{r},\Delta\omega)\,G_{\Delta f}(\boldsymbol{r},\boldsymbol{r}_j,\Delta\omega)$, where $\boldsymbol{r}_b$ is the location of the broadcast transducer, and then normalized to have unit magnitude.

4.2.6 Difference Frequency Bandwidth

The last step for both types of frequency difference MFP is to combine the modeled replicas with the measured CSDM and bandwidth average, as is done conventionally in (4.4). This time, the bandwidth average is over the user-defined difference frequency bandwidth, as given in (4.10).

$$B_{\Delta f}^{(in)coherent}(\boldsymbol{r}) = \int_{\Delta\Omega_L}^{\Delta\Omega_H} \frac{d\Delta\omega}{\Delta\Omega_H - \Delta\Omega_L} \left(\mathbf{w}_{\Delta f}^{\dagger}(\boldsymbol{r},\Delta\omega)\, \underline{\mathbf{R}}_{\Delta\omega}^{(in)coherent}(\Delta\omega)\, \mathbf{w}_{\Delta\omega}(\boldsymbol{r},\Delta\omega) \right) \quad (4.10)$$

4.3 Simulation Parameters

A very simple simulation is created to demonstrate, as a proof-of-concept, the target localization performance of Δf-MFP techniques as compared to conventional techniques. An ideal shallow ocean sound channel will be employed with a vertical array which allows a generally 3D problem to be reduced to an axisymmetric 2D problem. Many of the relevant simulation parameters are detailed in Figure 4.1a, with a more detailed description given below.

The shallow ocean under consideration is 200m deep, iso-speed at 1500 m/s, with a perfectly flat, rigid and non-absorptive bottom and perfectly flat, pressure-release surface. The broadcast transducer, at a depth of 20m, broadcasts a 100ms linear frequency modulated pulse (LFM, or chirp) from 2kHz to 5kHz with a raised-cosine window. A vertical line array

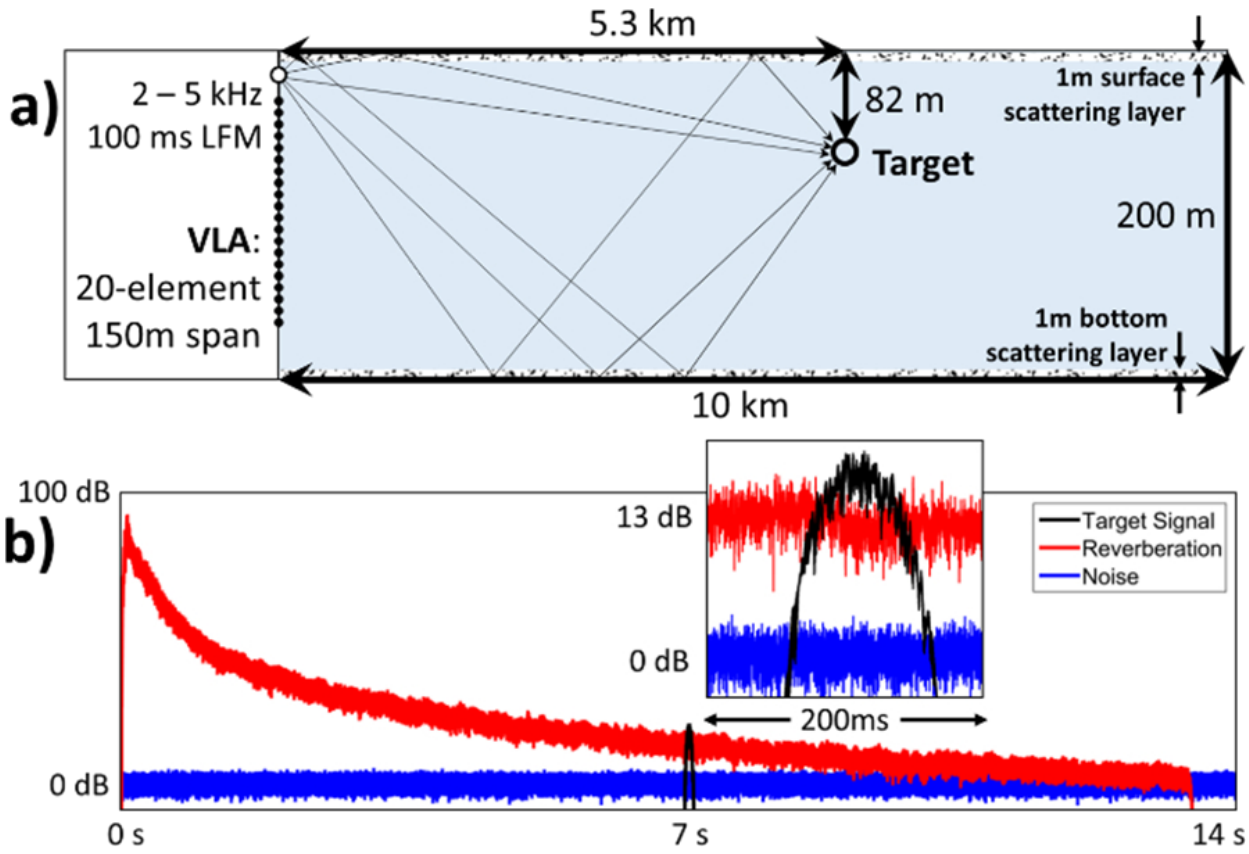

Figure 4.1: Simulation geometry and simulated hydrophone measurements

(VLA) with 20 elements and aperture 150m centered in the water column receives for 14 seconds at 25kHz sampling rate, and recording is synchronized to begin at the same time as the broadcast. A stationary target of interest is positioned at 5.3km in range away from the VLA, and is at a depth of 82m. The broadcast level is 220 dB, and the noise floor (simulated as white noise) is at 0 dB.

Wave propagation is evaluated using the method of images. To mimic realistic absorption from the surface and bottom, only 5 paths are kept, corresponding to two or less reflections. The one-way transmission loss and time delay spread is 90 dB and 25ms, respectively. To mimic environmental mismatch, random time delays are added to each path. These delays are different between hydrophones and paths, but the same for each frequency. These time

delays are Gaussian random with mean 0ms, and standard deviation 0.2ms, corresponding to 30cm path length variations. At the center frequency, this corresponds to 0.7 wavelengths, which is not significantly less than 1.0, the requirement for successful conventional MFP.

The target is an isotropic point scatterer with a scattering cross section, σ_s, of 300cm^2. By enforcing the isotropic condition and requiring that a single scatterer be energy conserving, the Greens function relating the amplitude of the outgoing spherical wave to the amplitude of the incident plane wave is fully specified (Foldy 1945). Under these conditions, the scattered amplitude is independent of frequency, and has a target strength of 26dB.

Reverberation is modeled by the addition of 10,000 very small scatterers in two scattering layers: one 1m thick at the surface, and another 1m thick at the bottom. The scatterers are placed uniform random within these layers, with sizes that are Rayleigh distributed with mean 3cm^2. These point scatterers are intended to mimic a rough ocean surface and bottom. Multiple scatterering effects are ignored. Despite offering a 20 dB smaller target strength, the high quantity of small scatterers leads to a reverberation level close to that of the desired target echo.

Using these simulation settings, a plot of the received power incident on all 20 elements of the VLA as a function of time is shown in Figure 4.1b. Blue is the noise floor, red is the reverberation, and black is the desired target echo.

For both conventional MFP and Δf-MFP, the replica search grid used is between 400m and 10km in range (spaced every 25m), and between 0m and 200m in depth (spaced every 2m). The time gating, as defined in Section 2.2, will use τ_1=50ms and τ_2=150ms. The signal bandwidth is between 2kHz and 5kHz. For Δf-MFP, the frequency difference bandwidth is chosen to be between 100Hz and 1kHz.

Inset on the right side of Figure 4.1 is a zoomed in plot showing the relative amounts of noise, reverberation, and target signal in a 200ms time gate. A signal-to-reverberation ratio

(SRR) may be defined using this 200ms wide time gate. By calculating the ratio of incident reverberation energy to the incident target echo energy in this time gate, the SRR is found to be 1.5dB.

4.4 Results

The target localization performance for the various signal processing techniques are discussed in this section, using the data generated from the previous section.

First, consider the conventional techniques. In the matched filter result (Figure 4.2a), a clear peak is seen to rise above the background reverberation. This distinct peak occurs at a two-way travel time corresponding to a range of very nearly 5.3km, which is the correct range for the target. Performing conventional MFP, the resulting ambiguity surface, shown in Figure 4.2b, is featureless, with no clear localization result (the true target depth and range is given by the thin black circle). This was expected given the severity of the environmental mismatch. Therefore, in this environment, conventional techniques are only able to, at best, successfully estimate a target range, but no depth estimate is possible.

Next, consider the two Δf-MFP techniques as outlined in Section 4.2.3. Figure 4.2c shows the incoherent Δf-MFP result, and Figure 4.2d shows the coherent Δf-MFP result. In both cases, a clear target localization is evident, at the correct range and depth. Therefore, already, this represents an improvement over conventional techniques. It is also important to note the difference in the two color scales. The peak in incoherent Δf-MFP can be seen to rise only 0.5dB above the background, whereas the peak in coherent Δf-MFP rises approximately 20dB above the background. Therefore, coherent Δf-MFP has much stronger sidelobe rejection and represents a more confident target localization than incoherent Δf-MFP.

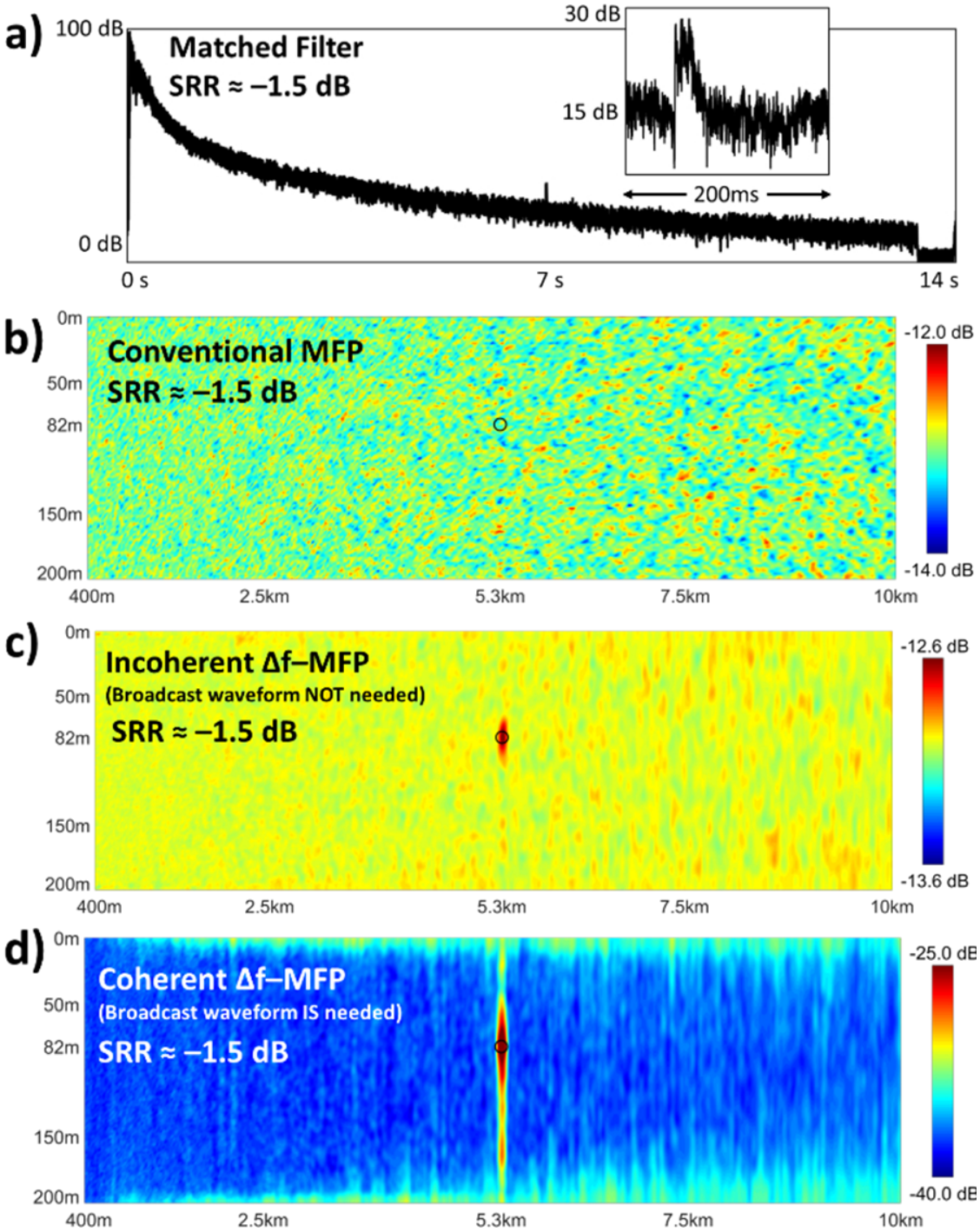

Figure 4.2: Target localization performance for conventional and Δf-MFP techniques

Frequency difference MFP is performing well under these simulation conditions, but so is the matched filter. Consider a more challenging situation: a target strength that is 11 dB weaker than before. The results are provided below in Figure 4.3 for a signal-to-reverberation ratio

of 12.5dB.

Additional important items are the features near the surface and bottom of the coherent Δf-MFP ambiguity surface. This is the clutter from the two scattering layers near the surface and bottom. Individual scatterers are not being localized, but this technique is still able to provide an estimate for the range and depth of clutter, which can be important for clutter/target discrimination.

The matched filter in Figure 4.3a is clearly featureless, and appears to be only reverberation. The ambiguity surface for coherent Δf-MFP, shown in Figure 4.3b, shows a localization of a mid-water-column target (note that the dynamic range has been adjusted to more clearly illustrate this peak). By decreasing the targets scattering cross section, it is found that incoherent Δf-MFP is able to localize at SRRs above 5 dB, and coherent Δf-MFP is able to localize at SRRs above 12.5 dB. Therefore, Δf-MFP is able to localize a mid-water-column target in the presence of strong reverberation and environmental mismatch, a situation for which all conventional techniques are unable to localize, or even detect.

4.5 Conclusions

The simulation results provided here are intended as a proof-of-concept for two Δf-MFP techniques. The simplicity of the simulations is undeniable, and there are numerous ways in which the model could be refined to mimic a realistic shallow ocean, including inhomogenous sound speed profiles, horizontal arrays, and anisotropic scattering, among many others. However, it is important to consider what *is* included in the model: a legitimate solution to the Helmholtz equation is used to localize a target in the presence of strong reverberation and environmental mismatch.

Δf-MFP has been shown to obtain depth estimates under conditions that no conventional

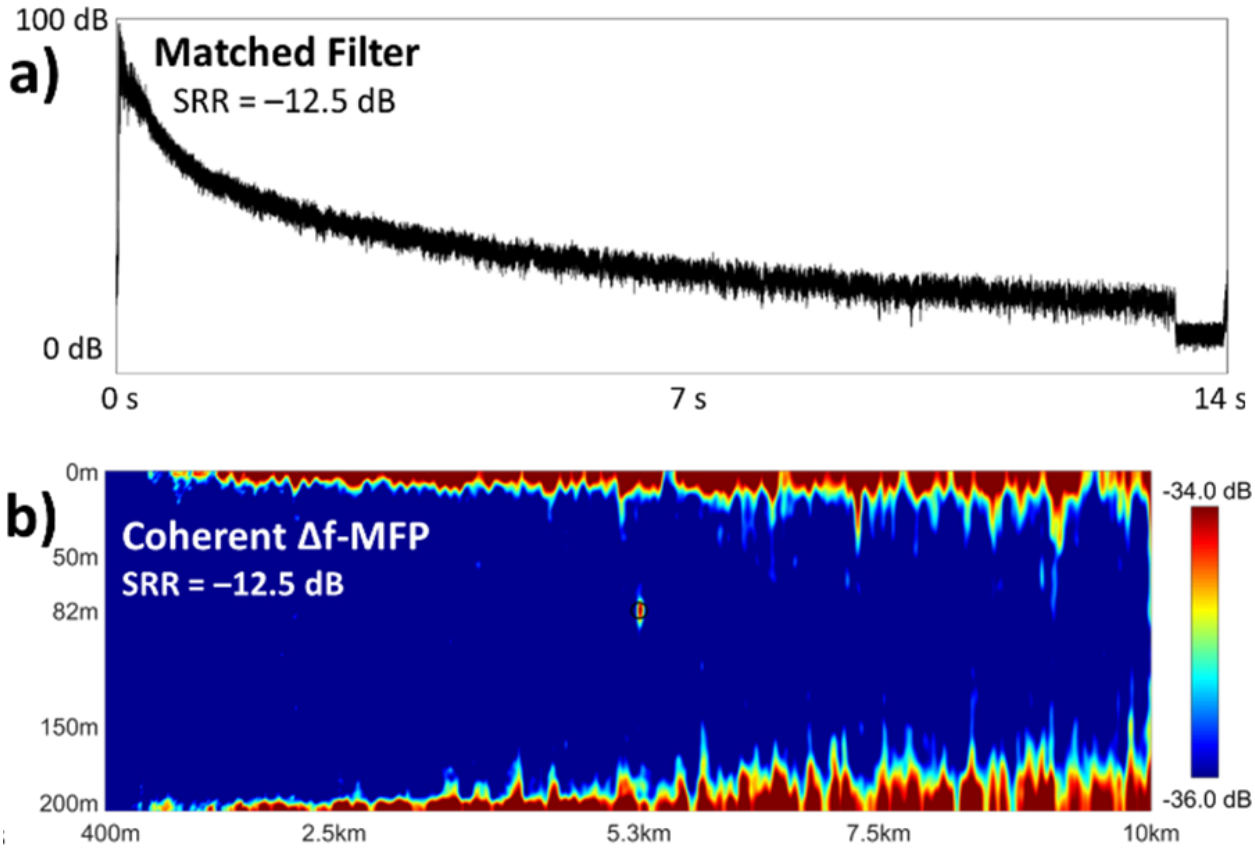

Figure 4.3: Comparison of localization techniques for weaker target

techniques can handle. Additionally, it is found to detect and localize targets for which conventional techniques are completely blind, at least in this environment.

Furthermore, the coherent Δf-MFP technique is found to approximately localize clutter in range and depth. This is an unexpected result, but may be very useful because this provides more information that can be used to discriminate between a target of interest and clutter. Localizing clutter as shown in this paper indicates a possible method for reducing the false-alarm rate of active sonar systems, particularly ones where mid-water-column targets are of interest, and the reverberation is dominated by surface and/or bottom scattering.

Lastly, because of the model-based nature of MFP, the techniques discussed here can be extended to more complex environments. None of the results provided in this paper seem intrinsically limited to this simple environment. It is likely that similar localization results

can be had with arbitrarily higher signal frequencies, though at higher frequency, absorption effects become more important. Further studies are required of the frequency difference technique, and specifically the autoproduct, to determine what the theoretical limitations are of the technique.

CHAPTER 5

The Frequency-Difference and Frequency-Sum Acoustic-Field Autoproducts

Abstract

The frequency-difference and frequency-sum autoproducts are quadratic products of solutions of the Helmholtz equation at two different frequencies ω_+ and ω_-, and may be constructed from the Fourier transform of any time-domain acoustic field. Interestingly, the autoproducts may carry wave-field information at the difference $\omega_+ - \omega_-$ and sum $\omega_+ + \omega_-$ frequencies even though these frequencies may not be present in the original acoustic field. This paper provides analytical and simulation results that justify and illustrate this possibility, and indicate its limitations. The analysis is based on the inhomogeneous Helmholtz equation and its solutions while the simulations are for a point source in a homogeneous half-space bounded by a perfectly reflecting surface. The analysis suggests that the autoproducts have a spatial phase structure similar to that of a true acoustic field at the difference and sum frequencies if the in-band acoustic field is a plane or spherical wave. For multi-ray-path environments, this phase structure similarity persists in portions of the autoproduct fields that are not suppressed by bandwidth averaging. Discrepancies between the bandwidth-averaged autoproducts and true out-of-band acoustic fields (with potentially modified boundary conditions) scale inversely with the product of the bandwidth and ray-

path arrival time differences.

5.1 Introduction

The Helmholtz equation has been used for more than a century and a half to predict and describe the properties of single-frequency (harmonic) wave fields. The Helmholtz equation and its solutions are used in nearly all branches of acoustics, and are especially valued in the realm of acoustic remote sensing and surveillance. In this realm, analytical and numerical solutions of the Helmholtz equation are commonly analyzed and compared to recorded acoustic signals at *in-band* frequencies (those within the signal's bandwidth) to determine information about the cause and place of origin of an acoustic signal, and the environment through which that signal has propagated (see Kuperman and Roux 2007, or Dowling and Sabra 2015). While the demonstrated capabilities of in-band signal processing for acoustic remote sensing and surveillance are impressive (*e.g.* exploring Earth's oceans and crust, and the interior of the human body), it is shown here that acoustic signals with nonzero bandwidth may also carry information at *out-of-band* frequencies above and below the signal's bandwidth. The purpose of this paper is to show analytically how this is possible and to illustrate the theoretical findings with simulations in a uniform half-space acoustic environment bounded by a reflecting surface.

The Helmholtz equation is a linear equation, so a sum of two or more of its solutions is also a solution. However, with some limitations, a *product* of Helmholtz equation solutions at two different in-band frequencies may retain some or all of the characteristics of a Helmholtz equation solution at the difference or sum frequencies. For simplicity, only quadratic wave-field products are considered here. Extensions of this effort to cubic, quartic, and higher-order field products are clearly possible, but are beyond the scope of this paper. In addition, the emphasis here is on scalar (*e.g.* acoustic) waves, even though the theory provided in Sections

5.2–5.4 may also apply to vector (*e.g.* elastic or electromagnetic) waves with polarization. Additionally, the emphasis here is on wave fields with frequency content in a single continuous bandwidth; extensions may be made to disjoint bandwidths, such as signals with higher harmonics, but such extensions are omitted here for clarity and brevity.

Specifically, this manuscript focuses on the properties of two different frequency-domain quadratic products of acoustic fields. These products, referred to herein as *autoproducts*, allow wave-field information to be extracted from acoustic fields at frequencies outside of the field's bandwidth via beamforming (Abadi *et al.* 2012) and matched field processing (Worthmann *et al.* 2015). It is shown in this paper that such out-of-band information extraction is possible when the in-band acoustic field meets four conditions. First, the in-band field must be well described by a ray-path sum. Second, the spatial gradient of the acoustic field must be dominated by phase (not amplitude) variations. Third, the product of the field's bandwidth with the ray-path propagation time differences must be much greater than unity. And fourth, there are no frequency-dependent wave propagation effects, such as frequency-dependent reflection coefficients or diffraction. When these conditions are met, the autoproducts formed from these fields are found to exhibit spatial phase structure similar to true acoustic fields above or below the original field's bandwidth. It should be noted, however, that these conditions are not general, and that other less restrictive condition sets may also allow the autoproducts to *mimic* out-of-band fields; herein *mimic* has a specialized meaning which is defined in Section 5.2.

The frequency-domain autoproducts are readily accessible when complex acoustic field values are known at the same location for different in-band frequencies. After predicting, computing, or recording an in-band time-domain field at locations of interest, the computational effort necessary to determine the autoproduct fields is minimal, involving only Fourier transforms and multiplication of complex amplitudes. Additionally, it should be noted that the out-of-band information provided by the autoproducts is complementary to, and not a

replacement for, that provided by the in-band field.

Given that out-of-band information extraction from an in-band field is unintuitive, use of the autoproducts for out-of-band acoustic remote sensing and surveillance might be considered an instance of signal-processing serendipity with little to no application in real world acoustic environments. However, more careful consideration is warranted; the autoproducts are shown here to be governed by an inhomogeneous Helmholtz equation that may have an additional source term that can be fully or partially suppressed by bandwidth averaging. Thus, the autoproducts can be considered auxiliary (or pseudo) out-of-band fields that have spatial phase structure and relative amplitudes that closely mimic those of a true out-of-band acoustic field.

The autoproducts are especially of interest for remote sensing and surveillance because they can accommodate an unusual level of signal-processing customization. Conventional in-band signal processing techniques examine fields at in-band frequencies and do not allow field examination at out-of-band frequencies. However, autoproduct-based techniques allow field examination at out-of-band frequencies chosen by the user, subject to constraints set by the quadratic autoproduct construction, the recorded signal's duration and bandwidth, and the acoustic environment.

The quadratic form of the autoproduct may be reminiscent of nonlinear acoustics, where high acoustic-field amplitudes activate quadratic nonlinearities inherent in the thermodynamics of the medium and/or in the conservation laws for a moving fluid (see Hamilton and Blackstock 1998). For example, the parametric array (Westervelt 1963) leverages naturally-occurring nonlinearities to mix high-frequency sounds with acoustic waves at a nearby frequency from a local oscillator to produce sound at the difference frequency. A radio frequency analogue to the parametric array, termed two-frequency modulation (Riris et al. 1996) also exploits similar physical nonlinearities to produce difference frequencies for detecting explosives. Although there are mathematical similarities between these physics-based nonlinearities and

the quadratic nonlinearities considered here, there are important differences as well. First, the autoproducts can be formed directly from the in-band frequency components of any acoustic field having non-zero amplitude and bandwidth. Thus, unlike physically-based nonlinearities, the autoproducts' occurrence or existence is independent of the in-band field's amplitude, the thermodynamics of the medium, and the conservation laws of a moving fluid. Second, the nonlinearities considered here are calculated after an acoustic field is predicted, computed, or recorded. And third, no local oscillator or harmonic reference field is needed to form either autoproduct. Instead, the quadratic nonlinearities leading to the autoproducts are forms of field- or signal-internal heterodyning, where the frequency reference is drawn from the in-band field, and the resulting heterodyne components at the difference and sum frequencies can be interpreted as auxiliary (or pseudo) out-of-band fields that accompany the in-band field.

Definitions, derivations, details, and illustrations of the autoproducts are presented in the following six sections of this paper. The next section provides the definitions of the two autoproducts and related parameters, and a derivation of their field equations from the inhomogeneous Helmholtz equation. The third section presents exact results for the autoproduct fields when the in-band acoustic field is a single ideal plane or spherical wave. The fourth section presents the autoproducts' field equations for the specific case of an inhomogeneous multipath environment when the in-band field is well represented by a sum of ray-path contributions and the signal spectrum is known. The fifth section describes how the autoproducts behave near flat reflecting boundaries and highlights how this behavior differs from that of the in-band acoustic field and the out-of-band acoustic fields the autoproducts may mimic. The sixth section provides illustrations of the analytical results in a uniform half-space acoustic environment (Lloyd's mirror) that is bounded by a reflecting surface. The final section summarizes this work and presents conclusions drawn from it.

5.2 Autoproduct Definitions and Field Equations

The starting point for the definition and subsequent analysis of quadratic frequency-domain acoustic-field autoproducts is the inhomogeneous Helmholtz equation for a single point source emitting a signal $s(t)$ with Fourier transform $S(\omega)$ in a spatially-dependent but time-independent environment with uniform density ρ_0 and non-dispersive sound speed $c(\boldsymbol{r})$:

$$\left(\nabla^2 + \frac{\omega^2}{c^2(\boldsymbol{r})}\right) P(\boldsymbol{r},\omega) = -S(\omega)\,\delta(\boldsymbol{r}-\boldsymbol{r}_s). \tag{5.1}$$

Here, $P(\boldsymbol{r},\omega)$ is the Fourier transform of the time-domain acoustic pressure $p(\boldsymbol{r},t)$, $\boldsymbol{r}$ is the field-point location, ω is the temporal frequency (in radians per second), the signal bandwidth is $\Omega_L \leq \omega \leq \Omega_H$, and $\boldsymbol{r}_s$ is the source location. Extension of this analysis to multiple sources is possible, but is not pursued here for brevity. Additionally, in this study, the effects of the presence of noise are omitted. Information about the effects of noise on source localization when using the autoproducts can be found in Worthmann *et al.* (2017).

The two quadratic products of interest here are the *frequency-difference autoproduct*

$$AP_\Delta(\boldsymbol{r},\omega,\Delta\omega) \equiv P(\boldsymbol{r},\omega_+)\,P^*(\boldsymbol{r},\omega_-) = P_+P_-^*, \tag{5.2}$$

and the *frequency-sum autoproduct*

$$AP_\Sigma(\boldsymbol{r},\omega,\Delta\omega) \equiv P(\boldsymbol{r},\omega_+)\,P(\boldsymbol{r},\omega_-) = P_+P_-, \tag{5.3}$$

where the upper frequency ω_+ and lower frequency ω_- are defined by

$$\omega_{\pm} \equiv \omega \pm \Delta\omega/2 \tag{5.4}$$

and both must lie within the signal bandwidth, $\Omega_L \leq \omega_{\pm} \leq \Omega_H$. Here, $\Delta\omega$ is the difference frequency and its bandwidth is constrained by the signal recording interval T and signal bandwidth: $2\pi/T \leq \Delta\omega \leq (\Omega_H - \Omega_L)$. The final equalities in (5.2) and (5.3) serve to define more compact notation since all the field variables depend on the same spatial coordinate r, and the +' and -' subscripts along with (5.4) indicate the frequencies of the constituent P-fields.

The definitions (5.2) and (5.3) are similar to other mathematical constructs. For brevity, such connections are merely mentioned here. When integrated over ω, (5.2) and (5.3) would define frequency-domain autocorrelation functions, and if ensemble averaged they would become the cross spectral coherences of P. The autoproducts as defined above are also related by single Fourier transforms to the Wigner transform and the ambiguity function from the field of bilinear time-frequency analysis (Cohen 1989, Borcea *et al.* 2006). These, like the autoproducts, are functions of two variables, and depend quadratically on the recorded signal. Additionally, (5.2) and (5.3) are related to two-frequency radar (Weissman 1973), also known as Δ k-radar (Popstefanija *et al.* 1993) and interferometric synthetic aperture radar (Sarabandi 1997), where information relevant to radar applications can be obtained by tracking the statistics of cross correlations between the measured field at two different frequencies measured at the same spatial location, or at the same frequency measured at two different spatial locations. Also, in the field of statistical optics, second order quantities such as the mutual coherence (Beran and Parrent 1964, Born and Wolf 1999) appear mathematically similar to autoproducts, however these quantities typically involve ensemble averaging, which is absent for the autoproducts discussed here. The autoproducts defined by (5.2) and (5.3) differ from these better-known functions and concepts in that they do not require ensemble averaging, additional Fourier transforms, or specialized signal broadcasts

(*e.g.* narrow pulses). Yet, appropriate frequency averaging of (5.2) and (5.3) can reveal out-of-band field information.

The name *autoproduct* was chosen because it indicates that the quantity is a product of complex field amplitudes at different frequencies drawn from the same wave field at the same spatial location. More general autoproducts may be defined that include both spatial and frequency shifts, but these are beyond the scope of this paper. The difference and sum designations used in (5.2), (5.3) and (5.4) arise from the fact that the properties of AP_Δ and AP_Σ may mimic those of solutions of the Helmholtz equation at the difference $\omega_+ - \omega_- = \Delta\omega$ and sum $\omega_+ + \omega_- = 2\omega$ frequencies, respectively.

Figure 5.1 illustrates this shifting of frequencies from the in-band field down to the AP_Δ field, or up to the AP_Σ field. The horizontal axis in Fig. 5.1 indicates the below band, in-band, and above-band frequency ranges for $\Delta\omega$, ω, and 2ω, respectively. The vertical axis shows the number of possible frequency pairs within each band that can be used for averaging to suppress cross terms that arise in multipath environments (see Section 5.4).

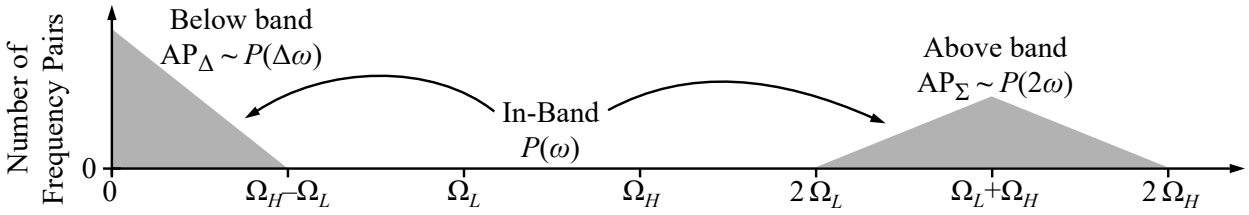

Figure 5.1: Frequencies for the in-band (true acoustic) and out-of-band (autoproduct) fields. The in-band field has frequencies ω between Ω_L and Ω_H. The frequency-difference autoproduct field, AP_Δ, uses this in-band field information to create out-of-band field information at lower frequencies between 0 and $\Omega_H - \Omega_L$. Similarly, the frequency-sum autoproduct field, AP_Σ, uses this in-band field information to create out-of-band field information at higher frequencies between $2\Omega_L$ and $2\Omega_H$. The vertical axis indicates the relative number of possible frequency pairs over which the autoproduct fields may be averaged when the entire signal bandwidth is used. The arrows indicate where the below-band and above-band field information originates.

As quadratic quantities, the autoproducts inherently have different units as well as different amplitudes than the out-of-band true acoustic fields they are intended to mimic. Since auto-

products cannot be compared one-to-one with their out-of-band acoustic-field counterparts, a normalization procedure must be implemented which removes these amplitude and unit discrepancies, leaving only the relative amplitude and spatial phase structure of both fields behind, which can then be compared directly. The normalization chosen here is:

$$(\quad)^{norm} \equiv (\quad) \left[\frac{1}{V} \int_V |(\quad)|^2 d^3\boldsymbol{r} \right]^{-\frac{1}{2}}, \tag{5.5}$$

where the superscript *norm* indicates a normalized version of the field defined as shown, and ( ) represents a placeholder field, meant for either an out-of-band true acoustic field such as $P(\Delta\omega)$ or $P(2\omega)$, or for the autoproduct fields AP_Δ and AP_Σ. Furthermore, V represents a spatial region over which the normalization is defined. This normalization procedure is similar to the cell-averaging constant false alarm rate (CA-CFAR) normalizer used in signal detection schemes (Nitzberg 1972). After normalization, field quantities are dimensionless and have an average magnitude-squared of unity, but they retain all phase and relative amplitude information. Additionally, it should be noted that the relative amplitude information found is dependent on the averaging window chosen, as well as the normalization technique employed.

To compare how well the spatial phase structure of an autoproduct field matches that of an out-of-band acoustic field, a cross-correlation coefficient χ can be defined between the two fields

$$\chi_{\Delta,\Sigma} = \frac{1}{V} \int_V \left| AP^{norm}_{\Delta,\Sigma}(\boldsymbol{r})\, P^{norm*}(\boldsymbol{r}) \right| d^3\boldsymbol{r}. \tag{5.6}$$

When this cross correlation coefficient is close to unity, the autoproduct fields, $AP^{norm}_\Delta(\boldsymbol{r}, \omega, \Delta\omega)$ and $AP^{norm}_\Sigma(\boldsymbol{r}, \omega, \Delta\omega)$, are said to (*i.e.* defined to) *mimic* the out-of-band acoustic fields $P^{norm}(\boldsymbol{r}, \Delta\omega)$ and $P^{norm}(\boldsymbol{r}, 2\omega)$, respectively.

Next, consider the field equations governing the autoproducts, which can be derived from (5.1). AP_Δ and AP_Σ are so similar mathematically that, throughout this paper, results for AP_Δ are derived and corresponding results for AP_Σ are simply stated. To derive the field equation governing AP_Δ, evaluate (5.1) at ω_+ and ω_-, complex conjugate the second equation, cross-multiply the equations with the P-field from the other equation, and add the equations together. These four steps produce:

$$P_-^*\nabla^2 P_+ + P_+\nabla^2 P_-^* + \left(\frac{\omega_+^2 + \omega_-^2}{c^2}\right) P_+ P_-^* = -\left(P_-^* S_+ + P_+ S_-^*\right)\delta\left(\boldsymbol{r} - \boldsymbol{r}_s\right). \tag{5.7}$$

Using (5.2), (5.4) and the identity $\nabla^2\left(P_+P_-^*\right) = P_-^*\nabla^2 P_+ + 2\nabla P_+ \cdot \nabla P_-^* + P_+\nabla^2 P_-^*$; defining $k = \omega/c$ and $\Delta k = \Delta\omega/c$; and rearranging terms leads to:

$$\left(\nabla^2 + (\Delta k)^2\right) AP_\Delta = -\left(P_-^* S_+ + P_+ S_-^*\right)\delta\left(\boldsymbol{r} - \boldsymbol{r}_s\right) + 2\left[\nabla P_+ \cdot \nabla P_-^* - \left(k^2 - \frac{(\Delta k)^2}{4}\right) P_+ P_-^*\right]. \tag{5.8}$$

Thus, AP_Δ will be equivalent to an acoustic field at the difference frequency ($\Delta\omega$) emitted from a point-source at $\boldsymbol{r}_s$ when the contents of the square brackets on the right side of (5.8) are negligible.

The field equation for AP_Σ is

$$\left(\nabla^2 + (2k)^2\right) AP_\Sigma = -\left(P_- S_+ + P_+ S_-\right)\delta\left(\boldsymbol{r} - \boldsymbol{r}_s\right) + 2\left[\nabla P_+ \cdot \nabla P_- + \left(k^2 - \frac{(\Delta k)^2}{4}\right) P_+ P_-\right], \tag{5.9}$$

and is obtained similarly to that for AP_Δ. In analogy with (5.8), AP_Σ is equivalent to the acoustic field at the sum frequency (2ω) emitted from a point-source at $\boldsymbol{r}_s$ when the contents

of the square brackets on the right side of (5.9) are negligible.

The form of these equations suggests how they govern the autoproducts and how out-of-band field information can be obtained. The left sides of (5.8) and (5.9) are both linear Helmholtz operators; (5.8) has wave number Δk and operates on AP_Δ, while (5.9) has wave number $2k$ and operates on AP_Σ. The right sides of both equations involve a point-source term with a Dirac-delta function (the *self* term), and a distributed-source term in square brackets (the *cross* term). Thus, when the cross terms in (5.8) and (5.9) are negligible compared to the other terms in these equations, AP_Δ and AP_Σ should follow the Helmholtz-equation at frequencies $\Delta\omega$ and 2ω, respectively. In general, $\Delta\omega$ can be below the signal bandwidth, and 2ω can be above it, so AP_Δ and AP_Σ can be interpreted as mimicking out-of-band fields. For specific circumstances, the similarities between AP_Δ and AP_Σ and true acoustic fields at $\Delta\omega$ and 2ω, respectively, are shown mathematically in Section 5.3 (plane and spherical waves) and Section 5.4 (sum-of-rays), and are illustrated in Section 5.6 (Lloyd's mirror).

5.3 Plane- and Spherical-wave Autoproduct Fields

To highlight the implications of (5.8) and (5.9), consider the autoproduct fields AP_Δ and AP_Σ when they are comprised of a single ideal plane or spherical wave. The plane-wave-field results are presented first and are followed by the spherical-wave-field results.

Consider a uniform unbounded environment in a region far from the source location where the field is a plane wave given by $P = A\exp\left(ik\hat{\mathbf{s}}\cdot\boldsymbol{r}\right)$, where A is a complex amplitude that may depend on frequency, $\hat{\mathbf{s}}$ is the unit vector that points in the direction of propagation. In this case,

$$\nabla P_+ \cdot \nabla P_-^* = \left(ik_+ s P_+\right)\cdot\left(-ik_- s P_-^*\right) = \left(k^2 - \frac{(\Delta k)^2}{4}\right) P_+ P_-^*. \tag{5.10}$$

Thus, the cross term within the square brackets in (5.8) is identically zero, and a similar result is found for the cross term in (5.9). Thus, when the acoustic field is a single plane wave, (5.8) and (5.9) imply:

$$\left(\nabla^2 + (\Delta k)^2\right) AP_\Delta = 0 \tag{5.11}$$

$$\left(\nabla^2 + (2k)^2\right) AP_\Sigma = 0, \tag{5.12}$$

and AP_Δ and AP_Σ are exact solutions of the Helmholtz equation at the difference and sum frequencies, respectively. These facts can also be ascertained by applying the definitions (5.2) and (5.3) to the presumed plane-wave field:

$$AP_\Delta = A_+ A_-^* \exp\left(i\Delta k \hat{\mathbf{s}} \cdot \boldsymbol{r}\right), \tag{5.13}$$

$$AP_\Sigma = A_+ A_- \exp\left(i\left(2k\right)\hat{\mathbf{s}} \cdot \boldsymbol{r}\right). \tag{5.14}$$

Here the autoproducts are plane waves at the out-of-band frequencies, with modified amplitudes. Spatially cross-correlating (5.13) and (5.14) with plane waves propagating in the same direction at the difference and sum frequencies, respectively, would yield a perfect cross correlation, as defined in (5.6), of unity.

Now consider the equation governing the frequency-difference autoproduct AP_Δ when it is created from the acoustic field from a point source in a uniform unbounded environment, $P = (A/r)\exp(ikr)$ where $r = |\boldsymbol{r} - \boldsymbol{r}_s|$. In this case, when $r \neq 0$, (5.8) simplifies to:

$$\left(\nabla^2 + (\Delta k)^2\right) AP_\Delta = (\Delta k)^2 \left(\frac{2}{(\Delta kr)^2} - \frac{2i}{\Delta kr}\right) AP_\Delta. \tag{5.15}$$

At sufficient distance from the source, *i.e.* when $\Delta kr \gg 1$ the right side of this equation is algebraically small compared to the second term on the left side, so AP_Δ should mimic the field from a point source at the difference frequency. And, just like the plane wave case, this observation can also be ascertained by applying the definition (5.3) to the presumed ideal point-source field:

$$AP_\Delta = A_+ A_-^* \frac{\exp(i\Delta kr)}{r^2}. \tag{5.16}$$

Here the final form only differs by an amplitude factor ($A_+A_-^*/r^2$ vs. A/r) from an ideal spherically-expanding wave at the difference frequency. The algebraically small terms on the right-hand side of (5.15) are the reason for the extra $\frac{1}{r}$ factor, but if the normalization window in (5.5) is chosen to be sufficiently far from the source where the fields' amplitudes vary little over the averaging region V, then the normalized autoproducts do indeed mimic spherical waves at the difference frequency. For example, consider a spherical wave centered on the origin, where the normalization window is chosen to be a spherical shell with an outer radius of $r_0 + \Delta r/2$ and an inner radius of $r_0 - \Delta r/2$. Define the dimensionless quantity $\alpha = \Delta r/(2r_0)$, which is by definition positive and less than unity. A narrow window far from the origin corresponds to small α, and a window at any location that is wide enough to include the origin corresponds to $\alpha = 1$. The cross correlation in (5.6) may be found analytically for this simple case: $\chi_{\Delta,\Sigma} = \sqrt{1-\alpha^2}\ln\left((1+\alpha)/(1-\alpha)\right)/(2\alpha)$. This result behaves correctly in the expected limits - a thin window ($\alpha \to 0$) gives a strong cross correlation ($\chi_\Delta \to 1$), and a wide window ($\alpha \to 1$) gives a very poor cross correlation ($\chi_\Delta \to 0$). For some intermediate values, for example $\alpha = 0.1$, 0.5, and 0.9, the cross correlations are 0.998, 0.95, and 0.71, respectively. Therefore, as long as the normalization region is chosen to be thin compared to

the overall distance to the source, then AP_Δ from (5.16) successfully mimics a point-source acoustic field at the difference frequency.

For the frequency sum autoproduct AP_Σ, the equivalents of (5.15) and (5.16) are:

$$\left(\nabla^2 + (2k)^2\right) AP_\Sigma = (2k)^2 \left(\frac{2}{(2kr)^2} - \frac{2i}{2kr}\right) AP_\Sigma. \tag{5.17}$$

$$AP_\Sigma = A_+ A_- \frac{\exp(i2kr)}{r^2}. \tag{5.18}$$

Equation (5.17) implies that AP_Σ should mimic the field from a point source at the sum frequency when $2kr \gg 1$, while (5.18) shows that it only differs from a point source field by an amplitude factor (A_+A_-/r^2 vs. A/r). And, the formula given above for $\chi_{\Delta,\Sigma}$ applies for the frequency sum autoproduct as well.

5.4 Autoproduct Fields in the Ray Approximation

The purpose of this section is to determine the conditions under which the two autoproducts might mimic acoustic fields at the possibly out-of-band difference and sum frequencies in fields that are well-described by the ray approximation.

The starting point for this analysis is the Green's function for (5.1) that solves:

$$\left(\nabla^2 + \frac{\omega^2}{c^2(\boldsymbol{r})}\right) G(\boldsymbol{r}, \boldsymbol{r}_s, \omega) = -\delta(\boldsymbol{r} - \boldsymbol{r}_s) \tag{5.19}$$

Comparison of (5.1) and (5.19), both linear equations, leads to the familiar conclusion:

$$P(\boldsymbol{r},\omega) = S(\omega)\, G(\boldsymbol{r},\boldsymbol{r}_s,\omega)\,. \tag{5.20}$$

Inserting (5.20) into (5.8) and using the notation simplification of (5.2) - (5.4) for G, produces:

$$\left(\nabla^2 + (\Delta k)^2\right) G_+ G_-^* = -\left(G_-^* + G_+\right)\delta(\boldsymbol{r}-\boldsymbol{r}_s) + 2\left[\nabla G_+ \cdot \nabla G_-^* - \left(k^2 - \frac{(\Delta k)^2}{4}\right) G_+ G_-^*\right] \tag{5.21}$$

where the common factor of $S_+ S_-^*$ has been divided out. Thus, the signal waveform does not play a role in the spatial structure of the Δf autoproduct field. However, this simplification is not possible unless the signal spectrum S is known.

The Green's function used for the analysis here is the ray approximation (Kinsler *et al.* 2000):

$$G(\boldsymbol{r},\boldsymbol{r}_s,\omega) = \sum_m \exp\left(i\omega\tau_m(\boldsymbol{r},\boldsymbol{r}_s)\right)\left[A_m^{(0)}(\boldsymbol{r},\boldsymbol{r}_s) + \mathcal{O}\left(\frac{A_m^{(1)}}{\omega}\right)\right], \tag{5.22}$$

where $A_m^{(0)}$ is the slowly-varying amplitude of the mth ray, and τ_m is the acoustic travel time from $\boldsymbol{r}_s$ to r along the mth ray path. The elementary ray theory discussed here only considers the solutions to the eikonal and transport equations, or in other words, it neglects amplitude terms of higher order than $A_m^{(0)}$. By making this approximation, frequency-dependent wave propagation phenomena such as diffraction, caustics, shadow zones, turning points, volume attenuation, dispersion, rough surface scattering, and frequency-dependent reflection coefficients (such as those originating from fine-scale layering in the bottom in ocean acoustics) are explicitly *not* considered in this analysis. Consideration of such phenomena is beyond the scope of the current paper. Therefore, this analysis is limited to regions of the acoustic environment where elementary ray theory is an adequate description of the acoustic field.

In this paper, such regions are said to be *well-ensonified*.

Dropping the $A_m^{(1)}$ term from (5.22) and substituting the remaining sum into the right side of (5.21) requires the evaluation of the gradient of this version of (5.22), which is:

$$\nabla G_{\pm} = \sum_m \left(\frac{\nabla A_m^{(0)}}{A_m^{(0)}} + i\omega_{\pm} \nabla \tau_m \right) A_m^{(0)} \exp\left(i\omega_{\pm}\tau_m\right), \tag{5.23}$$

where simplified notation similar to that in (5.2) - (5.4) has been used. As a further approximation in this analysis, the first term in parentheses in (5.23) (the spatial variation of the amplitude), is assumed to be negligible compared to second term (the spatial variation of the phase). Additionally, $\nabla \tau_m = \frac{s_m}{c}$, where s_m is the unit vector in the local direction of propagation along the mth ray path and c is the local sound speed; $\frac{s_m}{c}$ is often referred to as the slowness vector. Thus, (5.23) can be approximately simplified to:

$$\nabla G_{\pm} \approx \sum_m ik_{\pm} s_m A_m^{(0)} \exp\left(i\omega_{\pm}\tau_m\right). \tag{5.24}$$

Note, in this approximation, each ray-path contribution (G_m) is treated locally as a plane wave, since $\nabla G_m \approx iks_m G_m$. Substituting (5.22) and (5.24) into the right-hand side of (5.21) and simplifying yields:

$$\begin{aligned}
&\left(\nabla^2 + (\Delta k)^2\right)\left(G_+ G_-^*\right) = -\sum_m \mathrm{Re}\left[2A_m^{(0)}\right]\delta\left(\boldsymbol{r} - \boldsymbol{r}_s\right) \\
&-2\left(k^2 - \frac{(\Delta k)^2}{4}\right)\sum_l \sum_m \left(1 - \hat{\mathbf{s}}_m \cdot \hat{\mathbf{s}}_l\right) A_m^{(0)} A_l^{(0)*} \exp\left(i\omega\left(\tau_m - \tau_l\right) + i\Delta\omega\frac{\tau_m + \tau_l}{2}\right),
\end{aligned} \tag{5.25}$$

where the τ_m have dropped out of the first term on the right side of (5.25) because $\tau_m = 0$ when $\boldsymbol{r} = \boldsymbol{r}_s$ and this coordinate-matching condition is ensured by the delta-function.

The right side of (5.25) has two terms that together lead to two important conclusions. The

first term, with the delta-function, is the self-term sum, with an amplitude set by the sum of the ray-path amplitudes. The second term is the cross-term sum, and without it (5.25) would simplify to the Helmholtz equation for a point source. This second term arises when multiple rays arrive at the same point but from a different angle. Note, however, the diagonal terms (when $m = l$) in this double sum are zero and do not contribute to the summation; thus, this double sum is composed entirely of *cross terms*. Another way to understand these cross terms is to apply the ray approximation in (5.22) directly to the autoproduct definition in (5.2). This yields:

$$G_+ G_-^* = \sum_m \left|A_m^{(0)}\right|^2 e^{i\Delta\omega\tau_m} + 2\sum_l \sum_{m>l} \left|A_m^{(0)} A_l^{(0)*}\right| e^{i\Delta\omega\frac{\tau_m+\tau_l}{2}} \cos\left(\omega\left(\tau_m - \tau_l\right) + \phi_{ml}\right), \quad (5.26)$$

where $\phi_{ml} = \arg\left(A_m^{(0)}\right) - \arg\left(A_l^{(0)}\right)$. The first right-side term in (5.26) corresponds to the delta-function term in (5.25), and it mimics an acoustic field with the same arrival times as (5.22), but at the difference frequency and with a modified ray amplitude ($|A_m^{(0)}|^2$ instead of $A_m^{(0)}$, see Section 5.5 for further discussion). The second term in (5.26) corresponds to the cross-term sum in (5.25). Both terms in (5.26) are of the same order of magnitude; thus the autoproduct field may not mimic an acoustic field at the difference frequency when the self- and cross-term sums contribute equally (see Section 5.6 for an example).

However, an average of (5.25) through the signal bandwidth, $\Omega_L \leq \omega \leq \Omega_H$, can be used to reduce or eliminate the cross-term sum. Define such a frequency average as:

$$\langle\ \ \rangle_\omega \equiv \frac{1}{\Omega_H - \Omega_L - \Delta\omega} \int_{\Omega_L + \frac{\Delta\omega}{2}}^{\Omega_H - \frac{\Delta\omega}{2}} (\ \ )\, d\omega. \quad (5.27)$$

Applying this frequency average to (5.25) produces:

$$\left(\nabla^2 + (\Delta k)^2\right) \langle G_+ G_-^* \rangle_\omega = -\sum_m \mathrm{Re}\left[2A_m^{(0)}\right] \delta\left(\boldsymbol{r} - \boldsymbol{r}_s\right)$$
$$- 2\sum_l \sum_m \left(1 - \hat{\mathbf{s}}_m \cdot \hat{\mathbf{s}}_l\right) A_m^{(0)} A_l^{(0)*} \exp\left(i\Delta\omega \frac{\tau_m + \tau_l}{2}\right) \langle \left(k^2 - \frac{(\Delta k)^2}{4}\right) \exp\left(i\omega\left(\tau_m - \tau_l\right)\right) \rangle_\omega. \tag{5.28}$$

Here, the final factor inside the double sum includes an algebraic frequency factor in parentheses and a complex phase term that depends on the product of ω and travel time differences between ray paths. If the phase term is averaged over a sufficiently-wide ω-bandwidth, the average will include all possible phases and will tend to zero. The necessary bandwidth-time-difference-product inequality is $\Omega_H - \Omega_L - \Delta\omega) \left|\tau_m - \tau_l\right| \geq 2\pi$, and is satisfied for signal bandwidths of order 1 kHz or larger when ray travel time differences are of order 1 ms or longer. The effect of the difference frequency on this inequality is also shown schematically in Figure 5.1 as the grey right-triangle on the left side of the diagram; low difference frequencies have many pairs over which to average out the cross-term sum, whereas higher difference frequencies (approaching $\Omega_H \Omega_L$) do not have as many possible pairs over which to average, and are therefore affected more strongly by the cross-term sum.

Thus, with sufficient frequency averaging, $\langle G_+ G_-^* \rangle_\omega$ obeys a Helmholtz-equation at the difference frequency $\Delta\omega$ for a point source at $\boldsymbol{r}_s$:

$$\left(\nabla^2 + (\Delta k)^2\right) \langle G_+ G_-^* \rangle_\omega \approx -\sum_m \mathrm{Re}\left[2A_m^{(0)}\right] \delta\left(\boldsymbol{r} - \boldsymbol{r}_s\right). \tag{5.29}$$

It should be noted that although (5.29) was derived under the ray approximation (appropriate for high signal frequencies), that approximation may not hold well at the difference frequency, which can in general be much lower. For example, in a waveguide, an appropriate solution to (5.29) may be a sum of modes instead of rays (see Worthmann *et al.* 2015).

The field equation for the frequency-sum Green's function autoproduct G_+G_- is obtained from (5.9) using (5.20) to reach:

$$\left(\nabla^2 + (2k)^2\right) G_+G_- = -\left(G_- + G_+\right)\delta\left(\boldsymbol{r} - \boldsymbol{r}_s\right) + 2\left[\nabla G_+ \cdot \nabla G_- + \left(k^2 - \frac{(\Delta k)^2}{4}\right) G_+G_-\right], \tag{5.30}$$

which is the frequency-sum analogue of (5.21).

The frequency-sum autoproduct can be bandwidth averaged over $\Delta\omega$. If ω is chosen to be the center frequency, then the range of possible $\Delta\omega$ ranges from 0 to $\Omega_H - \Omega_L$, the total bandwidth available in the original field. Thus, a bandwidth average for frequency-sum autoproducts may be defined as:

$$\langle\ \rangle_{\Delta\omega} \equiv \frac{1}{\Omega_H - \Omega_L}\int_0^{\Omega_H - \Omega_L} (\quad)\, d\left(\Delta\omega\right). \tag{5.31}$$

While (5.31) only applies when ω is chosen to be the center frequency, any value of ω in the bandwidth could be chosen instead. However, near the upper and lower bounds of the bandwidth, there exist very few difference-frequency pairs over which to average. The upper bound on $\Delta\omega$ becomes $2\min\left(\Omega_H - \omega, \omega - \Omega_L\right)$, which is always less than the total bandwidth, and should thus replace $\Omega_H - \Omega_L$ in (5.31) in general. Applying (5.31) to (5.30), the frequency-sum equivalent of (5.28) is found to be:

$$\begin{aligned}\left(\nabla^2 + (2k)^2\right)\langle G_+G_-\rangle_{\Delta\omega} &= -\sum_m 2A_m^{(0)}\delta\left(\boldsymbol{r} - \boldsymbol{r}_s\right) \\ &+ 2\sum_l\sum_m \left(1 - \hat{\mathbf{s}}_m \cdot \hat{\mathbf{s}}_l\right) A_m^{(0)}A_l^{(0)} \exp\left(i2\omega\frac{\tau_m + \tau_l}{2}\right)\left\langle\left(k^2 - \frac{(\Delta k)^2}{4}\right)\exp\left(i\Delta\omega\frac{(\tau_m - \tau_l)}{2}\right)\right\rangle_{\Delta\omega}.\end{aligned} \tag{5.32}$$

Here, the factor inside the double sum and difference-frequency average includes an algebraic frequency factor in parentheses and a complex phase term that depends on $\Delta\omega$ and travel time differences between ray paths. Interestingly, the requirements to reduce the importance of the cross-term sum in (5.32) are essentially the same as they are in (5.28). Additionally, Figure 5.1 shows this difference-frequency bandwidth average schematically with the grey isosceles-triangle on the right. The most frequency pairs for averaging is obtained when $\omega = \omega_c =$ the center frequency, and decreases in either direction, until ω reaches Ω_L or Ω_H, where the lack of difference-frequency bandwidth means that the AP_Σ field is affected more strongly by the cross-term sum.

Thus, with sufficient frequency-difference averaging, $\langle AP_\Sigma \rangle_{\Delta\omega}$ obeys a Helmholtz-equation at the sum frequency $2\omega$for a point source at r_s:

$$\left(\nabla^2 + (2k)^2\right) \langle G_+ G_- \rangle_{\Delta\omega} \approx -\sum_m 2A_m^{(0)} \delta\left(\boldsymbol{r} - \boldsymbol{r}_s\right), \tag{5.33}$$

even though 2ω may lie above the signal bandwidth.

5.5 Autoproducts Near Reflecting Boundaries

In the prior section, appropriate frequency-averages of the autoproducts are shown to follow, or nearly follow, a Helmholtz-equation at out-of-band frequencies. Thus, the frequency-averaged autoproducts should mimic, but not necessarily match, true acoustic fields at the difference and sum frequencies. The distinction is important because the autoproducts behave differently near boundaries than true acoustic fields. Such differences occur because the autoproducts are not directly subject to standard conservation laws, Newtonian mechanics, or any constitutive relationship involving elasticity or viscosity. However, their constituent acoustic fields, P_+ and P_- are subject to physics-based boundary conditions. Thus, the

boundary conditions for AP_Δ and AP_Σ come from the boundary conditions satisfied by P_+ and P_-. Here, in light of the high frequency approximation inherent in (5.22), the behavior of single plane-wave components of AP_Δ and AP_Σ near boundaries is developed in terms of R, the complex acoustic-plane-wave reflection coefficient for a flat, two-fluid interface,

$$R\left(\theta_I\right) = \frac{\rho' c' \cos\left(\theta_I\right) - \rho c \cos\left(\theta_T\right)}{\rho' c' \cos\left(\theta_I\right) + \rho c \cos\left(\theta_T\right)}, \tag{5.34}$$

(see Kinsler *et al.* 2000), where ρ and c are the density and sound speed of the acoustic medium containing the incident plane wave, ρ' and c' are the density and sound speed of the acoustic medium on the other side of the interface, θ_I is the angle of incidence measured from the normal to the surface, and θ_T is the angle of transmission measured from the surface normal, which satisfies Snell's Law: $\sin\left(\theta_I\right)/c = \sin\left(\theta_T\right)/c'$. With this formulation, hard surfaces ($\rho'/\rho \to \infty$) and pressure-release surfaces ($\rho'/\rho \to 0$) lead to reflection coefficients of +1 and -1, respectively. Note that for a flat two-fluid interface, R may be complex, but it is not frequency-dependent.

5.5.1 Frequency-Independent Reflection Coefficients

For an acoustic plane-wave incident at angle θ_I on a flat surface, the pressure field $P_\pm$ due to an incident plane wave with an amplitude of $A_\pm$ in the region near the surface is:

$$P_\pm = P_{\pm,I} + P_{\pm,R} = A_\pm \exp\left(ik_\pm\left[x\sin\theta_I - y\cos\theta_I\right]\right) + RA_\pm \exp\left(ik_\pm\left[x\sin\theta_I + y\cos\theta_I\right]\right), \tag{5.35}$$

where the "'I"' and "'R"' subscripts denote incident and reflected waves, $A(\omega_\pm) = A_\pm$, $k_\pm = \omega_\pm/c$, the locally reacting surface coincides with $y = 0$, and the geometry and coordinates are

shown in Figure 5.2. The reflection coefficient R is treated as frequency independent here, but may be complex, such that it may be represented as $R_0 e^{i\phi_0}$, where R_0 is the amplitude of the reflection coefficient, and ϕ_0 is its complex phase. The incident and reflected acoustic fields at the upper and lower frequencies on the surface ($y = 0$) are related by:

$$\lim_{y\to 0} P_{\pm,R} = R \lim_{y\to 0} P_{\pm,I}, \tag{5.36}$$

and this equation serves as a pressure-boundary-condition statement for $P_{\pm}$.

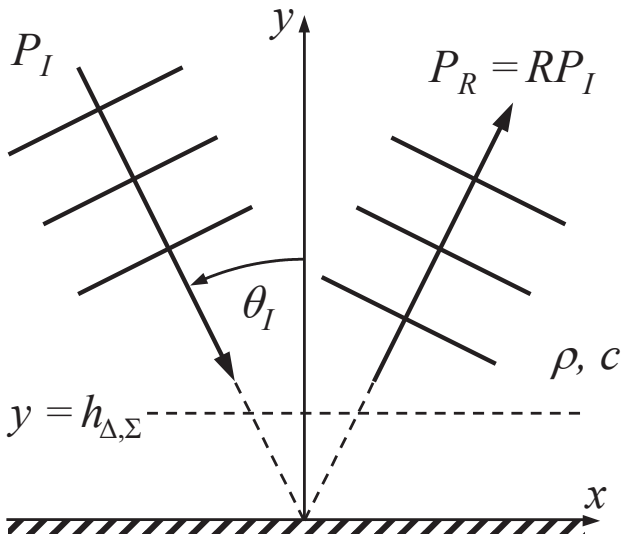

Figure 5.2: Coordinates and wave orientations for an acoustic plane-wave P_I incident at angle θ_I on a two-fluid interface at $y = 0$ (see Kinsler *et al.* 2000). The reflected plane wave is $P_R = RP_I$, where R is the surface reflection coefficient. The total field near the surface is the sum of P_I and P_R. The near-surface interference layer where the autoproducts will not mimic acoustic fields at the sum and difference frequencies nominally exists for $y < h_{\Delta,\Sigma}$.

Substituting (5.35) into the frequency-difference autoproduct definition in (5.2) gives:

$$AP_{\Delta} = AP_{\Delta,I} + AP_{\Delta,R} + 2A_{+}A_{-}^{*}R_0 \exp\left(i\Delta kx \sin\theta_I\right) \cos\left(2ky\cos\theta_I + \phi_0\right), \tag{5.37}$$

where $AP_{\Delta,I}$ and $AP_{\Delta,R}$ are the incident and reflected autoproduct-field components, respectively:

$$AP_{\Delta,I} = P_{+,I}P^*_{-,I} = A_+A^*_- \exp\left(i\Delta k\left[x\sin\theta_I - y\cos\theta_I\right]\right), \tag{5.38}$$

$$AP_{\Delta,R} = P_{+,R}P^*_{-,R} = A_+A^*_- R_0^2 \exp\left(i\Delta k\left[x\sin\theta_I + y\cos\theta_I\right]\right). \tag{5.39}$$

The remaining terms on the right side of (5.37) are the cross terms that arise from there being both incident and reflected paths to any (x, y)-point in the plane shown in Fig. 5.2. The travel time difference between these paths is $\tau_{IR} = (2y/c)\cos(\theta_I)$, and does not depend on x. When (5.37) is averaged through the signal bandwidth following (5.27), and $\Omega_H - \Omega_L - \Delta\omega)\tau_{IR}$ is large enough so that the bandwidth averages of the complex exponentials in this term approach zero, then

$$\langle AP_\Delta\rangle_\omega \approx \langle AP_{\Delta,I}\rangle_\omega + \langle AP_{\Delta,R}\rangle_\omega. \tag{5.40}$$

This statement is the difference frequency analogue to the first equality of (5.35) but it only applies when $y > h_\Delta$, where h_Δ is defined as the distance from the surface where $\langle\exp\left(\pm\frac{2i\omega h_\Delta\cos\theta_I}{c}\right)\rangle_\omega \ll 1$. Closer to the surface ($y < h_\Delta$), the cross terms are no longer negligible even after bandwidth averaging. They lead to an interference pattern which prevents the Δf autoproduct from mimicking an acoustic field at the difference-frequency - at least within this interference layer'. The interference layer thickness h_Δ can be estimated by setting $2(\Omega_H - \Omega_L - \Delta\omega)h_\Delta\cos\theta_I/c \approx 2\pi$, which implies:

$$h_\Delta \approx \frac{\pi c}{(\Omega_H - \Omega_L - \Delta\omega)\cos\theta_I}. \tag{5.41}$$

The limit of (5.40) as y 0 can still be taken to determine the equivalent of (5.36) for the AP_Δ-field (neglecting the effects of the near-surface interference layer):

$$\lim_{y\to 0}\langle AP_{\Delta,R}\rangle_{\omega} = R_0^2 \lim_{y\to 0}\langle AP_{\Delta,I}\rangle_{\omega}. \tag{5.42}$$

Thus, when R is frequency-independent, the effective reflection coefficient for AP_{Δ} outside of the surface-interference layer is $|R|^2$, not R, so AP_{Δ} responds to impedance surfaces differently than the in-band field and a true acoustic field at $\Delta\omega$. An example of this boundary condition change is provided in the next section, where AP_{Δ} outside the interference layer is found to respond to a pressure-release surface as if the surface were hard.

The near-surface relationships for AP_{Σ} can be obtained from an algebraic effort similar to that provided above for AP_{Δ}. The frequency-sum analogues to (5.40) - (5.42) are:

$$\langle AP_{\Sigma}\rangle_{\Delta\omega} \approx \langle AP_{\Sigma,I}\rangle_{\Delta\omega} + \langle AP_{\Sigma,R}\rangle_{\Delta\omega}, \tag{5.43}$$

$$h_{\Sigma} \approx \frac{\pi c}{(\Omega_H - \Omega_L)\cos\theta_I} \tag{5.44}$$

$$\lim_{y\to 0}\langle AP_{\Sigma,R}\rangle_{\Delta\omega} = R_0^2 e^{i2\phi_0} \lim_{y\to 0}\langle AP_{\Sigma,I}\rangle_{\Delta\omega}. \tag{5.45}$$

Additionally, (5.44) may be modified for $\omega \neq \omega_c$ by replacing $\Omega_H - \Omega_L$ with $2\min(\omega - \Omega_L, \Omega_H - \omega)$ again. Note here that (5.43) applies above the interference layer, $y > h_{\Sigma}$. Thus, when R is frequency-independent, the effective reflection coefficient for AP_{Σ} is R^2, not $|R|^2$ or R, so AP_{Σ} responds to impedance surfaces differently than AP_{Δ}, the in-band field, and a true acoustic field at 2ω. An example of this boundary condition change is also provided in the next section.

5.5.2 Frequency-Dependent Reflection Coefficients

To consider a frequency dependent reflection coefficient, the amplitude and phase of the reflection coefficient can be expanded in a Taylor series about the center frequency, Ω_c:

$$R(\omega) \approx (R_0 + R_1(\omega - \Omega_c)) \exp\left(i\left(\phi_0 + \phi_1(\omega - \Omega_c) + \frac{\phi_2(\omega - \Omega_c)^2}{2}\right)\right). \tag{5.46}$$

where the subscripts 1 and 2 indicate first and second derivatives with respect to frequency evaluated at the center frequency, Ω_c. Using (5.35) with the reflection coefficient shown in (5.46) and bandwidth averaging, modifications can be found to (5.42) and (5.45). If the amplitude variation of the reflection coefficient is slow over the bandwidth such that $|(\Omega_H - \Omega_L - \Delta\omega) R_1/R_0|$ and the second derivative of the phase with respect to frequency is small such that $|\phi_2 \Delta\omega (\Omega_H - \Omega_L - \Delta\omega)| \ll 2\pi$, and the time-difference-and-bandwidth product are large such that $|2y\cos\theta_I/c + \phi_1|(\Omega_H - \Omega_L - \Delta\omega) \geq 2\pi$ so that the cross terms are small, then the frequency-dependent reflection coefficient version of (5.42) becomes:

$$\lim_{y\to 0}\langle AP_{\Delta,R}\rangle_\omega = \left(R_0^2 \exp(i\phi_1\Delta\omega)\right) \lim_{y\to 0}\langle AP_{\Delta,I}\rangle_\omega. \tag{5.47}$$

The effective reflection coefficient for the frequency-difference autoproduct still resembles the magnitude squared, but an additional phase factor is added which is proportional to the derivative of the phase with respect to frequency.

For the frequency-sum autoproduct, a similar set of assumptions about the amplitude being slowly varying over the bandwidth such that $|(\Omega_H - \Omega_L - \Delta\omega)R_1/R_0| \ll 1$ and the second derivative of the phase with respect to frequency is small such that $\left|\phi_2(\Omega_H - \Omega_L)^2\right| \ll 2\pi$ then as long as the time difference and bandwidth product are large enough such that $|2y\cos\theta_I/c + \phi_1|(\Omega_H - \Omega_L) \geq 2\pi$, then the frequency-dependent reflection coefficient ver-

sion of (5.45) is:

$$\lim_{y\to 0}\langle AP_{\Sigma,R}\rangle_{\Delta\omega} = R_0^2 e^{i(2\phi_0+2\phi_1(\omega-\Omega_c))}\lim_{y\to 0}\langle AP_{\Sigma,I}\rangle_{\Delta\omega}, \tag{5.48}$$

where the reflection coefficient is effectively still $R^2(\omega)$ as suggested by (5.45) for the frequency-independent reflection coefficient case.

While the propagation formulation provided in Section 5.4 did allow for the frequency-dependent wave propagation, this section offers some means of predicting what those effects might do to the bandwidth-averaged autoproduct fields. If the frequency-dependent phase factor varies approximately linearly in frequency over the relevant bandwidth, then (5.47) and (5.48) show how the autoproducts' reflection characteristics change. However, if the second derivative of the phase with respect to frequency is too large over the relevant bandwidth, then it would be anticipated that the results shown in this section would break down. Thus, if R varies too quickly with phase, autoproducts, even with an effective reflection coefficient, may be unable to suitably correlate well. Yet in many situations, R may be sufficiently frequency independent for (5.42) and (5.45), or (5.47) and (5.48) to hold. Even in ocean acoustics where the seabed may have a frequency-dependent reflection coefficient (*e.g.* fine layering in the ocean bottom), the penetration depths of high-frequency sound that is well described by (5.22) may be insufficient for R to display this dependence (Jackson and Richardson, 2007). While the next section returns to a frequency-independent reflection coefficient, it should be noted that some amount of reflection coefficient frequency-dependence can still be tolerated in the autoproduct fields as formulated here.

Finally, it should be noted that the analysis provided throughout this paper does not exhaustively include all possible acoustic wave propagation effects. For example, dispersive media where the phase speed is a function of frequency is omitted from consideration here. Also, any frequency-dependent propagation effects such as diffraction, rough-surface scattering,

volume attenuation, and wave propagation near caustics or turning points are also omitted. However, a sum-of-ray-paths is applicable to many acoustic scenarios.

5.6 Autoproduct Fields in a Lloyd's Mirror Environment

To provide visual and quantitative confirmation of the mathematical analysis outlined in the previous sections, wave propagation simulations were conducted in a Lloyd's mirror environment: a homogeneous half-space with a constant speed of sound (1500 m/s) bounded above by a flat pressure-release surface (see Figure 5.3). An omnidirectional point source located 100 m below the surface broadcasted a known pulse with $S(\omega) = 1$ for 1 kHz $\leq \omega/2\pi \leq$ 2 kHz, and $S(\omega) = 0$ otherwise. True acoustic P-fields at all relevant frequencies, AP_{Δ} at a difference-frequency of 100 Hz, and AP_{Σ} at a sum frequency of 3.0 kHz were calculated. For visual and quantitative comparisons, the real parts of these complex fields were computed in rectangular windows adjacent to the surface and centered at a range of 1 km. To compensate for the wide range of wavelengths, two sample-window sizes were used: 20 m wide by 200 m deep for the lower frequencies (solid line in Fig. 5.3), and 7.5 m wide by 75 m deep for the higher frequencies (dashed line in Fig. 5.3). Both windows are used in the normalization procedure described in (5.5) such that autoproduct fields can be quantitatively compared directly to out-of-band acoustic fields. All field plots in this section, specifically Figures 4-6, have color scales that vary from -2 to +2, and are dimensionless as required by (5.5).

Figure 5.4 provides reference information and shows the normalized real part of six true acoustic fields, $\mathrm{Re}\,[P^{norm}]$, in the sample windows at five different frequencies with two different reflecting surface boundary conditions. Figures 5.4a) and 5.4b) show below-band 100 Hz acoustic fields in the 20-m-by-200-m sample window when the surface reflection condition is pressure-release (R = -1) and rigid (R = +1), respectively. The 100 Hz acoustic

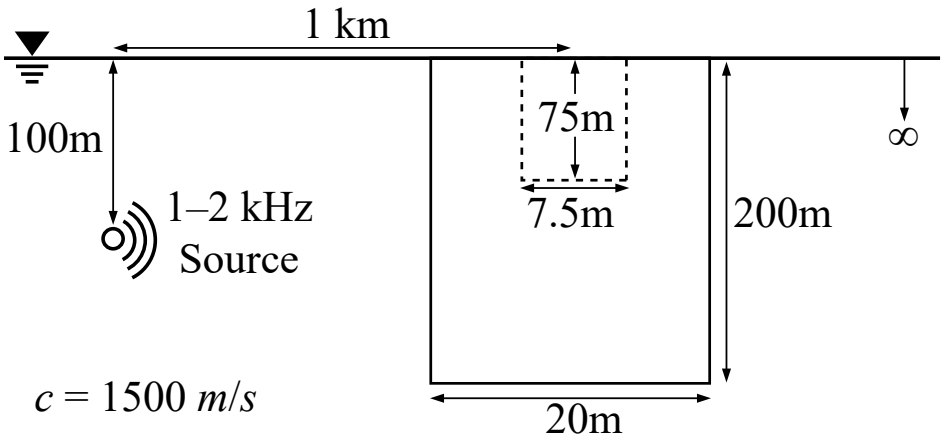

Figure 5.3: Schematic for the Lloyd's mirror environment, a homogeneous half-space with a pressure-release surface. The source is 100 m below the surface and broadcasts a known 1 - 2 kHz pulse. The fields are then sampled in one of two sampling windows, depending on the frequency. Low frequency fields (100 Hz) are sampled in the larger 20-m-wide-by-200-m-deep window (solid line). High frequency fields (kHz range) are sampled in the smaller 7.5-m-wide-by-7.5-m-deep window (dashed line). The figure is not to scale.

field shown in Fig. 5.4a) responds to the physical boundary condition for this environment, and a field node occurs at the reflecting surface. The alternative 100 Hz acoustic field shown in Fig. 5.4b) should be comparable to AP_{Δ} when the difference frequency is 100 Hz. Here a pressure anti-node occurs at the reflecting surface. However, neither of these fields were part of the 1 kHz to 2 kHz broadcast from the source. Figs. 5.4c), 5.4d) and 5.4e) show acoustic fields at in-band frequencies of 1.0 kHz, 1.1 kHz, and 2.0 kHz in the 7.5-m-by-75-m sample window when R = -1. These panels show samples of the in-band constitutive fields that are used to generate the AP_{Δ} and AP_{Σ} fields shown in Figs. 5.5 and 5.6. Fig. 5.4f) shows an above-band acoustic field at a frequency of 3.0 kHz in the 7.5-m-by-75-m sample window when $R = +1$. This field is provided here for comparisons with AP_{Σ} when the sum frequency is 3.0 kHz; it was not part of the 1 kHz to 2 kHz broadcast from the source.

Figure 5.5 shows simulation results for AP_{Δ} when the difference frequency is $\Delta f = 100$ Hz. All panels in this figure show the 20-m-by-200-m sample window. Fig. 5.5a) shows AP_{Δ} evaluated at f = 1.05 kHz and Δf = 100Hz. It is the normalized product of the complex acoustic fields shown in Figs. 5.4c) and 5.4d). Although a strong interference pattern is

apparent (seen here as many white horizontal striations), the curving nodal-line geometry and placement of colors match that of Fig. 5.4b). Fig. 5.5b) shows AP_Δ evaluated at $f = 1.95$ kHz and $\Delta f = 100$Hz. It is the normalized product of the field in Fig. 5.4e) at 2.0 kHz with the acoustic field at 1.9 kHz (figure omitted). Fig. 5.5b) is similar in structure to that of Fig. 5.5a) but the interference pattern has a higher spatial frequency. Figures 5.5a) and 5.5b) show individual samples of AP_Δ with $\Delta f = 100$ Hz when it is constructed at the two extremes of the signal bandwidth. Note that the striations here are visual manifestations of the cross terms, which for Figs. 5.5a) and 5.5b), are not being suppressed at all by bandwidth averaging. These two samples of AP_Δ with $\Delta f = 100$Hz can be combined with all the other possibilities afforded by the signal bandwidth to form the normalized bandwidth-averaged $\Delta\ f$ autoproduct, $\langle AP_\Delta \rangle_\omega^{norm}$, at $\Delta f = 100$Hz, and the real part of this field is shown on Fig. 5.5c). Although there are still visible horizontal striations in the $\langle AP_\Delta \rangle_\omega^{norm}$ field in Fig. 5.5c), particularly near the surface, it is nearly identical to the below-band 100 Hz acoustic field in Fig. 5.4b). These remaining horizontal striations near the surface correspond to cross terms which are not effectively averaged away, due to insufficient bandwidth, and form what is termed the interference layer. In quantitative terms, the spatial cross correlation coefficient, as defined in (5.6), between these two panels is 98.7%. This comparison validates the contention that $\langle AP_\Delta \rangle_\omega$ can mimic an out-of-band acoustic field with a modified boundary condition. The striations that appear in Fig. 5.5c) occur because of near-surface interference effects (see Section 5.5). These striations decrease in amplitude with increasing distance from the surface and can be highlighted by subtracting Fig. 5.5c) from Fig. 5.4b). The result of such subtraction is shown as Fig. 5.5d) where the dashed horizontal line is at a depth equal to the nominal interference-layer thickness h_Δ specified by (5.41). This figure panel shows that the differences between P^{norm} at $f = 100$Hz, and $\langle AP_\Delta \rangle_\omega^{norm}$ at $\Delta f = 100$Hz in this environment are confined near the reflecting surface and are vanishingly small away from it.

Figure 5.6 shows simulation results for AP_Σ when the sum frequency is $\Sigma f = 3.0$kHz.

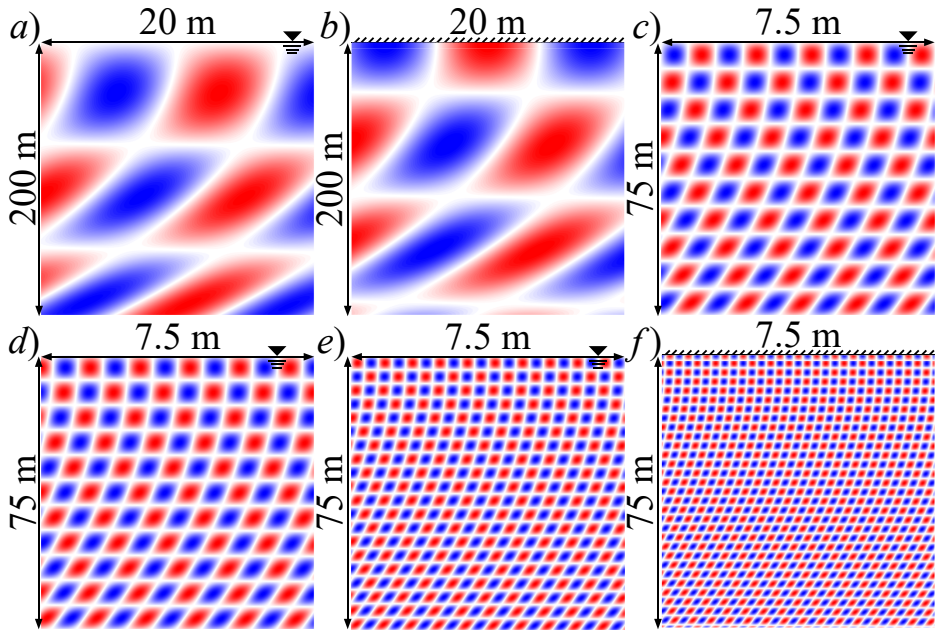

Figure 5.4: The real part of true acoustic fields in the Fig. 5.3 environment normalized according to (5.5) at a source-to-window-center range of 1.0 km when the sample window's upper edge coincides with the reflecting surface. White indicates a null, while red and blue indicate positive and negative values. The color scale ranges between ± 2. Part a) shows a below-band 100 Hz field in the 20-m-by-200-m sample window with a pressure release surface (R = -1). Part b) shows a below-band 100 Hz field in the 20-m-by-200-m sample window with a rigid surface ($R = +1$). Parts c), d) and e) show in-band 1.0 kHz, 1.1 kHz, and 2.0 kHz fields, respectively, in the 7.5-m-by-75-m sample window with a pressure release surface (R = -1). Part f) shows an above-band 3.0 kHz field in the 7.5-m-by-75-m sample window with a hard surface ($R = +1$). These true acoustic fields provide the constituent elements and comparison data for the autoproduct field results shown in Figs. 5.5 and 5.6.

All panels in this figure show the 7.5-m-by-75-m sample window. Fig. 5.6a) shows AP_Σ evaluated at Σf = 3.0kHz and Δf = 100Hz. Fig. 5.6b) also shows AP_Σ evaluated at Σf = 3.0kHz but here Δf = 1.0 kHz. This is the normalized product of the fields in Figs. 5.4c) and 5.4e). Although alignment of the patterns in Figs. 5.6a) in 5.6b) is not immediately apparent, a more uniform structure emerges when AP_Σ evaluated at Σf = 3.0kHz is averaged through the difference frequency bandwidth between 0 Hz and 1.0 kHz. Fig. 5.6c) shows the real part of the normalized Δf-bandwidth-averaged Σf autoproduct, $\langle AP_\Sigma \rangle_{\Delta\omega}^{norm}$, at Σf = 3.0kHz. Although there are variations in the patterning near the top of Fig. 5.6c), the spatial structure is much more uniform in the lower half of this panel. And, this lower-

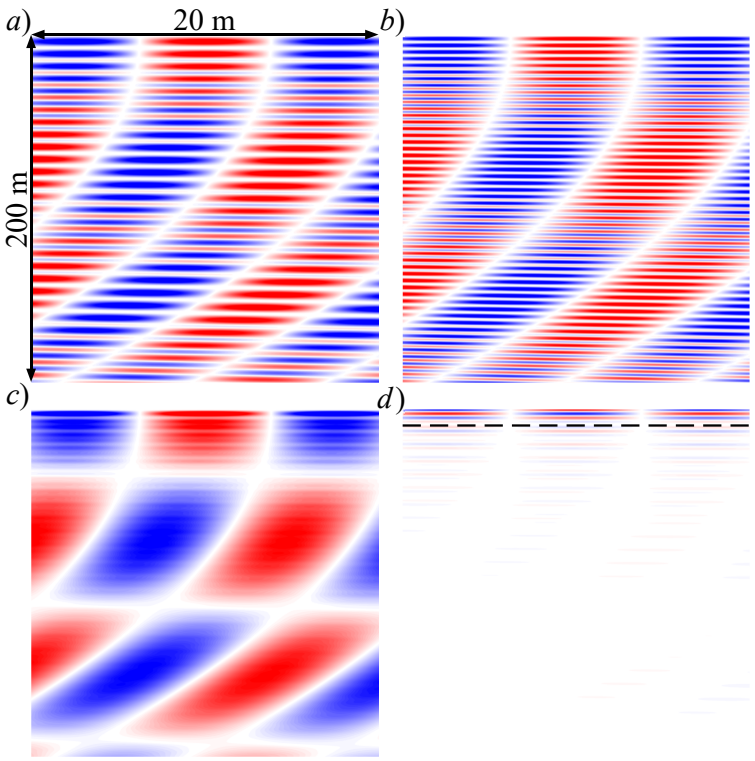

Figure 5.5: Frequency-difference autoproduct field results at $\Delta f = 100$Hz in the Fig. 5.3 environment normalized according to (5.5) in the 20-m-by-200-m sample window for a 1.0 kHz to 2.0 kHz in-band field. The color scale is the same as Fig. 5.4. Panel a) shows $\mathrm{Re}\,[AP_{\Delta}^{norm}]$ at a center frequency of 1.05 kHz. Panel b) shows $\mathrm{Re}\,[AP_{\Delta}^{norm}]$ at a center frequency of 1.95 kHz. Panel c) show the signal-bandwidth-averaged $\mathrm{Re}\,[\langle AP_{\Delta}\rangle_{\omega}^{norm}]$ and is nearly identical to Fig. 5.4b) away from the surface. Panel d) shows the difference between Fig. 5.4b) and Fig. 5.5c), and the dashed line is at the depth h_{Δ} specified by (5.41).

half spatial structure in Fig. 5.6c) matches that of the above-band 3.0 kHz acoustic field shown in Fig. 5.4f). In quantitative terms, the spatial cross correlation coefficient between Figs. 5.6c) and 5.4f) is 95.3% and this rises to 98.1% in the larger 20-m-by-200-m sample window. The difference between these two panels is shown in Fig. 5.6d). Again, there is an interference pattern that weakens with increasing distance from the reflecting surface. The dashed horizontal line in Fig. 5.6d) is at a depth equal to the nominal interference-layer thickness h_{Σ} specified by (5.44). The differences shown in Fig. 5.6d) appear larger and more extensive than those shown in Fig. 5.5d) because the sample window for Fig. 5.6) is smaller. Overall, Figs. 5.4f), 5.6c), and 5.6d) validate the contention that $\langle AP_{\Sigma}\rangle_{\Delta\omega}$ can mimic an out-of-band acoustic field with a modified boundary condition.

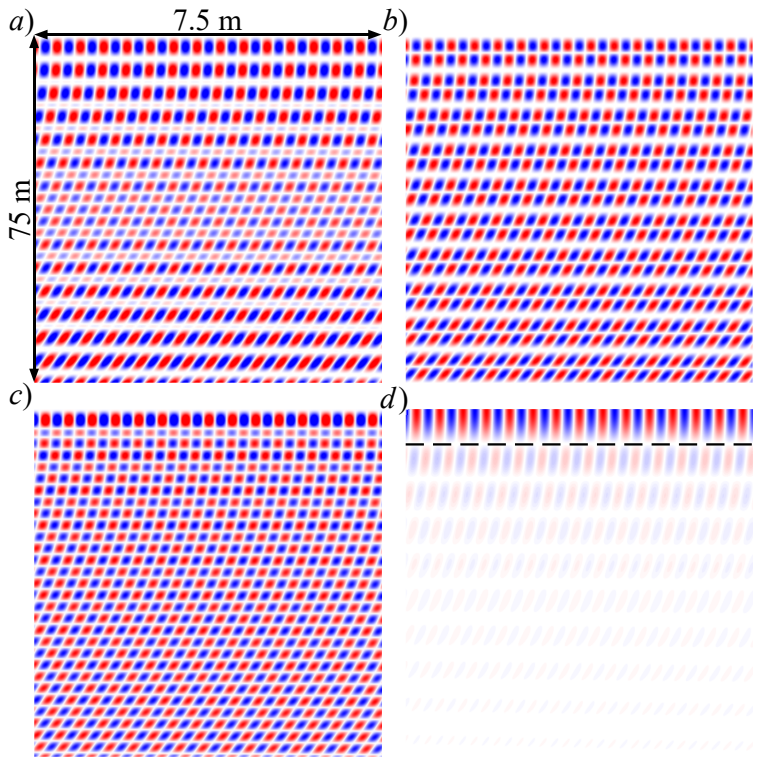

Figure 5.6: Frequency-sum autoproduct field results at $\Sigma f = 3.0$kHz in the Fig. 5.3 environment normalized according to (5.5) in the 7.5-m-by-75-m sample window for a 1.0 kHz to 2.0 kHz in-band field. The color scale is the same as Fig. 5.4. Panel a) shows $Re\left[AP_{\Sigma}^{norm}\right]$ at $\Delta f = 100$Hz. Panel b) shows $\mathrm{Re}\left[AP_{\Sigma}^{norm}\right]$ at $\Delta f = 1.01.0$ kHz. Panel c) shows the difference-frequency-averaged $\mathrm{Re}\left[\langle AP_{\Sigma}\rangle_{\Delta\omega}^{norm}\right]$ and is nearly identical to Fig. 5.4f) away from the surface. Panel d) shows the difference between Fig. 5.4f) and Fig. 5.6c), and the dashed line is at the depth h_{Σ} specified by (5.44).

An assessment of the spatial dependence of the out-band-acoustic-field to averaged-autoproduct-field matching is shown in Figure 5.7 for the Fig. 5.3 environment. Here, $1 - \chi_{\Delta,\Sigma}$, as defined in (5.6), is plotted as a function of the range and depth of the center of the sample window, r_c and z_c respectively, and then converted to decibels through $10\log_{10}(1 - \chi_{\Delta,\Sigma})$.

Fig. 5.7a) shows cross correlation results for $\langle AP_{\Delta}\rangle_{\omega}$ at $\Delta f = 100$Hz and Fig. 5.7b) shows results for $\langle AP_{\Sigma}\rangle_{\Delta F\omega}$ at $\Sigma f = 3.0$kHz, both calculated using the 20-m-by-200-m sample window. In both cases, P^{norm} is a normalized out-of-band acoustic field at the appropriate frequency (100 Hz, or 3.0 kHz) computed in the Fig. 5.3 environment with $R = +1$.

The dynamic range in both panels of Fig. 5.7 is −30 dB to 0 dB, corresponding to cross correlations between 0.999 and 0, respectively.

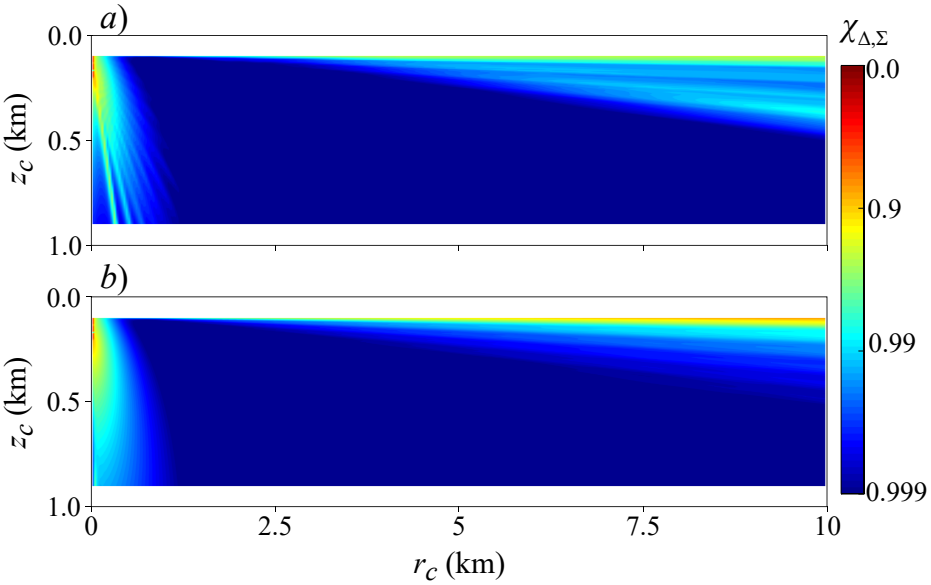

Figure 5.7: Difference between the cross correlation coefficient from (5.6) and unity in dB, $10\log_{10}(1-\chi_{\Delta,\Sigma})$, between normalized true out-of-band acoustic fields and normalized averaged autoproduct fields as a function of normalization-window center range, r_c, and center depth, z_c, using the 20m-in-range-by-200m-in-depth sample window. The color scale varies from −30 dB, or $\chi = 0.999$ (dark blue) to 0 dB, or $\chi = 0$ (dark red). Panel a) shows results for the Δf autoproduct with $\Delta f = 100$Hz. Panel b) shows results for the Σf autoproduct with $\Sigma f = 3.0$kHz. In both cases, frequency-averaged autoproduct fields mimic out-of-band acoustic fields away from the source and the reflecting surface. The white regions around the edges of both figures are a result of the fixed size of the normalization window.

Both parts of Fig. 5.7 show that the spatial cross correlations are near unity in a large fraction of the range and depth investigated. However, poor cross correlations between true-acoustic and autoproduct fields occur near the surface and near the source. Near the surface, the interference associated with the direct and reflected paths having nearly the same ray-path travel time, relative to the full signal bandwidth, is the culprit. As specified by (5.41) and (5.44), more signal bandwidth would make these layers thinner and increase the extent of darkest blue in both parts of Fig. 5.7. Near the source, the poor cross correlations are associated with the $1/R$ vs. $1/R^2$ spherical-spreading difference between true-acoustic and autoproduct fields which are not being normalized away due to the normalizing window

being too large, relative to its distance from the source (see section 5.3 for the discussion about the effect of normalization around point sources). Similarly, these discrepancies can be related to a breakdown in the assumption that the amplitude gradients are negligible.

Additionally, the striations observed near the source in Fig. 5.7a) occur because the normalization window is not much larger than the distances between nulls in the Lloyd's mirror field at the 100Hz difference frequency. This means that the normalization window at certain locations coincidentally includes a large portion of the field where the self-terms are small, meaning the otherwise small cross-terms are no longer negligible, and they create an apparently slightly poorer cross correlation. Such striations are less evident in Fig. 5.7b) because the normalization window is much larger than the distance between the nulls in the Lloyd's mirror field at 3 kHz, and therefore the regions where cross terms are small but no longer negligible are less detrimental to the spatial cross correlation coefficient.

Far from the source, spreading losses in both types of fields do not alter relative field amplitudes significantly within either sample window, and a good match between normalized field amplitudes and phases is found. Therefore, at a sufficient distance from the source and surface, the autoproduct fields can be considered to have spatial phase structure and relative amplitudes similar to true out-of-band acoustic fields that satisfy different boundary conditions.

As a final note, all the parameter values for the simulations shown in this section were chosen for convenience. They are not special or optimal. Comparable results can be obtained with other values for the difference frequency, signal bandwidth, sum frequency, source depth, normalization window size, etc.

5.7 Summary and Conclusions

The frequency-difference and frequency-sum autoproducts can be formed at each point in space from the product of two Helmholtz-equation solutions for the same acoustic environment but at different frequencies. The autoproducts can be interpreted as auxiliary or pseudo fields that may obey the Helmholtz equation at the difference and sum frequencies even when these frequencies lie outside the bandwidth of the original field. This paper provides fundamental analytical results for the autoproducts including their governing field equations, their form for simple analytical acoustic fields, the boundary conditions they satisfy, and the conditions under which they are likely to behave like true acoustic fields at the difference and sum frequencies. Sample results from a Lloyd's mirror environment confirm the analytical predictions.

This research effort supports three conclusions. First, under the right conditions, signal-bandwidth or frequency-difference-bandwidth averages of the autoproduct fields will mimic out-of-band acoustic fields in the same environment as the original acoustic field, but the autoproduct fields may satisfy different boundary conditions than the original acoustic field. The conditions identified in this study for this mimicry (which may not be general) are: (*i*) the actual acoustic propagation must be well described by a ray-path sum; (*ii*) the acoustic field gradient must be dominated by phase, not amplitude, variations; (*iii*) products of the signal bandwidth and ray-path travel-time differences must be large enough so that a signal-bandwidth average suppresses ray-path cross terms; and (*iv*), frequency-dependent wave propagation effects, such as frequency-dependent reflection coefficients or diffraction, do not play important roles in the acoustic field. However, even with these restrictions, the equivalence of autoproduct fields with true acoustic fields may occur and be potentially important in many applications, including acoustic remote sensing in refracting and multipath environments. In addition, these restrictions are sufficient for ensuring the bandwidth-averaged

autoproducts' mimicry of acoustic fields at the sum and difference frequencies, but all four restrictions may not be necessary. Particularly regarding the fourth condition, the influence of frequency-dependent wave propagation phenomena on the findings presented here has not yet been determined.

Second, wave-field information (like remote-source and reflecting-boundary locations) can be obtained from the autoproducts in well-ensonified portions of an acoustic environment at out-of-band difference and sum frequencies. Such information recovery is possible because the autoproducts' field equations each retain a point source term at the original in-band acoustic field's source location, and the boundary conditions felt by the autoproducts (although possibly different than those felt by the original in-band field) apply at the same location(s) in the environment as they did for the original in-band field. Thus, out-of-band remote sensing may be performed using the autoproducts as the inputs to acoustic signal processing schemes.

And third, the field information available from broadband acoustic signals exceeds that which is conventionally accepted. Non-zero bandwidth acoustic fields whose Fourier transforms solve the Helmholtz equation can now be seen to carry both in-band (expected) and out-of-band (unexpected) field information. The extra field information may be revealed by forming, and then appropriately averaging the autoproducts. This finding may be important for expanding the capabilities of acoustic remote sensing applications involving active and passive sonar, ultrasound, reflection seismology, structural health monitoring, and nondestructive evaluation. Additionally, there may be similar implications for radar and other electromagnetic-wave-based technologies as well.

CHAPTER 6

Measurement of Autoproduct Fields in a Lloyd's Mirror Environment

Abstract

Conventional frequency-domain acoustic-field analysis techniques are typically limited to the bandwidth of the field under study. However, this limitation may be too restrictive, as prior work suggests that field analyses may be shifted to lower or higher frequencies that are outside the field's original bandwidth [Worthmann and Dowling (2017). *J. Acoust. Soc. Am.* **141**(6.6), 4579–4590]. This possibility exists because below- and above-band acoustic fields can be mimicked by the frequency-difference and frequency-sum autoproducts, which are quadratic products of frequency-domain complex field amplitudes at a pair of in-band frequencies. For a point source in a homogeneous acoustic half-space with a flat, pressure-release surface (a Lloyd's mirror environment), the prior work predicted high correlations between the autoproducts and genuine out-of-band fields at locations away from the source and the surface. Here, measurements collected in a laboratory water tank validate predictions from the prior theory using 40-to-110-kHz acoustic pulses measured at ranges between 175 and 475mm, and depths to 400 mm. Autoproduct fields are computed, and cross-correlations between measured autoproduct fields and genuine out-of-band acoustic fields are above 90% for difference frequencies between 0 and 60 kHz, and for sum frequencies between 110 and

190kHz.

6.1 Introduction

Whenever an acoustic field is analyzed to obtain information about its source or the environment through which it has passed, the analysis nearly always seeks to extract such information from within the acoustic field's bandwidth. However, confinement of information extraction to frequencies within the bandwidth (i.e., to *in-band* frequencies) may not be a restriction in general. As shown recently (Worthmann and Dowling, 2017), nonzero-bandwidth acoustic fields may carry additional information at frequencies above and below the original field's bandwidth (i.e., at *out-of-band* frequencies). This out-of-band information may be extracted by forming the *frequency-difference* and *frequency-sum autoproducts*, which are quadratic products of frequency-domain complex field amplitudes at a pair of in-band frequencies. The frequency-difference and frequency-sum autoproducts can, when averaged through the signal bandwidth, mimic genuine acoustic fields at frequencies below and above the signal bandwidth, respectively. In the recent study, autoproducts were investigated theoretically in a Lloyd's mirror environment. In this study, those predictions are tested by measuring autoproduct fields in a laboratory water tank and comparing those fields to theoretical autoproduct fields and theoretical out-of-band fields. The results presented here show that experimentally measured autoproducts can correlate strongly with genuine out-of-band fields at more than 80% of the possible difference frequencies and at nearly 60% of the possible sum frequencies, percentages that compare favorably with theory.

The autoproducts share features with other better-known concepts. The shifting to lower and higher frequencies is also an attribute of the parametric array (Westervelt, 1963); however, the out-of-band frequencies generated by the parametric array exist due to nonlinearities in the propagation medium, whereas autoproducts do not physically exist, and are created

through an intentional mathematical nonlinearity. The construction of autoproducts as a product of complex field amplitudes at a pair of frequencies is reminiscent of the mutual coherence function in statistical optics (Beran and Parrent, 1964; Born and Wolf, 1999) and the formative concepts of Δk-radar (Weissman, 1973; Popstefanija *et al.*, 1993). Furthermore, single Fourier transforms of the frequency-difference autoproduct lead to the Wigner-Ville transform and the ambiguity function (Cohen, 1989).

Prior experimental studies have used autoproducts in the source-localization techniques of beamforming (Abadi *et al.*, 2012; Douglass *et al.*, 2017) and matched-field processing (Worthmann *et al.*, 2015, 2017) within the realm of underwater acoustics. However, these techniques do not utilize the autoproduct fields themselves but rather cross-spectral density matrices, allowing the localization schemes to be independent of the source waveform. In contrast, this study measures autoproduct fields *directly* and requires a known source waveform (much like active inversion techniques) to verify the claims in Worthmann and Dowling (2017). Moreover, although this study uses water as the propagation medium, the techniques outlined here need not be confined strictly to underwater acoustics, and could also apply to other acoustic-wave propagation regimes such as diagnostic ultrasound or room acoustics.

The results in Worthmann and Dowling (2017) predict that autoproduct fields will correlate strongly with genuine out-of-band acoustic fields when the in-band acoustic field is well described by elementary ray acoustics provided that two conditions are satisfied: (*i*) the gradient of the acoustic pressure is dominated by phase variations and not amplitude variations, and (*ii*) multipath arrivals have sufficient temporal separation so that the product of the arrival-time differences with the signal bandwidth is much greater than unity. Simulations in a homogeneous acoustic half-space bounded by a flat, pressure-release surface (a Lloyd's mirror environment) confirmed these conditions. Regions very close to the source gave poor spatial cross-correlations between the autoproducts and genuine out-of-band acoustic fields due to a violation of condition (*i*), while regions near the reflecting surface gave poor

cross-correlations due to a violation of condition (*ii*). Away from the source and surface, near-perfect cross-correlations were found. However, these predictions were made using a set of assumptions that may or may not apply in reality, e.g., that the acoustic environment is homogenous with a perfectly known sound speed and perfectly known geometry. Thus, for this paper, experimental measurements were collected to quantitatively support or refute the achievability of the theory in practice.

The remainder of this paper is divided into four sections. Section 6.2 provides an overview of the relevant theory and defines the theoretical fields and comparison metrics used throughout the rest of the paper. Section 6.3 details the experimental method, including efforts to characterize the source and the acoustic environment. Section 6.4 presents the measurements of autoproduct fields and the comparisons to theoretical fields. Section 6.5 provides a summary of this work and the conclusions drawn from it.

6.2 Theoretical Fields and Comparison Metrics

This section provides an overview of relevant autoproduct theory and specifies how the theory and measurements may be compared. Definitions for autoproduct quantities are provided first, including normalization and cross-correlation procedures. Theoretical acoustic and autoproduct fields for a Lloyd's mirror environment are then presented and discussed.

6.2.1 Autoproduct Definitions

In this paper, $P(\boldsymbol{r}, \omega)$ represents the frequency-domain complex pressure field measured at position $\boldsymbol{r}$ and angular frequency ω due to an omnidirectional point source at position $\boldsymbol{r}_s$ that broadcasted a waveform with source spectrum $S(\omega)$. The frequency-difference autoproduct (AP_Δ) and frequency-sum autoproduct (AP_Σ), constructed from $P(\boldsymbol{r}, \omega)$, are defined as

$$AP_{\Delta}\left(\boldsymbol{r},\omega,\Delta\omega\right) \equiv P\left(\boldsymbol{r},\omega_{+}\right)P^{*}\left(\boldsymbol{r},\omega_{-}\right)$$
$$AP_{\Sigma}\left(\boldsymbol{r},\omega,\Delta\omega\right) \equiv P\left(\boldsymbol{r},\omega_{+}\right)P\left(\boldsymbol{r},\omega_{-}\right), \tag{6.1}$$

where the asterisk denotes a complex conjugate, and $\omega_{\pm} \equiv \omega \pm \frac{\Delta\omega}{2}$ defines a pair of frequencies with difference frequency $\Delta\omega = \omega_{+} - \omega_{-}$ and sum frequency $\Sigma\omega = \omega_{+} + \omega_{-} = 2\omega$. Bandwidth-averaged autoproducts, denoted by angle brackets $\langle\ \ \rangle$, are defined as

$$\left\langle AP_{\Delta}\right\rangle\left(\boldsymbol{r},\Delta\omega\right) = \frac{1}{\Omega_{BW}^{\Delta}}\int_{\Omega_C-\frac{1}{2}\Omega_{BW}^{\Delta}}^{\Omega_C+\frac{1}{2}\Omega_{BW}^{\Delta}} \frac{AP_{\Delta}\left(\boldsymbol{r},\omega,\Delta\omega\right)}{S\left(\omega_{+}\right)S^{*}\left(\omega_{-}\right)}d\omega$$
$$\left\langle AP_{\Sigma}\right\rangle\left(\boldsymbol{r},\Sigma\omega\right) = \frac{1}{\Omega_{BW}^{\Sigma}}\int_{0}^{\Omega_{BW}^{\Sigma}} \frac{AP_{\Sigma}\left(\boldsymbol{r},\omega,\Delta\omega\right)}{S\left(\omega_{+}\right)S\left(\omega_{-}\right)}d\left(\Delta\omega\right). \tag{6.2}$$

In this formulation, $\Omega_L \leq \omega \leq \Omega_H$ defines the signal bandwidth, $\Omega_C = \frac{(\Omega_L+\Omega_H)}{2}$ defines the in-band center frequency, and $\Omega_{BW}^{\Delta} = \Omega_H - \Omega_L - \Delta\omega$ and $\Omega_{BW}^{\Sigma} = min\left(2\Omega_H - \Sigma\omega, \Sigma\omega - 2\Omega_L\right)$ define the signal bandwidth available for averaging AP_{Δ} and AP_{Σ}, respectively. By defining the limits on the integrals of (6.2a) and (6.2b) in this manner, the integrands contain only acoustic-field amplitudes within the signal bandwidth, and encompass all possible in-band frequency pairs that have a difference of $\Delta\omega$ or a sum of $\Sigma\omega$. Note that Ω_{BW}^{Δ} and Ω_{BW}^{Σ} take on the maximum value of $\Omega_H - \Omega_L$ at $\Delta\omega = 0$ and $\Sigma\omega = 2\Omega_C$, respectively. Moreover, although the difference- and sum-frequency bandwidths ($0 \leq \Delta\omega \leq \Omega_H - \Omega_L$ and $2\Omega_L \leq \Sigma\omega \leq 2\Omega_H$, respectively) may include some frequencies *within* the signal bandwidth, $\Delta\omega$ and $\Sigma\omega$ are still termed *out-of-band* in this paper for simplicity. Finally, note that the definitions of the bandwidth-averaged autoproducts in (6.2a) and (6.2b) include the source spectrum.

To compare autoproduct fields with out-of-band acoustic fields, a normalization must be

performed since autoproducts and ordinary fields have different units (pressure-squared vs. pressure). To normalize an acoustic or autoproduct field within a chosen region V, the following procedure is applied, where $(\ )^{norm}$ denotes the normalized version of a field quantity $(\ )$:

$$(\ )^{norm} = (\ ) \left[\frac{1}{V} \int_V |\,(\ )\,|^2 dV \right]^{-\frac{1}{2}}. \tag{6.3}$$

After normalization, the figure of merit considered here for how closely two fields align is the complex spatial cross-correlation coefficient, χ, defined by

$$\chi_{\Delta,\Sigma} \equiv \frac{1}{V} \int_V \left[\langle AP_{\Delta,\Sigma} \rangle (r) \right]^{norm} G^{norm*}_{\Delta,\Sigma} (r)\, dV, \tag{6.4}$$

where the "'Δ"' and "'Σ"' subscripts denote quantities associated with the frequency-difference and frequency-sum autoproducts, respectively, and$G_{\Delta,\Sigma}$ denotes the genuine out-of-band acoustic field that $\langle AP_{\Delta,\Sigma} \rangle$ should mimic. $G_{\Delta,\Sigma}$ is the Green's function (or impulse response) for the same acoustic environment evaluated at the out-of-band frequency $\Delta\omega$ or $\Sigma\omega$, respectively; however, it may satisfy different boundary conditions than the original in-band Green's function, $G(\boldsymbol{r}, \omega) \equiv P(\boldsymbol{r}, \omega)/S(\omega)$ (see Worthmann and Dowling, 2017). The complex cross-correlation coefficient χ is guaranteed to fall within the complex unit circle, and a perfect match of fields in phase and normalized magnitude within$V$ corresponds to $\chi = 1 + 0i$, while a perfect lack of correlation corresponds to $\chi = 0$. In addition, the expression $2\left(1 - Re\left[\chi_{\Delta,\Sigma}\right]\right)$ is equivalent to the L_2-norm of the difference between $\langle AP_{\Delta,\Sigma} \rangle^{norm}$ and $G^{norm}_{\Delta,\Sigma}$. In prior work (Worthmann and Dowling, 2017), only the magnitude of χ was reported. [Furthermore, an error exists in Eq. (6.6) of that paper; the absolute value bars should be outside the integral, not inside.] However, the full complex value of χ is considered here since a constant relative phase factor (such as an overall sign difference) between $\langle AP_{\Delta,\Sigma} \rangle$ and $G_{\Delta,\Sigma}$ is considered here to be a discrepancy between the fields.

6.2.2 Lloyd's Mirror Environment

To apply the preceding theory to the experimental Lloyd's mirror environment, start with a cylindrical coordinate system where r denotes the radial distance (range) from the source, z denotes the axial distance from the surface (depth), and the source is at depth $z = d$. In this environment, the theoretical in-band Green's function is

$$G(\boldsymbol{r}, z, \omega) \equiv \frac{P(\boldsymbol{r}, z, \omega)}{S(\omega)} = \frac{e^{i\omega\tau_1}}{r_1} - \frac{e^{i\omega\tau_2}}{r_2}, \tag{6.5}$$

where $r_{1,2} = \sqrt{r^2 + (z \mp d)^2}$ are the direct and reflected path lengths, respectively, between the field point$(\boldsymbol{r}, z)$ and source $(0, d)$, $\tau_{1,2} = \frac{r_{1,2}}{c}$ are the corresponding acoustic propagation times, and c is the speed of sound for the propagation medium. The last term in (6.5), corresponding to the reflected path, includes the pressure-release surface reflection coefficient of –1.

Inserting (6.5) into (6.1) and (6.2) yields the following bandwidth-averaged autoproducts:

$$\begin{aligned}
\langle AP_\Delta \rangle (\boldsymbol{r}, z, \Delta\omega) &= \frac{e^{i\Delta\omega\tau_1}}{r_1^2} + \frac{e^{i\Delta\omega\tau_2}}{r_2^2} - 2\frac{e^{i\Delta\omega(\tau_1+\tau_2)/2}}{r_1 r_2} \cos(\Omega_C \Delta\tau) \operatorname{sinc}\left(\frac{\Omega_{BW}^{\Delta} \Delta\tau}{2}\right) \\
\langle AP_\Sigma \rangle (\boldsymbol{r}, z, \Sigma\omega) &= \frac{e^{i\Sigma\omega\tau_1}}{r_1^2} + \frac{e^{i\Sigma\omega\tau_2}}{r_2^2} - 2\frac{e^{i\Sigma\omega(\tau_1+\tau_2)/2}}{r_1 r_2} \operatorname{sinc}\left(\frac{\Omega_{BW}^{\Sigma} \Delta\tau}{2}\right),
\end{aligned} \tag{6.6}$$

where $\Delta\tau = \tau_2 - \tau_1$ is the difference in arrival times, and $\operatorname{sinc}(x) = \frac{\sin(x)}{x}$. The first two terms in (6.6a) and (6.6b) arise from *same-path* products (direct-direct and reflected-reflected) and are the *self* terms. The last term in (6.6a) and (6.6b) arises from *different-path* products (direct-reflected and reflected-direct, simplified to a single term) and is the *cross* term.

The self terms in (6.6a) and (6.6b) are similar, but not identical, to the field in (6.5) evaluated

at $\Delta\omega$ or $\Sigma\omega$; thus, they can potentially correlate strongly with an out-of-band acoustic field. Compared to (6.5), each self term has an additional factor of r_1 or r_2 in the denominator, so a strong correlation is obtained when $1/r_{1,2}$ does not vary significantly in the region of interest (see Worthmann and Dowling, 2017), i.e., when $r_{1,2}$ is much larger than V in (6.3) and (6.4). Additionally, the reflected-path (second) self term in both (6.6a) and (6.6b) carries a positive sign, while the reflected-path term in (6.5) carries a negative sign. This sign difference arises because the quadratic nonlinearity rectifies the –1 reflection coefficient. Consequently, the autoproduct fields in (6.6) appear to mimic genuine out-of-band acoustic fields in a Lloyd's mirror environment having a rigid, rather than pressure-release, surface boundary condition. Further discussion of this modified reflection coefficient can be found in Worthmann and Dowling (2017).

The cross term in (6.6a) and (6.6b) is not present in (6.5), and thus permits or inhibits the autoproducts' potential mimicry of genuine fields, depending on its magnitude compared to the self terms. The magnitude is controlled by a sinc function, which arises from the bandwidth averaging. In regions where $\Omega_{BW}^{\Delta,\Sigma}\Delta\tau \gg 2\pi$ (i.e., away from the surface), the sinc factor suppresses the cross term and permits potentially strong cross-correlations between autoproducts and out-of-band fields. However, near the surface, an "'interference layer"' exists where the cross term is insufficiently suppressed, leading to poor cross-correlations. The nominal interference layer thickness, h, is taken to be the region where $\Omega_{BW}^{\Delta,\Sigma}\Delta\tau \leq 2\pi$. For a given range, source depth, signal bandwidth, and difference- or sum-frequency selection, h is given implicitly by

$$\sqrt{r^2 + (h_{\Delta,\Sigma} + d)^2} - \sqrt{r^2 + (h_{\Delta,\Sigma} - d)^2} = \frac{2\pi c}{\Omega_{BW}^{\Delta,\Sigma}}. \tag{6.7}$$

In regions where $r \gg |h_{\Delta,\Sigma} \pm d|$, (i.e., where propagation directions are close to horizontal), this relationship simplifies to $h_{\Delta,\Sigma} \sim \pi rc/\Omega_{BW}^{\Delta,\Sigma}d$. Thus, longer ranges thicken the interfer-

ence layer, while greater bandwidth averaging and source depth shrink the interference layer, and these trends also hold when the small-angle approximation does not apply.

6.3 Experiment

To measure bandwidth-averaged autoproduct fields and compare them to theory, the acoustic field, source waveform, and environmental parameters (geometry and sound speed) must be known. This section describes how these quantities were measured or characterized for a Lloyd's mirror laboratory environment.

6.3.1 Acoustic-Field Measurements

In this study, an acoustic field was generated and measured in a 107-cm-diameter cylindrical plastic water tank, filled to a depth of 90 cm with fresh water. A sound source and single receiver were used to broadcast sound from a fixed location and record the pressure waveform at a variable location, respectively. Source and receiver locations were chosen to ensure that arrival times via the direct and surface-reflected paths were temporally well separated from arrival times via tank-bottom and tank-side-wall reflected paths. Sound traveling on these additional paths was removed by time gating the measured signals, allowing the finite water tank to imitate a semi-infinite half-space.

Figure 6.1 provides a schematic of the experimental setup in panel a) and a corresponding photograph in panel b). The source, an ITC-1042 transducer (International Transducer Corp., Santa Barbara, CA), was positioned at depth $d = 200$ mm, and broadcasted a nominally 50-μ s Gaussian-enveloped sinusoidal pulse with a nominal center frequency of 70kHz. The receiver, a Reson TC4013 transducer (Teledyne Reson A/S, Slangerup, Denmark), was mounted via thin stainless-steel tubing to a 0.01-mm-resolution height gauge, and was placed

at depths between 0 and 100mm in increments of 1mm, and between depths of 100 and 400mm in increments of 5mm. The finer spacing near the surface was chosen to carefully measure the autoproducts in regions where the cross terms may be poorly suppressed (see Sec. 6.2.2). Additionally, tank-spanning bars allowed the receiver assembly to translate in range, which allowed data collection from three different source-to-receiver ranges: $r =$ 175, 325, and 475mm. The orientation of the transducers shown in Fig. 6.1b) was chosen to best achieve broadcast and receiving directional uniformity. Additionally, for each range and depth pair, the source broadcasted three identical pulses, providing an opportunity to check the repeatability of the measurements. The signal-to-noise ratio observed in the experiment was approximately 40dB. A total of 1,449 recordings (161 depths, 3 ranges, and 3 trials) serve as the experimental field measurements used in the remainder of the paper.

6.3.2 Source Characterization

To calculate the bandwidth-averaged autoproducts defined in (6.2), the source waveform and signal bandwidth must be known. While the nominal source waveform applied to the broadcast transducer could potentially provide this information, the imperfect frequency response of the transducer pair lead to noticeable distortion of the intended waveform. To compensate, a measured source waveform was determined from the time-domain acoustic-field measurements.

To determine the measured source waveform, direct-path waveforms were first extracted from recordings in which the arrival times were well separated (defined here as an arrival-time difference of 150 μ s or more, where 50μ s before and after the nominal pulse duration were included to provide robustness). This requirement allowed 291 of the 1,449 recordings to be used, which came primarily from the deeper sampling depths. These recordings were then scaled up by a factor of r_1 (to counteract spherical spreading losses), shifted in time to maximize their temporal cross-correlations with the nominal source waveform, and coherently

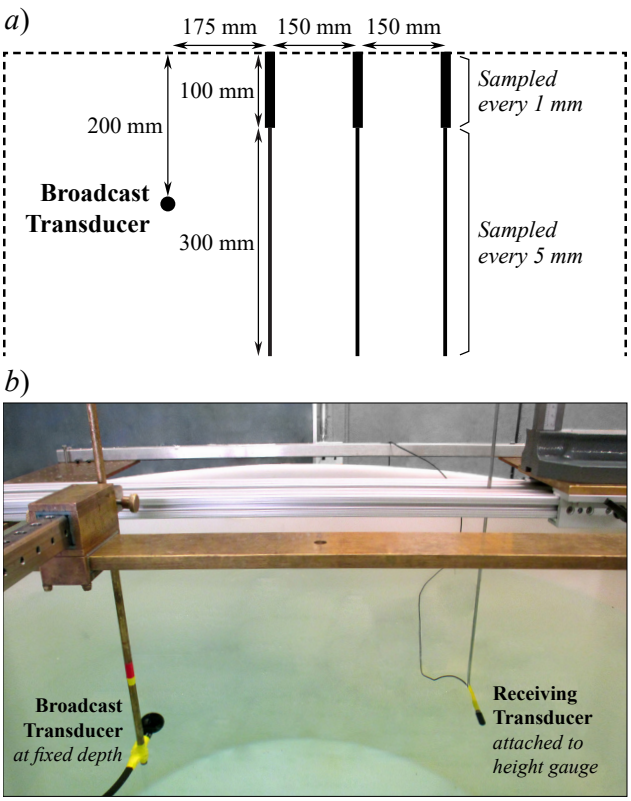

Figure 6.1: Schematic and photograph of the experimental setup. Panel a) illustrates the location of the broadcast transducer and the various locations of the receiving transducer relative to the walls of the water tank and the water surface, shown with the dashed lines around the edges. The receiver was positioned in 1-mm increments in the top 100mm of depth and in 5-mm increments in the next 300mm of depth, providing 400mm of depth sampled nonuniformly. Pressure waveforms were recorded at three source-to-receiver ranges: 175, 325, and 475mm. Panel b) shows the broadcast and receiving transducers, along with the tank's horizontal spanning bars, which allowed the height gauge (the base of which can be seen at the top right in dark gray) to translate in range.

averaged. Figure 6.2 shows the nominal, extracted, and coherent-average waveforms in the time domain in panel a) and frequency domain in panel b). In each panel, the nominal waveform (dashed black curve) is given a maximum amplitude of unity, the coherent average (solid black curve) is scaled to contain the same total signal energy as the nominal waveform, and the 291 individual signal samples (semitransparent red curves) are scaled by the same factor as the coherent average.

Figure 6.2 reveals imperfections in the broadcast and receiving transducers' responses. In the time domain, the recorded waveforms were temporally stretched to a duration of approx-

imately 75 μ s, consistent across all 291 signal samples. In the frequency domain, a shift in spectral peak from 70 to approximately 80 kHz is observed, consistent with the resonant frequency of the broadcast transducer, nominally 79 kHz. Additionally, Fig. 6.2b) shows an unexpected dip in direct-path waveform amplitudes near 63 kHz. A corresponding plot made using reflected-path waveforms (not shown) does not contain this dip. Thus, the origin of this dip is most likely frequency-dependent directionality of the broadcast and/or receiving transducers. Moreover, after correcting for spherical spreading losses, the coherent-average waveform for the reflected path had 1.3 dB *more* signal energy than for the direct path, providing further support for transducer directionality. This observed variation is consistent with the broadcast and receiving transducers' uniformity specifications, nominally $\pm$ 1–2 dB.

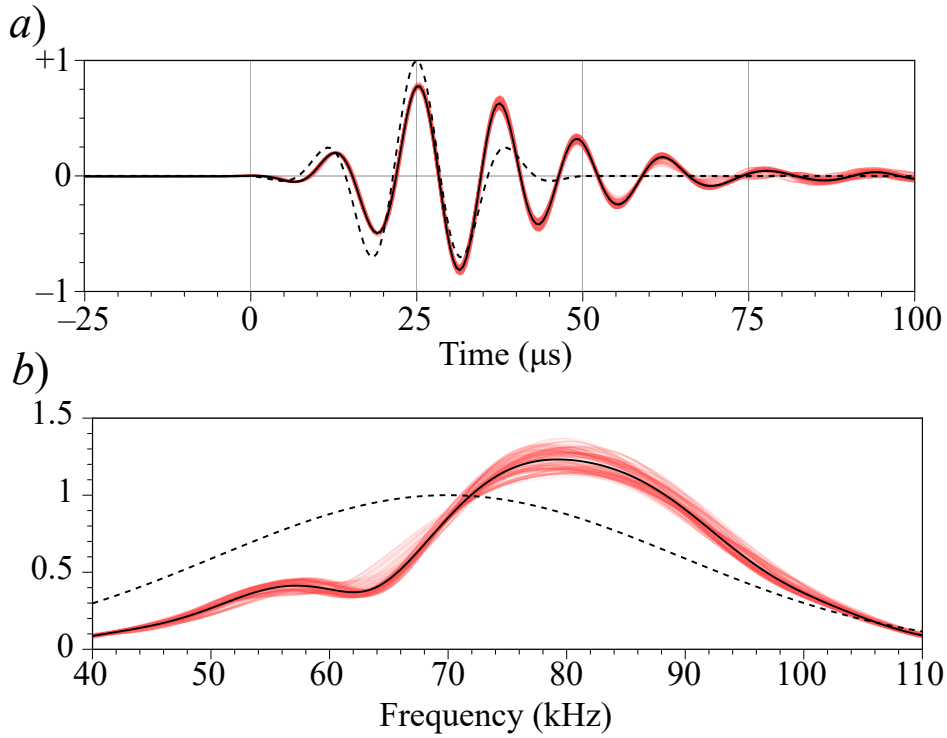

Figure 6.2: Measured direct-path waveforms in the time domain (upper panel) and frequency domain (lower panel). The nominal source waveform is shown with the dashed curves. The red semitransparent curves show the 291 signal samples used for characterization of the actual source waveform, scaled for spherical spreading and shifted in time to maximize their temporal cross-correlations with the nominal source waveform. The coherent-average direct-path waveform, shown with the solid black curves, is taken to be the experimentally determined source waveform, and is scaled vertically to contain the same total signal energy as the nominal source waveform.

Based on this source-characterization effort, the experimentally determined $S(\omega)$ used to construct the measured fields is the coherent average of the direct-path waveforms, shown with the solid black curve in Fig. 6.2b). Also, the experimentally determined bandwidth (defined here to be the range of frequencies that contain 99.9% of the recorded signal energy, rounded to the nearest 5kHz) is $\frac{\Omega_L}{2\pi} = 40$ kHz to $\frac{\Omega_H}{2\pi} = 110$ kHz, with a measured center frequency of $\Omega_C/2\pi = 75$ kHz.

6.3.3 Environmental Characterization

Evaluation of the theoretical acoustic and autoproduct fields requires values for environmental parametersspecifically, the ranges and depths of the source and receiver, and the sound speed. Although the nominal experimental values could be used, inaccuracies of order 1% could significantly influence comparisons between measured and theoretical fields, since the values of $\omega\tau_{1,2}$ in (6.5) are of order 10^2 for the bandwidth (40 to 110 kHz) and source-to-receiver ranges used in the experiment. Accurate environmental parameters are especially important at the higher frequencies of interest in this study, which can exceed 200 kHz for the frequency-sum autoproduct. Therefore, to mitigate the effects of experimental uncertainties and ensure the fairest comparisons of autoproduct measurements to theory, four experimental parameters were determined *a posteriori* by optimizing the cross-correlation of measured and theoretical *in-band* acoustic fields.

The four optimized parameters were a source-depth offset, receiver-depth offset, receiver-range offset, and sound-speed offset from the nominal experimental values. The source-depth offset (δd) was a vertical offset to the nominally 200-mm depth of the geometric center of the broadcast transducer. Throughout the experiment, receiver depth relative to an uncertain water-surface zero point was determined via the height gauge. The receiver-depth offset (δz) was a vertical offset to all measured receiver depths to account for uncertainty in the zero point, and the location of the receiver's acoustic center. Similarly, changes in

source-to-receiver range were well known, but the spatial location of zero range was not because of the finite sizes of the transducers; the receiver-range offset (δr) accounted for this range uncertainty. Finally, the sound-speed offset (δc) allowed refinement of the nominal experimental sound speed of 1451.2 m/s, determined from a measured water temperature (see equation 5.6.8 in Kinsler *et al.*, 2000).

The parameter optimization was performed by maximizing the overall correlation of measured in-band fields with theoretical in-band fields at all depths, trials, ranges, and in-band frequencies. The maximized quantity was the real part of the bandwidth-averaged cross-correlation between the measured and theoretical in-band fields, $Re\left[\langle\chi_{IB}\rangle\right]$. Here, χ_{IB}, and its bandwidth average $\langle\chi_{IB}\rangle$, were determined from

$$\chi_{IB}\left(\omega,\delta u\right)=\frac{1}{N_t}\frac{1}{N_r}\sum_{n=1}^{N_r}\sum_{m=1}^{N_t}\frac{1}{D}\int_{\delta z}^{D+\delta z}\left[\frac{P_{nm}\left(z,\omega\right)}{S\left(\omega\right)}\right]^{norm}\left[G_n^*\left(z,\omega,\delta u\right)\right]^{norm}dz$$

$$\langle\chi_{IB}\rangle\left(\delta u\right)=\frac{1}{\Omega_H-\Omega_L}\int_{\Omega_L}^{\Omega_H}\chi_{IB}\left(\omega,\delta u\right)d\omega, \tag{6.8}$$

where $\delta u=[\delta d,\delta z,\delta r,\delta c]$ is the vector of parameters to be optimized, $D=400$ mm is the deepest nominal depth of the measurements, and $N_t=3$ and $N_r=3$ are the number of trials and ranges, respectively. In (6.8a), $P_{nm}\left(z,\omega\right)$ is the measured complex field at the n th range and m th trial, taken to occur at the nominal receiver depth incremented by δz. $G_n\left(z,\omega,\delta u\right)$ is the theoretical in-band Green's function for the n th range, calculated from (6.5) using the nominal source depth, receiver range, and sound speed incremented by δd,δr, and δc, respectively. Here, and in the remainder of the paper, the normalization defined in (6.3) takes V to be a vertical line segment spanning 400 mm of depth, and normalization is performed separately for each range and trial. In (6.8a), the integral gives the cross-correlation between the measured and theoretical in-band field at one range, trial, and frequency; the two summations average the cross-correlation over the three trials and

three ranges. In (6.8b), the integral averages over all in-band frequencies to produce $\langle \chi_{IB} \rangle$. Then, $Re\left[\langle \chi_{IB} \rangle\right]$ is maximized by varying δu. Without optimization (i.e., $\delta u = [0, 0, 0, 0]$), $Re\left[\langle \chi_{IB} \rangle\right] = 0.906$. When a nonlinear optimization was performed, the following parameter corrections were found: $\delta d = +1.62mm$, $\delta z = -2.13mm$, $\delta r = -0.59mm$, and $\delta c = -0.76\frac{m}{s}$, yielding $Re\left[\langle \chi_{IB} \rangle\right] = 0.980$. All four fitted parameters are within their known or estimated ranges of uncertainty. In the remainder of this paper, unless otherwise specified, the optimized values of the source depth, receiver depth, receiver range, and sound speed are used.

6.4 Results and Comparisons

Using the measurements described in Sec. 6.3, experimental in-band fields and autoproduct fields may be computed and then compared to theoretical fields. This section presents these results visually with field plots and numerically with the cross-correlation coefficient χ.

The in-band Green's functionsthe constituents of the autoproduct fieldsmay be determined from the measured data as $\frac{P_{nm}(z,\omega)}{S(\omega)}$, and from theory using (6.5). Figure 6.3 shows plots of the real parts of the measured and theoretical normalized Green's functions at different ranges (r) and frequencies ($f = \omega/2\pi$). Panels a), b), and c) of Fig. 6.3 are evaluated at the center frequency, 75 kHz, and at $r = 175$, 325, and 475 mm, respectively. These three panels give a cross-correlation coefficient of $\chi_{IB} = 0.98 - 0.02i$. Panels d) and e) are evaluated at the middle range of 325 mm, and at the lower and upper limits of the signal bandwidth, 40 and 110 kHz, respectively. In each plot, the horizontal axis is the depth (0 mm $\leq z \leq$ 400 mm), the vertical axis varies from –4 to +4, the normalized theoretical Green's function is the solid black curve, and the normalized measured Green's function is plotted with red $\times$'s for the three trials. As the plots show, the spatial sampling is five times finer for $z \leq 100$ mm, and the repeatability between trials is excellent. Overall, the measured data match the theoretical results wellas they should when the in-band field is well described by (6.5)since

the environmental parameters were optimized to maximize the cross-correlation between the measured and theoretical in-band fields.

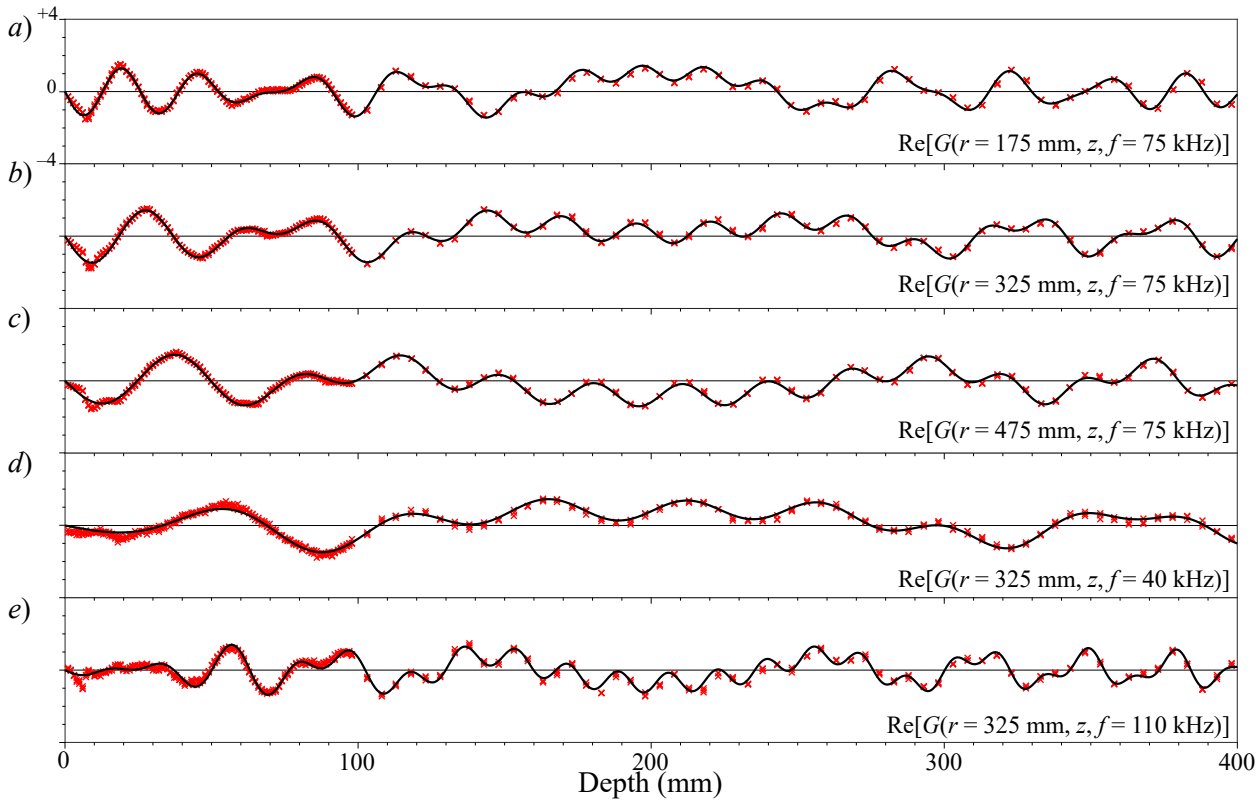

Figure 6.3: In-band field plots. The measured in-band Green's functions are shown with red "'×"'s. The theoretical in-band Green's functions are shown with the black curves. All five panels have the same horizontal axes (depth from 0 to 400 mm) and vertical axes (normalized units from –4 to +4). The range and frequency for each panel is indicated in the lower right corner, with ranges from 175 to 475 mm, and frequencies from 40 to 110 kHz.

From the in-band Green's functions, the bandwidth-averaged autoproducts, $\langle AP_{\Delta,\Sigma} \rangle$, may be calculated using (6.2) and normalized via (6.3). Once normalized, the measured autoproduct fields may then be compared to the theoretical autoproduct fields from (6.6), and to theoretical out-of-band acoustic fields from (6.5) using the modified surface boundary condition discussed in Sec. 6.2.2. In Fig. 6.4, the normalized real parts of five $\langle AP_{\Delta} \rangle$ fields and five $\langle AP_{\Sigma} \rangle$ fields are plotted vs. depth on the horizontal axis. The red × 's are the field measurements for the three trials, the solid black curves are the theoretical autoproduct fields, and the blue dotted curves are the theoretical out-of-band acoustic fields at

the difference or sum frequencies. Additionally, the vertical dashed lines show the depth of the interference layer [see (6.7)], below which autoproduct fields are expected to correlate strongly with corresponding out-of-band fields. Panels a), b), and c) of Fig. 6.4 are evaluated at a difference frequency ($\Delta f = \Delta\omega/2\pi$) of 30 kHz, and at r = 175, 325, and 475mm, respectively. Together, these three panels give $\chi_\Delta = 0.96 - 0.03i$, calculated as described below. Panels d) and e) show results for the 325-mm range at difference frequencies of 5and 60kHz, respectively. Panels f), g) and h) are evaluated at the sum frequency ($\Sigma f = \Sigma\omega/2\pi$) of 150kHz (twice the center frequency), and at r = 175, 325, and 475mm, respectively. These three panels give $\chi_\Sigma = 0.95 + 0.00i$. Panels i) and j) are evaluated at the middle range of 325mm, and at sum frequencies of 115and 185kHz, respectively, which are halfway between twice the center frequency and twice the lowest and highest frequencies.

In all ten panels of Fig. 6.4, the measured autoproducts (red × 's) closely follow the theoretical autoproducts (solid black curves), except for very shallow depths where the receiving transducer was not sufficiently submerged. Furthermore, trial repeatability is very good, and the measured autoproducts closely follow their associated theoretical out-of-band fields for depths below the interference layer ($z > h_{\Delta,\Sigma}$).

To provide a comparison of experimental and theoretical results at all possible frequencies, Fig. 6.5 shows the real parts of the cross-correlations between experimental fields and genuine acoustic fields as a function of below-band ($\Delta\omega$) , in-band (ω), or above-band ($\Sigma\omega$) frequency. At each frequency, the cross-correlation encompasses all depths, ranges, and trials. The in-band cross-correlation χ_{IB}, discussed in Sec. 6.4, is given in (6.8a). The below- and above-band cross-correlations, χ_Δ and χ_Σ, respectively, are given analogously by

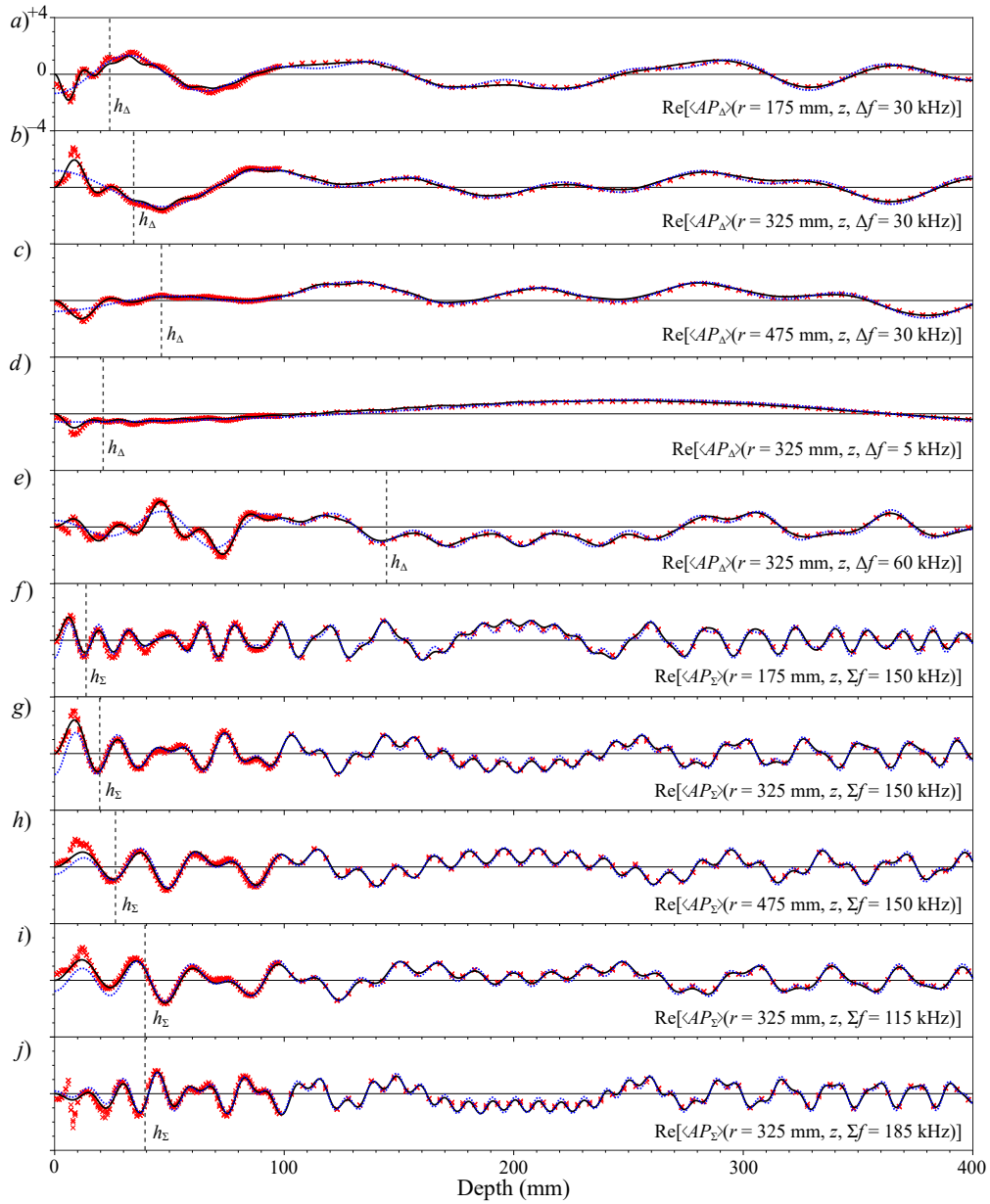

Figure 6.4: Autoproduct and out-of-band field plots. The measured bandwidth-averaged autoproducts are shown with red × 's. The theoretical autoproducts, calculated using the optimized values for the environmental parameters, are shown with the black solid curves. Theoretical out-of-band fields at the given difference or sum frequency, with modified (+1) reflection coefficient, are shown with the blue dotted curves. All ten panels have the same horizontal axes (depth from 0 to 400 mm) and vertical axes (normalized units from –4 to +4). The depth of the interference layer for each plot is given by the vertical dashed line, labeled as $h_{\Delta,\Sigma}$. The range and difference or sum frequency for each panel is indicated in the lower right corner, with ranges from 175 to 475mm, difference frequencies from 5 to 60kHz (of the possible 0 to 70kHz), and sum frequencies from 115 to 185kHz (of the possible 80 to 220kHz).

$$\chi_{\Delta}\left(\Delta\omega,\delta u\right)=\frac{1}{N_t}\frac{1}{N_r}\sum_{n=1}^{N_r}\sum_{m=1}^{N_t}\frac{1}{D}\int_{\delta z}^{D+\delta z}\left[\left\langle AP_{\Delta}\right\rangle_{nm}\left(z,\Delta\omega\right)\right]^{norm}\left[G_n^{*}\left(z,\Delta\omega,\delta u\right)\right]^{norm}dz$$

$$\chi_{\Sigma}\left(\Sigma\omega,\delta u\right)=\frac{1}{N_t}\frac{1}{N_r}\sum_{n=1}^{N_r}\sum_{m=1}^{N_t}\frac{1}{D}\int_{\delta z}^{D+\delta z}\left[\left\langle AP_{\Sigma}\right\rangle_{nm}\left(z,\Sigma\omega\right)\right]^{norm}\left[G_n^{*}\left(z,\Sigma\omega,\delta u\right)\right]^{norm}dz, \quad (6.9)$$

where $\langle AP_{\Delta,\Sigma}\rangle_{nm}$ is the measured bandwidth-averaged autoproduct at the n th range and m th trial, and G_n uses the modified (+1) surface reflection coefficient, unlike in (6.8a).

The black (central) curves in Fig. 6.5 show cross-correlations for the in-band field as a function of in-band frequency. The solid black curve is $Re\left[\chi_{IB}\right]$, and compares the in-band field measurements to the theoretical in-band fields. The average of this curve over the signal bandwidth is 0.980, as described in Sec. . The black dashed line represents the maximum possible cross-correlation, which for the in-band field is simply unity. The thin black dotted curve is $Re\left[\chi_{IB}\right]$ without optimization (i.e., δu = [0,0,0,0]), and provides a measure of the robustness (or sensitivity) to experimental uncertainties. The cross-correlation between the measured and theoretical data (solid black curve) exhibits a noticeable dip around 63kHz, dropping by approximately 0.03. This drop in cross-correlation is attributed to the directionalities of the broadcast and receiving transducers (see Sec. 6.3.2). The steady drop in the cross-correlation for the unoptimized in-band results with increasing frequency (decreasing wavelength) is understandable since the cross-correlation is sensitive to path-length variations whenever they are a nonnegligible fraction of the acoustic wavelength.

The blue (red) curves on the left (right) of Fig. 6.5 show the cross-correlations between the frequency-difference (-sum) autoproducts and the corresponding theoretical acoustic fields at the difference (sum) frequencies. The frequency-difference autoproduct is plotted from 0 to 70 kHz, the full difference-frequency bandwidth, and the frequency-sum autoproduct is plotted from 80 to 220 kHz, the full sum-frequency bandwidth. The solid curves show

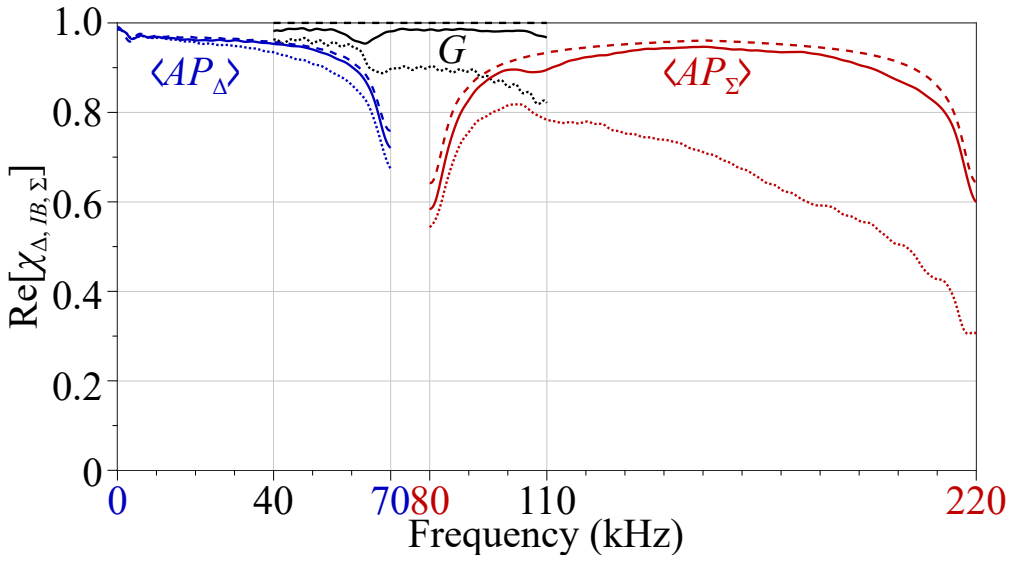

Figure 6.5: Cross-correlation vs. in-band or out-of-band frequency. Cross-correlations for the frequency-difference autoproduct, in-band field, and frequency-sum autoproduct are shown from left to right in blue, black, and red, respectively. The solid curves show the cross-correlation between measured fields and genuine acoustic fields. The dashed curves show the cross-correlation between theoretical fields and genuine acoustic fields, and serve as an upper bound for the solid curves. The dotted curves show the cross-correlation between measured fields and genuine acoustic fields using the unoptimized environmental parameters. The genuine acoustic fields use the unmodified (-1) surface reflection coefficient for the in-band fields and the modified $(+1)$ surface reflection coefficient for the out-of-band fields.

$Re\,[\chi_{\Delta,\Sigma}]$ from (6.9), and specify how well the measured autoproduct fields match their corresponding genuine out-of-band fields. The dashed curves show the cross-correlation between theoretical autoproduct fields and theoretical out-of-band fields, and are an upper bound for the performance of the measured data shown with the solid curves. The inability of the autoproducts to achieve the upper bound can again be linked to the transducers' directionalities. The drop in cross-correlation at high $\Delta\omega$ and at low and high $\Sigma\omega$ can be attributed to the larger thickness of the interference layer relative to the total size of the normalization region V, or to the insufficient signal bandwidth available for suppressing the cross terms via averaging, $\Omega_{BW}^{\Delta,\Sigma}$. Similarly, the highest cross-correlations occur at frequencies where $\Omega_{BW}^{\Delta,\Sigma}$ is a maximum and the interference layers are thinnest ($\Delta\omega = 0$ and $\Sigma\omega = 2\Omega_C$). Figure 6.5 shows that the real part of the cross-correlation between measured autoproduct fields and theoretical out-of-band fields exceeds 0.90 for difference frequencies between 0 and

60 kHz, and for sum frequencies between 110 and 190 kHz, which correspond to 86% and 58% of the difference- and sum-frequency bandwidths, respectively. Theory predicts these percentages to be 89% and 77%, respectively.

In Fig. 6.5, the blue (red) dotted curve shows the cross-correlation between measured frequency-difference (-sum) autoproduct fields and their corresponding theoretical out-of-band fields when the nominal experimental parameters without optimization are used. Thus, the sensitivity of the autoproducts to imperfect environmental parameters is easily seen. As expected for low frequencies, the blue dotted curve is not significantly lower than the results with optimized parameters (solid blue curve), implying that the frequency-difference autoproduct is robust to environmental uncertainties. The red dotted curve, however, falls well below the results with optimized parameters (red solid curve), showing the expected sensitivity to environmental uncertainties at high frequencies. This sensitivity motivated the in-band optimization described in Sec. . In both cases, the divergence between the results with optimized and unoptimized parameters generally grows with increasing difference or sum frequency. Again, this fact is consistent with fixed distance-and-sound-speed errors but increasing frequency. The imaginary parts of the cross-correlation χ were omitted from Fig. 6.5 for clarity and because they are typically small compared to the real parts. Furthermore, note that the horizontal axis only contains positive frequencies. Because the original, time-domain data is real, Fourier analysis guarantees negative frequency content as well, which is a complex conjugate away from the positive frequency content. Thus, the horizontal axis in Fig. 6.5 *could* be extended into the negative frequencies, however, due to the real-valued measurements and the associated Fourier analysis symmetry, the plot would simply be mirrored across the vertical axis.

6.5 Summary and Conclusions

The purpose of this study was to determine whether the theoretical claims made in prior work (Worthmann and Dowling, 2017) about the ability of autoproducts to mimic genuine out-of-band acoustic fields could be realized experimentally in a Lloyd's mirror environment. Measurements of a 40-to-110-kHz acoustic field in a laboratory water tank were used to calculate bandwidth-averaged autoproducts. After characterizing the source waveform and acoustic environment, these autoproducts were found to correlate very well with genuine out-of-band acoustic fields ($Re\left[\chi_{\Delta,\Sigma}\right] \geq 0.90$) for difference frequencies between 0 and 60 kHz, and for sum frequencies between 110 and 190 kHz. The correspondence of measured and theoretical fields was found to be excellent. The observed minor discrepancies likely arise from the (uncompensated) directionalities of the broadcast and receiving transducer pair.

This research effort supports the following three conclusions. First, frequency-difference and frequency-sum autoproduct fields constructed from acoustic-field measurements in a Lloyd's mirror environment can mimic out-of-band acoustic fields at the difference and sum frequencies in an equivalent environment with a modified surface reflection coefficient. This conclusion supports the unconventional claim made in prior work (Worthmann and Dowling, 2017) that acoustic fields with nonzero bandwidth may provide acoustic-field information at frequencies outside this bandwidth. This conclusion is drawn from Figs. 4 and 5, which show high spatial correlations between measured autoproducts and out-of-band fields for the same environment with the modified reflection coefficient. In addition, the theoretically predicted deviations between autoproducts and genuine acoustic fields within the near-surface interference layer were observed experimentally, providing further support for the predictions and limitations stated in prior work.

Second, the experimental effort needed to successfully measure the autoproducts does not

appear to exceed that of successfully measuring the in-band Green's function. Efforts in this study to characterize the source waveform and determine accurate environmental parameters using in-band analysis serve to directly improve in-band results, and indirectly improve autoproduct results. In other acoustic environments or experimental setups, additional or reduced efforts of this sort may be required. However, no experimental difficulties unique to measuring autoproducts have been uncovered by this study.

Third, the frequency-difference autoproduct is less sensitive to mild mismatch between the actual and measured distances and sound speed than the frequency-sum autoproduct. However, both display a general trend of increasing mismatch sensitivity with increasing difference or sum frequency. This sensitivity trend is consistent with the expectations for genuine sound fields at increasing acoustic frequencies, and thus supports the first conclusion as well.

CHAPTER 7

Autoproducts In and Near Acoustic Shadow Zones Created by Barriers

Abstract

Autoproducts are nonlinear mathematical constructs that may permit the effective shifting of acoustic fields with non-zero bandwidth to frequencies that are much lower or higher than the original bandwidth. The ability to move signal processing to different user-selectable frequency regimes has the potential to influence a variety of signal processing algorithms. Based on prior work, the limitations on the ability of autoproducts to mimic out-of-band fields are well understood when the in-band acoustic field is well-represented by ray acoustics. However, the focus in this chapter is regions where ray-path contributions are not an adequate field description, specifically the diffraction of sound behind barriers, where the acoustic shadow zone contains an acoustic field that a ray-based description cannot predict. Diffraction is expected to be a detriment to autoproduct techniques due to diffraction's sensitivity to frequency. To test this, two model environments with analytic solutions are considered: Sommerfeld's half-plane problem, also known as knife-edge diffraction, and the Mie scattering from a sphere. With a few exceptions in the deep shadow zone, it is found that in most regions of the acoustic fields, autoproducts experience only mild degradation in field-mimicry performance when compared to what the ray-based theory would predict

where it is valid.

7.1 Introduction

Recently, it has been shown that finite bandwidth acoustic fields can produce, through nonlinear mathematical constructs termed *autoproducts*, new fields which *may* mimic acoustic fields at frequencies much lower or much higher than the original field's bandwidth, referred to herein as out-of-band fields (Worthmann and Dowling 2017). Being able to shift signal processing of certain data to frequency regimes outside of which they were recorded has the potential to dramatically improve the flexibility of signal processing algorithms. Improvements have already been observed in blind deconvolution (Abadi *et al.* 2012), direction of arrival finding (Douglass *et al.* 2018), source localization (Worthmann *et al.* 2015; Worthmann *et al.* 2017), target localization (Worthmann and Dowling 2016) and improved spatial resolution of passive cavitation imaging (Abadi *et al.* 2018). This frequency-shifting possibility has been studied within theory, simulation, and experiment for simple acoustic environments where the ray approximation is applicable (Worthmann and Dowling 2017; Lipa *et al.* 2018). Within the ray approximation, the limitations governing the ability of frequency-sum and frequency-difference autoproducts to shift frequencies up and down, respectively, are well understood. Specifically, two requirements are necessary for autoproducts to mimic out-of-band acoustic fields: (i) ray amplitudes should spatially vary slowly as compared to the wavelength, and (ii) the difference in acoustic travel times along the rays should be much larger than the inverse of the bandwidth available for averaging. However, in regions of the acoustic field where the ray approximation is no longer valid, the ability of the autoproducts to mimic out-of-band fields is unknown.

While the ray approximation is suitable for a variety of acoustic domains, it does not capture all the physics inherent in the wave equation. Diffraction, in particular, is not captured by

ray acoustics, and is typically strongly frequency dependent. This frequency dependence of diffraction is expected to be detrimental for the autoproduct formulation, which relies on a acoustic fields having a particular kind of frequency-dependence, which may or may not align with the effects of diffraction. An open question, however, is just *how* detrimental the effects of diffraction are on autoproducts.

In this chapter, the diffraction considered is that which occurs behind opaque barriers. Depending on the geometry, ray acoustics could predict the acoustic field in spatial regions reached by one or more rays these are defined here to be the well-ensonified region of the acoustic field. There may also exist regions of the acoustic field where no rays are predicted, defined here to be the acoustic shadow zones, where the ray approximation falsely specifies the acoustic field to be identically zero. However, diffraction from well-ensonified regions fills the acoustic shadow zone behind the barrier with a non-zero amount of sound. The central aim of this paper is to study the effects that diffraction behind barriers has on the ability of autoproducts to mimic out-of-band fields, and to link this to the potential performance of autoproduct-based signal processing schemes, such as source localization.

Accurately simulating diffraction can be difficult in arbitrary environments, and numerical schemes all have trade-offs in terms of accuracy and speed. In this paper, instead of focusing on numerical solutions to diffraction, simple geometries are chosen where analytic solutions exist. Analytic solutions guarantee that the wave equation, along with the specific boundary conditions and source terms, are solved and matched exactly. Use of such solutions is advantageous for accuracy, and also for significantly reducing the necessary computational resources compared to some numerical schemes, such as FEM (Jensen 2011). An added benefit is that simple environments are easier to understand and analyze, as regions can be easily characterized as having multiple, one, or no rays present.

The two environments chosen for this study are (i) the Sommerfeld half-plane problem, also known as knife edge diffraction (Skudrzyk 1971), and (ii) the Mie scattering solution for

scattering from a sphere (Pierce 1981). In both environments, the incident field is chosen to be a plane wave, though analytic solutions for point source illumination exists for both problems (Skudrzyk 1971). The first problem is fundamentally two dimensional, while the second is fundamentally 3D, though axisymmetry permits two dimensional plots without a loss of generality. In both problems, regions exist where ray acoustics is an adequate description of the field, and other regions, particularly behind the barrier, where no rays exist, and a ray-path sum is an inadequate field description.

This chapter is organized as follows. Section 7.2 describes autoproduct definitions, normalizations, and other important details. Section 7.3 describes the Sommerfeld half-plane problem, its solution, and a side-by-side comparison of autoproducts and out-of-band fields. Section 7.4 analogously describes the Mie scattering problem, its solution, and side-by-side comparisons of autoproducts and out-of-band fields. Section 7.5 summarizes the result of this research, and presents the conclusions that can be drawn from it.

7.2 Autoproduct Definitions

For an acoustic field $P(\boldsymbol{r}, \omega)$, where $\boldsymbol{r}$ is the spatial coordinate and ω is the frequency, in radians, then the frequency difference and frequency sum autoproducts, AP_Δ and AP_Σ, respectively are defined as:

$$AP_\Delta(\boldsymbol{r}, \omega, \Delta\omega) \equiv P(\boldsymbol{r}, \omega_+) P^*(\boldsymbol{r}, \omega_-) \leftrightarrow P(\boldsymbol{r}, \Delta\omega) \tag{7.1}$$

$$AP_\Sigma(\boldsymbol{r}, \omega, \Delta\omega) \equiv P(\boldsymbol{r}, \omega_+) P(\boldsymbol{r}, \omega_-) \leftrightarrow P(\boldsymbol{r}, \Sigma\omega) \tag{7.2}$$

where $\omega_\pm = \omega \pm \frac{\Delta\omega}{2}$, and $\Sigma\omega = 2\omega$. The right-most equations in (7.1) and (7.2) indicate

what out-of-band acoustic field the autoproducts are meant to mimic, where the $\leftrightarrow$ symbol here refers to mimic' (mathematically defined later in this section).

In this chapter, the source waveform is assumed to be known, and is further assumed to be impulsive; in other words, $P(\boldsymbol{r},\omega)$ is assumed to be identical to $G(\boldsymbol{r},\omega)$, which is the Green's function (or impulse response) for the given environment. When the in-band field $P(\boldsymbol{r},\omega)$ contains a certain bandwidth, suppose $\Omega_L \leq \omega \leq \Omega_H$, then bandwidth averaged autoproducts may be defined. This bandwidth averaging has been shown to be advantageous for autoproducts in multipath environments (Worthmann and Dowling, 2017), and may also be useful for regions with significant diffraction. All pairs of frequencies within the allowed bandwidth that have the specified difference (or sum) are averaged in the bandwidth-averaged frequency-difference (or frequency-sum) autoproducts:

$$\langle AP_{\Delta}\rangle(\boldsymbol{r},\Delta\omega) = \frac{1}{\Omega_H-\Omega_L-\Delta\omega}\int_{\Omega_L+\frac{\Delta\omega}{2}}^{\Omega_H-\frac{\Delta\omega}{2}} AP_{\Delta}(\boldsymbol{r},\omega,\Delta\omega)\,d\omega \tag{7.3}$$

$$\langle AP_{\Sigma}\rangle(\boldsymbol{r},\Sigma\omega) = \frac{1}{\Omega_H-\Omega_L}\int_{0}^{\Omega_H-\Omega_L} AP_{\Sigma}(\boldsymbol{r},\omega,\Delta\omega)\,d\Delta\omega \tag{7.4}$$

In general, $\Omega_H-\Omega_L$ in (7.4) should be replaced with $min(2\Omega_H-\Sigma\omega, \Sigma\omega-2\Omega_L)$, however, in this chapter, $\Sigma\omega$ is always chosen to be $\frac{(\Omega_H+\Omega_L)}{2}$.

To compare autoproduct fields with out-of-band fields, a normalization procedure must be specified. This is because autoproducts are fundamentally quadratic quantities, and as a result, have different units than genuine acoustic fields at out-of-band frequencies. A general procedure for normalizing requires the definition of a normalization region; this could be a collection of points (strictly greater than one point), or a line, area, or volume. Collectively, these possibilities will all be called V. Any field, as denoted by [ ] can be normalized through the equation:

$$[\ \ ]^{norm} = [\ \ ] \left(\frac{1}{V} \int_V |[\ \ ]|^2 dV \right)^{-\frac{1}{2}} \tag{7.5}$$

It was stated previously that autoproduct fields can mimic out-of-band acoustic fields. At this point, we have the necessary definitions to quantify what is meant by *mimic*. In this paper, we define *mimic* to mean a high cross correlation between normalized bandwidth-averaged autoproduct fields and normalized out-of-band acoustic fields, or in other words:

$$\chi_\Delta(\Delta\omega) = \frac{1}{V} \int_V \left[\langle AP_\Delta \rangle (\boldsymbol{r}, \Delta\omega)\right]^{norm} \left[P^*(\boldsymbol{r}, \Delta\omega)\right]^{norm} dV \tag{7.6}$$

$$\chi_\Sigma(\Sigma\omega) = \frac{1}{V} \int_V \left[\langle AP_\Sigma \rangle (\boldsymbol{r}, \Sigma\omega)\right]^{norm} \left[P^*(\boldsymbol{r}, \Sigma\omega)\right]^{norm} dV \tag{7.7}$$

These cross correlations are in general complex, and thanks to the normalizations, necessarily lie somewhere within the complex unit circle. A perfect match would produce a $\chi_{\Delta,\Sigma}$ of exactly 1. A less perfect match where the autoproduct and the out-of-band acoustic field differed by an overall phase factor of, for example ϕ, would have a cross correlation of $\chi_{\Delta,\Sigma} = \exp(i\phi)$. An even less perfect match, such as between two mutually incoherent noise sources, would produce $\chi_{\Delta,\Sigma} \approx 0$.

In source localization algorithms, such as beamforming (Jensen 2011) or matched field processing (Bucker 1976), the weighted output of the beamformer or ambiguity surface is related to the magnitude-squared of the quantities in (7.6) and (7.7). Thus, for source localization purposes, only $|\chi_{\Delta,\Sigma}|^2$ matters, implying that in regions where autoproducts differ by an overall phase factor from their genuine out-of-band equivalents, then this may produce an imperfect (non-unity) $\chi_{\Delta,\Sigma}$, but as long as $|\chi_{\Delta,\Sigma}|^2$ is near-unity, then beamforming and matched field processing algorithms can still succeed. Throughout this chapter, both magnitude and phase information for $\chi_{\Delta,\Sigma}$ is reported for completeness, though it is noted here

that only the magnitude of $\chi_{\Delta,\Sigma}$ is important, in principle, for source localization.

In the preceding paragraphs, the discussion assumed some known normalization region. For the two environments under consideration here, choosing a normalization region with polar symmetry makes the most sense. Here, the normalization region V is chosen to be a 2D concentric circular sector, or in other words, $V \in [r_1, r_2] \times [\theta_1, \theta_2]$, where $dV = rdrd\theta$. The entire domain is divided into many normalization regions, which respect to the symmetry of each problem, holding each region at constant area with an aspect ratio (arclength vs difference in radius) kept as close to unity as possible. The length scale of the normalization region should be at least $\lambda_{\Delta,\Sigma}$ (the wavelength at the out-of-band difference or sum frequency). Normalization regions smaller than $\lambda_{\Delta,\Sigma}$ don't sample the fields wide enough to observe phase variations (which can artificially inflate cross correlations). On the other hand, normalization regions that are too large don't help discriminate between different regions of the various fields. For the study here, the chosen length scale is $\lambda_{\Delta,\Sigma}$.

To calculate the bounds on each normalization region, the innermost circle (radius of 0 for the Sommerfeld half-plane problem, radius of a for the Mie scattering problem) is divided into an integer number of θ subsets such that the inner arclength of each sector is as close as possible to $\lambda_{\Delta,\Sigma}$, while guaranteeing that the integer is a non-zero multiple of 4 or 2 (for the Sommerfeld half-plane problem and the Mie scattering problem, respectively this guarantees the normalization regions respect the symmetry of each problem). Then, the outer radius is found by forcing the total area to be $2\lambda^2_{\Delta,\Sigma}$ (where the factor of 2 is an arbitrary choice). After this ring of normalization regions is specified, the procedure is then repeated serially, with the previous outer radius now being the new inner radius dimension. The iterative procedures ends once the outer radius exceeds the domain of interest. This polar grid is reminiscent of the equal-area grid definition procedures discussed here (Beckers and Becker 2012).

As discussed in prior work (Worthmann and Dowling, 2017), the out-of-band acoustic fields

that autoproducts mimic may not satisfy the same boundary conditions as the in-band fields. Specifically, a pressure-release boundary condition for the in-band field creates an autoproduct field which mimics an out-of-band field which contains a rigid boundary condition instead. The reasons for this are motivated by the ray-based explanation that the frequency-difference and frequency-sum autoproducts have effective reflection coefficients at boundaries of $|R|^2$ and R^2, respectively, where R is the in-band reflection coefficient. Thus, a pressure-release boundary, in which $R = -1$, has an effective reflection coefficient of $|R|^2 = R^2 = +1$, corresponding to a rigid boundary condition. Thus, the out-of-band fields described here will have rigid boundaries, regardless of the in-band boundary condition.

In multi-path environments, autoproducts can create undesired cross-terms, which with bandwidth averaging, may be suppressed. However, there are some regions where there is not enough bandwidth to be able to suppress these cross terms. These regions, known as interference layers' (Worthmann and Dowling, 2017) are typically near reflecting boundaries, and the autoproduct fields in these regions are unlikely to correlate well with a genuine out-of-band field due to these cross-terms. From a ray-based formulation of a two-path environment (Lipa *et al.* 2018), it is found that the interference layer exists when the following inequality holds:

$$(\Omega_H - \Omega_L - \Delta\omega)\left(\tau_2\left(\boldsymbol{r}\right) - \tau_1\left(\boldsymbol{r}\right)\right) \leq 2\pi, \tag{7.8}$$

where τ_1 and τ_2 are the time-of-arrivals for the two paths as measured at the spatial coordinate $\boldsymbol{r}$. The Sommerfeld half-plane problem and the Mie scattering problem both feature regions where a ray-based description of the acoustic field lead to a two-path environment, and so this interference layer terminology will be useful in some of the analyses given Sections 7.3 and 7.4.

One final autoproduct behavior that is well understood is the discrepancies that arise due to

spherical spreading. More specifically, a point source in free space has an amplitude which decays as $1/r$. However, an autoproduct based on this environment sees an amplitude which decays as $1/r^2$. The size of the normalization region, as compared to the distance between the normalization region and the source, dictates how much of an effect this has discrepancy has. In other words, normalization handles the absolute amplitude discrepancies easily; however, the relative amplitude variations associated with the differences between $1/r$ and $1/r^2$ across the normalization region can lead to imperfect cross correlations. However, it is found that $\chi_{\Delta,\Sigma}$, as defined in (7.6) and (7.7), is much more sensitive to different phase variations than different amplitude variations. As a result, this $1/r$ vs $1/r^2$ discrepancy typically leads to only mild degradation in $\chi_{\Delta,\Sigma}$, typically less than a few percent for most regions.

The next section details the Sommerfeld half-plane problem, and provides comparisons of autoproduct fields to out-of-band acoustic fields.

7.3 Sommerfeld Half-Plane Problem

Originally developed in 1896, (Sommerfeld 1896) the Sommerfeld half-plane problem, also known as knife-edge diffraction, presents an ideal model for looking at the effects of diffraction around a barrier. A unity-amplitude plane wave is incident from the left on a perpendicular semi-infinite rigid barrier of negligible thickness. Figure 7.1 shows the geometry of the problem, where the domain of interest is taken to be a circle around the tip of the barrier of radius R. Fig. 7.1 also shows the normalization regions chosen for this environment.

Mathematically, the solution to this problem is given by

$$P(r,\theta) = e^{ikx} f\left(+2\sqrt{\frac{kr}{\pi}}\sin\left(\frac{\theta}{2}\right)\right) + e^{-ikx} f\left(-2\sqrt{\frac{kr}{\pi}}\cos\left(\frac{\theta}{2}\right)\right), \tag{7.9}$$

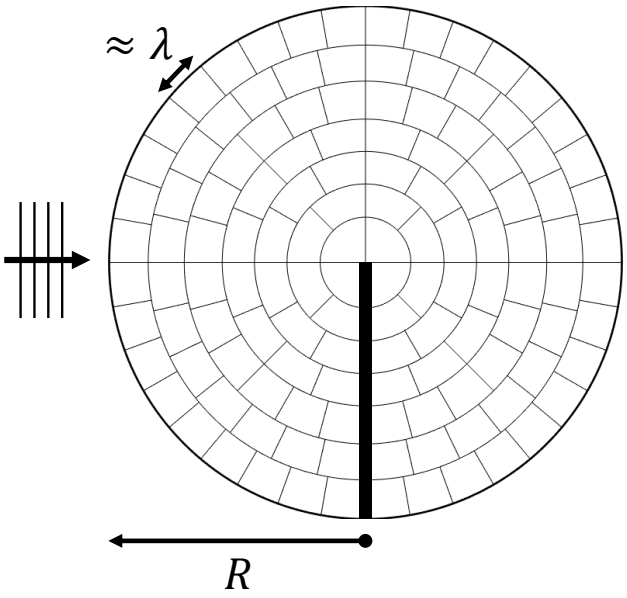

Figure 7.1: Schematic for the Sommerfeld half-plane problem, showing a plane wave incident from the left onto a rigid barrier of negligible thickness at the origin. The circular domain of interest, of radius R, is subdivided into smaller normalization regions that are roughly one wavelength squared in area, where $kR = 40$ for the grid shown here.

where $x = r\cos\theta$ is the horizontal coordinate, k is the wavenumber, r is the radial distance from the origin (also the barrier tip), θ is the angle from the horizontal axis, and $f(z)$ is a function governing the amplitude of these two waves, as defined here:

$$f(z) = \frac{1}{2} + \frac{1-i}{2}\text{FresnelC}(z) + \frac{1+i}{2}\text{FresnelS}(z). \tag{7.10}$$

The Fresnel cosine and sine integrals are defined as $\text{FresnelC}(z) = \int_0^z \cos\left(\frac{\pi u^2}{2}\right) du$ and $\text{FresnelS}(z) = \int_0^z \sin\left(\frac{\pi u^2}{2}\right) du$, respectively (Abramowitz and Stegun 1965). See dlmf.nist.gov/7.3.3 for plots of these functions. Crucially, in (7.9), θ must be defined to vary from $-\frac{\pi}{2}$ to $+\frac{3\pi}{2}$ to (in other words, with the branch cut located on top of the barrier) such that the discontinuity across the barrier can be accommodated. Furthermore, in the limit of high frequency (i.e. the ray approximation), $f(z) \to H(z)$, where H is the unit step function.

Additionally, more general forms of the Sommerfeld half-plane problem exist, including ones with arbitrary plane wave arrival angle as well as arbitrarily-located point sources (Skudrzyk 1971). However, these additional parameters introduce many additional degrees of freedom, which for simplicity, are neglected here.

An interesting property of the Sommerfeld half-plane problem is its length scale dependence. Notably, all spatial variables in (7.9) enter through kr, meaning that higher frequency fields can be replicated by keeping frequency constant and zooming out spatially. This kr-scaling suggests that instead of using physical dimensions, all the length scales can be non-dimensionalized by the wavelength. Since there are multiple wavelengths in this problem, care will be taken to refer to the appropriate wavelength. For clarity however, physical dimensions will be reported as well.

In Figure 7.2, the magnitude (a) and phase (b) for $kR = 40$ is provided, as well as magnitude (c) and phase (d) for $kR = 400$. The magnitude color scale is logarithmic, spanning 20 to +10 dB, and the phase color scale is linear, ranging through $\pm\pi$ radians. In physical dimensions, these plots correspond to 1 kHz and 10 kHz, for a domain radius of 10 meters and speed of sound of $\frac{\pi}{2}1000 \approx 1587 m/s$.

The following discussion focuses primarily on the frequency-difference autoproduct: the frequency-sum autoproduct has qualitatively similar results, and thus is omitted here. The plan is to use acoustic information between the frequencies 9 kHz and 11 kHz (in-band wavenumbers of $360 \leq k_{IB}R \leq 440$) to create an autoproduct field which is intended to mimic an out-of-band field at 1 kHz (difference-frequency wavenumber of $k_\Delta R = 40$). In other words, the autoproduct field will attempt to shift from a center frequency of 10 kHz ($k_c R = 400$) to a difference-frequency of 1 kHz ($k_\Delta R = 40$) using 1 kHz of bandwidth ($k_{BW}^\Delta R = 40$) for averaging. The frequency-difference autoproduct created under these conditions is provided in Figure 7.3. Fig. 7.3a and 3b show the autoproduct magnitude and phase, respectively. The magnitude color scale is logarithmic, and spans 40 dB to +20dB,

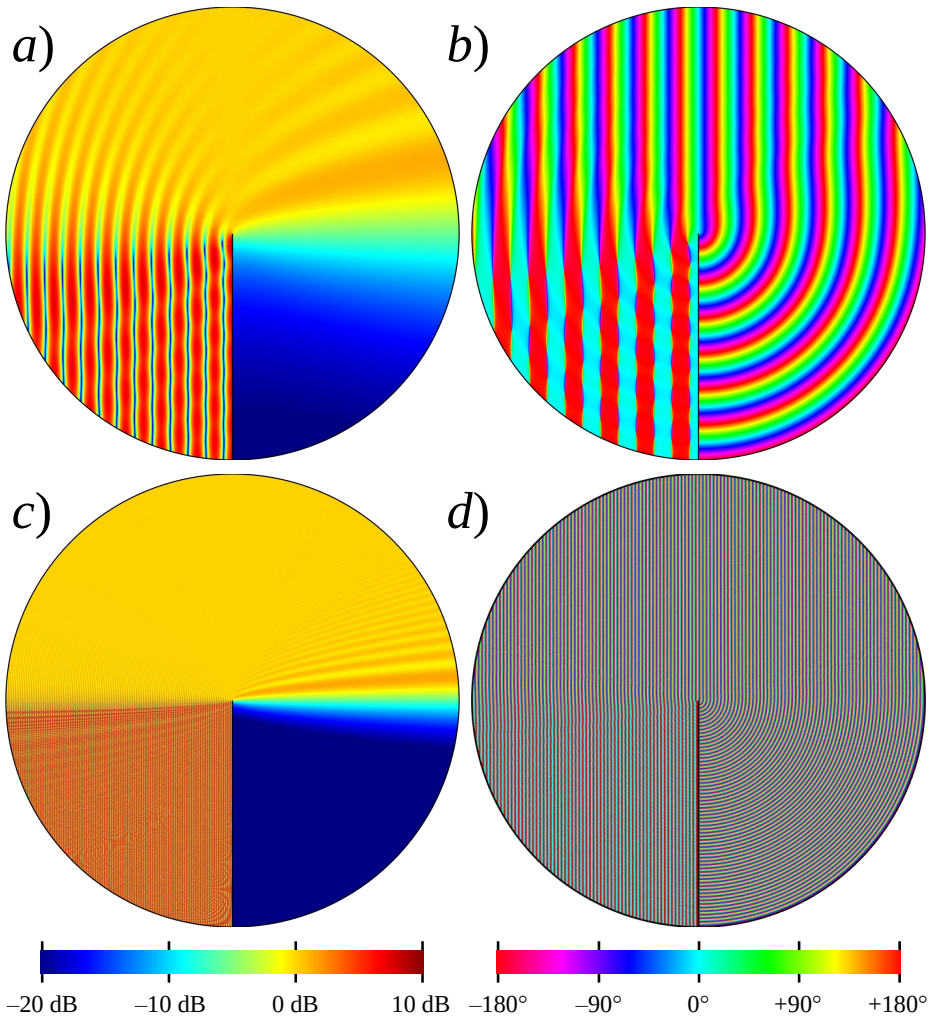

Figure 7.2: Acoustic field plots for the Sommerfeld half-plane problem for $kR = 40$ (magnitude and phase in panels a and b, respectively), and for $kR = 400$ (magnitude and phase in panels c and d, respectively).

or double the span of the color scale in Figs. 7.2a and 7.2c. The phase color scale in Fig. 7.3b remains the same as in Figs. 7.2b and 7.2d. There exist many qualitative similarities between the autoproduct in Figs. 7.3a and 7.3b, as compared to the out-of-band field in Fig. 7.2a and 7.2b.

To quantitively compare the autoproducts in Fig. 7.3 with the out-of-band field in Figs. 7.2a and 7.2b, the cross-correlation metric, defined in Section 7.2, is used. A plot of the magnitude and phase of χ_Δ is shown in Figure 7.4a and 7.4b, respectively. The magnitude is

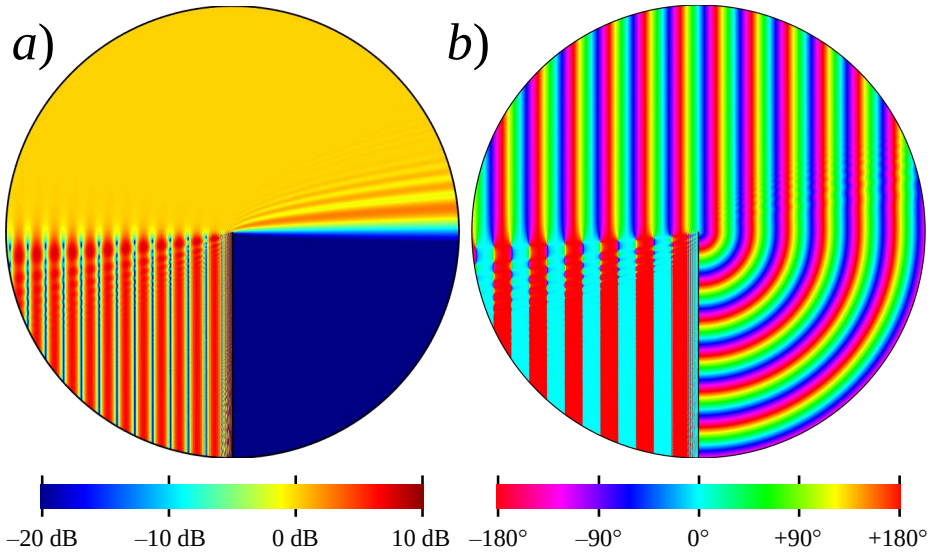

Figure 7.3: Frequency-difference autoproduct field plots for the Sommerfeld half-plane problem, with magnitude and phase in panels a and b, respectively. The plots shown are for parameters $k_c R = 400$, $k_\Delta = 40$, and $k_{BW}^{\Delta} R = 40$.

shown on a logarithmic scale, spanning from 0 to 0.999, where $|\chi_\Delta|$ near 0 is poor, and $|\chi_\Delta|$ of 1 is perfect. The phase is shown on a linear scale, spanning $\pm$ 60° . This plot provides many interesting results.

First, the magnitude of the cross-correlation is greater than 0.9 (red) over almost all the normalization regions chosen (only 8 of the 128 regions are below 0.9, the lowest of which is 0.73). Broadly speaking, this cross-correlation magnitude plot suggests four sources of discrepancies between the autoproduct field and the out-of-band field those due to (i) interference layers, (ii) acoustic field nulls, (iii) spreading losses, and (iv) diffraction-related amplitude variations.

The interference layer on the negative-x side of the rigid boundary in Fig. 7.3a) is a region where the path length time differences are very close, meaning insufficient bandwidth exists to average away cross-terms that arise. Thus, normalization windows that overlap with this interference layer are expected to have poorer cross correlations.

In the standing wave region, there are approximately vertical lines where there are acoustic

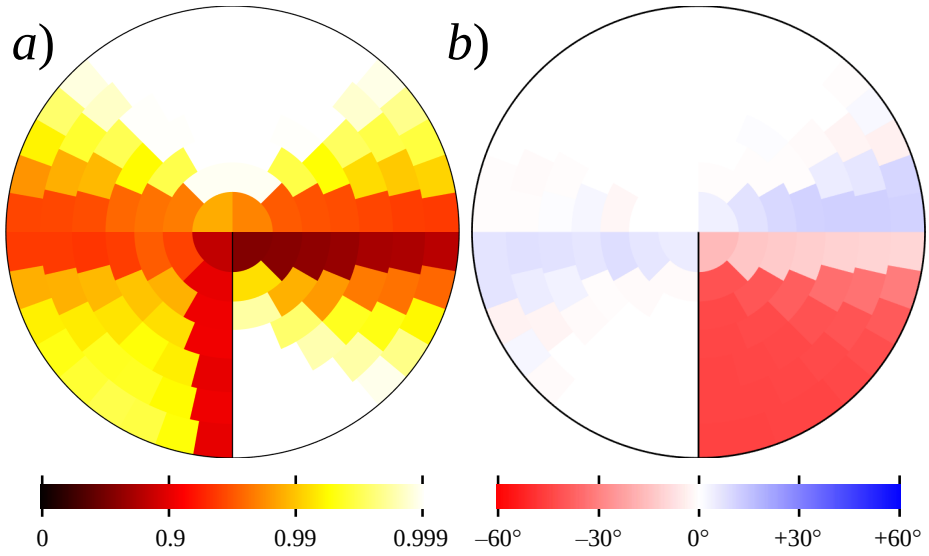

Figure 7.4: Cross correlations between the frequency-difference autoproduct ($k_c R = 400$, $k_\Delta R = 40$, $k_{BW}^{\Delta} = 40$) and an out-of-band acoustic field at $kR = 40$. Panel a) shows the magnitude of χ_Δ on a logarithmic color scale, and panel b) shows the phase of χ_Δ.

nulls (in other words, destructive interference). The cross terms outside of the interference layer are small compared to the standing wave amplitude, but specifically near the field null, the cross terms can become a larger fraction of the overall field (though still small overall). The choice to keep normalization regions at an area of at least λ_Δ^2 was done to mitigate this effect, since having poor cross correlations near a standing-wave null seems artificial and not representative of the larger trend in the standing wave region.

Another effect is the spreading losses of the scattered wave. The form of the scattered field can be thought of as a cylindrical wave originating at the tip of the barrier, modulated by some angular amplitude dependence. While the scattered field is not *precisely* a cylindrical wave, it is fair to describe it as such approximately. A cylindrical wave, as required by energy conservation, spreads as $1/\sqrt{r}$. However, the autoproduct field has a scattered field that varies as $1/r$ as a consequence of the quadratic nonlinearity. The relative variation between $1/\sqrt{r}$ and $1/r$ over the normalization region is another source of discrepancies, and is the primary source of discrepancies in the shadow zone region.

The final discrepancy suggested by the cross-correlation's magnitude is related to this cylindrical wave as well, but instead of its spreading loss, this effect relates to its phase, or more specifically its interference with the single path region in the upper half of the domain. There exist constructive interference peaks in a roughly parabolic shape to the left and to the right of the barrier tip, and these are frequency-dependent. To analyze their origin, consider a related problem of a cylindrical wave and a plane wave: $\exp(ikx) + exp(ikr)$. These fields experience constructive interference whenever $k(\boldsymbol{r} - |x|)$ is some multiple of 2π. The lowest order peak (lying off the $y = 0$ axis) occurs when $k(\boldsymbol{r} - |x|) = 2\pi$, which in cartesian coordinates occurs when $y = \pm\lambda\sqrt{1 + 2|x|/\lambda}$, which can be approximated, for horizontal coordinates many wavelengths away from the tip, as $y \approx \sqrt{2\lambda|x|}$. Thus, the location where this parabola of increased amplitude lies is a function of frequency. Therefore, when downshifting from 10 kHz ($k_c R = 400$) down to 1 kHz ($k_\Delta R = 40$), the autoproducts retain the same peak location as the in-band field, and are unable to capture the shifted peak that would occur for a genuine 1 kHz out-of-band field. These effects occur in all but the shadow zone quadrant, where there is only the cylindrical wave present.

Finally, Fig. 7.4b), the cross-correlation phase, provides one more interesting result. In the three regions containing at least one ray path, the phase discrepancies are quite minimal, generally within $\pm$ 10° . However, in the fourth quadrant, an interesting phenomenon occurs. In the acoustic shadow zone, the acoustic field appears to pick up a phase shift, relative to an unshifted cylindrical wave of $\exp(ikr)/\sqrt{kr}$. It can be shown mathematically that as θ approaches $-\frac{\pi}{2}$ from above, the in-band acoustic field behind the barrier asymptotically approaches $(1+i)e^{ikr}/(\sqrt{2\pi kr})$ for large kr. This clearly illustrates an additional 45° phase shift relative to an unshifted cylindrical wave. A frequency-difference autoproduct field, on the other hand, loses this phase shift due to the complex conjugate in $P(\omega_+)P^*(\omega_-)$, the definition of AP_Δ. Thus, when evaluating χ_Δ, which places the complex conjugate on the out-of-band field $P(\Delta\omega)$, there arises an overall phase shift of 45° , which is borne out by the color plot in Fig. 7.4b), where the majority of the acoustic shadow zone carries

this 45° phase mismatch. The reader is reminder however, that this phase mismatch does not influence source localization performance, since it would simply appear as if the source waveform contained an additional 45° phase across all frequencies. Additionally, with respect to localization, it is important to realize that the vast majority of the fourth quadrant is very quiet, especially at high frequency. In this simulation, that doesn't pose a problem, thanks to the high signal-to-noise ratio limited only by computational precision. However, in realistic experimental conditions, measurements in this quadrant would be plagued with noise, and therefore robust localization would be challenging with or without autoproduct techniques.

The frequency-sum autoproduct carries many of the same features as its frequency-difference analogue. In this case, the center frequency 10 kHz ($k_c R = 400$) is shifted up to the out-of-band frequency 20 kHz ($k_\Sigma R = 800$), using 1 kHz of bandwidth averaging ($k_{BW}^\Sigma R = 40$). Compared to the frequency difference plots at 1 kHz ($k_\Delta R = 40$), these much higher frequencies (in-band: 9.5 to 10.5 kHz, or $380 \leq kR \leq 420$; out-of-band: 20 kHz, or $k_\Sigma R = 800$) the individual phase and magnitude plots have significantly more fine-scale structure, which can be hard to resolve visually in a small plot. The cross-correlation plots, on the other hand, are more easily resolved. Additionally, by keeping the normalization regions at a constant area of $2\lambda_\Sigma^2$, the normalization regions are much smaller, and thus finer scale structure can be seen from these plots.

Figure 7.5a) and 5b), which show the magnitude and phase of χ_Σ, respectively. All of the same discrepancies described for AP_Δ also apply to AP_Σ, though thanks to the smaller normalization regions, the interference layer and standing wave null regions have poorer cross-correlations than χ_Δ, and the regions affected primarily by spreading losses and diffraction-related amplitude variations have improved cross-correlations over χ_Δ. The most notable feature is that in Fig. 7.5b), the phase shift in the shadow zone quadrant is found to be +45° , which is because the frequency-sum autoproduct asymptotically approaches a cylindrical

wave with a +90° phase shift (due to the *lack* of a complex conjugate in the $P(\omega_+)\,P(\omega_-)$ definition).

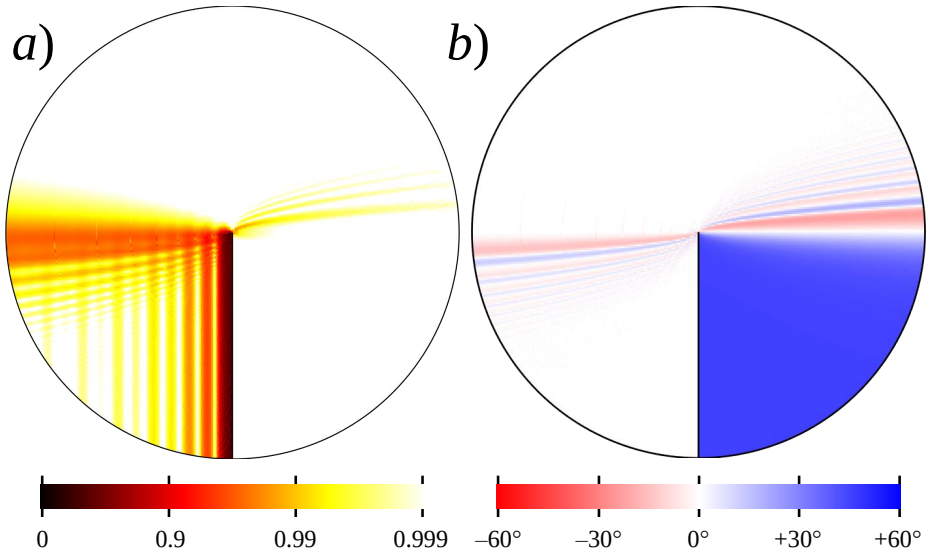

Figure 7.5: Cross correlations between the frequency-sum autoproduct ($k_cR = 400$, $k_\Sigma R = 800$, $k_{BW}^{\Sigma} = 40$) and an out-of-band acoustic field at $kR = 800$. Panel a shows the magnitude of χ_Σ on a logarithmic color scale, and panel b shows the phase of χ_Σ.

Overall, autoproduct fields and out-of-band fields in well-ensonified regions (regions with at least one ray path) of the Sommerfeld half-plane solution generally have strong (¿0.9) cross-correlations. In these regions, the primary cause of discrepancies comes from amplitude variations, not phase variations. In the shadow zone quadrant, strong cross-correlation magnitudes persist, though an overall phase shift of approximately $\pm$ 45° appears for reasons that are well-understood mathematically.

7.4 Mie Scattering from a Sphere

An alternative geometry with significant shadowing is that of Mie scattering from a sphere. The solution to this problem is also well-known (Pierce 1981, Morse and Feshbach 1953)and involves the summation of spherical Bessel functions. In general, a penetrable sphere with homogenous density and sound speed can be specified. However, for the sake of simplicity,

two extremes are taken: the hard (rigid) sphere, and the soft (pressure-release) sphere. When a plane wave with unity amplitude and wavenumber k is incident upon these spheres of radius a from the left, the solution as a function of r and θ is given by:

$$P(r,\theta) = e^{ikx} + \sum_{n=0}^{N} A_n h_n(kr) P_n(\cos\theta) \tag{7.11}$$

where the first term is the incident plane wave, with the horizontal coordinate x equal to $r\cos\theta$, h_n is the nth order spherical Hankel function, P_n is the nth order Legendre polynomial, and the coefficient A_n varies for the type of boundary condition on the sphere, as shown below:

$$A_n^{\text{Hard}} = -i^n (2n+1) \frac{j_n(ka)}{h_n(ka)} \tag{7.12}$$

$$A_n^{\text{Soft}} = -i^n (2n+1) \frac{j_n'(ka)}{h_n'(ka)}. \tag{7.13}$$

Here, primes indicate derivatives, and j_n is the nth order spherical Bessel function. The number of terms, N, to use in (7.11) should be infinite mathematically, but practically must be truncated. Numerically, it was found to be sufficient to use $N = 2ka + 10$. However, for very large ka, this was slightly less than double what is practically necessary, so for efficiency, terms in the series whose coefficient A_n has a magnitude-squared of more than 200 dB below unity were neglected. Even this cutoff may be unnecessarily conservative, but for the parameters used in this study, the calculation of these terms was found to be sufficiently fast on a modern computer.

It is worth noting here that in addition to spheres of a specified density and sound speed, other analytic solutions exist, particularly for other shapes such as a cylinder, or prolate/oblate

spheroid (Pierce 1981). Solutions also exist for a point source excitation instead of a plane wave excitation. Furthermore, solutions for the diffraction of sound through a circular or rectangular aperture, as well as a diffraction past a circular or rectangular screen also exist, though these solutions are typically not exact, and apply only in the Fresnel or Kirchhoff approximations (Primakoff 1947, Lucke 2006), which don't capture some of the physics desired, such as reflections/backscatter. For simplicity, only the hard and soft spheres are considered here, though the qualitative results provided by the hard/soft sphere shown here are expected to apply to these more complicated geometries as well.

This spherical geometry provides a convenient counterpart to the Sommerfeld half-plane problem: this problem is axisymmetric 3D whereas the prior problem was 2D; this scattered field can be thought of as originating from an angular-dependent source distributed over the sphere's surface, whereas in the prior problem, the scattered field could be thought of as originating from an angular-dependent line source coincident with the barrier tip. Furthermore, this problem has a plane wave filling in the shadow zone from both sides, whereas in the prior problem, the plane wave encroached on the shadow zone from only one side.

Unlike in the Sommerfeld half-plane problem, a second length scale enters this problem, which means there are now two dimensionless parameters needed: kr and ka. As before, the physical dimensions of the problem will be reported for clarity, in addition to the dimensionless (wavenumber-scaled) variables.

Figure 7.6 shows the schematic for this problem, as well as the normalization regions as defined by the procedure in Section 7.2. Throughout this section, R, the outer radius of the domain of interest, will be kept at a constant $10a$, where a is fixed at 1 meter and the sound speed is fixed at $\frac{\pi}{2}1000\frac{m}{s} \approx 1587\frac{m}{s}$. Thanks to the vertical symmetry of this problem, both hard and soft sphere results can be reported on the same plot: the upper half provides hard sphere results, and the lower half provides soft sphere results.

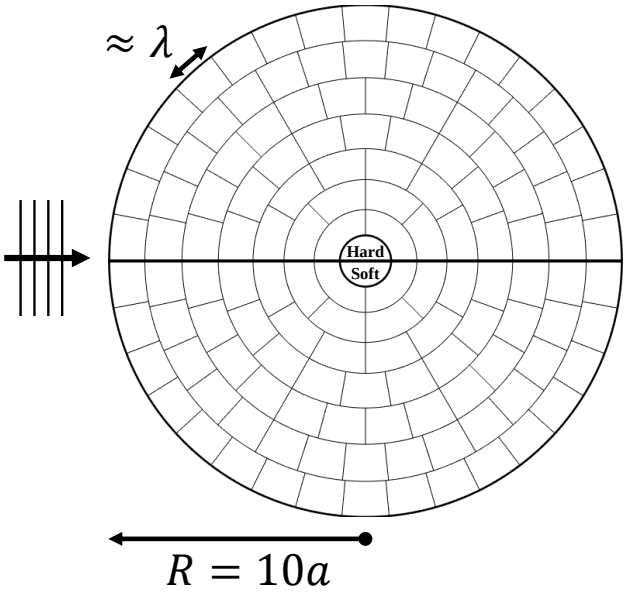

Figure 7.6: Schematic for Mie scattering from a sphere, showing a plane wave incident from the left onto a hard (soft) sphere as shown in the upper (lower) half of the plot. The circular domain of interest has radius R, which is 10 times the radius of the sphere a, and is subdivided into smaller normalization regions that are roughly one wavelength-squared in area, where $kR = 40$ and $ka = 4$ for the grid shown here.

Figure 7.7a) and 7.7b) show the magnitude and phase, respectively, of the acoustic field for a frequency of 1 kHz ($kR = 40; ka = 4$); Figs. 7.7c and 7.7d show the results for a frequency of 10 kHz ($kR = 400; ka = 40$).

There are a few interesting features worth pointing in these solutions. Perhaps the most interesting is to point out the field amplitude peak that occurs directly behind the sphere, which is particularly evident for the upper half of the plot in Fig. 7.7c), near $\theta = 0$. This is the acoustic equivalent of the well-known Arago-Poisson spot from optics (Fresnel 1866), in which a bright spot appears along the center of the shadow zone behind a flat circular object illuminated by a plane wave the Arago-Poisson spot is typically cited in textbooks as a classic proof of the wave nature of light and/or sound (Hecht 2016). This spot forms in this Mie scattering problem for a similar reason: sound diffracting around the sphere interferes constructively along the line of symmetry in the shadow zone, creating a peak with a width proportional to the wavelength. This peak, while fundamentally formed from

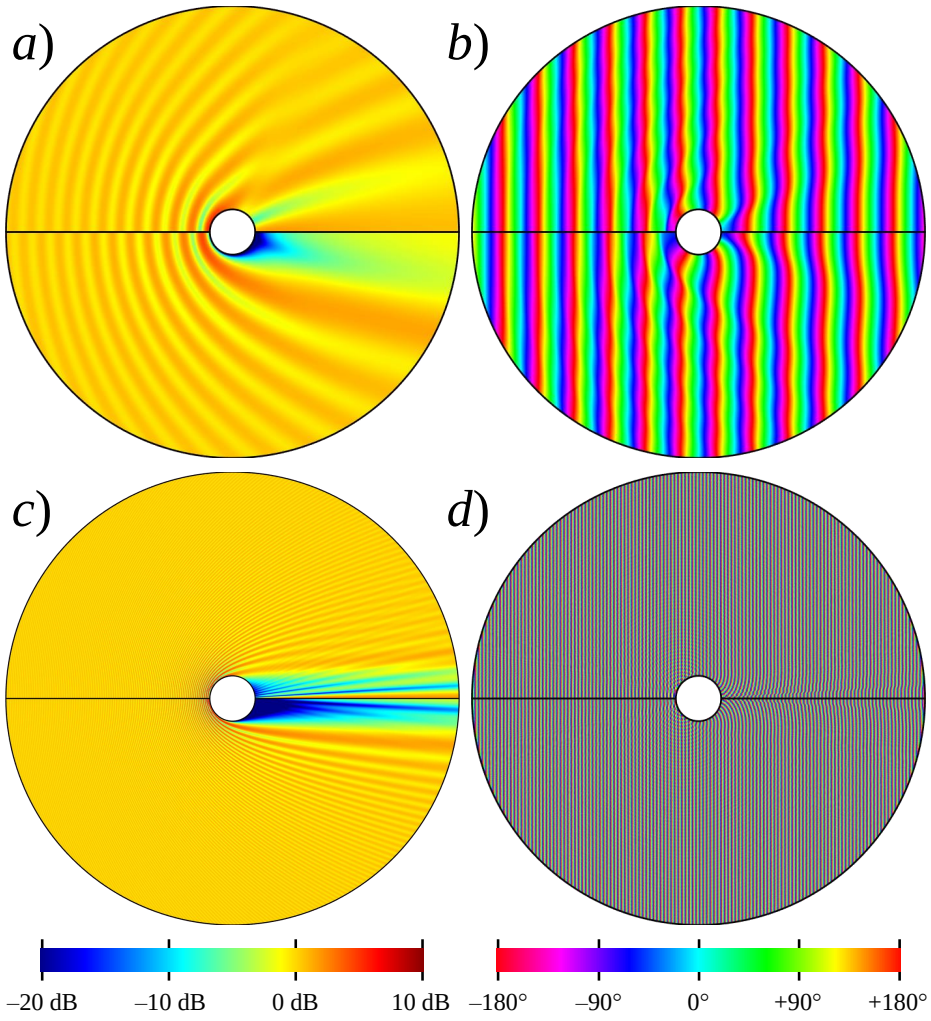

Figure 7.7: Acoustic field plots for the Mie scattering from a sphere problem, with $ka = 4; kR = 40$ shown in panel a (magnitude) and panel b (phase), and $ka = 40; kR = 400$ shown in panel c (magnitude) and panel d (phase).

diffraction, is also directly related to the high level of symmetry this model problem has a more complicated geometry with fewer symmetries should not be expected to have this kind of behavior in the shadow zone.

Another interesting phenomenon is the interference patterns that the incident wave and the reflected wave create that roughly appear as concentric parabolas emanating from around the sphere. It's clear from the phase plots, Figs. 7.7b) and 7.7d), that the incident field largely dominates the phase contribution away from the sphere (unlike in Fig. 7.2b where

the standing wave region primarily showed oscillations between phase angles of 0° and 180°). The scattered wave from the sphere propagates away spherically, meaning that far from the sphere, the reflected/scattered field is negligible compared to the incident field.

To better understand the scattered field, especially outside of the shadow zone, one can look to the solution of the geometric problem of horizontal rays reflecting off the curved surface of the sphere to determine ray time-of-arrivals. Additionally, by looking at how two initially nearby rays spread apart after reflection from the sphere, a conservation-of-energy argument can be made to determine the amplitude of the scattered field. The details of this derivation are omitted here, and left as an exercise for the reader.

The time of arrival and amplitude of the incident field is straightforward to calculate:

$$\tau_{incident}\left(r,\theta\right) = \frac{a}{c_0}\left(\frac{R}{a} + \frac{r}{a}cos\theta\right) \tag{7.14}$$

$$A_{incident}\left(r,\theta\right) = 1. \tag{7.15}$$

Here, c_0 is the speed of sound, R is the outer radius of the domain, (r,θ) are the typical spherical coordinates, and a is the radius of the sphere. R enters here, and in the next equation, as a means of setting $\tau = 0$ to occur along $x = -R$ (the leftmost edge of the domain). With this definition, τ is always strictly positive in the domain. However, R could just as easily be set to zero in this ray-based formulation of the arrival times, since what matters the most for the physical field is the *difference* in time-of-arrivals.

Evaluation of the arrival time and amplitude is predictably more complicated. First, implicitly define the angle β as a function of (r,θ) such that:

$$\arcsin\beta + r\sin\left(2\beta+\theta\right) = 0. \tag{7.16}$$

Here, β corresponds to the angle (as measured from the negative x-axis) to the point on the sphere at which a ray must have reflected in order to have arrived at the specified (r,θ) coordinate. An analytic solution for $\beta\left(r,\theta\right)$ is not available, but it is straightforward to interpolate values for β given (r,θ). Note: not all values of (r,θ) have a corresponding β specifically, (r,θ) within the shadow zone do not have a real-valued solution for β. Additionally, all of these results are not valid for $r < a$, which corresponds to the unphysical situation of a ray inside the sphere.

With β known, the following equations can be evaluated, which lead to the time-of-arrival and amplitude information for the reflected rays.

$$\tau_{reflected}\left(r,\theta\right) = \frac{a}{c_0}\left(\frac{R}{a} - cos\beta + \sqrt{\frac{r^2}{a^2}+1+2\frac{r}{a}cos\left(\theta+\beta\right)}\right) \tag{7.17}$$

$$A_{reflected}\left(r,\theta\right) = \pm\frac{a}{r}\sqrt{\frac{sin\beta\cos\beta}{sin\theta}}\left[\left(cot\beta - cot\left(2\beta+\theta\right)\left(2-\theta'\right)\right)^2+\theta'^2\right]^{-\frac{1}{4}} \tag{7.18}$$

Here, θ' is an intermediate result (related to the derivative of θ with respect to β), which is given by the relationship:

$$\theta' = \frac{3sin\beta - sin\left(3\beta+2\theta\right)}{\left(2sin\beta+sin\left(2\beta+\theta\right)\right)^2}. \tag{7.19}$$

For a hard (soft) sphere, the positive (negative) solution of $A_{reflected}$ should be chosen, corresponding to an effective reflection coefficient of +1 (1) off a rigid (pressure-release) surface. It is not immediately obvious from these equations what the reflected amplitude

is as $\theta \to \pi$ (the normal incidence reflection); a careful limit evaluation leads to reflected amplitude of $\frac{a}{(a-2r)}$.

With these results, a ray-based acoustic field can be evaluated for the environment, given by:

$$P_{rays}(r,\theta,\omega) = A_{incident}(r,\theta)\exp\left(i\omega\tau_{incident}(r,\theta)\right) + A_{reflected}(r,\theta)\exp\left(i\omega\tau_{reflected}(r,\theta)\right) \tag{7.20}$$

The magnitude of this ray-based field is evaluated for 1 kHz ($ka = 4$; $kR = 40$) and 10 kHz ($ka = 40; kR = 400$), and is shown in Figures 7.8a) and 7.8b), respectively. Here, it is easily seen that the rays reproduce very similar results as the full Mie scattering solution does. Exceptions exist directly in the shadow zone of course, but other subtler differences can also be seen at the rear of the sphere, including some nulls that originate in the shadow zone, but eventually extend beyond the shadow zone. But other than these minor differences, it's clear that the concentric parabola-like features seen in the standing wave regions of Figs. 7.7a and 7.7c originate from a ray-based understanding of the fields. The phase structure of the ray-based fields is also quite close to the full Mie scattering solution, and as such, these results are omitted.

With the behavior of the in-band field well-understood, now attention can be moved to the frequency-difference autoproduct. Much like in Section 7.3, a center frequency of 10 kHz ($k_c R = 400; k_c a = 40$) is shifted down to a difference frequency of 1 kHz ($k_\Delta R = 40; k_\Delta a = 4$) by bandwidth averaging over 1 kHz ($k_{BW}^{\Delta} R = 40; k_{BW}^{\Delta} a = 4$). Figure 7.9 gives the magnitude and phase of AP_Δ with these parameters. It should be noted that the out-of-band field that these autoproducts are mimicking is a field scattering off a *hard* sphere at the difference frequency (*i.e.* the upper halves of Figs. 7.7a and 7.7b). This is true even for the field formed from scattering at a soft sphere (see the discussion in Section 7.2 on effective

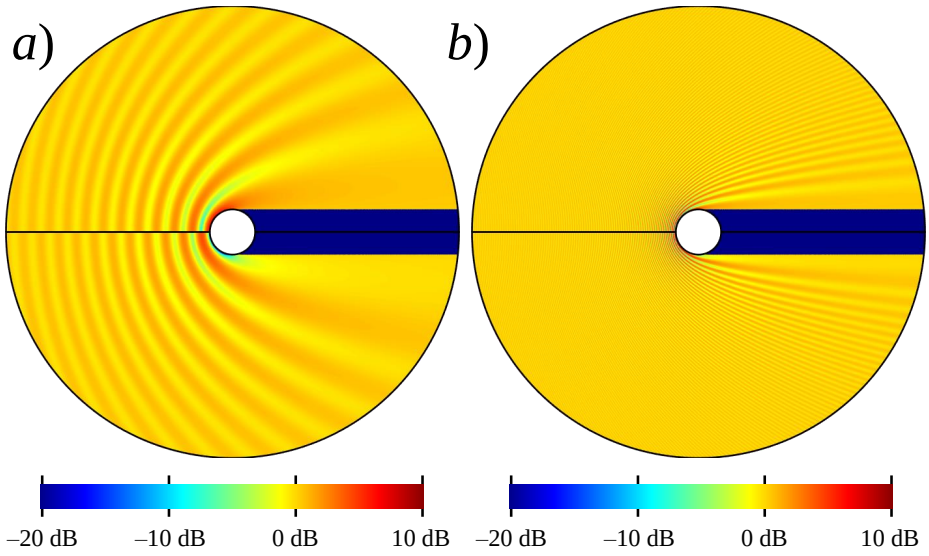

Figure 7.8: Acoustic field magnitude plots of Mie scattering from a sphere in the ray approximation for $ka = 4; kR = 40$ and $ka = 40; kR = 400$ in panels a and b, respectively.

reflection coefficients).

The resulting magnitude and phase of the cross-correlation χ_Δ across the normalization regions given in Fig. 7.6 are given in Figure 7.10a) and 10b). This time, there are three main sources of discrepancies. In the well-ensonified regions, interference layers and spreading losses dominate the discrepancies (see discussion in Section 7.3, except the spreading loss here is associated with $1/r$ vs $1/r^2$). In the shadow zone, the strongly frequency dependent nature of the diffracted field instead leads to poor cross-correlations. Especially considering the similarity of the autoproduct phases (Fig. 7.9b) and the out-of-band phase (upper half of Fig. 7.7b), it is reasonable to conclude that the majority of the poor cross-correlations observed in the shadow zone of Fig. 7.10a) can be explained in terms of amplitude variations. Additionally, it is noted that for these parameters, the phase discrepancy (see Fig. 7.10b) is small no phase shifts between autoproducts and out-of-band fields are observed here.

The analogous frequency-sum autoproduct results to Fig. 7.10 are given in Figure 7.11, where 10 kHz ($k_c a = 40; k_c R = 400$) is shifted up to the sum-frequency of 20 kHz ($k_c a = 80; k_c R = 800$) through the use of 1 kHz of frequency-sum bandwidth averaging

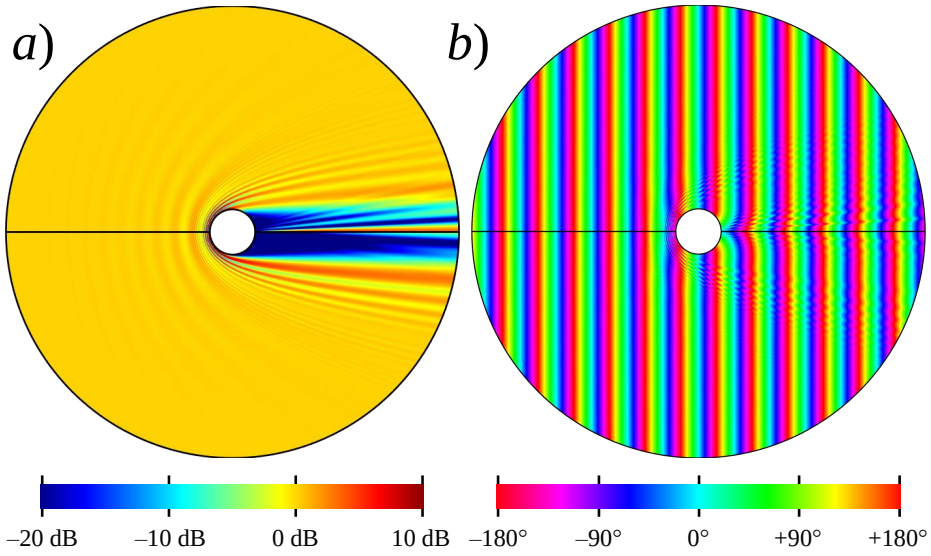

Figure 7.9: Frequency-difference autoproduct field plots for the Mie scattering from a sphere environment, with $k_c a = 40$, $k_\Delta a = 4$, and $k_{BW}^{\Delta} a = 4$. Magnitude and phase shown in panels a and b, respectively

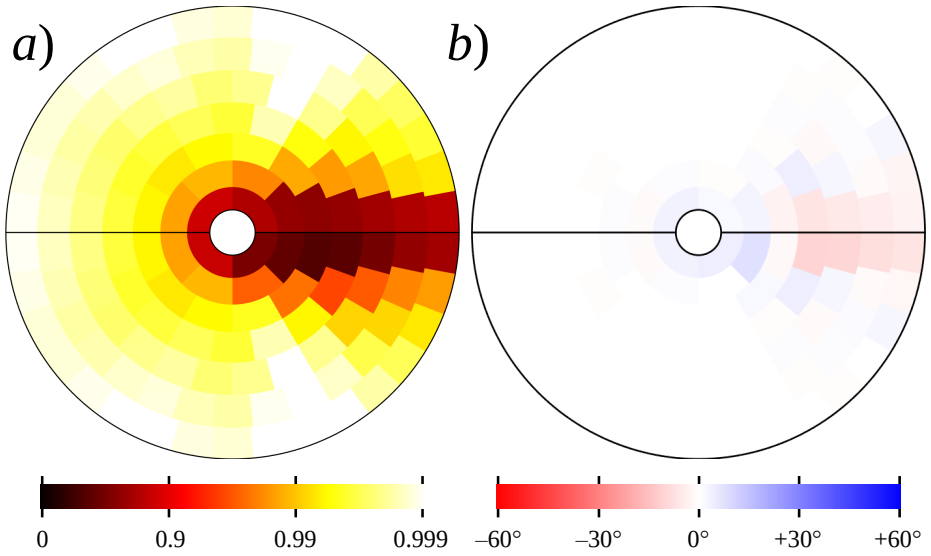

Figure 7.10: Cross correlations between the frequency-difference autoproduct and out-of-band fields in the Mie scattering from a sphere environment. Magnitude of χ_Δ given in panel a on a logarithmic scale; phase of χ_Δ given in panel b.

$\left(k_{BW}^{\Sigma} a = 4; k_{BW}^{\Sigma} R = 40\right)$. As before, the normalization regions are much smaller for AP_Σ so finer scale structure can be assessed. There are magnitude discrepancies due to the interference layer and spreading loss reasons discussed before. Additionally, it appears that the amplitude of the field inside the shadow zone is very frequency dependent, and so poor

cross-correlations persist in some parts of the shadow zone.

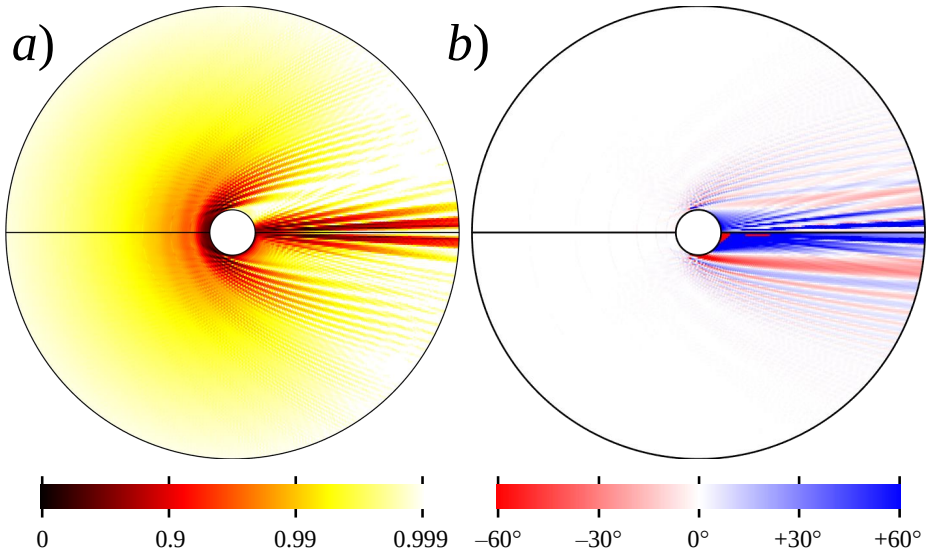

Figure 7.11: Cross correlations of frequency-sum autoproducts and out-of-band fields in the Mie scattering from a sphere environment, with parameters $k_c a = 40$, $k_\Sigma a = 80$, and $k_{BW}^{\Sigma} a = 4$. Magnitude and phase of χ_Σ is shown in panels a and b, respectively.

Having developed the ray-based version of this environment, a ray-based version of the cross-correlations has also been developed (where ray-based autoproducts are compared to ray-based out-of-band fields). The magnitude of the cross-correlations is provided in Figure 7.12a) and 12b) for AP_Δ and AP_Σ, respectively. Here, it becomes clear that outside of the shadow zone, the cross-correlations observed in Figs. 7.10a) and 7.11a) are well-understood strictly in terms of rays.

Additionally, to further assess the role of magnitude and/or phase discrepancies in poor cross-correlations, consider Figure 7.13a) and 13b), which show plots of the phase of $AP_\Delta P_\Delta^*$ and $AP_\Sigma P_\Sigma^*$, respectively. Figure 7.13a) shows that phase variations play a very minor role in the cross correlations observed, since the phase differences throughout the domain are quite close to zero therefore, amplitude variations dominate the cross-correlation behavior. At higher frequency, phase differences also become important, as is shown particularly in the lower half (soft sphere) in Fig. 7.13b), where in the shadow zone, phase discrepancies range all the way up to a full 180° difference.

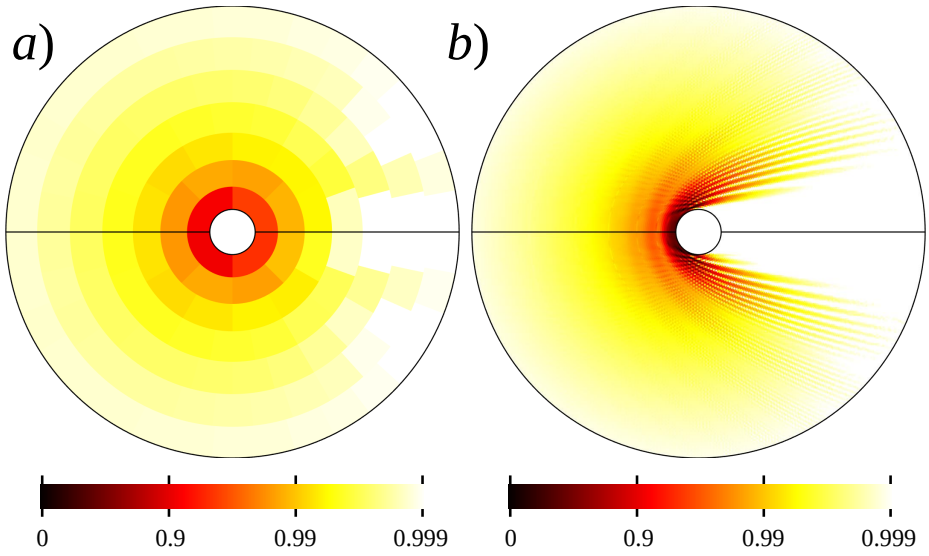

Figure 7.12: Magnitude of the cross correlations for χ_Δ (panel a) and χ_Σ (panel b) when the autoproducts and out-of-band fields are evaluated in the ray approximation. Fields in a given normalization region that are identically zero (*i.e.* in the shadow zone) are defined to be a perfect match ($\chi = 1$).

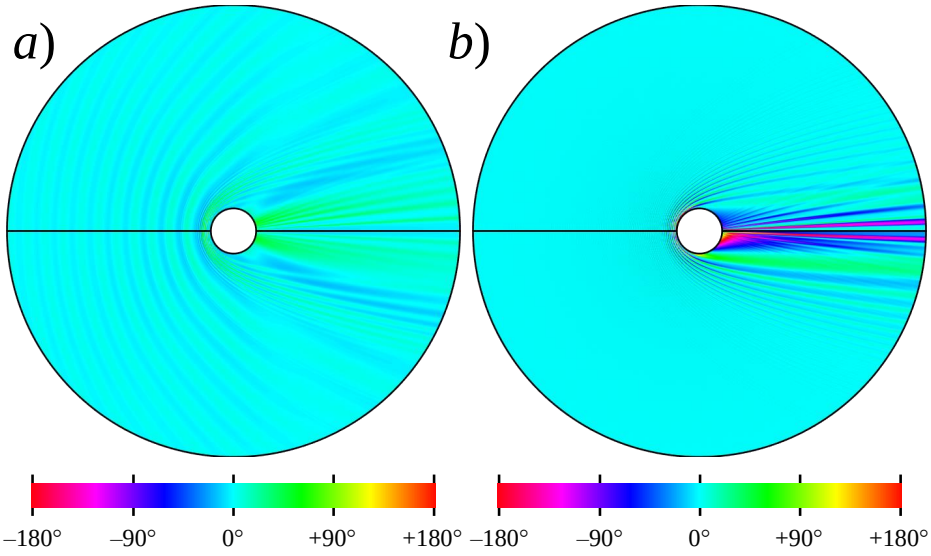

Figure 7.13: Point-wise phase differences between frequency-difference (frequency-sum) autoproducts and out-of-band fields are shown in panel a (panel b).

Overall, in Mie scattering, the results in the well-ensonified (one- or two-path regions) have reasonably strong cross-correlations, except at locations where the ray-based theory had already predicted poor results (such as near interference layers). In the shadow zone, where no rays appear to enter, the cross-correlation results are much poorer at low frequency,

amplitude variations dominate. However, at high frequency, both amplitude *and* phase variations dominate. Other than that, many of the same sources of discrepancies observed in Section 7.3 also apply here.

7.5 Summary and Conclusions

In this study, two analytic environments were studied for the purposes of understanding the detrimental role, if any, that diffraction behind barriers plays in the ability of frequency-difference and frequency-sum autoproducts to mimic out-of-band acoustic fields at the difference and sum frequencies, respectively. The limitations with respect to rays are already well-understood however, in and near acoustic shadow zones formed by barriers, diffraction plays a much more important role. The two environments considered were the Sommerfeld half-plane barrier problem (also known as the knife edge diffraction problem), and the Mie scattering from a sphere problem. Broadly speaking, both environments had some regions of strong cross-correlations between autoproducts and genuine out-of-band fields. Mathematical analyses and further simulation results were shown to able to tease out the role that relative amplitude variations and/or relative phase variations played on the cross-correlations observed.

This study supports three main conclusions. The first is that even in the presence of a diffracted and scattered field, the well-ensonified portions of acoustic fields were able to produce strong cross-correlations between autoproducts and out-of-band fields, subject to the known limitations of ray-based fields. This is not particularly surprising, since the diffracted and scattered fields are typically much quieter than the incident and reflected fields, and so these well-ensonified regions can reasonably be approximated to be ray-like.

The second conclusion is that diffraction seems to play a significant role in creating amplitude variations between autoproducts and out-of-band fields, but these variations are not

especially detrimental to cross-correlation calculations, at least with out-of-band-wavelength-sized normalization regions.

The third conclusion is that diffraction can lead to two types of phase mismatch: an overall phase shift, and phase variations. An overall phase shift was found in nearly the whole shadow zone quadrant in the Sommerfeld knife-edge problem, but this phase shift wouldn't be detrimental for source localization schemes. Phase variations however were found in the deep shadow zone of the Mie scattering problem, and these phase variations would be very detrimental for source localization schemes. However, in the deep shadow zone the absolute amplitudes are much lower than the incident wave, and so it's likely that finite signal-to-noise considerations would impact source localization before these autoproduct-related phase variations would.

Overall, diffraction was found to negatively impact the ability of autoproducts to mimic out-of-band fields, but the extent of this negative impact is minimal except in a few narrow regions deep in the acoustic shadow zones. Additionally, the known limitations of ray-based autoproduct theory appear to explain nearly all of the autoproducts' cross-correlation performance in the well-ensonified regions.

CHAPTER 8

The Effects of Refraction and Caustics on Autoproducts

Abstract

Nonlinear mathematical constructions have made it possible to take acoustic fields with non-zero bandwidth, and create new field quantities, denoted autoproducts', that can mimic acoustic fields at frequencies much lower, or much higher than the original field's bandwidth, termed here as out-of-band fields. While this has been found to be very promising for a variety of signal processing applications, the theoretical extent to which it is possible has thus far only been studied under the ray approximation. In this study, the combined effects of refraction and diffraction are considered in environments where neighboring rays cross and caustics are formed. Acoustic fields in and near caustics are not well-predicted by elementary ray-acoustic theory. Furthermore, caustics introduce a strong frequency dependence to the nearby acoustic field, and also introduce a phase shift on the acoustic waves that pass through them. The effects these caustics have on autoproducts is assessed here using two simple, range-independent waveguides with sound speed profiles that are n^2-quadratic and n^2-linear. It is found that, in multipath regions where rays have passed through differing numbers of caustics, the ability of autoproducts to mimic out-of-band fields is substantially hindered.

8.1 Introduction

In linear acoustics, an excitation by a broadband source creates an acoustic field containing those same frequencies – termed the in-band field. Nonlinear mathematical constructions have recently been shown to be able, within some limitations, to use these in-band fields to create a new field quantity called an autoproduct which may mimic an out-of-band field – a field with frequency content either below or above the original bandwidth (Worthmann and Dowling 2017). Such techniques have been found to improve a variety of signal processing techniques, such as beamforming with sparse arrays (Abadi 2012; Douglass 2017), matched field processing in uncertain environments (Worthmann 2015; Worthmann 2017; Geroski 2018), and passive cavitation imaging for higher resolution (Abadi 2017).

The extent of the ability of these autoproducts to mimic genuine out-of-band acoustic fields has not been extensively studied. However, the available theoretical (Worthmann and Dowling 2017) and experimental (Lipa *et al.* 2018) studies have found that, for acoustic fields adequately satisfying the ray approximation, autoproducts have two primary limitations. First, the amplitude of the rays must be sufficiently slowly varying in space, relative to the wavelength. Second, in multipath environments, the difference in ray arrival times should be smaller than the inverse of the bandwidth available for averaging. Under these two conditions, autoproducts formed from rays have been shown to have strong cross-correlations with out-of-band acoustic fields also formed from rays.

Not all acoustic fields adequately satisfy the ray approximation. The effects of diffraction, in particular, are not captured in the ray approximation. Diffraction is interesting to study because of its strong frequency dependence, and it is not obvious whether these frequency-dependent diffraction effects allow autoproducts to mimic out-of-band fields. To study the effects of diffraction, two separate studies are proposed. The first, in a sister study to this one (Chapter 7), diffraction behind barriers is considered – these results suggest that diffraction

effects do not significantly impact the ability of autoproducts to successfully mimic out-of-band fields in most regions of the environment. The second study, proposed here, is to look at strong refraction, and more specifically the formation of caustics, and their effects on autoproducts' ability to mimic out-of-band fields. Near caustics and in shadow zones, some detrimental effects on autoproducts' mimicry of out-of-band fields are expected at a level comparable to the barrier diffraction results. But, even more interesting are the cumulative effects that caustics may have on the acoustic waves that have traveled through them, particularly when such acoustic waves are no longer near caustics.

Caustics occur when refraction causes two neighboring ray paths to cross, and typically form a one-dimensional curve (in a two-dimensional range-depth plane) on one side of which there are at least two rays, and on the other side of which there may be zero rays. Within elementary ray acoustics (*i.e.* the solution to the eikonal and transport equations only), acoustic fields evaluated at the caustic are predicted to be infinite (because the ray's cross sectional area drops to zero), and just beyond the caustic, amplitudes are predicted to be identically zero (due to the absence of rays) (Jensen 2011, Chapman 2004). This is of course unphysical, as diffraction would enforce continuous, finite amplitudes in acoustic fields around the caustic. But it does so with a strong frequency dependence, which may or may not be compatible with what is needed for autoproducts to mimic out-of-band fields. Strictly speaking, there are many types of caustics, including fold-type, cusp-type, swallowtail-type, butterfly-type, among others (Kravtsov and Orlov 1993). For the purposes of this study, only the simplest type – fold-type caustics – are considered.

To study the effects of caustics on autoproducts, simple environments that exhibit caustic phenomena are desired. This preference for simplicity is two-fold: (8.1) so that caustic effects can be studied separately from other wave propagation effects, such as reflections, and (8.2) so that exact solutions to the wave equation can be used, both for computational speed as well as guaranteed satisfaction of the wave equation. For this study, a waveguide with a

range-independent but depth-dependent sound speed profile is chosen, since modal decompositions are exact solutions to the wave equation. There is interest in studying autoproducts in and near shadow zones as well, and so it is also convenient to avoid the use of reflecting boundaries in the solution, which may reflect sound into the shadow zone. Therefore, unbounded environments with continuous sound speed profiles are sought. Sound speeds should also not diverge to infinity or to zero anywhere, as this may also cause unphysical effects. Finally, for mathematical simplicity, waveguides that are symmetric in depth are considered, since sources placed at the point of symmetry allows the computation of only even-symmetry modes, instead of odd-symmetry modes too.

To satisfy these requirements, refractive index ($n(z) \equiv c_\infty / c(z)$) profiles of the following form are sought:

$$\begin{aligned} n^2(|z| \leq L) &= n_0^2 - \left(n_0^2 - 1\right) f\left(\frac{|z|}{L}\right) \\ n^2(|z| \geq L) &= 1 \end{aligned} \tag{8.1}$$

where n_0 is the maximum refractive index in the medium (strictly greater than unity, and occurs at $z = 0$), L is the half-height of the inhomogeneous portion of the waveguide which is symmetric in depth about $z = 0$, c_∞ is the sound speed at depths $|z| \geq L$, and f is a function to be chosen. $f(0)$ and $f(1)$ should equal 0 and 1, respectively, and f should be continuous and vary monotonically between these two points. Furthermore, f should correspond to a sound speed profile in which caustics are created, and have a closed form solution to the depth-separated Helmholtz equation:

$$\left[\frac{d^2}{dz^2} + \left(k_\infty^2 n^2(z) - k_r^2\right)\right] \psi(z) = 0 \tag{8.2}$$

where k_∞ is the wavenumber in the homogeneous medium, ω / c_∞, and ψ and k_r are the mode

shapes and corresponding eigenvalues, respectively. Subject to all of these constraints, the author has found two possible choices for $f(x)$, namely x and x^2, referred to hereafter as the n^2-linear and n^2-quadratic sound speed profiles. See Figure 8.1 for a plot of the sound speed versus depth for n^2-quadratic (solid line) and n^2-linear (dotted line) profiles, using c_∞, n_0 and L of 1500 m/s, 1500/1450, and 100 m, respectively.

Using a modal decomposition in an unbounded environment can create some mathematical difficulties, especially the presence of so called *leaky modes*, or modes which correspond to sound that propagates in *both* the inhomogeneous and homogeneous regions (Jensen 2011). This is in contrast to *trapped modes*, which correspond to sound that propagates in the inhomogeneous region, but decays exponentially in the homogeneous region; and these stand in contrast to *evanescent modes* which decay exponentially in both regions. Many waveguides also include a branch-cut associated with a discontinuous sound speed profile (*e.g.* at the water-sediment interface in the shallow ocean), though the continuity requirement specified here does not require such a branch cut (Bartberger 1977, Stickler 1975). Evanescent modes can typically be safely neglected several wavelengths from the source. Trapped modes are important for accurately modeling the field in the inhomogeneous region. Leaky modes are important in the homogeneous region, but the physics of interest here occurs within the inhomogeneous region, where leaky modes may still be important. Computation of trapped modes is typically straightforward, whereas leaky mode computations can present many difficulties (Labianca 1973, Tindle 1976, 1979, Sticker and Ammicht 1980, 1984, Buckingham 2006). For the two environments proposed here, leaky modes are neglected in the n^2-quadratic profile, and evaluated approximately in the n^2-linear profile. Omission of the leaky modes does not locally affect the satisfaction of the wave equation – however, without the leaky modes, the perfect point source requirement is only satisfied approximately. Overall, just the trapped modes should provide the qualitative behavior sought in this study, but including the leaky modes allows for more confident quantitative results. Other numerical wave propagation schemes can also be used (*e.g.* parabolic equation solvers

like RAM (Collins 1996), though their satisfaction of the wave equation may no longer be mathematically exact, and may be computational expensive at high frequencies.

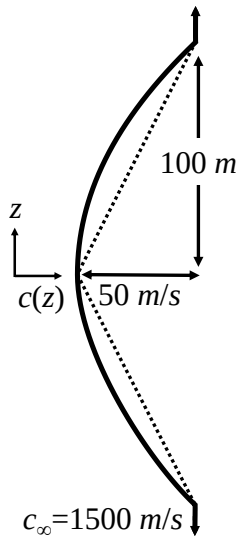

Figure 8.1: Sound speed profiles for the two range-independent but depth-dependent waveguides in this study: the n^2-quadratic (solid line) and the n^2-linear (dotted line) profile. These waveguides are symmetric and infinite in extent, though the inhomogeneous portion of the sound speed profile has a finite depth of 100 m, and has a sound speed minimum of 1450 m/s.

In Section 8.2, autoproducts and their associated cross correlations are defined. In Section 8.4, the acoustic field in the n^2-quadratic profile is found, autoproducts are computed, and cross correlations between autoproducts and out-of-bands are presented alongside a discussion of the results. In Section 8.4, analogous results are provided for the n^2-linear profile. In Section 8.5, the results from this study are summarized, and the conclusions that can be drawn from this study are described.

8.2 Autoproduct Definitions

Define $P(\boldsymbol{r}, \omega)$ to be the solution to the inhomogeneous Helmholtz equation:

$$\left(\nabla^2 + \frac{\omega^2}{c^2(\boldsymbol{r})}\right) P(\boldsymbol{r},\omega) = -\delta(\boldsymbol{r} - \boldsymbol{r}_s) \tag{8.3}$$

where $\boldsymbol{r}_s$ is the location of the source. Notably, the definition of $P(\boldsymbol{r},\omega)$ here is synonymous with a Green's function – in other words, the source waveform is assumed to be an impulse. Or in terms of measured data, the source waveform is to be known such that an impulse response can be estimated from the data.

Bandwidth averaged autoproducts are defined to be:

$$\langle AP_\Delta \rangle (\boldsymbol{r},\Delta\omega) \equiv \frac{1}{\Omega_H - \Omega_L - \Delta\omega} \int_{\Omega_L + \frac{\Delta\omega}{2}}^{\Omega_H - \frac{\Delta\omega}{2}} P\left(\boldsymbol{r},\omega + \frac{\Delta\omega}{2}\right) P^*\left(\boldsymbol{r},\omega - \frac{\Delta\omega}{2}\right) d\omega \tag{8.4}$$

$$\langle AP_\Sigma \rangle (\boldsymbol{r},\Sigma\omega) \equiv \frac{1}{\Omega_H - \Omega_L} \int_0^{\Omega_H - \Omega_L} P\left(\boldsymbol{r},\omega + \frac{\Delta\omega}{2}\right) P\left(\boldsymbol{r},\omega - \frac{\Delta\omega}{2}\right) d\Delta\omega \tag{8.5}$$

where $\Sigma\omega = \Omega_L + \Omega_H$, and the original acoustic field's bandwidth is contained within $\Omega_L \leq \omega \leq \Omega_H$. The expectation is that these bandwidth averaged frequency-difference and frequency-sum autoproducts are similar to acoustic fields at the difference and sum frequency, respectively. However, a direct equivalence between autoproducts and genuine out-of-band acoustic fields is not possible because they have fundamentally different units (pressure-squared vs. pressure). To correct this, a normalization scheme is defined where autoproducts and out-of-band fields are divided by the root-mean-square of their amplitudes over a certain region, defined to be the normalization region V. Then, after normalization, a cross-correlation metric can be defined which quantifies how closely autoproducts mimic out-of-band fields over the normalization region. This is given by:

$$\chi_{\Delta,\Sigma} \equiv \frac{\int_V AP_{\Delta,\Sigma}(\boldsymbol{r})\, P_{\Delta,\Sigma}(\boldsymbol{r})\, dV}{\sqrt{\int_V |AP_{\Delta,\Sigma}(\boldsymbol{r})|^2 dV \int_V |P_{\Delta,\Sigma}(\boldsymbol{r})|^2 dV}} \tag{8.6}$$

where $P_{\Delta,\Sigma}(\boldsymbol{r})$ refers to the out-of-band field at the difference or sum frequency, $\Delta\omega$ or $\Sigma\omega$. In this study, the normalization regions are defined to be rectangular regions in range and depth. Notably, dV is evaluated as $drdz$, not $rdrdz$.

8.3 n^2-Quadratic

In this section, a depth-symmetric and range-independent waveguide with refractive index given by equation (8.1) with $f(x) = x^2$ is detailed. In this environment, trapped modes take on the form of confluent hypergeometric functions (Abramowitz and Stegun 1965), also known as Kummer M functions, which are matched at the $|z| = L$ boundary with exponentially decaying functions. Some of the details of the mathematical derivation can be found in Appendix B. Here, only trapped modes ($k_\infty \leq k_r \leq n_0 k_\infty$) are considered, primarily due to the high computational expense associated with the complex root finding algorithms that would be necessary. Evaluating confluent hypergeometric functions with complex parameters is especially expensive because a symbolic calculation is required, instead of a simple floating-point calculation (Nardin 1992).

For this study, the following parameters are chosen: $c_\infty = 1500$ m/s, $n_0 = \frac{1500}{1450}$, and $L = 100$ m. These acoustic fields are studied over depths from 0 to $\pm$ 100 m, and over ranges from 0 to 5 km. Figure 8.2a indicates the trajectory of the rays as calculated from a source at $(\boldsymbol{r}, z) = (0, 0)$, and Fig. 8.2b indicates the transmission loss (amplitude) on a decibel (logarithmic) color scale for a 5 kHz source at the origin.

In can be seen in Fig. 8.2a that some of the rays propagate at a high angle (relative to horizontal) and escape from the domain into the homogeneous region (not pictured), where

they continue on straight-line path trajectories to $|z| \to \infty$; these rays roughly correspond to the leaky modes since energy is being *leaked* out of the waveguide. Other rays with shallower launch angles are able to return to $z = 0$, and continue in a cyclic manner up-and-down the waveguide. One of the salient features in Fig. 8.2 is the apparent ray cycle distance of slightly more than 1 km. In this environment, the shallow angle rays seem to converge to the same range – however this is only approximately true, as can be seen at the third or fourth convergence zone, where the ray intersections begin to smear out in range. The caustics that are formed can be found just before each of the convergence zones, where adjacent rays get very close together and, while not immediately obvious from the ray diagram, actually cross each other, forming caustics. It is more obvious in the amplitude plot in Fig. 8.2b, where the acoustic field has a much higher amplitude along the caustic. Notably, because this field was calculated with a modal decomposition, the field at the caustic does not have an infinite amplitude as predicted by ray theory, nor does the nearby shadow zone contain amplitudes of identically zero.

Other interesting features in Fig. 8.2b are the apparent interference patterns occurring at depths near $|z| = L$, which can be seen as a sort of checkerboard pattern. Relatedly, there is some faint horizontal structure deep in the shadow zones. Additionally, there appears to be no sound propagating at high angles (see the deep blue region near $r = 0$). All three of these behaviors are artifacts of not including the leaky modes – the acoustic field for a true point source would not have this checkerboard pattern nor the horizontal striations in the shadow zone, and would have sound propagating at high angles into the homogeneous medium. Despite these artifacts, the qualitative results described here are expected to be accurate, despite the omission of the computationally-challenging leaky modes.

In Figure 8.3a, the magnitude of a genuine acoustic-field at the difference frequency $\Delta\omega/2\pi = 500$ Hz is shown alongside Fig. 8.3b, where the magnitude of the bandwidth-averaged frequency-difference autoproduct $\langle AP_{\Delta} \rangle$ is given. Here, the in-band field's band-

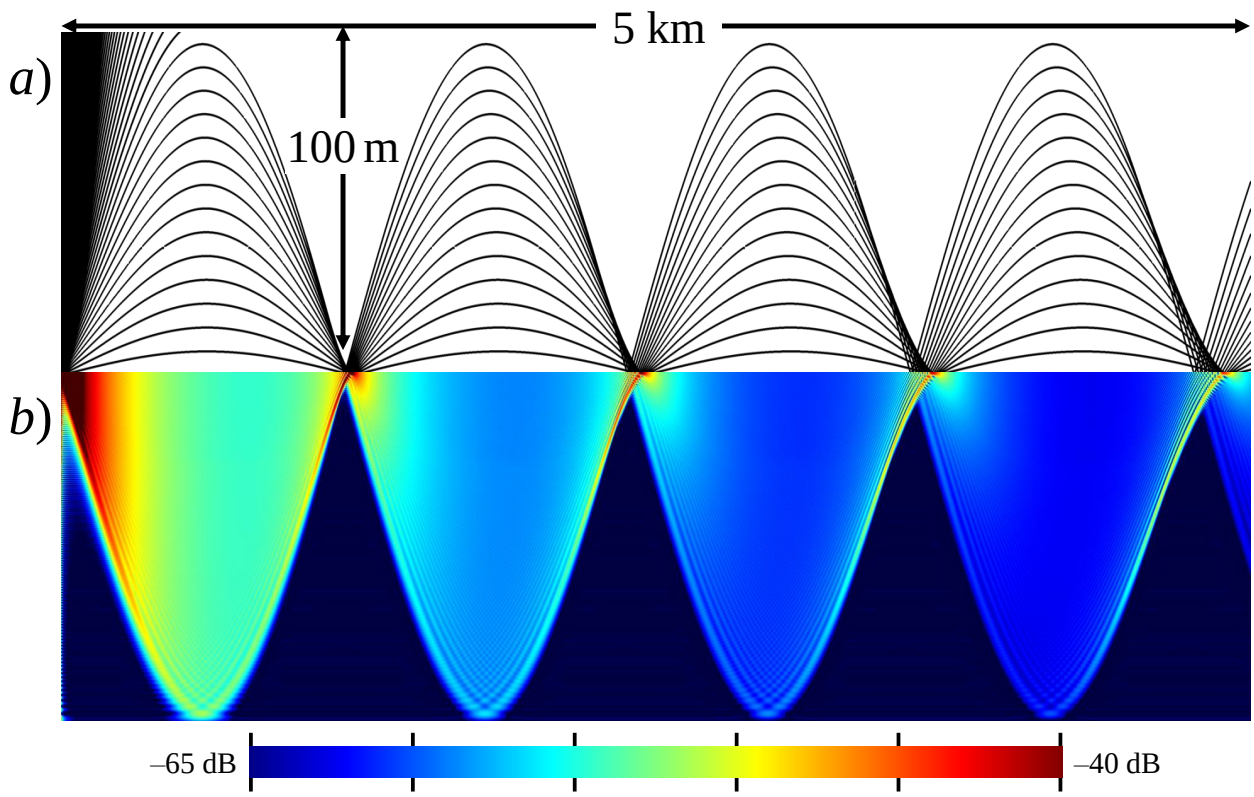

Figure 8.2: Plots of the ray trace (upper) and the acoustic amplitude (lower) for a 5 kHz source at the origin of the n^2-quadratic profile.

width is between $\Omega_L/2\pi$ and $\Omega_H/2\pi$ of 1 kHz and 5 kHz, respectively. The color scale for the upper plot spans 25 dB, while for the lower plot, it spans double that – the doubled decibel scale is a result of the fact that the autoproducts are formed from a multiplication of two in-band fields, and thus have effectively twice the transmission loss as a single in-band field.

It is evident in Fig. 8.3 that the autoproduct amplitudes do not match the out-of-band field amplitudes particularly well. Part of that is due to the checkerboard patterns in the Fig. 8.3a which are related to the absence of the leaky modes – Fig. 8.3b's checkerboard pattern is suppressed due to the bandwidth averaging. The acoustic field amplitude increase near caustics in Fig. 8.3b is narrow in size compared to the acoustic field amplitude increase near caustics in Fig. 8.3a; their width in Fig. 8.3b is on the order of the wavelength at the in-band frequencies, not the out-of-band frequencies. The size of the acoustic field amplitude increase near the convergence zones in Fig. 8.3b are similarly smaller compared their analogous sizes

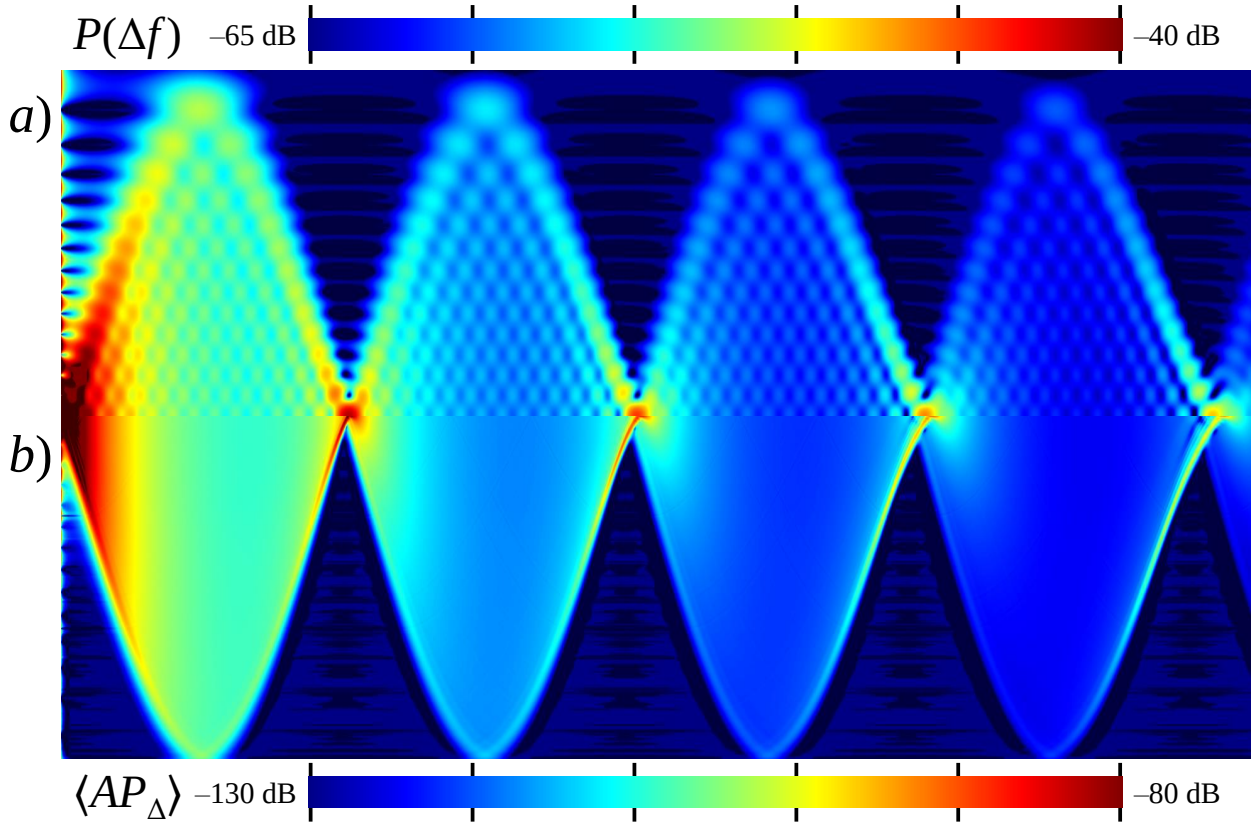

Figure 8.3: Plots of the transmission loss for the out-of-band field (upper) and frequency-difference autoproduct field (lower), for a difference frequency of 500 Hz, derived from in-band frequencies of 1 to 5 kHz. Note the dynamic range in the lower plot is twice that of the upper plot.

Fig. 8.3a. However, these plots only indicate magnitude, not phase. Phase plots spatially vary too quickly to be conveniently seen in a figure, but the phase information is crucial for the cross-correlation calculation in equation (#), whereas the amplitude variations are not so severely detrimental to cross-correlations.

The cross-correlation between the autoproduct and out-of-band fields shown in Fig. 8.3 is shown in Figure 8.4, with the magnitude and phase plotted separately. In Fig. 8.4a, the magnitude of χ_Δ is plotted on a linear color scale, with strong cross-correlations near unity corresponding to white, and poor cross-correlations near zero corresponding to black. In Fig. 8.4b, the phase angle of χ_Δ is plotted, with cyan corresponding to a phase angle of zero. The normalization regions here are rectangles that extend 50 m in range and 5 m in depth.

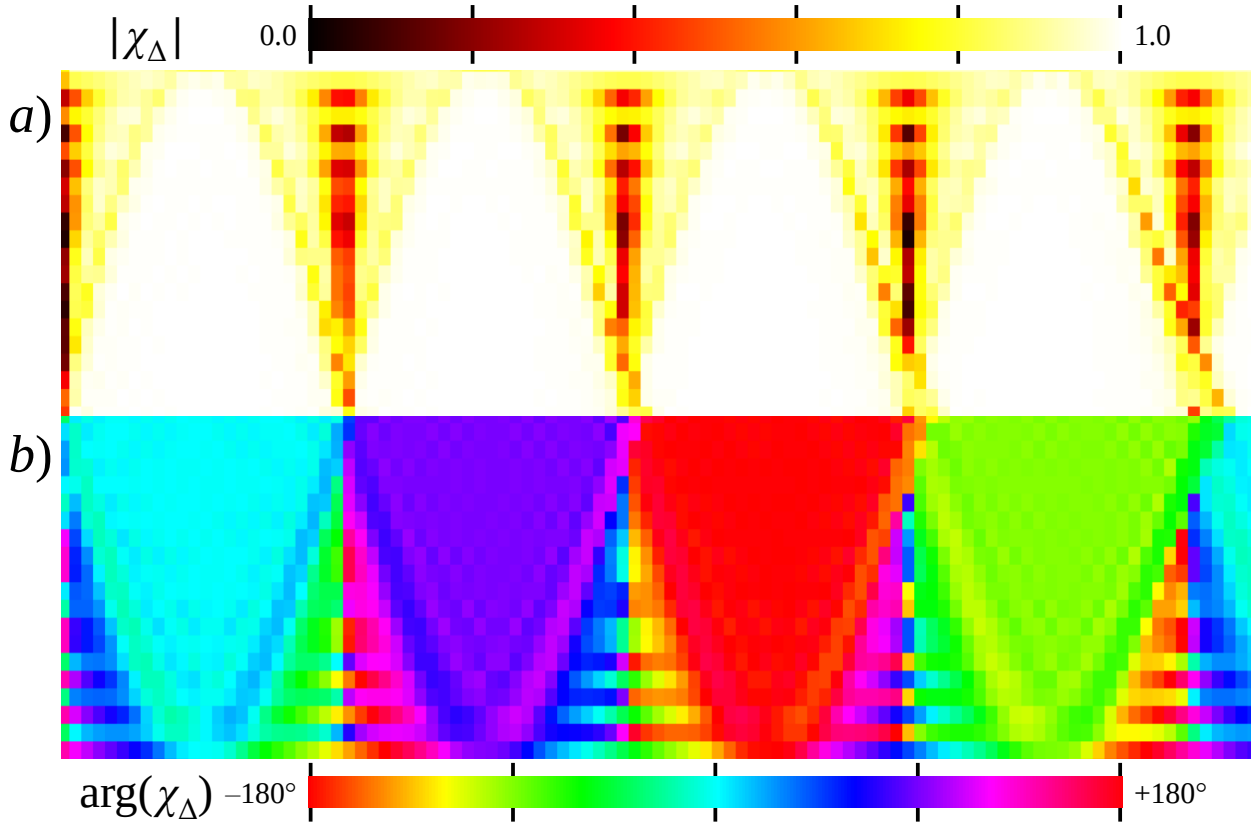

Figure 8.4: Cross correlation magnitude (upper) and phase (lower) for the frequency-difference autoproduct in the n^2-quadratic sound speed profile.

Fig. 8.4a shows that the magnitude of the cross-correlations in the well-ensonified regions (*i.e.* where rays are an adequate description of the local acoustic field) are very nearly unity. The magnitude plots also suggest mediocre results when evaluated on the edge of the well-ensonified region and the shadow zone. These mediocre cross-correlations are primarily a result of the amplitude variations near the caustic, and not phase variations. In the shadow zone, there are some regions with poor cross correlations, however due to the lack of leaky modes, the acoustic fields simulated in the shadow zones are not necessarily trustworthy.

In Fig. 8.4b, the phase of the cross correlations show a much more interesting result. Whereas prior studies have shown χ_Δ phases generally well under 90° , these plots show the full $\pm$ 180° variation. And more interestingly, between convergence zones, the well-ensonified region seems to show a constant phase shift. And as the sound passes through each convergence

zone, there appears to be a net $+90°$ phase shift in the cross-correlation. This behavior is due almost entirely to the caustic phase shift effect.

In elementary ray acoustics, infinite field amplitudes develop at caustics. However, if an additional term is carried out in the ray acoustics expansion, the so-called WKB approximation, this amplitude can be shown to be finite, but an additional phase factor of $-i$ develops for all acoustic waves passing through the caustic (Jensen 2011, Ludwig 1966). For environments with more complicated types of caustics (*i.e.* cusp-type), this caustic phase can become -1, or for particularly more exotic types of caustics, this phase shift can even be $+i$ (Kravtsov and Orlov 1993). A generalization of this phase shift for all caustics types is the KMAH index (Cerveny 1977, Chapman 2004, Kravtsov and Orlov 1993), which is an integer describing the effective number of simple (*i.e.* fold-type) caustics a particular ray has passed through; the net phase shift that acoustic fields described by that ray inherit then is $(-i)^n$, where n is the cumulative KMAH index of that ray.

To understand the effect of this caustic phase shift on the phase of χ_Δ, it is convenient to think of a ray passing through a caustic as comparable to a ray reflecting off a boundary where the acoustic field experiences an effective reflection coefficient of R, where $R = -i$ for simple caustics. The frequency-difference autoproduct, which is computed as $P(\omega_+)\, P^*(\omega_-)$, sees an effective reflection coefficient of $|-i|^2 = 1$. In other words, the frequency-difference autoproduct does not observe a caustic phase shift. Therefore, in the cross-correlation definition in (#), when $AP_\Delta P_\Delta^*$ is calculated, the net phase observed is $+i$, or $+90°$: exactly the same as observed in Fig. 8.4b. after the rays have passed through the first caustic. After each caustic, there is an accumulation of a $+90°$ phase shift on χ_Δ. This is clearly seen in Fig. 8.4b, with the regions between caustic zones vary with range as $0°$, $+90°$, $\pm$ $180°$, $90°$, and the edge of the next $0°$ region can be seen near the 5 km range.

Figures 8.5 and 8.6 are analogous figures to Figs. 8.3 and 8.4, except they depict the frequency-*sum* autoproduct instead, where the sum frequency $\Sigma\omega/2\pi$ is 6 kHz, averaged over

a difference frequency bandwidth from zero to $\frac{(\Omega_H - \Omega_L)}{2\pi} = (5-1)$kHz=4kHz. Specifically, Fig. 8.5a shows an amplitude plot of an out-of-band field at 6 kHz; Fig. 8.5b shows an amplitude plot of the frequency-sum autoproduct with twice the dynamic range; and in Figs. 8.6a and 8.6b, the magnitude and phase of χ_Σ, the cross correlation between the two plots shown in Figs. 8.5a and 8.5b, are shown. Note that the normalization region in these plots is also defined as rectangles that are 50m in range and 5 m in depth.

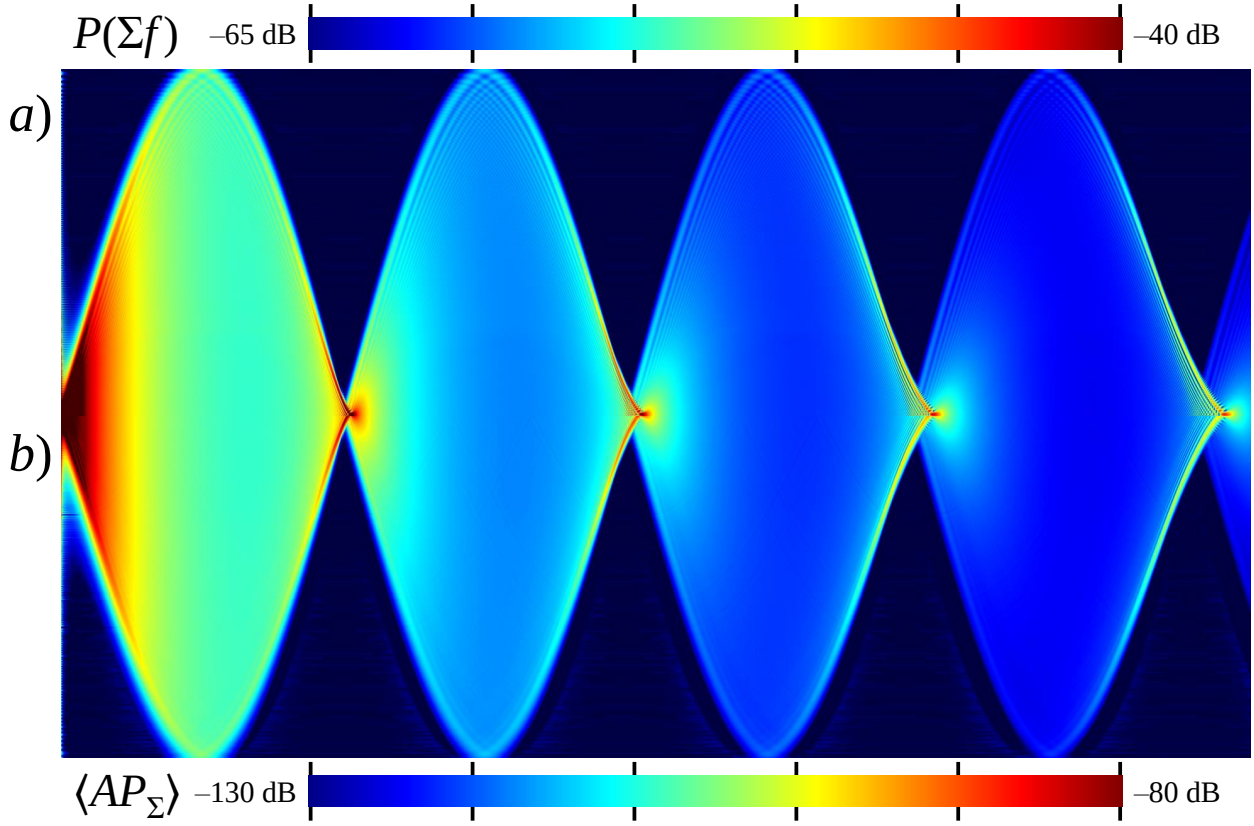

Figure 8.5: Transmission loss plot for the out-of-band (upper) and frequency-sum autoproduct (lower) field for a sum frequency of 6 kHz, derived from a bandwidth of 1 to 5 kHz. Note the dynamic range in the lower plot is double that of the upper plot.

Figs. 8.5a and 8.5b are much more similar to one another than Figs. 8.3a and 8.3b, particularly in the relative sizes of the caustics and convergence zones. This is primarily because the ratio of the center frequency (3 kHz) to the difference frequency (500 Hz) is larger than the ratio of the sum frequency (6 kHz) to the center frequency (3 kHz). As a result, Fig. 8.6a shows stronger cross correlations near the caustics than Fig. 8.4a. Additionally, it can

be seen in Fig. 8.6b that the frequency-sum autoproduct exhibits similar behavior in the phase of χ_Σ as χ_Δ does in Fig. 8.4b, except that the phase trend is reversed. Because the frequency sum autoproduct is defined as $P(\omega_2)\,P(\omega_1)$, the effective reflection coefficient for passing through a caustic is $(-i)^2 = -1$. Then, calculating χ_Σ as proportional to $AP_\Sigma P_\Sigma^*$, the net phase is thus $(-1)\,(-i)^* = -i$, or a 90° phase shift for each caustic passed through. This can be found in Fig. 8.6b, where the phase between convergence zones for increasing range varies as 0° , 90° , 180° , +90° , and then followed again by 0° at the far right of Fig. 8.6b.

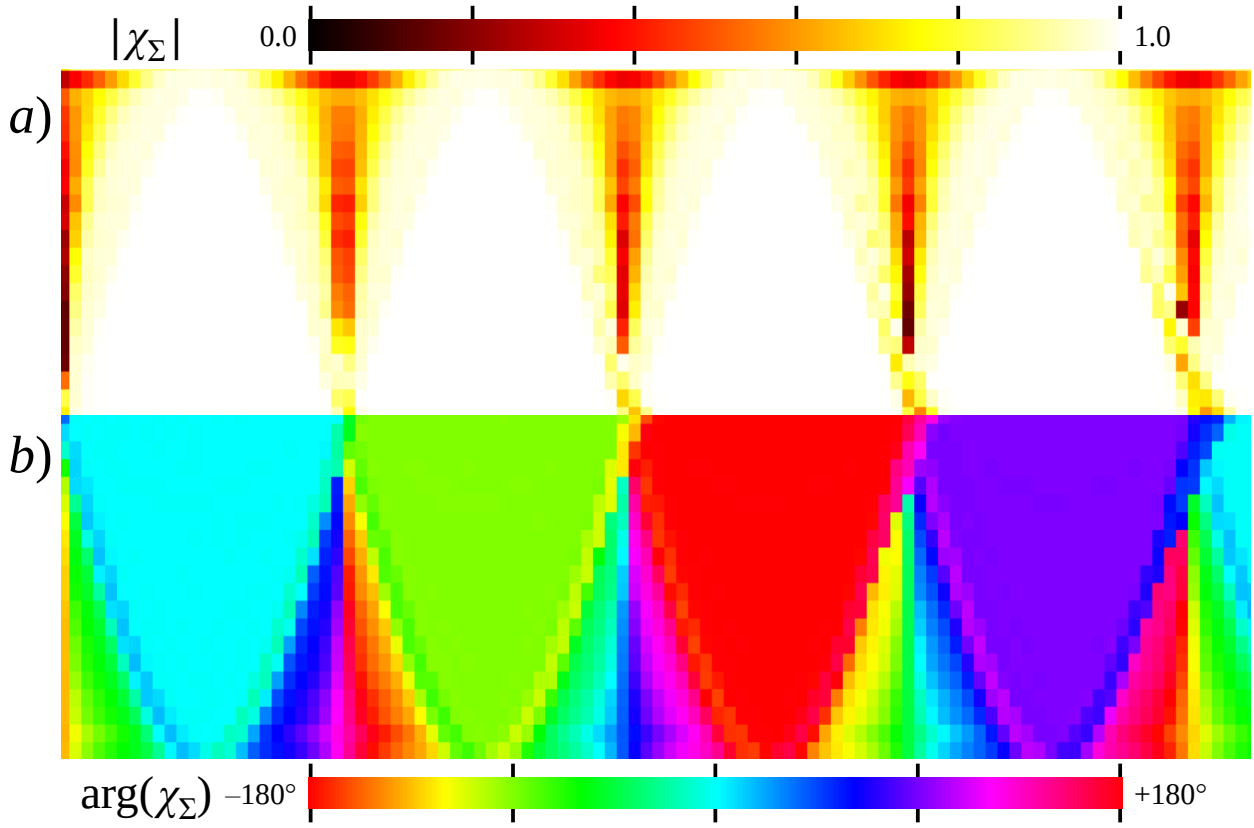

Figure 8.6: Frequency-sum autoproduct cross-correlations for a sum frequency of 6 kHz in the n^2-quadratic sound speed profile.

Overall, the 90° caustic phase shift causes phase shifts in $\chi_{\Delta,\Sigma}$ that are proportional to the number of caustics a ray has passed through. However, the magnitude of the cross correlation is generally still quite strong in well-ensonified regions, suggesting that autoproduct-based source localization techniques won't be impeded significantly. These findings are limited to

the n^2-quadratic profile, where the majority of the well-ensonified regions contain only one ray path. This changes for other profiles, such as the n^2-linear profile.

8.4 n^2-Linear

In this section, the range-independent waveguide with a refractive index given by equation (8.1), where $f(x) = x$ is given. In this environment, mode shapes in the inhomogeneous region are given by Airy functions (of the first and second kind), and are matched across the $|z| = L$ with either exponential decaying mode shapes in homogeneous region for trapped modes, or sinusoidal varying mode shapes in the homogeneous region for leaky modes. Both trapped and leaky modes are calculated exactly, though the eigenvalue root-finding calculation for the leaky modes is performed numerically. Details of this derivation can be found in Appendix B.

As in Section , the following parameters are used: $c_\infty = 1500$ m/s, $n_0 = 1500/1450$, and $L = 100$ m, with the plot domain varying from 5 km in range and $\pm$ 100 m in depth. Figure 8.7a and 8.7b show the ray trace and the transmission loss (amplitude) plot for a source at $(\boldsymbol{r}, z) = (0, 0)$ and frequency 5 kHz. Fig. 8.7b has a dynamic range of 100 dB.

In this environment, there are still rays that propagate at high angle (which correspond to leaky modes), and rays that propagate at low angle (which correspond to trapped modes). In this environment, there are many caustics, which all stem from the origin. Additionally, there are spatial regions reached by a variety of ray numbers, including zero rays (*e.g.* in the shadow zone), one ray (*e.g.* near the source, and after the first caustic), two rays (*e.g.*, the roughly triangular region where rays approach and return from the first caustic), and many rays (such as the rectangular region with three rays, where two are approaching and returning from the second caustic, and a third ray has exited the first caustic, and is passing through the second caustic).

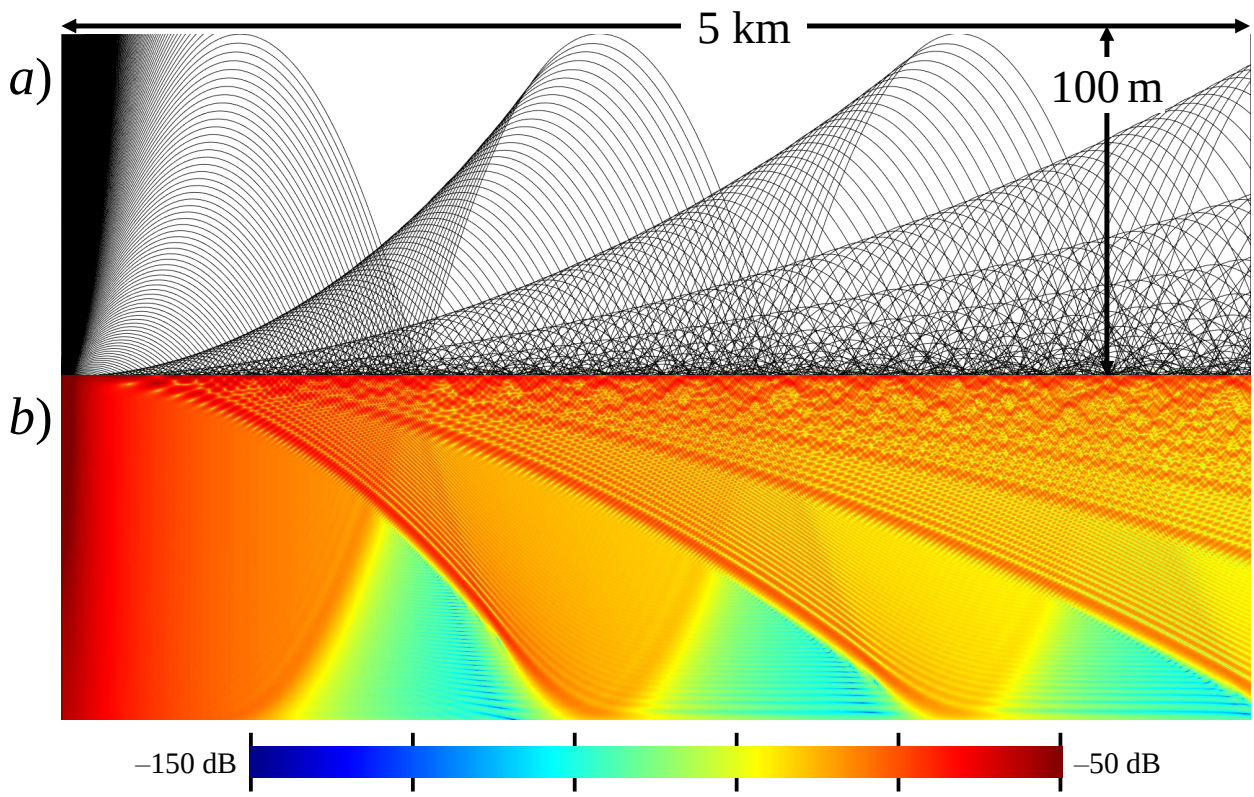

Figure 8.7: Plots of the ray trace (upper) and the transmission loss (lower) for a 5 kHz source at the origin of the n^2-linear sound speed profile.

Notably, due to the inclusion of the leaky modes, the acoustic field amplitudes at high propagation angles are non-zero, and close to the source, the amplitudes decay as approximately $1/r$, where r is the distance from the source - all of which are physically accurate. The shadow zones have amplitudes approximately 30 dB below the well-ensonified regions, and the structure observed in the shadow zones, including the patterning of nulls in depth, are physically accurate, again because of the inclusion of the leaky modes.

In Figure 8.8a, the magnitude of the out-of-band field is plotted at the difference frequency $\Delta\omega/2\pi = 1$ kHz, and in Fig. 8.8b, the magnitude of the autoproduct is plotted for the same difference frequency, but bandwidth averaged between $\Omega_L/2\pi = 4$ kHz and $\Omega_H/2\pi = 6$ kHz. The upper plot also spans 100 dB, and for similar reasons as in Fig. 8.3 and Fig. 8.5, the autoproduct plot spans 200 dB.

In Fig. 8.8, just as in Fig. 8.3, the downshifting of frequencies from a center frequency of 5 kHz to a difference frequency of 1 kHz creates significant differences in amplitudes. Beyond the caustics, there exists striations parallel to the caustic, which correspond to the interference layer (which describes the region where rays have a time-difference-of-arrival that is smaller than the inverse of the bandwidth available for averaging, which here is 1 kHz – see Chapter 5 for further discussion of interference layers). Beyond this interference layer, there is an interference pattern that emerges, creating a pattern of peaks that appear approximately as hexagons. These hexagons are roughly the same size as in the genuine out-of-band field in Fig. 8.8a., though happen to appear at slightly different locations. In this case, hexagons appear due to the presence of three rays traveling in different directions.

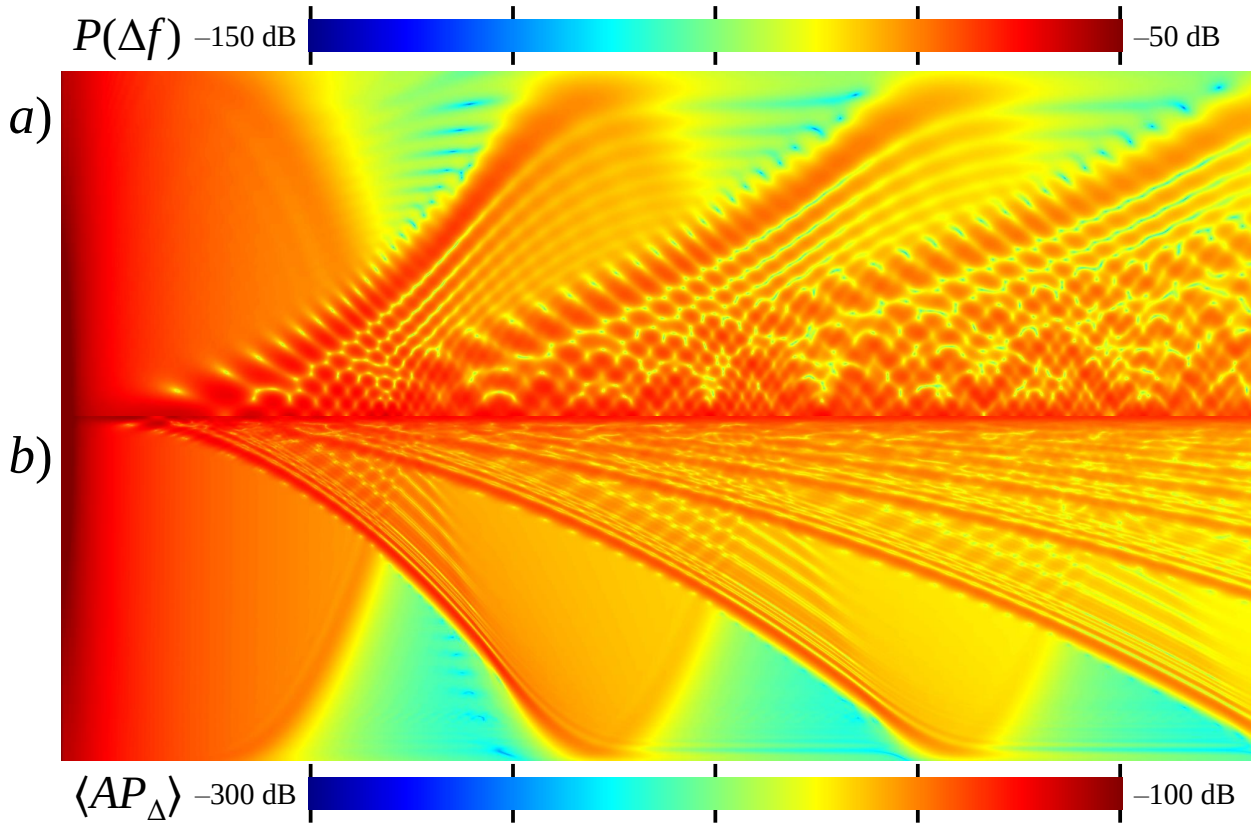

Figure 8.8: Transmission loss plots of the out-of-band field (upper) and frequency-difference autoproduct at a difference frequency of 1 kHz, derived from in-band fields between 4 and 6 kHz. Note that the dynamic range of the lower plot is double that of the upper plot.

The cross correlations between Fig. 8.8a and 8b can be found in Figure 8.9, where the

normalization regions are rectangles spanning 50 m in range, and 2 m in depth. In terms of the magnitude of χ_Δ, the high-angle regions near the source have strong cross correlations. Even the first shadow zone, along with subsequent shadow zones, have strong cross correlations – except at the shadow zone nulls, where poorer cross correlations exist – likely due to amplitude variations. Generally, it seems that in single-ray-path regions, there are strong cross correlations. In the single-ray-path regions, the caustic phase shift can be seen in Fig. 8.9b as well, where a cumulative +90° phase shift is observed in χ_Δ after each caustic.

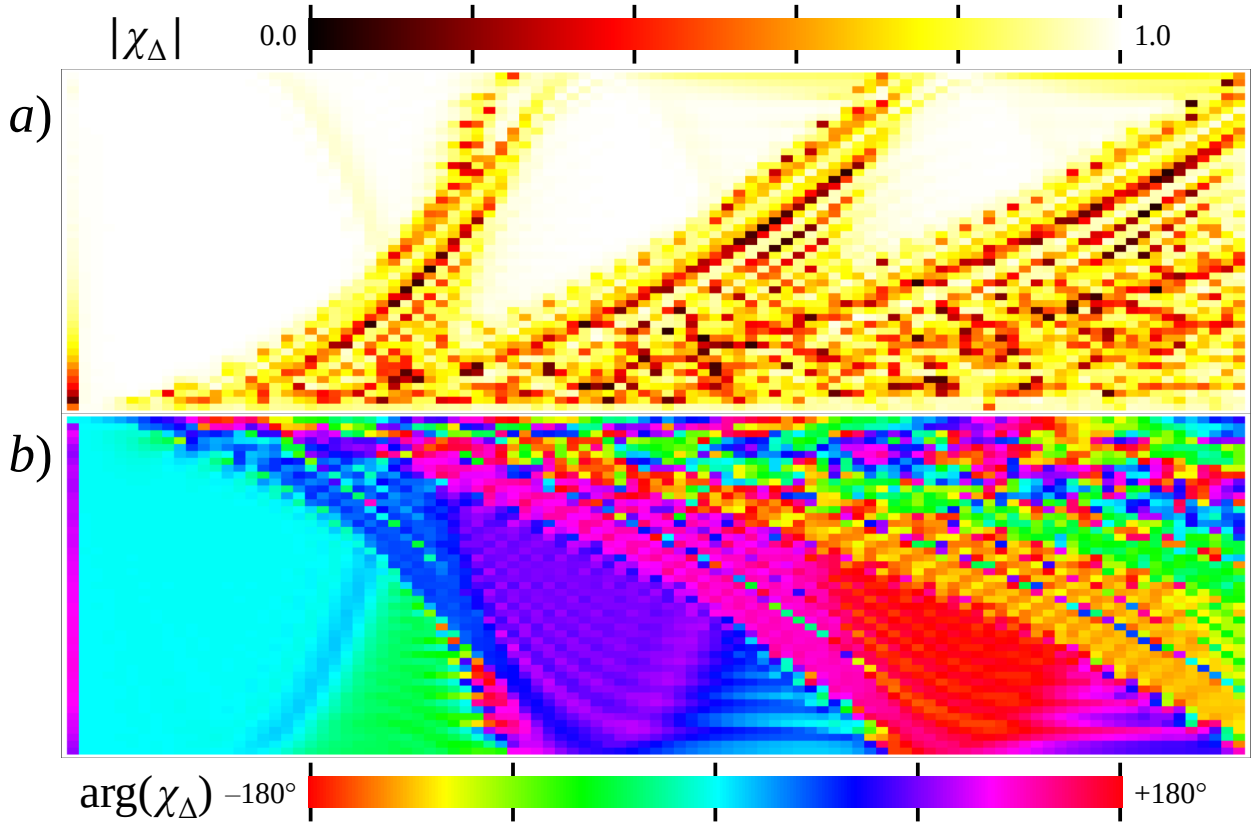

Figure 8.9: Cross correlation magnitude (upper) and phase (lower) between the frequency-difference autoproduct and an out-of-band field for a difference frequency of 1 kHz and a bandwidth of 4 to 6 kHz.

However, unlike in the n^2-quadratic profile, this n^2-linear profile features regions with multiple ray paths. In particular, there are regions where two rays exist – one that's approaching the caustic, and another that has passed through it and is now leaving the caustic. In these environments, much poorer cross-correlation magnitudes are observed. In these regions,

there also exist some exceptionally poor (near zero) cross correlations, particularly along lines that appear to travel parallel to the caustic, but in the two-path regions. These appear to stem from interference layers, which are associated with not having sufficient bandwidth with which to average over. This effect, combined with the amplitude variations associated with the larger downshift in frequency (from 5 kHz center frequency to 1 kHz difference frequency), create many regions of poor cross correlations in Fig. 8.9.

Another set of autoproducts is thus defined which does not shift down in frequency as far, and uses much more bandwidth for averaging. In Figure 8.10a, the magnitude of the field at a difference frequency of 5 kHz is shown alongside Fig. 8.10b, where a bandwidth averaged autoproduct is given with a $\Delta\omega/2\pi$ equal to 5 kHz, using an in-band bandwidth of $\Omega_L/2\pi =$ 1 kHz to $\Omega_H/2\pi = 9$ kHz. Note that here, the difference frequency is not truly outside the bandwidth of the original field – in fact the difference frequency is equal to the center frequency. Autoproducts formed in this manner are not expected to be particularly interesting for signal processing purposes, since the difference frequency field is already available in-band. However, for analysis purposes here, a center-frequency-to-difference-frequency ratio of unity is convenient, as is the wide bandwidth available for averaging. As a result, the amplitude variations and interference layers observed in Fig. 8.8 are now mitigated.

In Figure 8.11, the magnitude and phase of χ_Δ is plotted for the two fields given in Fig. 8.10. Here, both Fig. 8.11a and 11b show a smoother spatial variation in χ_Δ than in Fig. 8.9, but otherwise show roughly the same trends in terms of which regions have which cross-correlation magnitude and phase. The lines of poor cross-correlation magnitude that appear to follow the caustics are actually just below the true caustic. Along the caustic, strong cross correlation magnitudes exist. Just below the caustic there are interference layers that are still not averaged away, though their spatial extent is thin enough, relative to the normalization regions, that the effect of these interference layers is effectively only 1 normalization region in size now, unlike in Fig. 8.9 where the interference layers spanned over many normalization

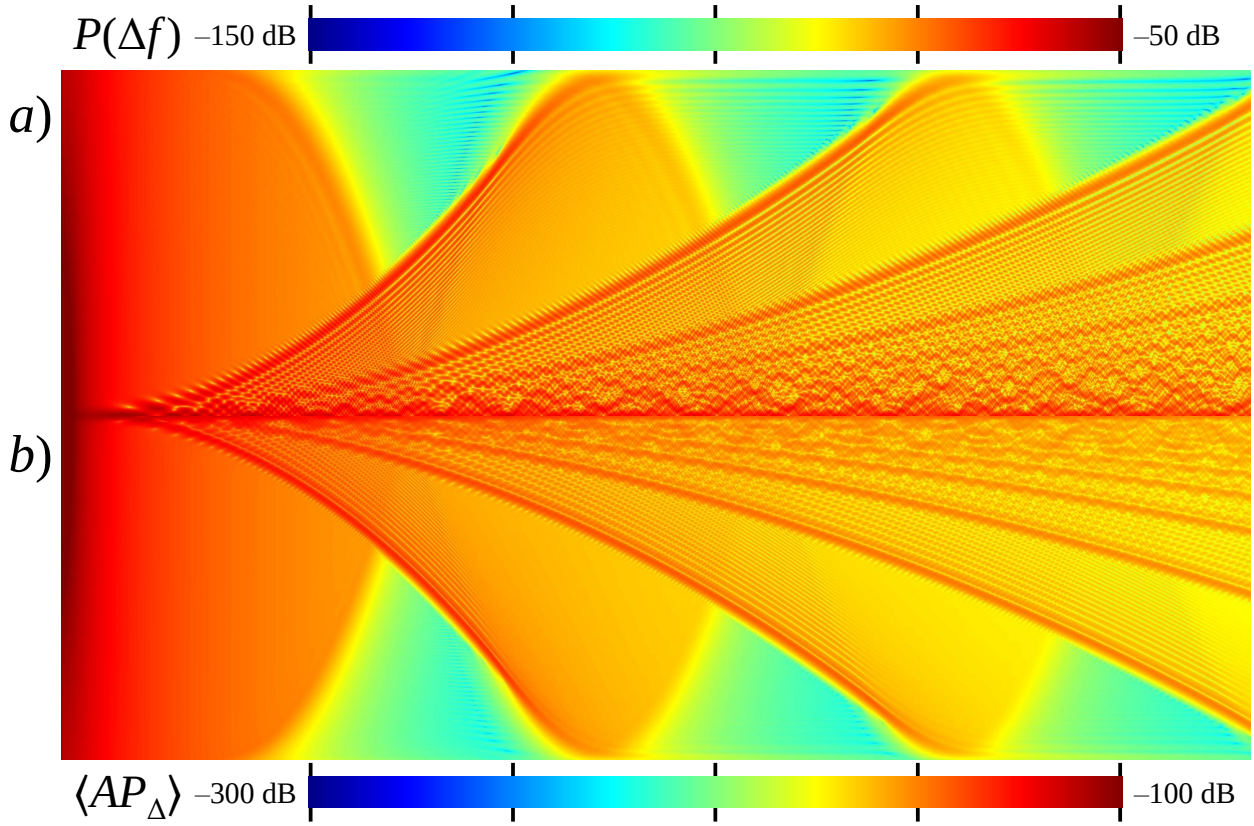

Figure 8.10: Transmission loss plots of the out-of-band field (upper) and frequency-difference autoproduct at a difference frequency of 5 kHz, derived from in-band fields between 1 and 9 kHz. Note that the dynamic range of the lower plot is double that of the upper plot.

regions in size. In the shadow zones, generally strong cross-correlation magnitudes still exist, with the significant exception of near the nulls that are formed in the shadow zone, where poor cross correlations emerge, some dropping as low as zero.

In the single-path regions, the phase of χ_Δ can be seen here to vary as before, with a $+90°$ phase shift being picked up after each caustic (see the cyan, violet, and red regions of the Fig. 8.11b, along with the light green region at the far-right edge of Fig. 8.11b), and these regions all have a corresponding $|\chi_\Delta|$ near unity.

In two-path regions, the phases of χ_Δ are now half-way between the $+90°$ increments. Specifically, consider the blue, magenta, orange, and bright green regions, which are associated approximately with $+45°$, $+135°$, $135°$ and $45°$, respectively. These regions have cross

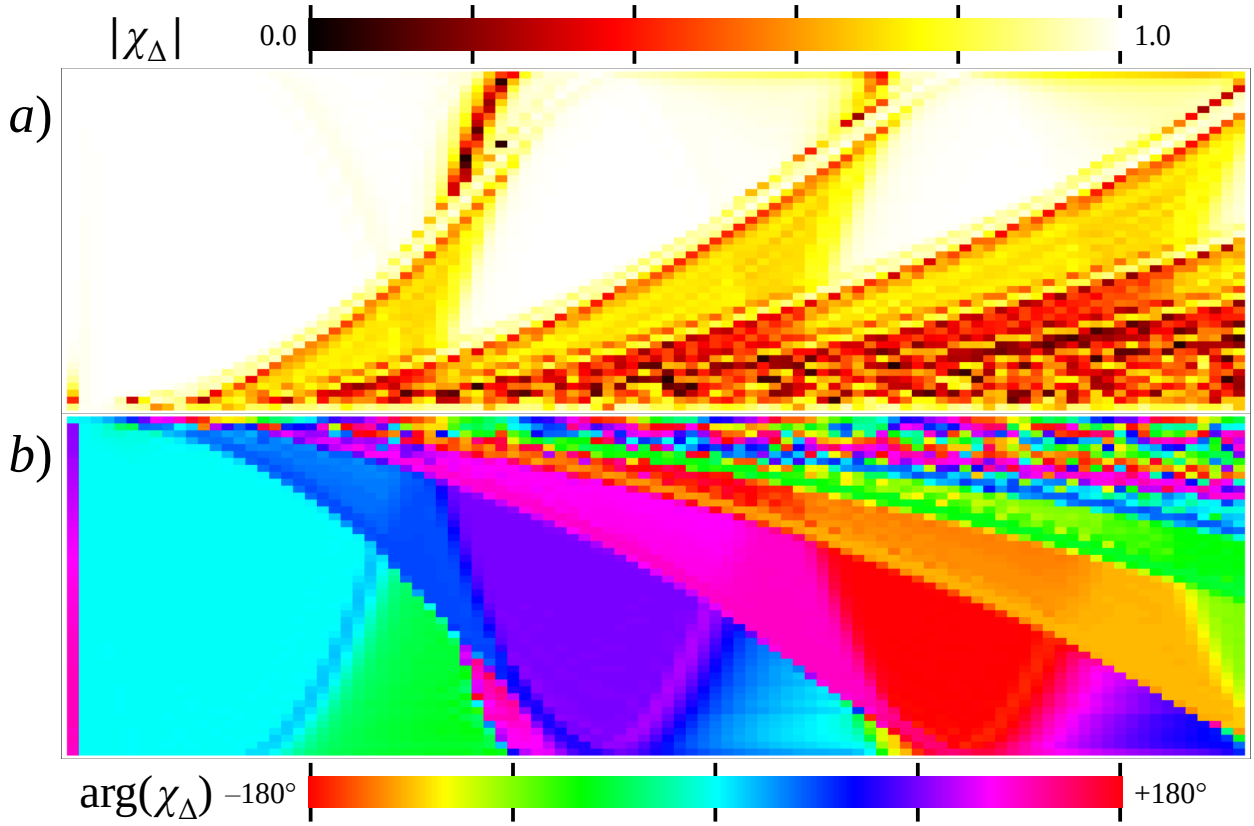

Figure 8.11: Cross correlation magnitude (upper) and phase (lower) between the frequency-difference autoproduct and an out-of-band field for a difference frequency of 5 kHz and a bandwidth of 1 to 9 kHz.

correlation magnitudes corresponding to approximately 0.7. To understand this behavior, consider an environment where a unity amplitude plane wave reflects off a boundary with effective reflection coefficient of $(-i)$, which is chosen to mimic passage of a ray through a caustic. In this two-path, plane wave environment, the acoustic field can be written as:

$$P = \exp(i\omega\tau_1) - i\exp(i\omega\tau_2), \tag{8.7}$$

where $\tau_{1,2}$ are plane wave propagation times for rays before and after reflecting from the boundary. Forming an autoproduct from this creates:

$$\langle AP_\Delta \rangle = \exp\left(i\Delta\omega\tau_1\right) + \exp\left(i\Delta\omega\tau_2\right) - i\exp\left(i\Delta\omega\frac{(\tau_1+\tau_2)}{2}\right)\mathrm{sinc}\left(\frac{\Omega_{BW}^{\Delta}\left(\tau_2-\tau_1\right)}{2}\right). \quad (8.8)$$

This last term is the cross term, which for $\Omega_{BW}^{\Delta}\left(\tau_2-\tau_1\right) \gg 2\pi$ (*i.e.* outside the interference layer), can be neglected. By normalizing these two fields over some normalization region (such as a region with plenty of variation in $\tau_{1,2}$, such that $\Delta\omega\left(\tau_2-\tau_1\right) \geq 2\pi$), it can be shown that

$$\chi_\Delta = \frac{1+i}{2} = \frac{\exp\left(\frac{i\pi}{4}\right)}{\sqrt{2}}. \quad (8.9)$$

Therefore, in the two-path region where rays are entering/exiting a caustic, when evaluated outside of the interference layer, and when amplitude variations can be neglected, the cross correlation has a magnitude of $\frac{1}{\sqrt{2}} \approx 0.71$ and a phase angle of $+45°$, just as observed in the darker blue regions of Fig. 8.11b. Generalizing this result for rays entering a caustic with a KMAH index of n, and exiting the caustic with a KMAH index of m, $\chi_\Delta = i^n\frac{\left(1+i^{m-n}\right)}{2}$. In other words, when passing through a simple (fold-type) caustic which increments the KMAH index by 1, χ_Δ will have a magnitude of $1/\sqrt{2}$ and a phase angle of $n \times 90° + 45°$. For a KMAH increment of 2, such as in a cusp-type caustic (Kravstov and Orlov 1993), χ_Δ acquires a magnitude of zero. And for a KMAH increment of 3, which might happen in some more exotic types of caustics – see Ch. 10 of (Kravstov and Orlov 1993), χ_Δ returns to a magnitude of $1/\sqrt{2}$, but has a phase angle of $n \times 90° - 45°$.

Finally, in regions that contain three rays, such as in the slightly lighter blue region bordering the one-path cyan region and the two-path blue region in Fig. 8.11b, the overall phase angle of χ_Δ can be thought of as a linear combination of the phase angle expected of χ_Δ for each ray individually. But because the two rays entering/exiting the caustic are of higher

amplitude than the one ray passing through the caustic, the net phase angle of χ_Δ in these three-path regions is very close to that of the neighboring two-path region.

Due to the symmetry and geometry of this problem, near $z = 0$, there are many rays propagating into and out of very shallow angle caustics. At $z = 0$ exactly, there are technically infinitely many caustics. This isn't particularly realistic for other environments, and is primarily an artifact of having a perfectly symmetric waveguide with a perfectly n^2-linear sound speed profile, with a source located perfectly along the line of symmetry. Therefore, the messy cross correlations near $|z| = 0$ are not particularly insightful for more realistic environments. Additionally, frequency-sum autoproduct plots behave mostly as anticipated, with the primary change being the phase angles of χ_Σ have the opposite sign relative to the plots of χ_Δ shown in Figs. 8.9b and 8.11b, and so for this reason, these plots are omitted.

8.5 Summary and Conclusion

Autoproducts have been found to be useful in a variety of applications (Abadi 2012, Worthmann 2015, Douglass 2017), but their theoretical limitations have only been studied within the ray approximation of acoustics. In this study, the effect of refraction and diffraction around caustics on the ability of autoproducts to mimic out-of-band fields was assessed. This was done by considering simple, range-independent waveguide environments with two different sound speed profiles: n^2-quadratic and n^2-linear. Cross correlations between autoproducts and out-of-band fields were computed, and their magnitude and phase were understood in the context of ray approximations. Particularly of interest were regions of acoustic fields near caustics, near shadow zones, near convergence zones, and regions well-described by rays that may have passed through caustics. Below, five conclusions from this study are described.

First, it is found that caustics introduce phase shifts in genuine acoustic fields that both

frequency-difference and frequency-sum autoproducts do not contain. This leads to overall phase offsets between genuine-acoustic and autoproduct fields that may or may not be a problem for autoproduct-based signal processing techniques.

Second, in single-ray-path regions, generally strong cross correlation magnitudes are observed; however, there exists an overall phase shift between autoproducts and out-of-band fields. This phase shift in the cross correlation for frequency-difference (frequency-sum) increments by $+90^\circ$ (90°) for each caustic that the acoustic waves pass through. But because many source localization algorithms typically only depend on relative phase difference across the array, then as long as the array is wholly contained within the same one-ray-path region (or at least approximately so), then this phase shift is not expected to be detrimental. Alternatively, if the source waveform were known, the number of caustics through which a particular ray has passed (mod 4) could be estimated.

Third, in regions with multiple rays, particularly regions where rays entering and leaving a particular caustic co-exist, cross correlations between autoproducts and out-of-band fields are degraded, with the upper bound of cross-correlation magnitudes in this environment being only $1/\sqrt{2}$ now, instead of the ideal value of 1. This is very problematic for signal processing algorithms such as matched field processing which require accurate phase estimates. Therefore, it is anticipated that in environments where multiple rays co-exist which have passed through different numbers of caustics, that the ability of a technique such as frequency-difference matched field processing would be substantially degraded. However, it is noted that mild caustic effects can still be overcome – for example, the KAM 11 environment used in Chapters 1 and 2 technically included rays which passed through caustics, but because several other rays were measured which did not pass through caustics (and were instead reflected), source localization here was not substantially degraded. So while the presence of caustics is not helpful for frequency-difference matched field processing, it may not necessarily cause it to catastrophically fail.

Fourth, regions with multiple rays were found to exhibit interference layers, the size of which are inversely proportional to the bandwidth available for averaging the autoproducts. These interference layers derived from caustics differ only in shape from the interference layers formed from flat reflecting boundaries, as described in prior work (Worthmann and Dowling 2017). Depending on environmental parameters, rays may travel on separate paths, but can still arrive at a particular point at nearly the same time (such as what happens near caustics). If the product of the time-difference-of-arrival and the bandwidth available for averaging is not much greater than unity, then cross terms formed in the autoproduct can substantially degrade autoproduct-to-out-of-band cross correlations.

Fifth, beyond the difficulties the caustic phase introduces, amplitude variations exist which are related, and proportional to, how far from unity the ratio of the out-of-band frequency to the center frequency of the in-band field is. In other words, shifting down in frequency too far can cause some amplitude related problems, since the autoproduct retains many of the same amplitude features as the in-band signal.

Overall, this study shows that the caustic phase represents a substantial challenge for autoproducts to mimic out-of-band fields, as well as a challenge for autoproduct-based signal processing algorithms which rely on accurate phases, such as matched field processing. It is possible that ad hoc phase corrections could resolve some of these problems. Resolving these difficulties may also be possible through the development of an alternative formulation of matched field processing which is based on matching autoproduct fields directly.

CHAPTER 9

Cross Term Analysis for Dynamic Range Expansion

Abstract

Matched field processing, or MFP, is well-known to be sensitive to environmental uncertainties, a problem that leads to *mismatch* between the measured and modeled fields. This sensitivity increases with frequency and routinely causes conventional MFP techniques to fail in imperfectly known environments at frequencies of interest. Frequency-difference MFP techniques, on the other hand, involve a nonlinear signal processing step that shifts the signal processing to lower frequencies where MFP is known to be robust to environmental uncertainties. While shown in previous work to be successful at localizing sources that conventional techniques are unable to, the dynamic range of the resulting frequency-difference MFP ambiguity surfaces (the outputs of MFP) were relatively low (single-digit dB), potentially suggesting a lack of robustness that was not commensurate with the observed level of robustness. In this study, theoretical models of simple multi-path environments are employed to learn about the reasons for this decreased dynamic range, and the culprit is found to be the production of cross-terms, one of the unintended side effects of the nonlinear frequency-difference technique. Pre- and post-processing correction techniques are developed that are designed to mitigate the effects of these cross terms. The performance of these

techniques within a simulated Lloyd's mirror environment, a simulated ideal sound channel, and with experimental data suggests that the dynamic range can be robustly improved for frequency-difference MFP techniques.

9.1 Introduction

Physics based source localization algorithms, such as matched field processing (MFP) (Bucker 1976), are well-known to be sensitive to environmental uncertainty (Baggeroer 1993). Frequency-difference MFP (Δf-MFP) is a recently developed source localization algorithm which, by construction, is robust to imperfect environmental knowledge at arbitrarily high frequencies. The technique is based upon a nonlinear mathematical construction called the frequency-difference autoproduct, which has the ability to take high frequency acoustic fields with some bandwidth, and create from them a new field which can mimic an acoustic field at a lower frequency, subject to some limitations. These limitations have been explored within the ray approximation (Worthmann and Dowling 2017, Lipa 2018), where it was found that multipath environments lead to the production of unwanted cross terms in the autoproducts. It is suspected that these cross terms lead to a degradation in the performance of Δf-MFP, but the exact mechanism is unknown. The purpose of this study is to better understand the physical and mathematical implications of autoproduct cross terms, and to develop signal processing techniques to mitigate their detrimental effects on Δf-MFP.

Autoproduct-based localization techniques, such as Δf-MFP and frequency-difference beamforming (Abadi *et al.* 2012, Worthmann *et al.* 2015, Douglass *et al.* 2017), have been shown to be robust to well-known array signal processing problems, such as environmental mismatch (Worthmann *et al.* 2015) and array sparseness (Douglass *et al.* 2017) – both of which tend to become problems at high frequency. By shifting the signal processing down to lower frequency, autoproduct techniques can be thought of as trading spatial resolution for robust-

ness. However, one of the unintended side effects of autoproduct techniques is the decreased dynamic ranges that emerge in the beamformer outputs and the Δf-MFP ambiguity surface. Typically, poor dynamic range is associated with low signal-to-noise ratios, or more generally, a localization result that is not robust. But Δf-MFP techniques have been found to in fact be robust, despite what their poor dynamic range may imply. Adaptive Δf-MFP techniques were investigated (Worthmann *et al.* 2017), and while many of these adaptive techniques were found to improve the dynamic range, generally the improvement was only marginal (just a few dB). Therefore, this study to learn the fundamental causes behind the decreased dynamic range is important, and is the first step toward improving the dynamic range of autoproduct-based techniques.

The most likely cause of the decreased dynamic range, which is evident even in simple simulations with infinite signal-to-noise ratios, is the production of cross-terms due to the multiplication of multi-path acoustic fields. It was shown in prior work (Worthmann and Dowling 2017) that autoproducts may mimic out-of-band fields (*i.e.* fields at frequencies lying outside the original bandwidth) within the ray approximation under two conditions. First, the amplitude of the rays must spatially vary slowly, relative to the wavelength. Second, in multi-path regions, the difference in time-of-arrival of any two rays at a point should be large, relative to the inverse of the bandwidth available for averaging – in other words, rays should be well separated in time. By bandwidth averaging autoproducts to mitigate cross terms, these two conditions were found to be sufficient to match autoproduct fields with out-of-band fields. However, direct matching of fields is only possible when the source waveform is known; Δf-MFP techniques require indirect matching of fields due to the unknown source waveform. This paper uses simple acoustic fields to study how cross terms affect the indirect matching of the fields necessary for Δf-MFP, and techniques to mitigate their detrimental effect are considered.

In Section 9.2, autoproducts and Δf-MFP techniques are defined. In Section 9.4.2, the

Lloyd's mirror environment is defined, and a discussion of the cross terms' effect on dynamic range is discussed. In Section 9.4, techniques to mitigate cross terms are described. In Section 9.5, results of these cross-term mitigation techniques are provided for a Lloyd's mirror environment, as well as other, more complicated environments. In Section 9.6, a summary of this study is given, along with the conclusions that can be drawn from it.

9.2 Autoproducts and Δ f-MFP Overview

9.2.1 Definitions

The frequency-difference autoproduct is defined as a product of an acoustic field as measured at two different frequencies, but the same location, or in other words:

$$AP_{\Delta}\left(\boldsymbol{r}, \Delta\omega, \omega\right) = P\left(\boldsymbol{r}, \omega + \frac{\Delta\omega}{2}\right) P^{*}\left(\boldsymbol{r}, \omega - \frac{\Delta\omega}{2}\right) \tag{9.1}$$

where $P\left(\boldsymbol{r}, \omega\right)$ is the in-band field which was measured or simulated, the difference (center) frequency of the frequency pair is $\Delta\omega$ (ω), and the asterisk represents a complex conjugate. To perform conventional MFP, a quantity called the cross-spectral density matrix, or CSDM, is required, which is defined as:

$$\left[\underline{\mathbf{R}}_{conv}\left(\omega\right)\right]_{nm} = P\left(\boldsymbol{r}_{n}, \omega\right) P^{*}\left(\boldsymbol{r}_{m}, \omega\right) \tag{9.2}$$

where $\boldsymbol{r}_{n}$ is the position of the nth receiver, and $\underline{\mathbf{R}}_{conv}$ is the conventionally-defined CSDM. For Δf-MFP, the CSDM is defined similarly with the in-band field P switched out and with the autoproduct field AP_{Δ} switched in:

$$\left[\underline{\mathbf{R}}_{AP}\left(\Delta\omega\right)\right]_{nm} = \frac{1}{\Omega_H - \Omega_L - \Delta\omega} \int_{\Omega_L + \frac{\Delta\omega}{2}}^{\Omega_H - \frac{\Delta\omega}{2}} AP_{\Delta}\left(\boldsymbol{r}_n, \Delta\omega, \omega\right) AP_{\Delta}^{*}\left(\boldsymbol{r}_m, \Delta\omega, \omega\right) d\omega \qquad (9.3)$$

where the CSDM includes a bandwidth average over ω, where all possible pairs of $\omega \pm \Delta\omega/2$ within the signal bandwidth between Ω_L and Ω_H are included. Note that the bandwidth average is performed in the same manner as an ensemble average over multiple realizations (snapshots) would be handled in conventional MFP (Jensen 2011). However, all the results presented here are based upon only a single snapshot of the recorded field.

The purpose of a CSDM is to create a quantity that depends on source-to-array propagation but is independent of the source's waveform. Typically, the source is not broadcasting a perfect impulse (where $S\left(\omega\right) = 1$), and is in general unknown. However, in the case where there is only one source, the phase at one array element *relative* to other array elements, is independent of the source waveform's phase, and depends only on the Green's function connecting the true source location to the array elements. The amplitude of the source waveform is treated here as constant with respect to frequency, and after a normalization procedure defined later, cancels out entirely. However, a variable amplitude source waveform (*e.g.* Gaussian shading) can either be compensated for before the bandwidth average (by artificially amplifying frequency information to be constant across the bandwidth) or treated as entirely unknown (which means higher amplitude frequencies are weighted to be more important for localization than lower amplitude frequencies).

To perform localization, MFP compares measured and modeled fields. Or, more specifically, the relative phase and amplitude information in the CSDM is correlated with relative phase and amplitude information from a modeled field, or replica. This modeled field, $w_n\left(\boldsymbol{r}, \omega\right)$ is the simulated acoustic field at a set of receivers at position $\boldsymbol{r}_n$ due to a source at frequency ω at a guessed location $\boldsymbol{r}$. An ambiguity surface is formed by comparing how well the

measured data (CSDM) correlates with the modeled data (replica), as a function of guessed source locations. Mathematically, the ambiguity surface, $B(\boldsymbol{r})$, is defined as:

$$B_{conv}(\boldsymbol{r},\omega) = \frac{\mathbf{w}_{conv}^{\dagger}(\boldsymbol{r},\omega)\cdot\underline{\mathbf{R}}_{conv}^{norm}(\omega)\cdot\mathbf{w}_{conv}(\boldsymbol{r},\omega)}{\mathbf{w}_{conv}^{\dagger}(\boldsymbol{r},\omega)\cdot\mathbf{w}_{conv}(\boldsymbol{r},\omega)} \tag{9.4}$$

for conventional MFP, where $\mathbf{w}_{conv}$ is a vector of field calculations at the in-band frequency ω for each array element, the † symbol indicates a complex conjugate and transpose, and the 'norm' superscript refers to the following normalization scheme:

$$[\ \ ]^{norm} = \frac{[\ \ ]}{\mathrm{trace}([\ \ ])} \tag{9.5}$$

For Δf-MFP, the following ambiguity surface definition is used:

$$B_{AP}(\boldsymbol{r},\Delta\omega) = \frac{\mathbf{w}^{\dagger}(\boldsymbol{r},\Delta\omega)\cdot\underline{\mathbf{R}}_{AP}^{norm}(\Delta\omega)\cdot\mathbf{w}(\boldsymbol{r},\Delta\omega)}{\mathbf{w}^{\dagger}(\boldsymbol{r},\Delta\omega)\cdot\mathbf{w}(\boldsymbol{r},\Delta\omega)} \tag{9.6}$$

The denominators in (9.4) and (9.6) are chosen such that B is guaranteed to be between 0 (for a very poor match, corresponding to an unlikely source location) and 1 (for a perfect match, corresponding to a likely source location).

9.2.2 Replica Calculation Modifications

The replica calculations for $\mathbf{w}_{conv}(\boldsymbol{r},\omega)$ and $\mathbf{w}(\boldsymbol{r},\Delta\omega)$ both satisfy the wave equation, though the former satisfies it at the in-band frequency, ω, and the latter satisfies it at the difference frequency, which in general can be much lower. Due to the quadratic nonlinearity however, the boundary conditions for the two replicas may different. In particular, a pressure-release boundary condition is typical for the ocean surface; however, for the difference frequency

replica, $\mathbf{w}(\boldsymbol{r}, \Delta\omega)$, the surface boundary condition should instead be treated as rigid. While seemingly unphysical, it is one of the byproducts of the nonlinear technique. More details on this boundary condition change can be found in (Worthmann *et al.* 2015) and (Worthmann and Dowling 2017).

Additionally, at the lower difference frequency, a different type of wave propagation calculation may be necessary. If the in-band, high frequency field satisfies the ray approximation, it is not guaranteed that the out-of-band, lower difference frequency field also satisfies the ray approximation. In prior work, it was found that in a shallow ocean environment, the difference frequency replica calculation should be performed using a modal decomposition (typical for low frequencies), *not* a ray code (typical for high frequencies). In most of the calculations here, the field at the difference frequency is evaluated using an exact or partial ray-path-sum Green's function, much like the higher frequency in-band fields. The one exception is the KAM 11 experimental results provided in Section 9.5.

9.2.3 Robustness to Environmental Uncertainties

Consider a simple single-ray-path environment, $P(\boldsymbol{r}, \omega) = A\exp(i\omega\tau(\boldsymbol{r}))$, where $\tau(\boldsymbol{r})$ and A are the ray-path travel time and amplitude from a source to the specified spatial location, r, respectively. The autoproduct for this situation is $AP_{\Delta}(\boldsymbol{r}, \Delta\omega) = |A|^2\exp(i\Delta\omega\tau(\boldsymbol{r}))$, which is the same as an out-of-band acoustic field at the difference frequency, with a modified amplitude. For the purposes of MFP, suppose there is some discrepancy between τ as measured and as modeled, due to environmental uncertainties. Define $\delta\tau \equiv \tau_{measured} - \tau_{modeled}$, which is a measure of the amount of environmental mismatch. Evaluating B_{conv} and B_{AP} for this simple environment, one arrives at $\cos(\omega\delta\tau)$ and $\cos(\Delta\omega\delta\tau)$, respectively, for the correct guessed source location. If the in-band frequency is too high, relative to the level of uncertainty, a poor match may be found at the true source location, leading MFP to fail to localize the source. However, with frequency-difference techniques, $\Delta\omega$ can be chosen

by the user, and therefore can be chosen to be small compared to $\delta\tau$, thus, in principle, allowing localization for any level of mismatch. However, at particularly low difference frequencies, spatial resolution of the ambiguity surface may be poor, since robustness is obtained in Δf-MFP by sacrificing spatial resolution.

9.2.4 Cross Terms

Consider the field in a two-path environment, defined as:

$$P(\omega) = A_1 \exp(i\omega\tau_1) + A_2 \exp(i\omega\tau_2) \tag{9.7}$$

where $A_{1,2}$ is a frequency-independent amplitude, and $\tau_{1,2}$ are ray-path travel times. Forming the autoproduct, as in (9.1) leads to:

$$AP_\Delta(\omega, \Delta\omega) = |A_1|^2 e^{i\Delta\omega\tau_1} + |A_2|^2 e^{i\Delta\omega\tau_1} + 2|A_1||A_2| e^{\frac{i\Delta\omega(\tau_1+\tau_2)}{2}} \cos(\omega(\tau_2 - \tau_1) + \phi) \tag{9.8}$$

where $\phi = \arg(A_2 A_1^*)$. The first two terms represent the two arrivals at the difference frequency (with modified amplitude coefficients), and the final term is the so-called cross term, formed from a mixing of the first and second arrivals at different frequencies. Its phase factor shows an arrival half-way between the two, modulated by an amplitude which depends on the center-frequency ω. In earlier work (Worthmann and Dowling 2017), this field was directly bandwidth averaged, which produced:

$$\langle AP_{\Delta} \rangle (\Delta\omega) = |A_1|^2 e^{i\Delta\omega\tau_1} + |A_2|^2 e^{i\Delta\omega\tau_1} + 2|A_1||A_2| e^{\frac{i\Delta\omega(\tau_1+\tau_2)}{2}} \cos(\Omega_C \Delta\tau + \phi) \operatorname{sinc}\left(\frac{\Omega_{BW}^{\Delta}\Delta\tau}{2}\right) \tag{9.9}$$

where $\Delta\tau = \tau_2 - \tau_1$; $\Omega_{BW}^{\Delta} = \Omega_H - \Omega_L - \Delta\omega$; $\Omega_C = \frac{(\Omega_H + \Omega_L)}{2}$; and $\operatorname{sinc}(x) = \frac{sin(x)}{x}$. Here, the cross-term is suppressed for $\Omega_{BW}^{\Delta}\Delta\tau \gg 2\pi$. If, given limited bandwidth, $\Omega_{BW}^{\Delta}\Delta\tau < 2\pi$, then this region is defined within the *interference layer*, effectively a region where the cross terms are not suppressed, and the autoproduct's ability to mimic out-of-band fields is degraded. However, this analysis relies upon bandwidth averaging AP_{Δ} fields *directly*, whereas Δf-MFP bandwidth averages autoproduct fields *indirectly*, by way of the CSDM. By studying bandwidth-averaged CSDMs themselves, rather than their constituent autoproduct fields, the effect of cross terms can more carefully assessed.

9.3 Cross Term Analysis

In order to carefully study autoproducts and their effect on Δf-MFP, a simple, but physically relevant problem is desired. For this purpose, the Lloyd's mirror environment is chosen, which is a two-path environment formed by a homogeneous semi-infinite medium bounded above by a flat, pressure-release boundary. First, the simulation parameters are described, and then a mathematical analysis follows for how a two-path environment affects Δf-MFP.

9.3.1 Simulation Parameters

In this study, an isotropic point source is located at $(r, z) = (500, 50)$ meters, where $z = 0$ refers to the flat pressure-release surface, and $r = 0$ corresponds to the location of the vertical line array recording the source's waveform (see Figure 9.1). The source's waveform spans

24 – 26 kHz, and has uniform amplitude within this spectrum. The specific details of the source waveform's phase structure (*i.e.* chirp, band-limited impulse, or randomized noise) will not affect the analysis here thanks to the use of a CSDM. The vertical line array has 34 elements, spanning from $z = 0$ to $z = 100$ meters (which for a sound speed of 1500 m/s corresponds to half-wavelength spacing for 250 Hz). To simulate environmental mismatch, each receiver element is moved from its nominal position in range and depth by δr and δz, which each have a mean of 0 and a standard deviation of 6 centimeters (one wavelength at the center frequency of 25 kHz). Each receiver's range and depth shift is independent of one another.

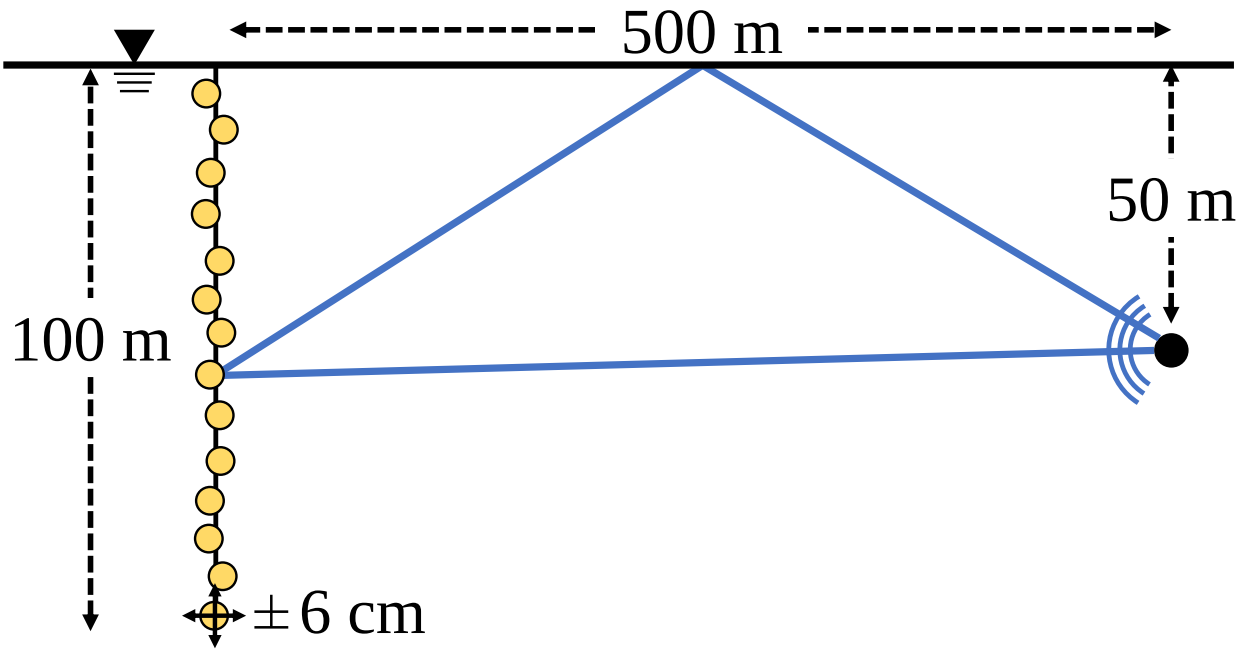

Figure 9.1: Schematic of the Lloyd's mirror environment, where a vertical line array with 34 elements, spanning 100 meters, receives a 24 – 26 kHz broadcast from a source at a range and depth of 500 meters and 50 meters, respectively.

Performing conventional MFP under these conditions gives the ambiguity surface shown in Figure 9.2a. Due to the severity of the mismatch chosen for this environment, conventional MFP is predictably unable to localize the source, which is evident in Fig. 9.2a due to the lack of a clear and unambiguous peak. Note that mismatch produces a fundamentally different effect than noise – mismatch destroys the desired peak, whereas noise hides it.

For the same simulation parameters (except a rigid boundary is used instead), a source broadcasting 250 Hz would produce the ambiguity surface in Fig. 9.2b, which can also be thought of as conventional MFP, just at the difference frequency. In this case, a clear peak is found in the ambiguity surface at the correct source location. Finally, in Fig. 9.2c, the Δf-MFP result is given, which uses the same data that Fig. 9.2a was created from, but applies it to equation (9.6) instead of (9.4). Here, a clear localization result is found as well, and is qualitatively very similar to Fig. 9.2b, which utilizes a genuine low frequency field. The similarity between Fig. 9.2b and 9.2c suggests that autoproducts do in fact mimic out-of-band fields at the difference frequency. Note that Fig. 9.2c cannot be used to resolve ambiguities in Fig. 9.2a, since there will not, in general, be a peak at the true source location of Fig. 9.2a. Thus, one must choose between in-band techniques which are high resolution but sensitive to mismatch, and frequency-difference techniques, which are low resolution but less sensitive to mismatch.

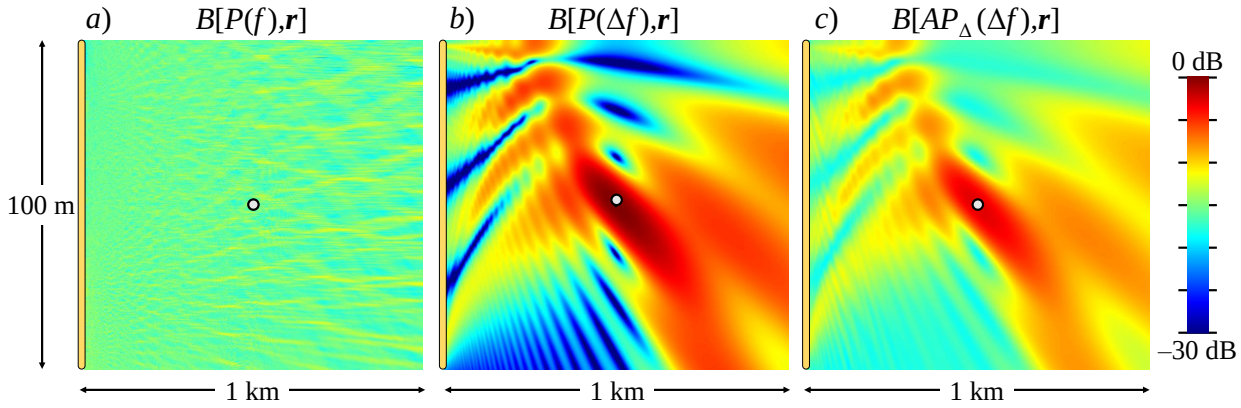

Figure 9.2: Ambiguity surfaces for a Lloyd's mirror environment. Panel *a*) shows the ambiguity surface for conventional MFP, performed between 24 and 26 kHz. Panel *b*) shows the ambiguity surface for conventional MFP at a lower frequency of 250 Hz. Panel *c*) shows the ambiguity surface for Δf-MFP, where 24 – 26 kHz is shifted down to 250 Hz.

The most important difference between Fig. 9.2b and 2c is the amount of dynamic range. Dynamic range is defined here to be the span of values B takes on over the sampled search grid of $\boldsymbol{r}$. Instead of utilizing the full maximum and minimum, which can be overly sensitive to the particular search grid used, so here, dynamic range is defined to be range of values

B spans in the middle 99% of values (in other words, the difference between the 99.5th and 0.5th percentiles). Fig. 9.2b has a dynamic range of 35 dB, and a maximum value (at the true source location) of 0.02 dB (of the maximum possible 0 dB). Fig. 9.2c, on the other hand, has a dynamic range of only 15 dB, and a maximum value of 3 dB. Since the only real difference between Figs. 2b and 2c are the presence of cross terms, one is forced to conclude that cross-terms are the cause of this decreased dynamic range and maximum. However, the cross-term analysis shown in Section 9.2.4, where the size of the cross-terms, relative to the desired self-terms, are proportional to $\text{sinc}\left(\Omega_{BW}^{\Delta}\Delta\tau/2\right)$, which for this environment has a magnitude of 0.026, or 32 dB. This would suggest the effects from cross-terms are negligible. However, this analysis was based upon averaging fields directly, not averaging CSDM's. A CSDM-based analysis is provided in the next subsection.

9.3.2 Self and Cross Term Analysis

For the Lloyd's mirror two-path environment, the in-band acoustic field can be represented with:

$$P\left(r,z,\omega\right)=S\left(\omega\right)\left(\frac{e^{i\omega r_1/c}}{r_1}-\frac{e^{i\omega r_2/c}}{r_2}\right)=A_1\exp\left(i\omega\tau_1\right)+A_2\exp\left(i\omega\tau_2\right) \tag{9.10}$$

where $A_1=S\left(\omega\right)/r_1$, $A_2=-S\left(\omega\right)/r_2$, $\tau_{1,2}=r_{1,2}/c$, and $r_{1,2}=\sqrt{\left(\boldsymbol{r}-\delta r\right)^2+\left(z+\delta z\mp d\right)^2}$, which corresponds to the direct and reflected paths between the source at range and depth (r,d), and the receiver at $(\delta r, z+\delta z)$. Forming the autoproduct from this gives:

$$AP_{\Delta}\left(\omega,\Delta\omega\right)=\left|A_1\right|^2e^{i\Delta\omega\tau_1}+\left|A_2\right|^2e^{i\Delta\omega\tau_2}+2\left|A_1\right|\left|A_2\right|e^{\frac{i\Delta\omega(\tau_1+\tau_2)}{2}}\cos\left(\omega\left(\tau_2-\tau_1\right)+\phi_{21}\right) \tag{9.11}$$

where $\phi_{21} = \arg\left(A_2 A_1^*\right) = \pi$. To simplify the following analysis, a factor of $|A_1|\,|A_2|\,e^{\frac{i\Delta\omega(\tau_1+\tau_2)}{2}}$ is taken from each of the terms to give:

$$AP_\Delta\left(\omega,\Delta\omega\right) = |A_1|\,|A_2|\,e^{i\Delta\omega\tau_c}\left(\frac{|A_1|}{|A_2|}e^{-\frac{i\Delta\omega\Delta\tau}{2}} + \frac{|A_2|}{|A_1|}e^{\frac{i\Delta\omega\Delta\tau}{2}} + 2\cos\left(\omega\Delta\tau+\phi_{21}\right)\right) \tag{9.12}$$

where $\tau_c = \frac{(\tau_1+\tau_2)}{2}$, $\Delta\tau = \tau_2 - \tau_1$. For mathematical convenience, one additional parameter is defined: $\alpha = \ln\left(|A_1|\,/\,|A_2|\right) = \ln\left(r_2/r_1\right)$ (where $\alpha \geq 0$, since $r_2 \geq r_1$). This allows the following simplification:

$$AP_\Delta\left(\omega,\Delta\omega\right) = C_n\cos\left(\frac{\Delta\omega\Delta\tau}{2} + i\alpha\right) + C_n\cos\left(\omega\Delta\tau+\phi_{21}\right) \tag{9.13}$$

where C_n is simply the common factor of $2\,|A_1|\,|A_2|\,e^{i\Delta\omega\tau_c}$. On the right-hand side, the first term is the desired self-term, and the second term is the unintentional cross-term. In an effort to evaluate $\underline{\mathbf{R}}_{AP}\left(\Delta\omega\right)$ in (9.3), the expression in (9.13) needs to be evaluated for the n th receiver and m th receiver, and then multiplied together with a complex conjugate.

$$AP_{\Delta,n}\left(\omega,\Delta\omega\right)AP^*_{\Delta,m}\left(\omega,\Delta\omega\right) = SS_{nm} + SC_{nm} + CC_{nm} \tag{9.14}$$

The three terms on the right-hand side correspond to the self-self terms, self-cross terms, and cross-cross terms, which are defined as:

$$SS_{nm} = C_n C_m^*\cos\left(\frac{\Delta\omega\Delta\tau_n}{2} + i\alpha_n\right)\cos\left(\frac{\Delta\omega\Delta\tau_m}{2} - i\alpha_m\right) \tag{9.15}$$

$$\begin{aligned} SC_{nm} =& C_n C_m^* \cos\left(\frac{\Delta\omega\Delta\tau_n}{2} + i\alpha_n\right)\cos\left(\omega\Delta\tau_m + \phi_m\right) \\ &+ C_n C_m^* \cos\left(\frac{\Delta\omega\Delta\tau_m}{2} - i\alpha_m\right)\cos\left(\omega\Delta\tau_n + \phi_n\right) \end{aligned} \tag{9.16}$$

$$CC_{nm} = C_n C_m^* \cos\left(\omega\Delta\tau_n + \phi_n\right)\cos\left(\omega\Delta\tau_m + \phi_m\right) \tag{9.17}$$

Next, a bandwidth average is required. At this point, in order to proceed, knowledge of $|S(\omega)|$ is needed. To keep the expressions analytic, it is convenient to define $|S(\omega)|$ to be constant, such as S_0. However, this restriction is not strictly necessary for Δf-MFP to robustly estimate source locations. As discussed in Section 9.2.1, allowing $|S(\omega)|$ to vary over the bandwidth means frequency pairs with higher amplitudes are weighted more heavily in the bandwidth average. However, it is more convenient here to assume $|S(\omega)| = S_0$. As a result, we may begin bandwidth averaging (9.15), (9.16) and (9.17), since the $|A_1||A_2|$ term inside $C_{n,m}$ is simply $S_0^2/r_1 r_2$, and, importantly, is independent of ω. This gives:

$$\left[\underline{\mathbf{R}}_{AP}(\Delta\omega)\right]_{nm} = \langle SS\rangle_{nm} + \langle SC\rangle_{nm} + \langle CC\rangle_{nm} \tag{9.18}$$

For the self-self term, none of the terms depend on ω, and so the bandwidth average leaves this untouched:

$$\langle SS\rangle_{nm} = C_n C_m^* \cos\left(\frac{\Delta\omega\Delta\tau_n}{2} + i\alpha_n\right)\cos\left(\frac{\Delta\omega\Delta\tau_m}{2} - i\alpha_m\right) \tag{9.19}$$

For the other two terms, it is convenient to note the following identities:

$$\langle\cos\left(\omega\tau + \phi\right)\rangle = \cos\left(\Omega_C\tau + \phi\right)\operatorname{sinc}\left(\frac{\Omega_{BW}^{\Delta}\tau}{2}\right) \tag{9.20}$$

$$2\cos(x+y) = \cos(x-y) + \cos(x+y) \tag{9.21}$$

Thus, for the self-cross terms, we find:

$$\begin{aligned}\langle SC\rangle_{nm} =& C_n C_m^* \cos\left(\frac{\Delta\omega\Delta\tau_n}{2} + i\alpha_n\right)\cos\left(\Omega_C\Delta\tau_m + \phi_m\right)\operatorname{sinc}\left(\frac{\Omega_{BW}^{\Delta}\Delta\tau_m}{2}\right)\\ &+ C_n C_m^* \cos\left(\frac{\Delta\omega\Delta\tau_m}{2} - i\alpha_m\right)\cos\left(\Omega_C\Delta\tau_n + \phi_n\right)\operatorname{sinc}\left(\frac{\Omega_{BW}^{\Delta}\Delta\tau_n}{2}\right)\end{aligned} \tag{9.22}$$

And for the cross-cross terms, we find:

$$\begin{aligned}\langle CC\rangle_{nm} =& \frac{1}{2}C_n C_m^*\left[\cos\left(\Omega_C\left(\Delta\tau_n + \Delta\tau_m\right) + \phi_n + \phi_m\right)\operatorname{sinc}\left(\frac{\Omega_{BW}^{\Delta}\left(\Delta\tau_n + \Delta\tau_m\right)}{2}\right)\right]\\ &+ \frac{1}{2}C_n C_m^*\left[\cos\left(\Omega_C\left(\Delta\tau_n - \Delta\tau_m\right) + \phi_n - \phi_m\right)\operatorname{sinc}\left(\frac{\Omega_{BW}^{\Delta}\left(\Delta\tau_n - \Delta\tau_m\right)}{2}\right)\right]\end{aligned} \tag{9.23}$$

In the final step, the normalization in (9.5) is performed:

$$\left[\underline{\mathbf{R}}_{AP}(\Delta\omega)\right]_{nm}^{norm} = \frac{\langle SS\rangle_{nm} + \langle SC\rangle_{nm} + \langle CC\rangle_{nm}}{\sum_p\left[\langle SS\rangle_{pp} + \langle SC\rangle_{pp} + \langle CC\rangle_{pp}\right]} \tag{9.24}$$

The denominator then is the sum over all the receivers, or $\sum_p[\ \ ]$, of the following three terms:

$$\langle SS\rangle_{pp} = |C_p|^2\,\frac{1}{4}\left(\frac{|A_{1,p}|^2}{|A_{2,p}|^2} + \frac{|A_{2,p}|^2}{|A_{1,p}|^2} + 2\cos\left(\Delta\omega\Delta\tau_p\right)\right) \tag{9.25}$$

$$\langle SC \rangle_{pp} = |C_p|^2 \cos\left(\frac{\Delta\omega\Delta\tau_p}{2}\right)\left(\frac{|A_{1,p}|}{|A_{2,p}|}+\frac{|A_{2,p}|}{|A_{1,p}|}\right)\cos\left(\Omega_C\Delta\tau_p+\phi_p\right)\operatorname{sinc}\left(\frac{\Omega_{BW}^{\Delta}\Delta\tau_p}{2}\right) \quad (9.26)$$

$$\langle CC \rangle_{pp} = \frac{1}{2}|C_p|^2\left[\cos\left(2\Omega_C\Delta\tau_p+2\phi_p\right)\operatorname{sinc}\left(\Omega_{BW}^{\Delta}\Delta\tau_p\right)+1\right] \quad (9.27)$$

Taken together, the self-self, self-cross, and cross-cross terms form the AP_{Δ} CSDM, the real part of which is plotted in Figure 9.3a for the Lloyd's mirror environment defined here. Compare that to Fig. 9.3b, which is the CSDM for a genuine out-of-band field at the true source location, or, effectively, is an outer product of the replica vector. In this context, B at the true source location is the double-dot-product between these two matrices. In Figure 9.3, the horizontal *and* vertical coordinates refer to receiver number, which because this is a vertical line array, both dimensions can be thought of as depth. The white areas in those matrices occur at depths corresponding to nulls at one of the two depth coordinates. To better understand the behavior of the CSDMs, these were sampled in depth much more finely than every 3 meters (for half-wavelength spacing at $\Delta\omega$). Because there are spatial features in the autoproduct CSDMs which occur at the in-band wavelength of 6 cm, these CSDMs were created from a spatial sampling of every 3 cm.

Fig. 9.3a and 9.3b share many macroscopic features, but differ in a few ways. First, the cross-hatching features that occur everywhere are associated with the environmental uncertainty that's introduced by moving the receivers around (which is still done in an uncorrelated, Gaussian random fashion, even for this finer sampling). Second, there are additional striations that occur along the top and left of Fig. 9.3a. Finally, there are additional noisy features that occur along the main diagonal of the matrix. Each of these features are explained below.

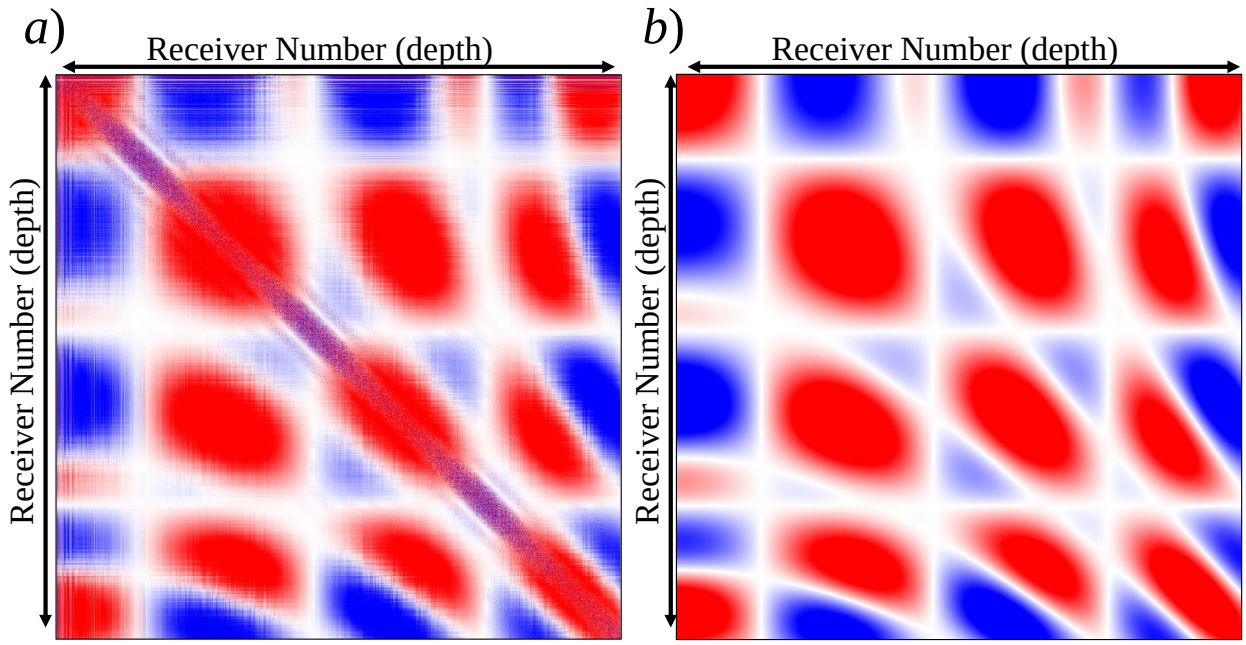

Figure 9.3: Real part of cross spectral density matrices. Panel a) shows the normalized and bandwidth averaged autoproduct CSDM, including environmental uncertainties. Panel b) shows the normalized out-of-band CSDM at the difference frequency, and excludes environmental uncertainties. The color scale in both plots is $\pm 0.9\sqrt{N}$, where N is the number of receivers, with red corresponding to positive values.

To better understand these features in Fig. 9.3a, three separate CSDM plots are shown in Figure 9.4. Figs. 9.4a, 9.4b, and 9.4c correspond to the self-self, self-cross, and cross-cross CSDMs for an autoproduct field without environmental uncertainty. Figs. 9.4d, 9.4e and 9.4f provide analogous results which include environmental uncertainty. The addition of Figs. 9.4d, 9.4e and 9.4f would reproduce Fig. 9.3a; the same color scale is used on all CSDM plots here.

It is evident from comparing Figs. 9.4a and 9.4d that environmental mismatch appears visually as cross-hatching, and that these self-self terms compare very favorably with Fig. 9.3b, which shows the CSDM for a true out-of-band field. These are the terms autoproducts were intended to create, and are the primary source of their utility for sound source localization.

In Figs. 9.4b and 9.4e, self-cross terms are pictured. Effectively, these can be thought of as the product of cross terms at one receiver multiplied by the self-terms at another receiver.

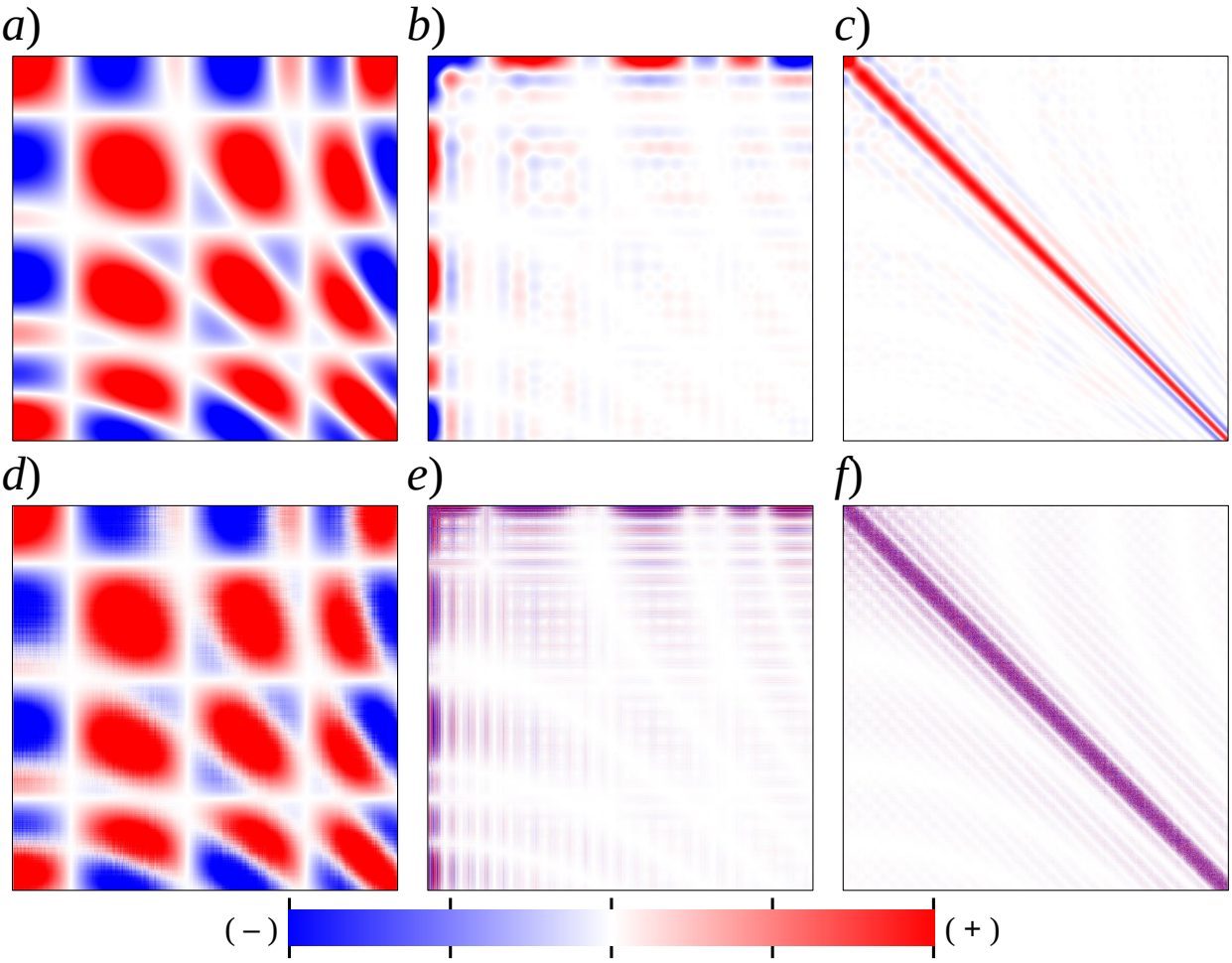

Figure 9.4: Real part of the autoproduct CSDM constituents: self-self terms (panels a and d), self-cross terms (panels b and e) and cross-cross terms (panels c and f). The upper row gives the CSDMs without environmental uncertainty; the lower row includes environmental mismatch. The color scale here, as before varies between $\pm 0.9\sqrt{N}$, where N is the number of receivers.

Thus, they contain nulls at similar locations as Fig. 9.4a and 4d, but this is modulated by a sinc $\left(\frac{\Omega_{BW}^{\Delta}\Delta\tau}{2}\right)$. This sinc-function creates peaks near the surface, where $\Delta\tau$ is close to zero, and thus the sinc-function takes on values close to 1. These are the expected cross-terms based upon earlier analyses. The environmental mismatch randomizes the phases here, as these cross terms are still sensitive to the center frequency in the form of the $\cos\left(\Omega_C\Delta\tau + \phi\right)$ terms appearing in (9.26). However, in the absence of uncertainty, these terms take on a very particular structure near the surface, as shown in Fig. 9.4b.

The cross-cross terms, after bandwidth averaging, have two contributions: one that depends on $\text{sinc}\left(\Omega_{BW}^{\Delta}\left(\Delta\tau_n + \Delta\tau_m\right)/2\right)$ and a second that depends on $\text{sinc}\left(\Omega_{BW}^{\Delta}\left(\Delta\tau_n - \Delta\tau_m\right)/2\right)$, as seen in (9.27). Since $\Delta\tau$ is strictly positive (except at the surface it's zero), it is simple to conclude that the first term should be negligible beyond the interference layer at the surface. The second term, on the other hand, is significant when the difference in the time-difference-of-arrival between any two array elements is small compared to the bandwidth available for averaging. Thus, it is anticipated that array elements which are close to each other (*i.e.* observe similar time-of-arrivals) are contributing to this cross-cross term's effect. In other words, on a CSDM, these terms can be seen to be concentrating on the main diagonal, which without mismatch take on strictly positive values on and near the diagonal, until the difference in time-difference-of-arrivals between successively farther away pairs of phones is now large compared to the bandwidth. Without mismatch, the phases are again randomized owing to the presence of the $\cos\left(\Omega_C\left(\Delta\tau_n - \Delta\tau_m\right) + \phi_n - \phi_m\right)$ term, which implies time-difference-of-arrival sensitivity to the center frequency, Ω_C. If there were some correlation length in depth associated with the movement of the receivers, then the off-diagonal elements close to the diagonal would retain more phase structure comparable to Fig. 9.4c.

To determine the effect that each of these terms has on source localization, the $\langle SS\rangle_{nm}$, $\langle SC\rangle_{nm}$, and $\langle CC\rangle_{nm}$ terms are each, independently, treated as the full $\underline{\mathbf{R}}_{AP}$ CSDM, and then plugged into (9.6). The ambiguity surface results are given in Figure 9.5. The addition of Figs. 5a, 5b, and 5c would reproduce Fig. 9.2c. Note that $\langle SC\rangle_{nm}$ is not positive semi-definite, which is required to guarantee that $B \geq 0$. In order to display these results on a logarithmic scale, a magnitude of B is taken for this case.

Fig. 9.5a shows the self-self terms, which have many of the same features as Fig. 9.2b, such as a high dynamic range. Notably, the maximum value of B is not negligibly close to 0 dB because the $\langle SS\rangle_{nm}$ terms were normalized with the full denominator in (9.24), and were *not* renormalized in (9.5) on their own. Had normalization been performed on $\langle SS\rangle_{nm}$ directly,

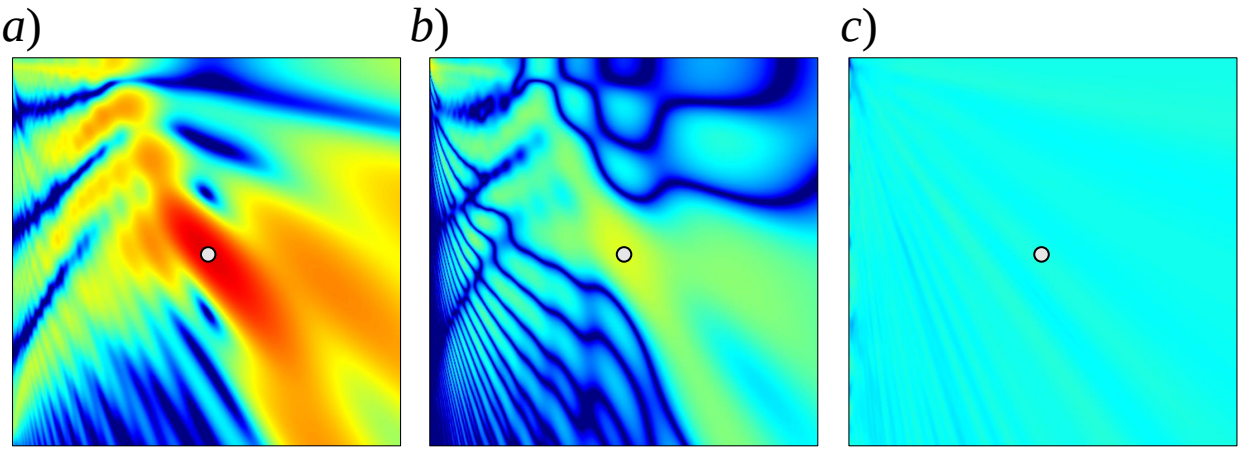

Figure 9.5: Frequency difference ambiguity surfaces for the self-self terms (a), self-cross terms (b), and cross-cross terms (c). The spatial and color axes span the same values as in Fig. 9.2.

Fig. 9.5a would be negligibly different from Fig. 9.2b.

Fig. 9.5b shows the self-cross terms. Due to the lack of positive semi-definiteness there are more nulls now, and these are no longer local minima, but rather occur along a curve, with the former local minima now appearing as local maxima. It is clear that these results are helping correct localization, but in a small way, since this peak is about 10 dB lower than the peak in Fig. 9.5a. In MFP, the dot product of replica matrices with CSDMs can be recast equivalently as the magnitude-squared of the dot product of the modeled field with the measured field, or $\left|P^{\dagger}\cdot\mathbf{w}\right|^{2}$. However, because R_{nm} for the self-cross terms are effectively the outer product of self terms and cross terms, (9.6) with $R_{nm}=\langle SC\rangle_{nm}$ can be thought of equivalently as $B=2\left(S^{\dagger}\cdot\mathbf{w}\right)\left(\langle C\rangle^{\dagger}\cdot\mathbf{w}\right)$, where S and $\langle C\rangle$ are the self and bandwidth-averaged cross term vectors, respectively. The lack of semi-positive-definiteness is evident from this form, as there is no guarantee that $\left(S^{\dagger}\cdot\mathbf{w}\right)$ and $\left(\langle C\rangle^{\dagger}\cdot\mathbf{w}\right)$ take on the same sign. However, in view of Fig. 9.5b being a product of two scalars: $\left(S^{\dagger}\cdot\mathbf{w}\right)$, which would contain a peak at the correct source location, and $\left(\langle C\rangle^{\dagger}\cdot\mathbf{w}\right)$ which is not anticipated to have any real structure in the presence of environmental mismatch. Thus, Fig. 9.5b appears as a lower amplitude version of Fig. 9.5a, which is the same as $\left|S^{\dagger}\cdot\mathbf{w}\right|^{2}$.

Fig. 9.5c shows the cross-cross terms. There is no evident structure in this result – it is effectively a DC offset to the results in Fig. 9.5a. Thus, the source of the degraded dynamic range is clear: the cross-cross terms in the presence of environmental mismatch lead to an ambiguity surface which is very similar to a pure Gaussian noise result. Looking at the terms in (9.18), it is suspected that the terms on the main diagonal of $\langle CC \rangle_{nm}$ are the main contributors to this noise-like structure.

Thus, it is evident that the bandwidth averaged cross-cross terms, hitherto not studied, are the source of the degraded dynamic range in Δf-MFP. Additionally, because cross terms are highly sensitive to environmental uncertainty (much like the high frequency in-band fields from which they are derived), their main contribution to the CSDM lies along the diagonal. In other words, for the nth receiver, the cross terms there correlate weakly with cross terms at all the receivers except itself, with which it of course correlates strongly. These diagonal cross-term correlations, found on the main diagonal of the autoproduct CSDM, are the culprit behind reduced dynamic range in Δf-MFP. In the next section, two techniques are outlined which attempt to mitigate these effects.

9.4 Cross Term Subtraction

Thanks to the analysis in the last section, the structure and form of the cross terms is now better understood. It would be tempting, then, to use this knowledge to compute the autoproduct, then compute the $\langle SC \rangle$ and $\langle CC \rangle$ contributions, and coherently subtract. In the absence of mismatch, this is certainly possible, and would be quite robust. However, in the presence of mismatch, it is found that the phase of the cross terms is sensitive to environmental mismatch. Thus, in order to coherently subtract the cross terms in a meaningful way, the time-of-arrivals must be known sufficiently well relative to the center frequency Ω_C. In other words, coherent subtraction of cross-terms is realistically only possible when in-band MFP is

successful, but then frequency-difference autoproduct techniques aren't needed, since there is no need to trade spatial resolution for increased robustness. And, because the source waveform is unknown in general, attempts to estimate times-of-arrival based on recorded data is not possible (however, in principle, blind deconvolution techniques could be used to try and resolve the time-of-arrivals anyway – this is not considered in this study). Effectively, due to the mismatch, cross terms behave the same way as uncorrelated noise on the array would.

So, cross terms cannot be subtracted coherently in a robust manner. In what follows, two techniques are proposed to mitigate the effect of these cross terms: Monte Carlo cross term subtraction, and diagonal-zeroing.

9.4.1 Monte Carlo Cross Term Subtraction

This idea was inspired by noise subtraction techniques, such as SEMWAN (Blacodon 2011), where in addition to some convex optimization procedures ignored here, there are also noise CSDMs which are repeatedly measured and averaged, and then subtracted from a signal-plus-noise CSDM to improve poor dynamic range. The idea here is to apply analogous techniques for Δf-MFP, where cross-term CSDMs are repeatedly simulated and averaged, and then subtracted from the self-plus-cross-term CSDM. The cross-term CSDMs are simulated repeatedly in the known environment, with many realizations of the uncertain environments included. The idea is that, if the statistics of the environmental uncertainty were known at least approximately, Monte Carlo random environmental realizations could be used to calculate the cross term CSDMs.

It is important to note that the form of the cross-terms is dependent upon where the source location is. In other words, this technique requires knowledge of the source's position. To estimate that, frequency-difference MFP finds a peak in the standard ambiguity surface, $B_{AP}(\boldsymbol{r}, \Delta\omega)$. Then, this peak location is treated as the true source location to be used

in calculating the cross-term CSDMs in this technique. Thus, this is a post-processing technique, and while it is expected to improve the dynamic range, the peak in the localization plot is not expected to move significantly.

In this scheme, depending on the kind of environmental uncertainties present, the coherent contributions to the cross-term CSDM would survive averaging and be useful for subtraction, while the incoherent, noise-like contributions would be averaged away. This is advantageous since, as assumed here, only one snapshot of the measured data is available; it is better to subtract nothing from a Gaussian random variable with mean zero (*i.e.* noise), than it is to subtract from it another mean-zero Gaussian random variable. On the other hand, cross-term components of the measured CSDM that are random but non-mean-zero *can* be subtracted away coherently, leaving behind a new Gaussian random variable with a mean of approximately zero. Of course, all of this requires having known statistics of the environment (*i.e.* means and variations of various environmental parameters, such as array-element shifts in range and depth). The situation of unknown, or imperfectly known, environmental statistics is not considered here, though it is not expected to be a major detriment to the technique.

In SEMWAN, the noise and signal-plus-noise CSDMs are formed from the same experimentally determined data sets, and thus the noise and signal-plus-noise CSDMs already contain the correct amplitude information for subtracting. However, in Δf-MFP, absolute amplitudes are not known, since the self-plus-cross-term CSDM may in principle be formed from experimental data, and the cross-term CSDMs that are to be estimated come from simulated data. Therefore, a normalization procedure must be utilized.

Define $[\underline{\mathbf{R}}_{CT}]_{nm}$ to be the cross term CSDM to be subtracted from the measured data. For this technique, this is evaluated as:

$$[\underline{\mathbf{R}}_{CT}]_{nm} = \langle \frac{\langle SC \rangle_{nm} + \langle CC \rangle_{nm}}{\sum_p [\langle SS \rangle_{pp} + \langle SC \rangle_{pp} + \langle CC \rangle_{pp}]} \rangle_{MC} \tag{9.28}$$

where $[\underline{\mathbf{R}}_{CT}]_{nm}$ represents the self-cross and cross-cross terms, normalized for the whole autoproduct CSDM, and averaged over many Monte Carlo trials, as indicated by $\langle \quad \rangle_{MC}$. This quantity is then subtracted from the normalized autoproduct CSDM formed from the measured data, normalized according to (9.5), and then plugged into the frequency-difference matched field processor given in (9.6). In other words,

$$B_{AP}^{MCCTS}(\boldsymbol{r}, \Delta\omega) = \left| \frac{\mathbf{w}^{\dagger}(\boldsymbol{r}, \Delta\omega) \cdot [\underline{\mathbf{R}}_{AP}^{norm}(\Delta\omega) - \underline{\mathbf{R}}_{CT}]^{norm} \cdot \mathbf{w}(\boldsymbol{r}, \Delta\omega)}{\mathbf{w}^{\dagger}(\boldsymbol{r}, \Delta\omega) \cdot \mathbf{w}(\boldsymbol{r}, \Delta\omega)} \right| \tag{29}$$

where the "'MCCTS"' superscript refers to Monte Carlo Cross Term Subtraction.

Figure 9.6 shows the cross-term CSDMs estimated with this Monte Carlo Cross Term Subtraction technique. Fig. 9.6a shows the cross-term CSDM for the extreme case where no mismatch is present. Fig. 9.6b shows the cross-term CSDM for a single realization (and a different realization than was used to create Fig. 9.3b and Figs. 9.4d, 9.4e, and 9.4f). Fig. 9.6c shows the cross-term CSDM after being averaged over 100 realizations, which is the number of realizations chosen for this study. Here, many of the off-diagonal terms are averaged away, with the main terms that survive existing on the matrix diagonal, which for these parameters appears as the thin dark line along the diagonal.

9.4.2 N-Path Estimates of Cross Terms

The Monte Carlos Cross Term Subtraction technique above requires the ability to evaluate $\langle SS \rangle$, $\langle SC \rangle$ and $\langle CC \rangle$, as given in (9.28). This is only possible, at present, for an acoustic field well-described by rays. Section provided these values for a two-path environment, but

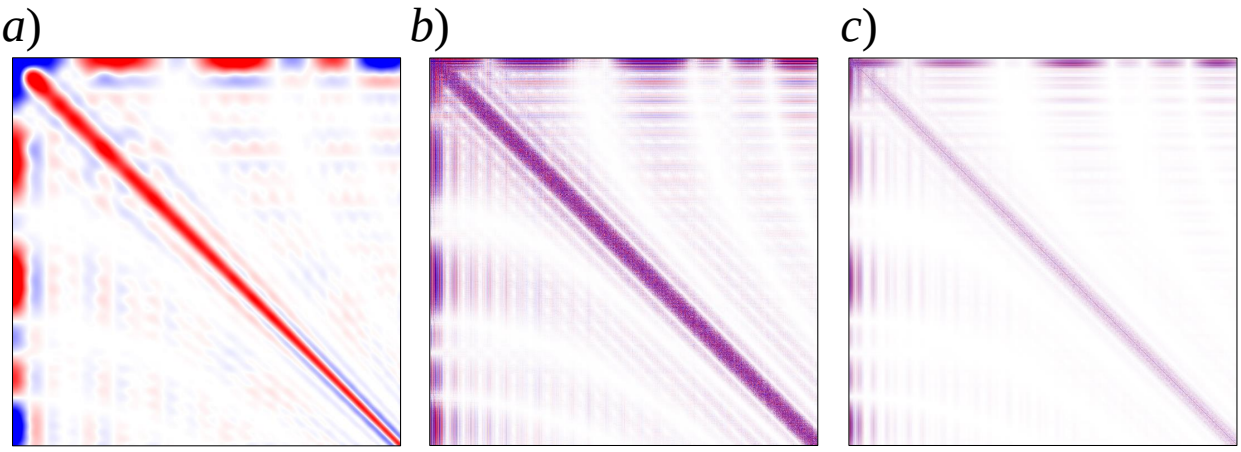

Figure 9.6: Cross-term CSDMs showing no mismatch (panel a), one realization with mismatch (panel b), and an average over 100 realizations with mismatch (panel c). The color scale is the same as in Figs. 9.3 and 9.4.

these results may be generalized to an N path environment. Assume the in-band field is well-described by a sum of N rays:

$$P_n(\omega) = \sum_{p=1}^{N} a_{pn} \exp(i\omega\tau_{pn}) \tag{9.29}$$

with the pth ray having an amplitude of a_{pn} and time-of-arrival of τ_{pn}, as measured at the nth receiver. The autoproduct for this is:

$$AP_{\Delta,n}(\omega, \Delta\omega) = \sum_{p=1}^{N} |a_{pn}|^2 e^{i\Delta\omega\tau_{pn}} + \sum_{J=1}^{\frac{N^2-N}{2}} A_{Jn} e^{i\Delta\omega\tau_{c,Jn}} \cos(\omega\Delta\tau_{Jn} + \phi_{Jn}) \tag{9.30}$$

where, for convenience, J is a new summation index representing all of the possible unique ray-path pairs, and ranges from 1 to $(N^2 - N)/2$. Thus, for the Jth ray pair, given by rays p and $q > r$, define the following terms: the effective amplitude $A_{Jn} \equiv 2|a_{pn}||a_{qn}|$, the average time-of-arrival $\tau_{Jn} \equiv (\tau_{pn} + \tau_{qn})/2$, the difference in time-of-arrival $\Delta\tau_{Jn} \equiv \tau_{pn} - \tau_{qn}$, and the phase factor $\phi_{Jn} \equiv arg\left(a_{pn}a_{qn}^*\right)$. While seemingly a burdensome notation change, this avoids dealing with a quadruple sum in the cross-cross terms. Note that in this notation,

the summations over ray variables are given in lowercase indices (such as p) and summations over ray-pair variables are given in uppercase indices (such as J). In (9.30), the self-terms are represented in the first summation, and the cross-terms are represented in the second summation.

For further convenience, the bandwidth-averaged self-terms and cross-terms are given as:

$$\langle S \rangle_n = \sum_{p=1}^{N} |a_{pn}|^2 \exp\left(i\Delta\omega\tau_{pn}\right) \tag{9.31}$$

$$\langle C \rangle_n = \sum_{J=1}^{\frac{N^2-N}{2}} A_{Jn} e^{i\Delta\omega\tau_{c,Jn}} \cos\left(\Omega_C \Delta\tau_{Jn} + \phi_{Jn}\right) \operatorname{sinc}\left(\frac{\Omega_{BW}^{\Delta}\Delta\tau_{Jn}}{2}\right) \tag{9.32}$$

which can both be calculated efficiently in a vectorized manner. With these terms in hand, the self-self and self-cross terms can be easily computed as:

$$\langle SS \rangle_{nm} = \langle S \rangle_n \langle S \rangle_m^* \tag{9.33}$$

$$\langle SC \rangle_{nm} = \langle S \rangle_n \langle C \rangle_m^* + \langle C \rangle_n \langle S \rangle_m^* \tag{9.34}$$

These calculations are very efficient, as they represent simple outer-products of two vectors. The bandwidth averaged cross-cross terms, on the other hand, are *not* equal to $\langle C \rangle_n \langle C \rangle_m$, and instead must be computed more carefully. The bandwidth averaged cross-cross terms are given as:

$$\langle CC \rangle_{nm} = \sum_{J=1}^{\frac{N^2-N}{2}} \sum_{K=1}^{\frac{N^2-N}{2}} A_{Jn} A_{Km} e^{i\Delta\omega\left(\tau_{c,Jn} - \tau_{c,Km}\right)} \frac{CC_1 + CC_2}{2} \tag{9.35}$$

$$CC_1 = \cos\left(\Omega_C\left(\Delta\tau_{Jn} + \Delta\tau_{Km}\right) + \phi_{Jn} + \phi_{Km}\right) \operatorname{sinc}\left(\frac{\Omega_{BW}^{\Delta}\left(\Delta\tau_{Jn} + \Delta\tau_{Km}\right)}{2}\right) \tag{9.36}$$

$$CC_2 = \cos\left(\Omega_C\left(\Delta\tau_{Jn} - \Delta\tau_{Km}\right) + \phi_{Jn} - \phi_{Km}\right) \operatorname{sinc}\left(\frac{\Omega_{BW}^{\Delta}\left(\Delta\tau_{Jn} - \Delta\tau_{Km}\right)}{2}\right) \tag{9.37}$$

These terms are much more difficult to calculate efficiently, and in general require many of separate evaluations (though the number of computations shown here can be reduced by around a factor of 2 by noting some symmetries in J and K). Note that as the number of ray paths, N, gets large, the number of terms to evaluate in this double-sum scales with N^4. Therefore, computing these terms (without approximations) can become computationally expensive, though at $N = 2$, there is only one term in this double-sum. Approximations for these terms are not considered in this study.

Thus, in an N path environment, all of the terms necessary to model $[\underline{\mathbf{R}}_{CT}]_{nm}$ in (9.28), are defined above.

9.4.3 Diagonal Zeroing

Another technique developed to mitigate the effect of the cross-cross terms on Δf-MFP is much simpler. Since the diagonal elements of the measured CSDM also tend to be where the cross-cross terms appear, one way to mitigate their effect is to set all the diagonal elements to zero. On the diagonal, there would be self-self terms that would ideally be kept, and then the cross-cross terms that are desired to be removed. So, by setting all the terms to zero, the effect of the cross-cross terms is being overestimated, and some degradation of the self-self terms are expected. Since MFP operates off of phase differences between array elements (*i.e.* off diagonal elements), it isn't anticipated that this diagonal-zeroing procedure should impact localization too detrimentally.

In order to normalize the resulting CSDM is some manner, a new normalization procedure must be defined, since (9.5) would lead to a division by zero. The Frobenius norm (Bickel and Levita 2008) is chosen for this purpose, which effectively requires that the sum of the squares of all the elements of the matrix is 1. Thus, for this technique:

$$B_{AP}^{DZ}\left(\boldsymbol{r},\Delta\omega\right)=\left|\frac{\mathbf{w}^{\dagger}\left(\boldsymbol{r},\Delta\omega\right)\cdot\left[\underline{\mathbf{R}}_{AP}\left(\Delta\omega\right)-\mathrm{diag}\left(\underline{\mathbf{R}}_{AP}\left(\Delta\omega\right)\right)\right]^{Frobenius}\cdot\mathbf{w}\left(\boldsymbol{r},\Delta\omega\right)}{\mathbf{w}^{\dagger}\left(\boldsymbol{r},\Delta\omega\right)\cdot\mathbf{w}\left(\boldsymbol{r},\Delta\omega\right)}\right| \tag{9.38}$$

where $diag\left(M\right)$ refers to a diagonal matrix made up of the diagonal elements of matrix $\underline{\mathbf{M}}$, and:

$$\left[\underline{\mathbf{M}}\right]^{Frobenius}=\frac{\underline{\mathbf{M}}}{\sqrt{\mathrm{trace}\left(\underline{\mathbf{M}}^{\dagger}\underline{\mathbf{M}}\right)}}. \tag{40}$$

Setting the diagonal elements of the CSDM to zero is not new. In fact, in the paper originally describing MFP techniques, Homer Bucker sets the diagonal terms to zero for the purposes of improved dynamic range (Bucker 1976, Baggeroer 1993), though the technique he outlined did not include a normalization of the CSDM.

9.4.4 Comparison of Techniques

These two techniques differ in many ways. The first technique, Monte Carlo Cross Term Subtraction, is done as a post-processing technique, requires a field well-described by rays, and is computationally expensive, both for the cross-cross term evaluations in environments with many arrivals, and also for the Monte Carlo random realizations of the environment. The second technique, Diagonal Zeroing, is a pre-processing technique, has no limitations on the local acoustic field description, and has negligible computational cost.

Which technique to use depends on how the environmental mismatch arises. In this study, moving the receivers around in an independent fashion can be thought of as an uncorrelated way to introduce mismatch. In contrast, array tilt could be thought of as a correlated way to introduce mismatch, where nearby array elements have similar offsets. Other environmental uncertainties, such as a rough surface, sloping bottom, or internal waves (Brekhovskikh and Lysanov 2003) can introduce mismatch that can be correlated over some receivers, and uncorrelated over others. When correlations are present, it is anticipated that the Monte Carlo Cross Term Subtraction technique would help capture some of the off-diagonal cross-term effects that Diagonal Zeroing would miss. Simulating correlated mismatch is not part of this study.

9.4.5 Positive Semi-Definiteness

As discussed in Section , positive semi-definiteness of the CSDM is important for producing an ambiguity surface B which varies from 0 to 1, and can thus be plotted on a dB scale easily. However, by manipulating the CSDM with the techniques proposed in this chapter, the resulting CSDMs are no longer positive semi-definite. The $\langle SC \rangle$ term in the numerator of (9.24) is not positive semi-definite, so neither is $\underline{\mathbf{R}}_{CT}$, and neither is the resulting CSDM used in $B_{AP}^{MCCTS}(\boldsymbol{r})$. Additionally, the subtraction of any two positive semi-definite matrices does not guarantee the result is positive semi-definite. Thus, even for the Diagonal Zeroing technique, positive semi-definiteness is not guaranteed.

To fix this, a simple correction is applied: the magnitude of B_{AP}^{MCCTS} and B_{AP}^{DZ} is taken. By doing this, local minima that were originally near $B = 0$ are now flipped, becoming (small) local maxima. The claim is that when regions of the field where B values were originally small (*i.e.* unlikely source locations) become negative, and are then flipped back to the positive side with the absolute value bars in (29) and (9.38), the resulting B values are still small, and thus still correspond to unlikely source locations. The cost for this is the

introduction of artificial-looking nulls in the field (seen in the following section). Alternative means could be proposed, such as setting all negative values to 0, but this artificially inflates most metrics for dynamic range. A final method could be the use of a linear ambiguity surface scale instead of a decibel scale, but this is fairly uncommon for ambiguity surfaces, so a decibel metric is retained here.

9.5 $\triangle f$-MFP Results with Cross Term Mitigation

In this section, ambiguity surfaces are provided for the Lloyd's mirror environment, as well as two other multipath environments.

Figure 9.7 gives the ambiguity surfaces for the Lloyd's mirror environment. Fig. 9.7a shows the standard $B_{AP}(\boldsymbol{r}, \Delta\omega)$, and shows a dynamic range (span of the middle 99% of data) of 15 dB. Fig. 9.7b processes the same data with the Monte Carlo Cross Term Subtraction technique, and shows a dynamic range of 34 dB. Fig. 9.7c processes the data in Fig. 9.7a with the Diagonal Zeroing technique, and also shows a dynamic range of 33 dB. Both of these techniques compare favorably with the conventional, low frequency ambiguity surface which has a dynamic range of 35 dB. The field maxima (at the source location) for Figs. 9.7a, 9.7b, and 9.7c are -2.9 dB, -0.2 dB, and $+0.1$ dB. Due to the overestimation of the cross term effects with the diagonal zeroing technique, the artificial looking nulls (described in the previous subsection) are evident. They also appear in Fig. 9.7b, but only in the deeper ambiguity surface nulls.

To test the application of these techniques to other environments, consider an ideal sound channel with a pressure release surface, and a 100-m-deep rigid bottom, with a source at the same location, broadcasting the same frequencies to the same array. Without a mechanism for loss, there would be infinitely many rays in a method-of-images solution; thus, only the first 10 arrivals are considered. Figure 9.8 shows these results.

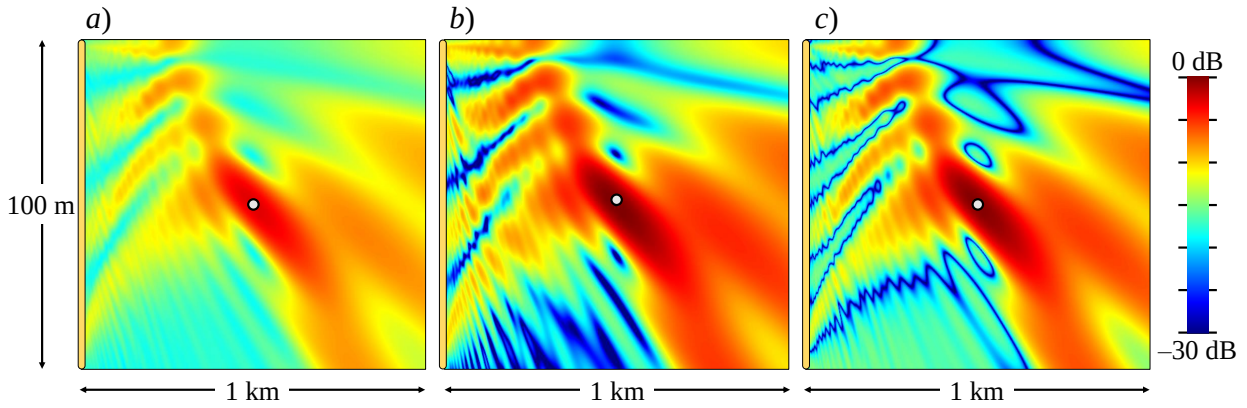

Figure 9.7: Ambiguity surfaces for $B_{AP}(\boldsymbol{r})$ (panel a), $B_{AP}^{MCCTS}(\boldsymbol{r})$ (panel b), and $B_{AP}^{DZ}(\boldsymbol{r})$ (panel c) in a Lloyd's mirror environment.

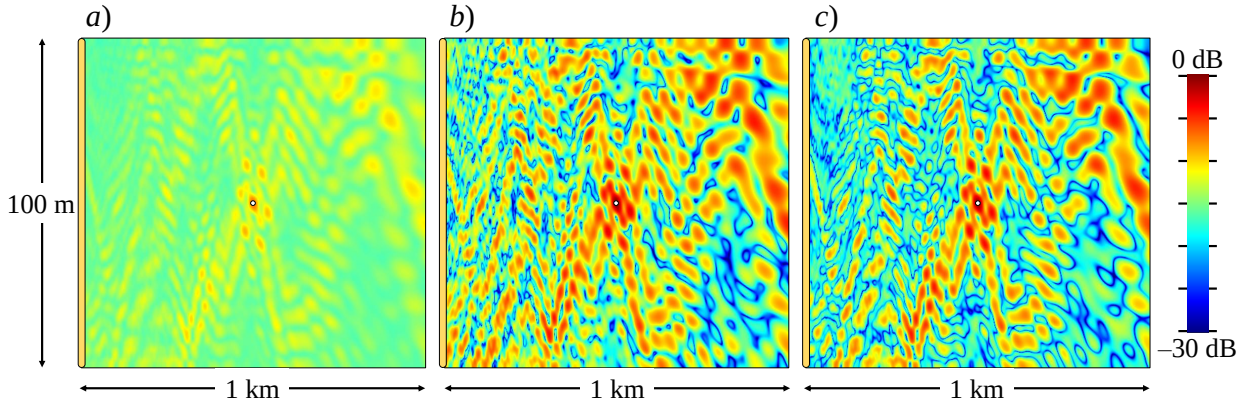

Figure 9.8: Ambiguity surfaces for $B_{AP}(\boldsymbol{r})$ (panel a), $B_{AP}^{MCCTS}(\boldsymbol{r})$ (panel b), and $B_{AP}^{DZ}(\boldsymbol{r})$ (panel c) in a method-of-images environment which includes 10 arrivals.

The dynamic range of the three plots in Fig. 9.7 are 6.0 dB, 24.2 dB, and 23.8 dB. The two cross term mitigation techniques produce ambiguity surfaces with dynamic range much closer to that of a genuine out-of-band field using conventional MFP, which has a dynamic range of 30 dB. In this highly multipath environment, the original Δ f-MFP result, in Fig. 9.7a, clearly has very limited dynamic range, and has a peak at the correct source location of -7 dB, compared to the other two techniques with a peak very close to 0 dB.

Given the drastic improvements in dynamic range found in these two simulation studies, this technique was then applied to experimental data. The experimental data chosen is from the KAM 11 experiment, which was an acoustic communications experiment performed near

Hawai'i in 2011. In it, 16 source depths broadcast 11-33 kHz data over 3 km to a vertical line array spanning most of the 106-m-deep sound channel, which had a downward refracting sound speed profile (see the references for more details of the experiment (Hodgkiss and Preseig 2012) and for more details of the Δf-MFP replica calculations used in prior work (Worthmann and Dowling 2015)). In Figure 9.9, results from a source depth of 60.2 m is provided. Due to the computational cost, and limited incremental benefit over diagonal zeroing, the Monte Carlo cross term subtraction technique was not used here.

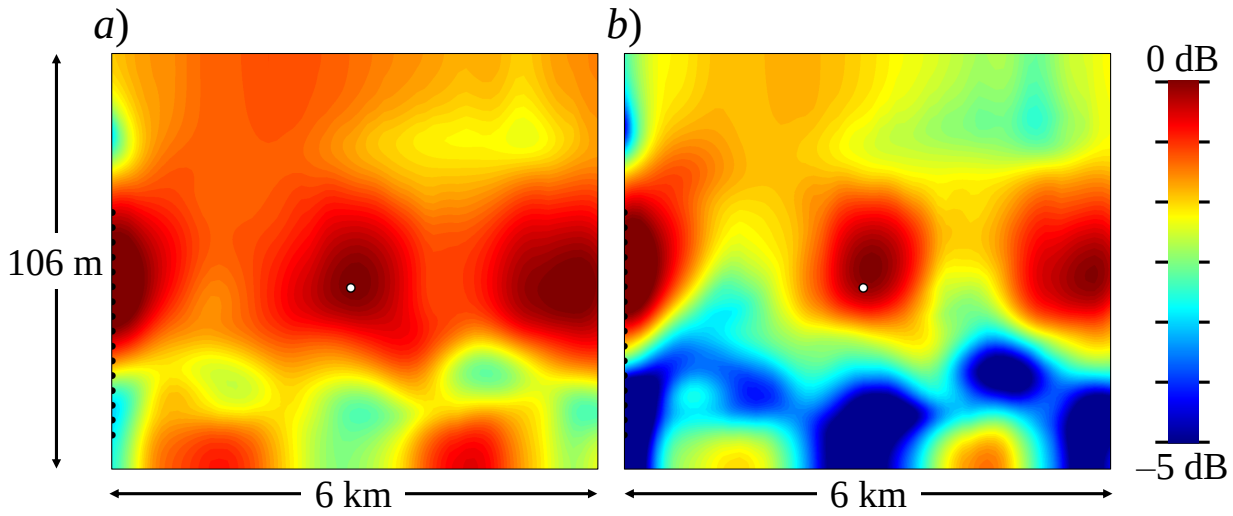

Figure 9.9: Ambiguity surfaces for $B_{AP}(\boldsymbol{r})$ (panel a) and $B_{AP}^{DZ}(\boldsymbol{r})$ (panel b) for the experimental KAM11 data, using a source at a depth of 60.2 m. The maximum in the field was scaled to 0 dB, and the color scale spans 5 dB.

Fig. 9.9a shows the original Δf-MFP ambiguity surface, which has a dynamic range of only 3.3 dB and peak of only -8.1 dB. Performing the diagonal zeroing on the same data leads to Fig. 9.9b, which has a dynamic range of 7.9 dB, and a peak of -3.0 dB. This is a significant increase in dynamic range, which compares favorably with an ambiguity surface generated from genuine low-frequency field under the same conditions, which has a dynamic range of 10.5 dB and peak of 0.0 dB. The other 15 trials provided comparable improvements in the ambiguity surface's peak value and its dynamic range, which saw an average of 5 dB improvement.

9.6 Summary and Conclusion

In this study, the theoretical reasons for the degraded dynamic range observed in Δf-MFP were explored using a simple Lloyd's mirror environment. It was found that the cross terms that result from the autoproduct technique, in the presence of environmental mismatch, contribute to the autoproduct CSDM in a manner very similar to noise. The correlation between cross terms that can be found on the main diagonal of the autoproduct CSDM was found to be the culprit in the decreased dynamic range observed in Δf-MFP techniques. To mitigate these effects, two techniques were presented, which in this study showed comparable levels of performance. The simpler of these techniques was applied to experimental results previously used in Δf-MFP studies, and dynamic ranges of the resulting ambiguity surfaces were improved by an average of 5 dB. There are three main conclusions that can be drawn from this research effort.

The first conclusion is that cross terms are the cause of the poor dynamic range, as suspected in the original Δf-MFP. Specifically, it was found that the correlation between cross-terms across the array, and particularly the autocorrelation of cross terms, were the reason for the decreased dynamic range.

The second conclusion is that the effect of cross-terms cannot be removed coherently due to the effects of environmental mismatch. However, two techniques were developed which attempt to mitigate the effect of these cross-terms, particularly the ones that appear on the main diagonal of the CSDM, which are the primary cause of the poor dynamic range in Δf-MFP. One technique, termed Monte Carlo Cross Term Subtraction, was a computationally expensive post-processing technique which estimated the effects of the cross terms throughout the CSDM. Another technique, which in this study performed comparably, was termed Diagonal Zeroing, and was a computationally cheap pre-processing technique that over-estimates the cross-term contributions on the main diagonal, and under-estimates their effect

elsewhere. These two techniques performed comparably.

The third conclusion is that these techniques – particularly the diagonal zeroing technique – were able to drastically improve the dynamic range of ambiguity surfaces for a Lloyd's mirror environment (by 19 dB), a method-of-images solution to an ideal sound channel (by 18 dB), and in the KAM 11 experimental data (by 5 dB). These techniques also improved the overall peak in the ambiguity surface by 3 dB, 7 dB, and 5 dB, respectively. Especially in the KAM 11 environment, the maximum in the ambiguity surface is now only -3 dB, which suggests a very strong cross-correlation between the experimentally measured autoproduct and the modeled low-frequency field.

Overall, the decreased dynamic range exhibited in Δf-MFP techniques were found to be associated not with a lack of robustness, but with byproducts of the nonlinear construction of the frequency-difference autoproduct. The techniques described here provide ways to mitigate their effect, allowing the recovery of Δf-MFP ambiguity surfaces with dynamic ranges more in line with their associated level of robustness. Additionally, this represents an example of theoretical autoproduct studies leading directly to improvements in autoproduct-based source localization algorithms.

CHAPTER 10

Summary, Conclusions, and Future Work

10.1 Summary

In linear acoustics, as with any linear field theory, sinusoidally-varying excitations (inputs) create sinusoidally-varying fields (outputs), where the input frequency is the same as the output frequency. This research, however, suggests that a propagating wave excitation with non-zero bandwidth carries with it information both within its bandwidth, as well as outside of this bandwidth. Or, more strictly speaking, the field information at the in-band frequencies can be mathematically manipulated to create new fields that appear very similar to fields at frequencies that did not propagate in the physical environment. Analyzing the theoretical reasons for, and limitations on, this frequency-shifting possibility in a variety of acoustic fields has formed approximately half of this thesis. The other half focuses on using this frequency-shifting capability to improve source localization algorithms, particularly to create new signal processing robustness at arbitrarily high frequencies that conventional techniques cannot achieve. Collectively, the nonlinear field constructions developed here are referred to as "autoproducts", or products of a frequency-domain signal with itself, at a different frequency. The following eight paragraphs provide summaries of Chapters 2 through 9 of this thesis.

Chapter 2 describes a proof-of-concept application for autoproducts where experimentally-

obtained signals from a high frequency underwater sound source (11-33 kHz) were down-shifted with this nonlinear signal processing technique to much lower frequencies (50-500 Hz), and then successfully processed at these lower frequencies using standard localization techniques. Conventional localization techniques available in literature are limited to source frequencies at or below 1 kHz in realistic ocean environments. Thus, successful source localization at frequencies an order of magnitude higher than this nominal limit represents a significant operational improvement.

Chapter 3 presents a follow-up study to the research presented in Chapter 2, where more complex signal processing techniques, such as adaptive processors, were applied to this frequency difference technique. Additionally, robustness to realistic ocean noise was investigated. The results presented in this chapter suggest that the localization performance described in Chapter 2 is robust, and can be marginally improved with adaptive techniques.

Chapter 4 offers another proof-of-concept for the application of autoproducts to active sonar, a signal processing regime that is frequently limited by reverberation. Targets in the mid-water-column are detected and localized at signal-to-reverberation levels lower than the operational limit for conventional techniques for the same tasks.

Chapter 5 addresses the question of just how far this ability to shift frequencies up and down can be extended. Using Helmholtz equation analyses and simulations of acoustic fields in simple environments, the extent of the ability of autoproducts to shift frequencies up and down while mimicking true acoustic fields at the shifted frequencies is assessed, particularly for the ray approximation.

Chapter 6 uses experimental measurements to verify the theoretical claims made in Chapter 5. This experiment shows that 40-110 kHz acoustic field recordings made in a simple two-path environment could be used to mimic lower frequency fields from 0 to 60 kHz, and higher frequency fields from 110 to 190 kHz with a cross correlation of 90% or higher.

Chapter 7 continues the theoretical analysis from Chapter 5, but addresses autoproduct mimicry of acoustic fields that do not satisfy the ray approximation specifically the diffracted sound field near and behind acoustic barriers. The results are based on exact solutions of the Helmholtz equation, and suggest that autoproducts are still able to mimic lower and higher frequency fields, but there are some regions where field-amplitude variations degrade performance.

Chapter 8 pursues the theoretical analysis of autoproducts subject to refraction and the formation of caustics. In two simple waveguide environments, it was found that the phase shift that acoustic fields undergo when passing through a caustic can potentially cause autoproducts to lose their out-of-band-field-mimicking properties, primarily because such caustic phase shifts are absent in autoproduct fields.

Chapter 9 uses the theoretical analyses described in Chapter 5 to draw new conclusions about the theoretical basis for autoproduct-based localization techniques, particularly as it pertains to their intrinsically poor dynamic range. Armed with this analysis, signal processing techniques are developed that improve the dynamic range of autoproduct-based localization techniques.

Overall, this thesis presents the theoretical development and limitations of the quadratic autoproducts in a wide variety of acoustic environments, and documents successful development applications for autoproducts, particularly for physics based source localization schemes.

10.2 Conclusions

This thesis supports several conclusions, described below.

10.2.1 Theory

Autoproduct motivation: Autoproducts formed from plane waves are able to exactly mimic planes waves from out-of-band fields that are at higher or lower frequencies outside the original bandwidth. Given some non-zero bandwidth, autoproducts can mimic lower frequency acoustic fields at a user-specified difference frequency which can be selected from any frequency less than the total bandwidth of the in-band field. Autoproducts can also mimic higher frequency acoustic fields at user-specified sum frequencies, which can be selected from any frequency that is double an in-band frequency. The ability to shift frequencies up or down as desired is potentially transformative for signal processing techniques, especially physics-based localization techniques. The principles described here were the motivation behind the rest of the thesis. (Ch. 5)

Multipath limitations: Autoproducts formed in multipath environments are only able to mimic out-of-band acoustic fields in an approximate sense, due to the production of cross terms. The effect of these cross terms can be mitigated with signal-bandwidth averaging, as long as the product of the bandwidth available for averaging and the difference in the ray-paths times-of-arrival is large compared to unity. However, regions of the acoustic field where the time-differences-of-arrivals are too small, such as near reflecting surfaces, will contain interference layers where the autoproducts ability to mimic out-of-band fields can be limited. (Ch. 5, 6, 7 and 9)

Experimentally robust: Autoproducts are not simple signal processing gimmicks or tricks, or in other words, they are not a flimsy foundation for signal processing techniques that only apply in a narrow range of applications, nor are they merely a theoretical construct that cannot be realized in experiments. Subject to the limitations outlined here, autoproducts have been found to be a robust means for obtaining out-of-band field information, and experimental evidence from lab-scale and ocean-scale experiments suggest that the autoproducts

are indeed useful, authentic, and measurable quantities. (Ch. 1, 2, and 6)

Amplitude variations: Because of the quadratic nature of autoproducts, spatial amplitude variations can lead to discrepancies between autoproducts and out-of-band fields. In the majority of environments considered here, these amplitude variation effects were not found to be a limiting factor in cross-correlation performance. In terms of spherical waves, the detrimental effects associated with the difference between an inverse-distance and inverse-distance-squared scaling from a point source were found to be negligible when the normalization region is much smaller than the normalization-region-to-source distance. In terms of ray acoustics, it is found that for autoproducts to accurately mimic out-of-band fields, the magnitude of the gradient of the rays amplitude should be much less than the magnitude of the ray amplitude times the wavenumber of sound. In terms of diffraction, amplitude variations particularly those caused by diffraction behind barriers tend to introduce discrepancies, but for the majority of conditions, these amplitude variations cause less than ten percent degradation in the autoproduct-to-out-of-band-field cross-correlation, and often lead to an order of magnitude or two smaller effect than that. (Ch. 5, 7)

Phase variations: In contrast to amplitude variations, phase variations can cause significant divergence between autoproducts and out-of-band fields. There are, broadly speaking, two types of phase variations: constant phase offsets, and spatial variations in phase. Cross-correlations are robust to constant phase offsets, and source localization schemes typically interpret a constant phase offset as an artifact of the source waveform, an interpretation these techniques are robust to. When autoproduct-to-out-of-band-field phase differences vary significantly within the (spatial) normalization region, poor cross-correlations are nearly guaranteed. It was found that caustics, in particular, can introduce such spatially-varying phase differences, particularly in multipath regions where different rays have passed through different numbers of caustics. (Ch. 7, 8)

10.2.2 Applications

Environmental uncertainties: Frequency-difference matched field processing, or Δf-MFP, is a source localization technique that trades spatial resolution for robustness to environmental uncertainties at arbitrarily high frequencies. Through the use of the frequency-difference autoproduct, the product of environmentally-induced time-delay uncertainties and the difference frequency can often be chosen to be less than unity, and this choice permits robust source localization. Experimentally, successful source localization in the shallow ocean was shown to be possible by shifting the 11-33 kHz recorded data down to 50-500 Hz, with range and depth localizations consistently within 6% and 10% of the source-to-array range and ocean depth, respectively. (Ch. 1, 2, 3, 9)

Source waveform independence: The source waveform does not need to be known for Δf-MFP techniques, due to their use of a cross-spectral density matrix. Several studies on experimental data are provided which show that source waveforms with a variety of phase structures, such as band-limited pulses, chirps, and Gaussian-like noise, all produce the same source localization results. (Ch. 1, 2, 9)

Cross term subtraction: Cross terms, which are unintentionally formed by autoproducts in multipath environments, are found to be the cause of the reduced dynamic range in Δf-MFP techniques. In the presence of environmental uncertainty, these cross terms are found to contribute in a noise-like manner. Two techniques were developed which can mitigate the effect of these cross terms to improve the dynamic range of Δf-MFP ambiguity surfaces, by nearly 20 dB in simulated fields, and approximately 5 dB in the KAM 11 environment. (Ch. 9)

Active sonar detection and localization: In simulated shallow ocean environments, frequency-difference-based active sonar techniques can detect mid-water-column targets at signal-to-reverberation ratios lower than conventional techniques. These techniques can also

localize targets, and clutter to a more limited extent, in range *and* depth, at least when the target is well-separated from the sources of clutter. (Ch. 3)

Rays and modes: One of the findings in this research is that autoproducts that are produced from high frequency acoustic fields well-described by the ray approximation can correlate well with a lower frequency field which is well-described by a modal decomposition. In addition, this lower frequency field satisfies a rigid boundary condition, instead of the more physically relevant pressure-release boundary condition. While a thorough theoretical explanation for this rays-to-modes conversion is a subject for future research, the work described here makes it clear that, even with experimental data, such an equivalence between high-frequency-ray-based autoproducts and low-frequency modes does exist, or at least enough for robust source localization purposes. (Ch. 1, 2)

10.3 Future Work

Below, a few possible directions for future work on this research are discussed.

Active sonar experimental data: The active sonar simulations described here are promising, and the next steps would include more realistic simulations, followed then by the analysis of experimental data. It will be interesting to see if the detection and localization performance of autoproduct-based techniques observed in simulation, particularly as compared to conventional techniques such as matched filtering, are still observed when using experimental data.

Dispersive media: Analyzing the effect of dispersive media on autoproducts, such as a frequency dependent sound speeds, is an important consideration, particularly when frequency-dependent propagation media are involved in the propagation environment. This may also include frequency-dependent absorption, which in addition to amplitude changes, may also

introduce phase changes as well.

Rays and modes equivalence: In the Δf-MFP results presented in Chapters 1 and 2, it was shown that a frequency-difference autoproduct comprised of rays-path contributions correlates well with a modal decomposition of a low frequency acoustic field. While there are some quantitative relationships between rays and modes, it is unclear how a product of rays can produce modes, or if a product of modes can produce rays. There may also be a relationship between modal phase and group velocities, and how useful that mode is for an autoproducts out-of-band mimicry. A theoretical study to better understand autoproducts from a modal perspective would be helpful, particularly for the potential improvements that could be made to Δf-MFP techniques. This additionally includes a study on cross-terms and how they arise in a modal decomposition, and what algorithms can be utilized to mitigate their effect.

High frequency measurement corrections: Conventional MFP at high frequencies has high resolution, but fails to localize due to environmental mismatch. Δf-MFP, on the other hand, has low resolution, but can succeed in source localization despite mismatch. With the source location known, at least at low resolution, it would be interesting if it were possible to make corrections to the original high frequency measurements to recover some utility of the conventional MFP algorithm. In other words, post-processing the high frequency data using information obtained from Δf-MFP could result in successful localization at *high* resolution at the in-band frequencies, rather than simply at low resolution at the out-of-band frequencies. Determining a robust way to perform these corrections is expected to be very challenging but the payoff in increased resolution could be substantial.

Generalized effective reflection coefficient: Thus far, this research explored ocean waveguides with bottom properties that were generally treated as rigid boundary conditions. However, ocean bottoms are more complicated than this, often including sand, mud, and sediment layers. These media generate reflection coefficients that can be strongly angle

and frequency dependent. For autoproducts in the ray approximation, magnitude-squared reflection coefficients would appropriately satisfy the theory. But reflection coefficients are not easily specified for an out-of-band field described by modes. Thus, for Δf-MFP purposes, the question is raised of how to define the effective bottom properties for out-of-band fields such that they correlate well with frequency-difference autoproducts.

Deep ocean autoproducts: The deep ocean is characterized by strong refraction and few surface and bottom reflections. Frequently caustics are involved in the wave propagation environment, which as shown here, can introduce difficulties for cross-correlation and localization purposes. It would be useful if a technique were developed which could correct for the caustic phase discrepancies. One possible solution could be the use of matched *autoproduct* processing, instead of matched *field* processing, where measured autoproduct fields are compared to modeled autoproduct fields, not modeled out-of-band acoustic fields.

Appendices

Appendix A

Relationships to Signal Processing Techniques

In this appendix, the relationship between autoproducts and more well-known signal processing techniques is discussed, including bilinear time-frequency analysis (Cohen 1989).

A.1 Definitions

To begin, assume a real-valued input signal of the form $p_R(t)$. For the purposes of the discussion here, the time-domain signal should be complex analytic, or in other words, the Hilbert transform (generalization of the harmonic conjugate) of the signal should be added to the real-valued signal.

$$p(t) \equiv p_R(t) + iH[p_R(t)] \tag{A.1}$$

where the $H[\,]$ refers to the Hilbert transform. This allows calculations to be performed with only positive frequency content, rather than both positive and negative frequency components. Additionally, the following Fourier transform convention is used, where $P(\omega)$ is the Fourier transform of $p(t)$, as shown below.

$$F_{t\to\omega}[p(t)] \equiv \int_{-\infty}^{+\infty} p(t)\, e^{i\omega t} dt = P(\omega) \tag{A.2}$$

$$F_{\omega\to t}^{-1}\left[P\left(\omega\right)\right] \equiv \frac{1}{2\pi}\int_{-\infty}^{+\infty} P\left(\omega\right) e^{-i\omega t} d\omega = p\left(t\right) \tag{A.3}$$

The following are the definitions of autoproducts and bandwidth averaged autoproducts, where for the purposes of this discussion, frequency-difference autoproducts are the primary consideration.

$$AP_{\Delta}\left(\omega, \Delta\omega\right) \equiv P\left(\omega + \frac{\Delta\omega}{2}\right) P^{*}\left(\omega - \frac{\Delta\omega}{2}\right) \tag{A.4}$$

$$\left\langle AP_{\Delta}\right\rangle \left(\Delta\omega\right) \equiv \int_{-\infty}^{+\infty} P\left(\omega + \frac{\Delta\omega}{2}\right) P^{*}\left(\omega - \frac{\Delta\omega}{2}\right) d\omega \tag{A.5}$$

Armed with these definitions, below are some relationships to more well-known signal processing techniques.

A.2 Auto-Correlation Relationships

Define the auto-correlation as

$$\left[f\left(t\right) * f\left(t\right)\right]\left(\tau\right) \equiv \int_{-\infty}^{+\infty} f^{*}\left(t\right) f\left(t+\tau\right) dt \tag{A.6}$$

It is straightforward to show that a small change of variables in the bandwidth averaged autoproduct definition yields the following:

$$\left\langle AP_{\Delta}\right\rangle \left(\Delta\omega\right) = \int_{-\infty}^{+\infty} P\left(\omega + \Delta\omega\right) P^{*}\left(\omega\right) d\omega = \left[P\left(\omega\right) * P\left(\omega\right)\right]\left(\Delta\omega\right) \tag{A.7}$$

Therefore, it is accurate to describe the bandwidth-averaged autoproduct as related to the frequency-domain auto-correlation.

Additionally, it is straightforward to show that the following relationship holds:

$$\langle AP_{\Delta} \rangle (\Delta\omega) = 2\pi F_{t \to \Delta\omega} \left[|p(t)|^2 \right] \tag{A.8}$$

Thus, the bandwidth-averaged autoproduct is also the Fourier transform of the instantaneous intensity, or magnitude-squared, of the signal, up to a factor of 2π .

A.3 Wigner Transforms and Ambiguity Functions

In addition to the frequency domain autoproduct defined in (A.4), another convenient definition, which, as is discussed below is related, is the time-domain autoproduct, defined here as:

$$ap_{\Delta}(t, \tau) \equiv p\left(t + \frac{\tau}{2}\right) p^*\left(t - \frac{\tau}{2}\right) \tag{A.9}$$

Note, the time-domain autoproduct is also the integrand of the auto-correlation function.

One of the two common bilinear time-frequency analysis functions, the Wigner transform, also known as the Wigner-Ville Distribution (Borcea 2007, Cohen 1989), is defined as:

$$W(t, \omega) \equiv \int_{-\infty}^{+\infty} p\left(t + \frac{\tau}{2}\right) p^*\left(t - \frac{\tau}{2}\right) e^{i\omega\tau} d\tau = F_{\tau \to \omega} \left[ap_{\Delta}(t, \tau) \right] \tag{A.10}$$

The Wigner transform is used in a variety of fields to measure the relationship between frequency and time with higher resolution than the short-time Fourier transform, also known

as a spectrogram (Ferguson 1994). It was originally developed for use in quantum mechanics, where position and momentum are the two Fourier conjugate variables instead (Wigner 1932).

The other common bilinear time-frequency analysis function is the Ambiguity Function (which is important to note is different than the ambiguity surface, as is frequently used in matched field processing applications), defined as:

$$AF\left(\Delta\omega,\tau\right)\equiv\int_{-\infty}^{+\infty}p\left(t+\frac{\tau}{2}\right)p^{*}\left(t-\frac{\tau}{2}\right)e^{i\Delta\omega t}d\Delta\omega=F_{t\rightarrow\Delta\omega}\left[ap_{\Delta}\left(t,\tau\right)\right] \tag{A.11}$$

The Ambiguity Function is used in the radar community for measuring Doppler shifts and time-delays (*i.e.* range) (Stein 1981).

All 4 of these functions $AP_{\Delta}\left(\omega,\Delta\omega\right)$, $W\left(t,\omega\right)$, $AF\left(\Delta\omega,\tau\right)$, and $ap_{\Delta}\left(t,\tau\right)$ are inter-related based on Fourier transforms between the pair of Fourier conjugate variables $\omega\leftrightarrow\tau$ and the other pair, $\Delta\omega\leftrightarrow t$. In other words, the following relationships can be defined:

$$W\left(t,\omega\right)=2\pi F_{\Delta\omega\rightarrow t}^{-1}\left[AP_{\Delta}\left(\omega,\Delta\omega\right)\right] \tag{A.12}$$

$$AF\left(\Delta\omega,\tau\right)=2\pi F_{\omega\rightarrow\tau}^{-1}\left[AP_{\Delta}\left(\omega,\Delta\omega\right)\right] \tag{A.13}$$

$$ap_{\Delta}\left(t,\tau\right)=\left(2\pi\right)^{2}F_{\Delta\omega\rightarrow t}^{-1}\left[F_{\omega\rightarrow\tau}^{-1}\left[AP_{\Delta}\left(\omega,\Delta\omega\right)\right]\right] \tag{A.14}$$

This is also illustrated in Figure A.1.

This inter-relationship between the frequency-difference autoproduct was explored. Of particular interest was the ability to mitigate cross terms through the use of various weighting

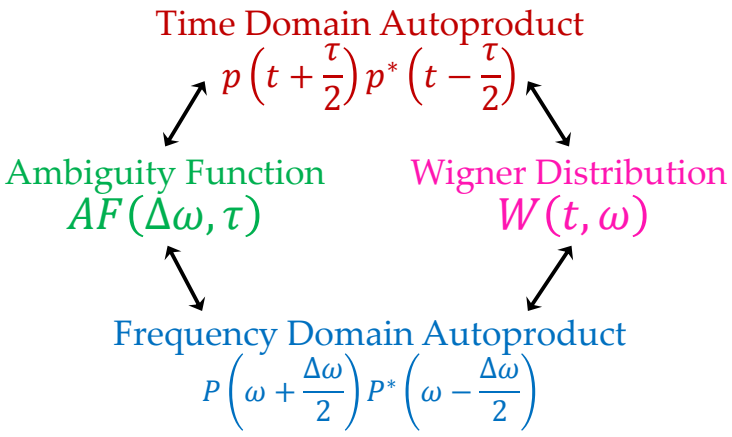

Figure A.1: Fourier transform relationships between various bilinear time-frequency analysis functions, and the frequency domain autoproduct.

functions in the integrand of the Wigner transform on the Ambiguity Function, as is common in the bilinear time-frequency analysis literature (Cohen 1989). However, it was determined that the effect of the cross terms on the *bandwidth-averaged* autoproduct is already minimized as much as is possible by virtue of averaging. In order to mitigate cross-terms, they must be subtracted coherently, and not simply averaged with a special weighting. And the subtraction of cross terms requires accurate time-of-arrival information, which is either difficult to estimate at the in-band frequency, or requires knowledge of the source waveform. Therefore, it seems that the Wigner transform and Ambiguity Function are convenient alternative descriptions for autoproducts, but the existing literature is not easily applied to the autoproduct techniques described in this thesis.

A.4 Cross-Correlation and MFP

There exist methods in literature that perform source localization based upon cross-correlation processing, such as Hursky *et al.* (2004). Conventional matched field processing and cross-correlation processing are inter-related in the following manner.

Consider measured data in the time domain at the jth hydrophone, $p_j(t)$, which is equal

to the source waveform $s(t)$ convolved with the impulse response $g_j(t)$. Without knowledge of the source waveform (as is typical in MFP applications), one must resort to a cross-correlation to be able to interrogate $g_j(t)$. Consider the cross-correlation of the ith and jth receiver, defined as:

$$r_{ij}(\tau) \equiv \int_{-\infty}^{+\infty} p_i^*(t)\, p_j^*(t+\tau)\, dt \tag{A.15}$$

Consider Figure 2, which uses KAM 11 data, as described in Chapters 2 and 3, from a source depth of 67.7m. Fig. A.2a is the measured data directly from the experiment. Fig. A.2b and A.2c are the measured and modeled impulse responses, where the source waveform is assumed known. Figs. A.2d, A.2e, and A.2f show plots of r_{ij} , where the ith receiver is plotted vertically, and the jth receiver, the reference signal, is the 1^{st}, 7^{th}, and 16^{th} receivers, respectively. Analogous plots are given in Figs. A.2g, A.2h, and A.2i, but for modeled data. The red curves correspond to autocorrelations, or in other words, when $i = j$ in r_{ij} .

It can be seen from Fig. A.2 that, despite the overlapping arrivals in Fig. A.2a, there exists sufficient bandwidth such that multipath structure can be resolved in the impulse responses in Figs. A.2b and A.2c. However, those plots required use of the source waveform. The remaining panels in Fig. A.2 use cross-correlations, which do not require the source waveform, however they produce additional apparent pulses, due to the quadratic form of the cross-correlation.

Qualitatively, the impulse responses are similar to the cross-correlations, and the measured cross-correlations are qualitatively similar to the modeled cross-correlations. To consider their quantitative similarity, consider the following processor:

$$B_{xcorr} = \frac{\langle r_{ij}^{measured}, r_{ij}^{modeled} \rangle}{\sqrt{\langle r_{ij}^{measured}, r_{ij}^{measured} \rangle \langle r_{ij}^{modeled}, r_{ij}^{modeled} \rangle}} \tag{A.16}$$

$$\langle r_{ij,1}(\tau), r_{ij,2}(\tau)\rangle = \sum_{ij} \int_{-\infty}^{+\infty} r_{ij,1}(\tau)\, r^{*}_{ij,2}(\tau)\, d\tau \tag{A.17}$$

Where $r_{ij}^{measured}$ and $r_{ij}^{modeled}$ are the time-domain cross-correlations between the ith and jth receiver, using measured and modeled data, respectively. In other words, for N receivers, N^2 cross-correlations are calculated (with N of them technically being auto-correlations). Then, a correlation is performed between these N^2 measured cross-correlations and the corresponding N^2 modeled cross-correlations, where this outer-most correlation is normalized to be between 0 and 1. Doing this with all 16 measurements for this KAM 11 trial, the overall correlation, B_{xcorr} is 3.2% . Keep in mind this is when the modeled field is equal to the *true* source location.

Despite the qualitative similarity between measured and modeled cross-correlations, the fundamentally high frequency nature of the measurements renders the overall correlation B_{xcorr} very sensitive to small variations another manifestation of the environmental mismatch problem! In fact, it can be shown with the convolution theorem that B_{xcorr} is effectively a time-domain equivalent of conventional MFP, and that assuming noise outside of the nominal bandwidth is filtered out first, then Parseval's theorem can show that B_{xcorr} is identical to conventional MFP.

The cross-correlation-processing techniques described in Hursky *et al.* (2004) do not directly use the cross-correlations, but rather use the cross-correlation *envelopes*. By comparing envelopes instead of the underlying high-frequency signals themselves, mismatch robustness may be obtained. Furthermore, since autoproducts are themselves related to cross-correlation envelopes (see the first subsection in this appendix), it is possible that the method described in Hursky *et al.* (2004) is related to Δf-MFP. Further studies are necessary to fully understand the similarities and differences between the two techniques.

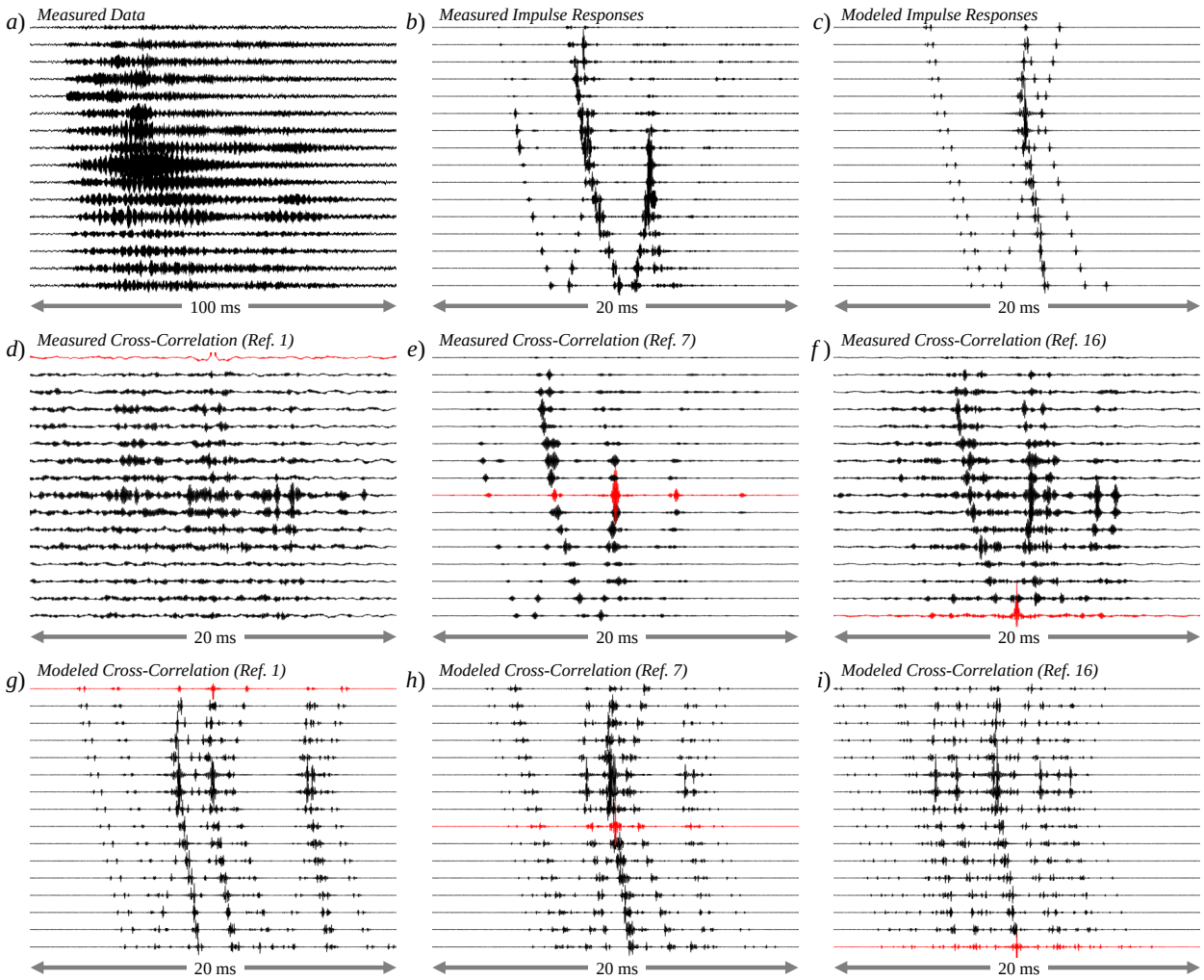

Figure A.2: Cross-correlations of measured and modeled KAM 11 impulse responses. All panels show all 16 hydrophone depths, from 41m (top) to 97m (bottom). The first plot has a horizontal axis spanning 100 ms, and the subsequent eight plots have horizontal axes spanning 20 ms. The red curves in the lower six plots correspond to autocorrelations.

A.5 Out-of-Time Processing Possibilities

This thesis details several topics, including the claim of out-of-band signal processing. So, owing to the relationship between frequency and time, the question is raised of the possibility of out-of-time processing. This section briefly addresses this possibility. The main question is: what, exactly, is out-of-time processing? Here, three definitions are provided, and the possibility for them is discussed.

The first definition is the possibility of processing recorded signals at different absolute times, but the same relative times. In this case, out-of-time processing is already possible, as standard beamforming techniques (as well as Δf-MFP) are robust to overall phase differences. This is for a similar reason as their source waveform independence. In other words, a given source waveform $s(t)$ looks the same for beamforming and MFP applications as a source waveform thats $s(t-t_0)$ instead. In this regard, out-of-time processing is possible, though this is trivial as standard techniques already offer this possibility.

The second definition is the possibility of changing *relative* time-of-arrivals. This is an irrelevant definition for a single-path environment, but for multipath this is a meaningful question. Standard beamforming and MFP techniques rely on capturing accurate relative time-of-arrivals across the array. Frequency-difference MFP techniques also rely on capturing accurate relative time-of-arrivals. Recall that the bandwidth-averaged autoproduct $\langle AP_\Delta \rangle (\Delta\omega)$ is a Fourier transform away from instantaneous intensity, $|p(t)|^2$. Given two arrivals such that $p(t) = s(t-t_1) + s(t-t_2)$, this instantaneous intensity is $|s(t-t_1)|^2 + |s(t-t_2)|^2 + 2s(t-t_1)\,s(t-t_2)$. The first two terms are still localized to t_1 and t_2 . The latter term is negligible when $s(t)$ is a band-limited impulse, and the two arrivals are well-separated (in other words, $\Omega_{BW}(t_2-t_1) \gg 2\pi$). When the arrivals are close, relative to their temporal width, then this time-domain cross-term is not negligible. In other words, the resolution limit for resolving two arrivals is unchanged for autoproduct techniques. But more importantly, the time-domain cross-term is temporally located between t_1 and t_2 . Thus, AP_Δ (and by similar arguments, AP_Σ) is unable to shift the relative time of arrivals. Said differently, autoproduct techniques can change frequency content within a given signals arrival envelope, but cannot change the envelope. So, the claim is then that autoproduct techniques, as defined here, cannot do out-of-band processing. But it is still possible that bilinear time-frequency representations *could* permit out-of-time processing, its just unlikely that autoproducts, or any of their Fourier transforms, could do accomplish this.

The third and final definition of out-of-time processing relates to causality. In other words, could a time domain recording from $t \in [0, t_1]$ be manipulated in such a way as to predict what will be recorded on the array between $[t_1, t_2]$, when t_2 is strictly greater than t_1 . If the prediction technique incorporated physics, then this could be possible, but it would be trivial. For example, if it is known to the signal processor that the measurement is from a two-path environment with only one source, and two arrivals are detected (either due to known source waveform, or an auto-correlation showing two peaks), then the prediction could be made by the signal processor that subsequent recordings will not contain any further arrivals. But the signal processor in this case has enough information about its environment that causality is not broken in this case. However, if the signal processor knows nothing about the incident signals character (*i.e.* number of arrivals to expect), then the claim that autoproduct techniques, or any physically possible technique, could predict from measurements at $t \in [0, t_1]$ what will happen between $t \in (t_1, t_2]$ is dubious at best. This is because causality is, of course, a fundamental law of physics. Thus, barring any bleeding-edge advances in theoretical physics or philosophy alleging otherwise, causality is not possible to violate. And so this definition of out-of-band processing is forbidden by fundamentals laws of physics.

Appendix B

n^2-Quadratic and n^2-Linear Modal Decomposition Derivations

This section details the derivations of the modal decomposition of the range-independent but depth-dependent waveguides that were defined in Chapter 8. Analytic solutions were preferred for computational efficiency and a guarantee that the wave equation was satisfied. For the two environments considered here, n^2 -quadratic and n^2 -linear, its found that trapped modes are somewhat easy to obtain. Leaky modes, on the other hand, are much more difficult to capture, and are not easily neglected for the purposes here. Both trapped and leaky modes are discussed in these two environments.

In creating these codes, especially with regards to the leaky mode calculations, a wide variety of resources were utilized. For the overall procedure to solve these problems, by way of a proper Sturm-Lioville problems, (Frisk 1994) was an invaluable resource. Additionally, the following papers were useful as well: Voitovich and Shatrov 1972, Labianca 1973, Stickler 1975, Tindle 1976, Bartberger 1977, Tindle 1979, Stickler and Ammicht 1980, Stickler 1980, Stickler and Ammicht 1984 and Buckingham 2006.

We begin with the standard Helmholtz equation in cylindrical coordinates, where axisymmetry is assumed, and the source term is located at $(r, z) = (0, 0)$.

$$\left[\frac{1}{r}\frac{\partial}{\partial r}\left(r\frac{\partial}{\partial r}\right)+\frac{\partial^2}{\partial z^2}+\frac{\omega^2}{c^2\left(z\right)}\right]P\left(r,z,\omega\right)=\frac{\delta\left(r\right)}{2\pi r}\delta\left(z\right)$$

We first solve the homogeneous equation, and then return later for the inhomogeneous case. Separation of variables allows $P\left(r,z\right)=R\left(r\right)\psi\left(z\right)$. Using k_r^2 as the constant linking the two equations gives $R\left(r\right)=H_0^{(1)}\left(k_r r\right)$ and the depth-separated Helmholtz equation for $\psi\left(z\right)$ as

$$\frac{d^2\psi\left(z\right)}{dz^2}+\left(k_\infty^2 n^2\left(z\right)-k_r^2\right)\psi\left(z\right)=0$$

where the refractive index $n\left(z\right)$ is greater than or equal to 1, and for the profiles described here, $n\left(|z|\geq L\right)=1$, $n\left(0\right)=n_0$, where n_0 is the maximum, and $n\left(z\right)$ varies monotonically from $z=0$ to $|z|=L$. Additionally, the waveguide is symmetric about $z=0$, meaning $n\left(z\right)=n\left(|z|\right)$. Additionally, $k_\infty=\omega/c_\infty$, where c_∞ is the reference sound speed, as well as the sound speed in the bulk medium.

The boundary conditions for this environment are (1) a rigid boundary condition at $z=0$, which is allowable due to the symmetry about this depth, and the placement of the source there (only even mode shapes will be excited), (2) continuous and (3) differentiable mode shapes across $z=L$, and (4) either a Sommerfeld radiation condition directly, or to satisfy the conditions for a proper Sturm-Liouville problem, a pressure release boundary at $z=L+H$, where at some point, H is taken to ∞ .

Below are just a few of the intermediate results in the derivation.

B.1 n^2-Quadratic

For the refractive index profile:

$$n^2\left(0 \le z \le L\right) = n_0^2 - \left(n_0^2 - 1\right)\left(\frac{z}{L}\right)^2$$

$$n^2\left(z > L\right) = 1$$

The depth-separated Helmholtz equation can be rewritten as:

$$y''\left(x\right) + \left(k_z^2 l^2 - x^2\right) y\left(x\right) = 0$$

Where $l^2 = \frac{c_\infty L}{\omega\sqrt{n_0^2 - 1}}$ is defined to nondimensionalize the distances such that $y\left(x\right) = \psi\left(xl\right)/l^2$, or $\psi\left(z\right) = l^2 y\left(\frac{z}{l}\right)$. Additionally, $k_z^2 = k_\infty^2 - k_r^2$. This equation can be rewritten, in the form of Kummers Equation (Abramowitz and Stegun 1965) for $b = \frac{1}{2}$ and $a = -\frac{\left(k_z^2 l^2 - 1\right)}{4} \equiv -\kappa$. These solutions are called Kummer's M and U functions ("hypergeom" and "kummerU" in MATLAB and "Hypergeometric1F1" and "HypergeometricU" in Mathematica). Not all of these solutions are well-behaved near the origin, so the following two solutions are chosen, thanks to their linear independence and finiteness at the origin. The mode shapes in the inhomogeneous region have solutions of the form:

$$y_1\left(x < \frac{L}{l}\right) = A\exp\left(-\frac{x^2}{2}\right) M\left(-\kappa, \frac{1}{2}, x^2\right)$$

$$y_2\left(x < \frac{L}{l}\right) = Bx\exp\left(-\frac{x^2}{2}\right) M\left(-\kappa + \frac{1}{2}, \frac{3}{2}, x^2\right)$$

Where $y_1\left(0\right) = A$, $y_1'\left(0\right) = 0$, and $y_2\left(0\right) = 0$, $y_2'\left(0\right) = B$. Thanks to the rigid boundary condition ($y'\left(0\right) = 0$), only the $y_1\left(x\right)$ is needed. The mode shape solutions for $z > L$ satisfy the equation:

$$y''(x) - 4(\kappa_{cutoff} - \kappa)\, y(x) = 0$$

Where $\kappa_{cutoff} = \frac{\left(\frac{L^2}{l^2} - 1\right)}{4}$. The solutions to this for trapped modes ($\kappa < \kappa_{cutoff}$) are:

$$y\left(x > \frac{L}{l}\right) = C \exp\left(-2\sqrt{\kappa_{cutoff} - \kappa}x\right)$$

By matching boundary conditions at $x = \frac{L}{l} \equiv x_L$, a dispersion relation can be developed.

$$\frac{x_L}{2\sqrt{\kappa_{cutoff} - \kappa}} = \frac{M\left(-\kappa, \frac{1}{2}, x_L^2\right)}{M\left(-\kappa, \frac{1}{2}, x_L^2\right) + 4M\left(-\kappa + 1, \frac{3}{2}, x_L^2\right)}$$

When κ is far from cutoff (at κ_{cutoff}), the solution is surprisingly simple: $\kappa_n = n$, where n is an integer starting at 0 and going up to κ_{cutoff} . For κ near cutoff, the full dispersion relation needs to be evaluated. Additionally, when κ is an integer, the confluent hypergeometric functions are related to associated Laguerre polynomials (see dlmf.nist.gov/13.6.19) which are faster to evaluate. Under the assumption the mode is far from cutoff ($n \ll \kappa_{cutoff}$), the modes can also be normalized approximately in a closed form, giving:

$$\psi_n(0 \le z \le L; n \ll \kappa_{cutoff}) = \left[2^{n-1}\sqrt{\pi}\frac{n!\,(2n)!!}{(2n)!}\right]^{-\frac{1}{2}} \exp\left(-\frac{1}{2}\left(\frac{z}{L}\right)^2\right) M\left(-\kappa_n, \frac{1}{2}, \left(\frac{z}{L}\right)^2\right)$$

When κ is near cutoff, the normalization constant should be evaluated numerically, since there are no closed form solutions for the indefinite integral of the square of confluent hypergeometric functions (though the above form is a reasonably close approximation). The corresponding eigenvalues are:

$$\frac{k_{rn}^2}{k_\infty^2} = n_0^2 - \frac{\sqrt{n_0^2 - 1}}{k_\infty L}\left(4\kappa_n + 1\right)$$

The modal sum for the trapped modes is then:

$$G\left(r, z, \omega\right) = \frac{i\pi}{2} \sum_{n=0}^{\kappa_{cutoff}} H_0^{(1)}\left(k_{rn} r\right) \psi_n\left(z\right) \psi_n\left(0\right)$$

The leaky modes are too computationally expensive to evaluate analytically, due to the need to evaluate confluent hypergeometric functions with complex parameter (κ_n). It was found that confluent hypergeometric functions do not have convenient Taylor series approximations as functions of their parameter, so approximate methods to find leaky modes were unsuccessful.

B.2 n^2-Linear

For a refractive index profile of:

$$n^2\left(0 \le z \le L\right) = n_0^2 - \left(n_0^2 - 1\right)\left(\frac{|z|}{L}\right)$$
$$n^2\left(z > L\right) = 1$$

Evaluating the depth-separated Helmholtz equation with this profile, and then nondimensionalizing with $z = ax$, the equation can be rewritten as:

$$\left(\frac{d^2}{dx^2} - \left(x - \alpha^2\right)\right) y\left(0 \le x \le x_L\right) = 0$$

$$\left(\frac{d^2}{dx^2}+k_z^2\right)y\left(x_L\leq x<x_L+x_H\right)=0$$

Where: $a^3\equiv\frac{L}{k_\infty^2\left(n_0^2-1\right)}$ and $y\left(\frac{z}{a}\right)\equiv\frac{\psi(z)}{a^2}$. Additionally, $\alpha^2\equiv a^2\left(k_\infty^2n_0^2-k_r^2\right)$, $k_z^2=a^2\left(k_\infty^2-k_r^2\right)$, and $\alpha^2=k_z^2+x_L$, where $x_L=\frac{L}{a}$. $x_H=\frac{H}{a}$, where H is the thickness of the homogeneous region (which is taken to ∞ eventually). The solution to this equation for $0\leq x\leq x_L$ are Airy functions of the first and second kind, namely:

$$y\left(x\right)=A\mathrm{Ai}\left(x-\alpha^2\right)+B\mathrm{Bi}\left(x-\alpha^2\right)$$

B.2.1 Trapped Modes

For trapped modes, $0\leq\alpha^2<x_L$, or equivalently $-x_L\leq k_z^2<0$, where these both correspond to the usual definition for trapped modes: $k_\infty^2<k_r^2\leq n_0^2k_\infty^2$. Defining one more convenient parameter, $\beta^2=-k_z^2$, one arrives at:

$$y_{trapped}\left(x\right)=C\exp\left(-\beta x\right)$$

Where the limit as $H\to\infty$ is already taken here. Enforcing rigid boundary conditions and continuity of the solution, one arrives at the dispersion relation:

$$\beta_n\left[\mathrm{Ai}\left(\beta_n^2\right)\mathrm{Bi}'\left(-\alpha_n^2\right)-\mathrm{Bi}\left(\beta_n^2\right)\mathrm{Ai}'\left(-\alpha_n^2\right)\right]=\mathrm{Ai}'\left(-\alpha_n^2\right)\mathrm{Bi}'\left(\beta_n^2\right)-\mathrm{Ai}'\left(\beta_n^2\right)\mathrm{Bi}'\left(-\alpha_n^2\right)$$

Away from cutoff, the solution to this is well approximated by $\mathrm{Ai}'\left(-\alpha_n^2\right)=0$, which has roots:

$$\alpha_n^2 = x_L - t_n^{\frac{2}{3}} \left[1 - \frac{7}{48 t_n^2} - \frac{5}{36 t_n^4} + O\left(\frac{1}{t_n^6} \right) \right]$$

Where $t_n = \frac{3\pi}{2}\left(n - \frac{3}{4}\right)$, and this relationship above is satisfied for large n . For small n , tables of zeros for Ai' exist. These Airy function properties can be found at dlmf.nist.gov/9.9. The total number of trapped modes is given approximately by $N_{modes} = \left(\frac{3}{4}\right) + \left(\frac{2}{3\pi}\right) x_L^{\frac{3}{2}}$. Near cutoff, the dispersion relation should be evaluated numerically, though the values given by the above relation are a good place to start a Newton-Raphson numerical scheme for finding the zeros.

With the trapped eigenvalues found, attention can be return to calculation of the trapped mode shapes, which are given by:

$$\psi_n\left(x = \frac{z}{a}\right) = C_n \left[\mathrm{Ai}\left(x - \alpha_n^2\right) \mathrm{Bi}'\left(-\alpha_n^2\right) - \mathrm{Bi}\left(x - \alpha_n^2\right) \mathrm{Ai}'\left(-\alpha_n^2\right) \right] \text{ for } 0 \le x \le x_L$$
$$\psi_n\left(x = \frac{z}{a}\right) = C_n \left[\mathrm{Ai}\left(\beta_n^2\right) \mathrm{Bi}'\left(-\alpha_n^2\right) - \mathrm{Bi}\left(\beta_n^2\right) \mathrm{Ai}'\left(-\alpha_n^2\right) \right] \exp\left(-\beta_n \left(x - x_L\right)\right) \text{ for } x \ge x_L$$

Where the normalization constant C_n is given by:

$$\frac{1}{a C_n^2} = \frac{\alpha_n^2}{\pi^2} + \frac{1}{2\beta_n} \left[\mathrm{Ai}\left(\beta_n^2\right) \mathrm{Bi}'\left(-\alpha_n^2\right) - \mathrm{Bi}\left(\beta_n^2\right) \mathrm{Ai}'\left(-\alpha_n^2\right) \right]^2$$

The above equations are exact, meaning that they exactly satisfy the wave equation, and the only numerical calculations that come into play are simple Newton-Raphson zero finding algorithms, where a good first guess at the location of the eigenvalue is known analytically. It is worth noting that even the normalization constant is exact, which is owed to the fact that squares of Airy functions have not just definite, but also indefinite closed form solutions.

B.2.2 Leaky Modes

To evaluate the leaky modes, care is taken to first specify a proper Sturm-Liouville problem (for finite H), solve the problem exactly, and then take a limit, where a sum of modes turns into an integral. This integral is then evaluated with residue theorem, which turns it back into a sum, but this time a sum of poles. These poles can then be thought of as improper modes, though these improper modes do not have many of the same convenient properties as their proper counterparts, such as real eigenvalues or being square-integrable.

Only a few intermediate steps are provided here. First, the original two equations to be solved:

$$\left[\frac{d^2}{dx^2} - \left(x - \alpha^2\right)\right] y\left(x < x_L\right) = 0$$

$$\left[\frac{d^2}{dx^2} + \kappa^2\right] y\left(x > x_L\right) = 0$$

Where $\kappa^2 = \alpha^2 - x_L$. Applying the boundary conditions (with a pressure release condition at $x = x_H$), the dispersion relation emerges:

$$-\kappa \frac{\mathrm{Bi}'\left(-\alpha^2\right)\mathrm{Ai}\left(-\kappa^2\right) - \mathrm{Ai}'\left(-\alpha^2\right)\mathrm{Bi}\left(-\kappa^2\right)}{\mathrm{Bi}'\left(-\alpha^2\right)\mathrm{Ai}'\left(-\kappa^2\right) - \mathrm{Ai}'\left(-\alpha^2\right)\mathrm{Bi}'\left(-\kappa^2\right)} = \tan\left(kx_H\right)$$

The normalization constant, after taking a limit for large x_H , is:

$$\frac{1}{C_n^2} = \frac{ha}{2} \frac{\left[\mathrm{Ai}\left(-\kappa_n^2\right) - \frac{\mathrm{Ai}'\left(-\alpha_n^2\right)}{\mathrm{Bi}'\left(-\alpha_n^2\right)}\mathrm{Bi}\left(-\kappa_n^2\right)\right]^2}{\sin^2\left(\kappa_n x_H\right)}$$

The dispersion relation can further simplify this (particularly the denominator). The modal sum, before the limit $x_H \to \infty$ is taken, (which turns this into an integral) is:

$$G(x,\rho) = \sum_n \frac{\frac{i}{2\pi h a} H_0^{(1)}\left(\rho\sqrt{\kappa_{max}^2 - \kappa_n^2}\right)\left[\mathrm{Bi}'(-\alpha_n^2)\,\mathrm{Ai}(x-\alpha_n^2) - \mathrm{Ai}'(-\alpha_n^2)\,\mathrm{Bi}(x-\alpha_n^2)\right]}{\left[\mathrm{Bi}'(-\alpha_n^2)\,\mathrm{Ai}(-\kappa_n^2) - \mathrm{Ai}'(-\alpha_n^2)\,\mathrm{Bi}(-\kappa_n^2)\right]^2 + \frac{1}{\kappa_n^2}\left[\mathrm{Bi}'(-\alpha_n^2)\,\mathrm{Ai}'(-\kappa_n^2) - \mathrm{Ai}'(-\alpha_n^2)\,\mathrm{Bi}'(-\kappa_n^2)\right]^2}$$

Where $\kappa_{max}^2 = \frac{x_L}{(n_0^2-1)}$ and $\rho = \frac{r}{a}$. This turns into an integral, where $\sum_n [\,] \to \int [\,]\, dn$, and $dn = \frac{h}{\pi} d\kappa$. The leaky mode values for κ range from $\kappa = 0$ (cutoff) $\kappa = \kappa_{max}$ (last leaky mode), but then continues on to $\kappa \to \infty$ for the evanescent modes, which decay in range and depth (and are more easily neglected). The integral is:

$$G(x,\rho) = \frac{i}{2\pi^2 a}\int_0^\infty d\kappa \frac{H_0^{(1)}\left(\rho\sqrt{\kappa_{max}^2 - \kappa^2}\right)\left[\mathrm{Bi}'(-\alpha^2)\,\mathrm{Ai}(x-\alpha^2) - \mathrm{Ai}'(-\alpha^2)\,\mathrm{Bi}(x-\alpha^2)\right]}{\left[\mathrm{Bi}'(-\alpha^2)\,\mathrm{Ai}(-\kappa^2) - \mathrm{Ai}'(-\alpha^2)\,\mathrm{Bi}(-\kappa^2)\right]^2 + \frac{1}{\kappa^2}\left[\mathrm{Bi}'(-\alpha^2)\,\mathrm{Ai}'(-\kappa^2) - \mathrm{Ai}'(-\alpha^2)\,\mathrm{Bi}'(-\kappa^2)\right]^2}$$

To continue, the zeros of the denominator must be found, such that residue theorem can occur. Complex values of κ are sought such that the denominator is zero. Near $\kappa = 0$, the full denominator must be used to search for zeros. However, for κ large, the denominator can be asymptotically approximated to:

$$D\left(\kappa;\kappa^2 \gg 1\right) = \frac{1}{\pi^2}\sqrt{\frac{\kappa^2 + x_L}{\kappa^2}}\left(1 - \frac{1}{4\kappa^3}\sin\left(\frac{4}{3}\left[\left(\kappa^2 + x_L\right)^{\frac{3}{2}} - \kappa^3\right]\right)\right)$$

Using this, numerical methods are used to find zeros namely a search grid in $\kappa = \kappa_R + i\kappa_I$

is defined. Stability is added to the method by ensuring that successive zeros, κ_n , do not change too quickly. Precision is added by taking the values in the 3x3 grid surrounding a local minimum, and fitting a least-squares-fit parabola to that data. The results for a variety of x_L values are shown below, where $n_0 = \frac{1500}{1450}$, $L = 100$ m, and $c_\infty = 1500$ m/s. In Figure 1, real and imaginary parts are plotted on a logarithmic scale. The first 100 leaky modes (after cutoff) are plotted with red dots to give an idea for the number of modes included. The black modes are the remainder of the leaky modes. The blue dots are for evanescent modes, which occur when $\kappa \geq \kappa_{max}$. The black line represents the line where real and imaginary parts are equal. Technically, there are infinitely many points, but calculations were stopped after $\kappa = 2\kappa_{max}$.

The residue at these poles is then required, which requires a derivative of the denominator, which is in principle straightforward to do (and is omitted here). The sum of improper (leaky) modes is:

$$G_{leaky}(\rho, z) = -\frac{1}{\pi a}\sum_n \frac{1}{D'(\kappa_n)} H_0^{(1)}\left(\rho\sqrt{\kappa_{max}^2 - \kappa_n^2}\right) \times \left[\mathrm{Bi}'\left(-\alpha_n^2\right)\mathrm{Ai}\left(x-\alpha_n^2\right) - \mathrm{Ai}'\left(-\alpha_n^2\right)\mathrm{Bi}\left(x-\alpha_n^2\right)\right]$$

Omitted from this study is a discussion of how to close the contour integral (*e.g.* which quadrants), asymptotic evaluations of Airy functions for complex argument, and the importance of accurately capturing modes that are right near cutoff, either on the leaky side or the trapped side. Additionally, with this representation, the improper modes are found to be divergent in the homogeneous layer. The proper way to handle this is not with residue theorem, but with a Mittag-Leffler expansion, which turns an integral into a summation just like residue theorem, except this time, the integral is not over a closed contour, and all poles are needed, not just the encircled ones. This presents a variety of challenges, further

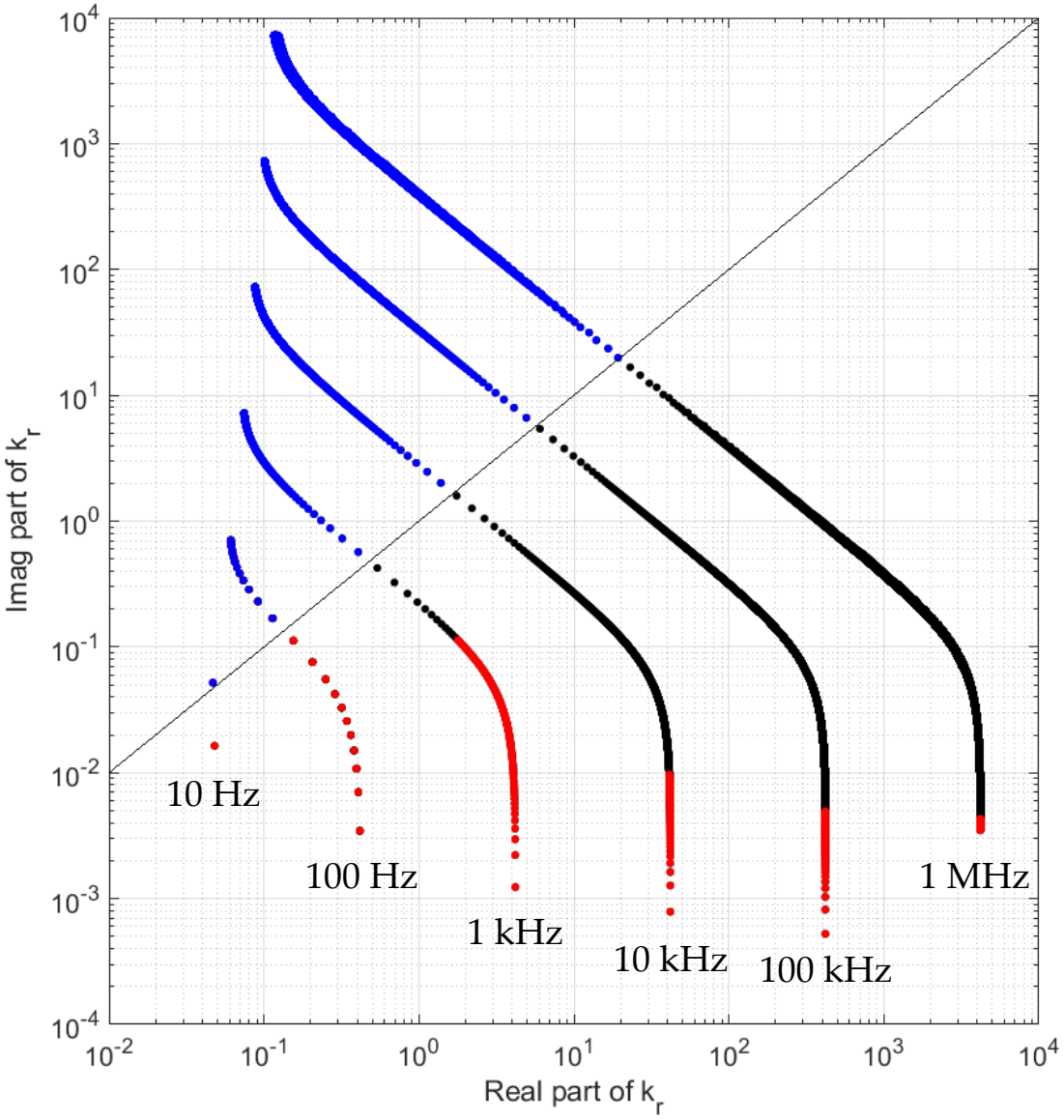

Figure B.1: Plots of the real and imaginary parts of the leaky mode eigenvalues (poles) for a variety of frequencies.

discussion of which is omitted here.

Using the techniques described, verifications studies were performed with Kraken (Porter and Reiss 1984) (a mode code), and RAM (Collins 1996) (a parabolic equation code). Figure B.2 shows a side-by-side comparison of these Airy modes (upper) and RAM (lower). The only discrepancies in Airy modes that occurred (not pictured) were when eigenvalues were found very close to the cutoff frequency, but Kraken also experienced similar troubles. Otherwise,

cross correlations between acoustic field predictions of Airy modes and of Kraken/RAM were found to be extremely high (0.999 and above) over a variety of depths, ranges, and frequencies. Airy modes offered similar computation times compared to Kraken and RAM, though an improvement in the zero-finding algorithm for the denominator would drastically improve these results. This is a subject of future work.

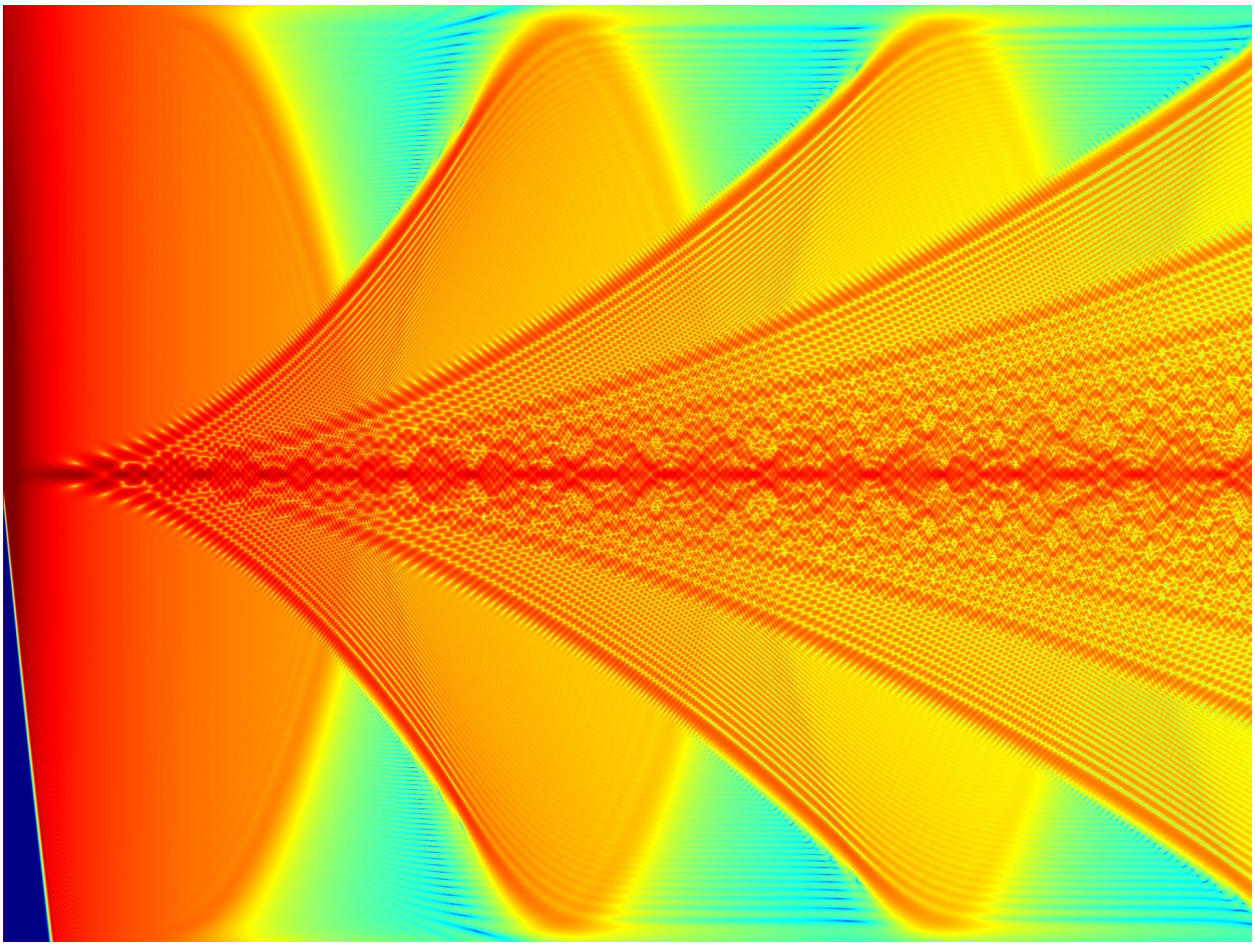

Figure B.2: Side by side comparison of Airy modes (upper half) and RAM, a parabolic equation solver (lower half). The plots show 5 km range and ± 100 m depth. The frequency evaluated is 5 kHz, with c_∞ =1500 m/s, $n_0 = \frac{1500}{1450}$, and $L = 100$ m. The color scale spans -150 to -50 dB.

Appendix C

Comparisons to Delta-K Radar

Δk radar is a technique that was first developed by Weissman in 1973, and has since been used for estimating sea-wave height variation (Weissman 1973), phase velocity of surface gravity waves (Popstefanija 1993), vegetation height (Sarabandi 1997), and snow-water equivalents (Engen 2004), among other applications. Further discussion of Δk radar for parameter estimation in random media can be found in Sarabandi and Nashashibi (1999), Sarabandi *et al.* (1999), and Lopez-Sanchez *et al.* (1998). In Δk radar, two frequencies are broadcast simultaneously and then recorded simultaneously. The complex amplitudes of these fields are then cross-correlated, which is termed the two-frequency correlation function. This formulation bears some resemblance to autoproducts, as defined here. The following is a comparison of autoproducts for ocean acoustic applications, and Δk radar for a variety of radar applications.

Definition: The two-frequency correlation function is defined in (Weissman 1973) as:

$$R \equiv \frac{\langle E\left(f_2\right)^* E\left(f_1\right)\rangle}{\sqrt{\langle\left|E\left(f_2\right)\right|^2\rangle\langle\left|E\left(f_1\right)\right|^2\rangle}}$$

where E is effectively the complex amplitude of the returned signal, and f_2 and f_1 are the two frequencies that are broadcast, and the $\langle\ \ \rangle$ symbols indicate an ensemble average over

multiple pings (snapshots). The denominator provides a normalization to compensate for different broadcast/receive amplitudes at different frequencies. The autoproduct, is defined as:

$$AP_{\Delta} \equiv P\left(f_2\right) P^{*}\left(f_1\right)$$

There are two main differences: the lack of an ensemble average (though bandwidth averaging, as is frequently performed, serves a similar mathematical purpose to reduce the impact of noise and increase robustness), and the lack of normalization (though normalization is used in autoproduct-based signal processing, the average amplitudes are estimated over a spatial region, rather than over an ensemble of samples).

Hardware differences in radar and sonar: In acoustics, it is common to broadcast a broadband signal, and to then record that signal on multiple array elements, where typically the transmitting and receiving transducers are physically distinct. In contrast, it seems that radar is limited practically to broadcasting at most two narrowband signals simultaneously, and that signal recording is done with the same antenna used for broadcast (Weissman 1973, Popstefanija 1993).

Bandwidth Averaging: In acoustics, autoproducts can be bandwidth averaged quite easily, again, because a broad range of frequencies can be measured and broadcast easily. However, in radar, a stepped-frequency delta K (SFDK) radar can be created (Popstefanija 1993). In that study, 16 pairs of frequencies were broadcast sequentially, and then recorded sequentially. That study found an improvement in the signal-to-clutter ratio (analogous to signal-to-noise ratio) by 6 dB (approximately a factor of $\sqrt{16}$ improvement). This SFDK technique appears to have required some hardware changes and careful timing to fit all 16 pings into the broadcast before the antenna was switched to receiving mode.

Amplitude vs. Phase: Many of the Δk radar techniques seem to not require the phase

information of the two-frequency correlation function. To simplify the analysis provided in (Weissman 1973), consider a sea-to-array distance of d , where d is a Gaussian random variable with mean d_0 , and standard deviation σ_d (in other words, the RMS sea level height). A single ping would produce a two-frequency correlation function of $exp\left(i\Delta kd\right)$. Ensemble averaging this over the Gaussian random variable d gives $R = exp\left(i\Delta kd_0\right) exp\left(-\frac{\left(\Delta k\sigma_d\right)^2}{2}\right)$. If the objective is to find σ_d , then it is natural to take the magnitude of this quantity, and plot how it changes with Δk . However, for sonar applications, phase information is more important, or more specifically, how the phase varies across the array. Thus, while the two-frequency correlation function in Δk radar does rely on phase differences, it does so in an indirect way (via magnitudes of ensemble averages), whereas autoproducts rely on the phases more directly (via cross spectral density matrices).

Cross Terms: In (Weissman 1973), a theoretical discussion is provided for a Δk radar system reflecting off a sea surface with multiple specular points (or, in more simple acoustics parlance, point scatterers). When forming the two-frequency correlation function, it is mentioned that the specular points need to be well-separated relative to the in-band wavelength, or in the authors words, have "deep phase modulation" . In that study, the specular points were sufficiently well-separated relative to the frequencies of radar being used, and so "cross product terms" , or as referred to here, cross terms, are not particularly detrimental. There is a similar requirement found for successful use of acoustic autoproducts that ray arrival times are well-separated relative to the signal bandwidth, though in some regimes the cross terms created can become detrimental. It seems that in the Δk radar regime, these cross terms are not as problematic as they are in ocean acoustic autoproducts.

Spatial Sampling: In acoustics, there are typically several acoustic elements in an array, which together can determine wavefront direction and arrival information. In comparison, radar typically has only one receiving element, but it is a directional element which allows for wavefront direction and arrival information to be retrieved. Other radar techniques exist

which allow more diverse spatial sampling, such as interferometric synthetic aperture radar (InSAR) techniques, which provide allow spatial sampling by moving the transmitting and receiving arrays relative to the target. Δk versions of InSAR have been developed, and have been successful for applications such as estimating forest canopy heights (Sarabandi 1997), and snow thickness (Engen 2004). Acoustic applications, on the other hand, can have potentially up to hundreds of spatially separated elements in the array, which allows for a wider variety of signal processing techniques, including autoproduct-based sonar techniques.

Out-of-Band Fields: In the Δk radar literature, it does not appear that comparisons are ever drawn between the two-frequency correlation function and a radar pulse that genuinely propagated at the difference frequency. Likely part of the reason is that absolute phase information (*i.e.* the phase that depends on the overall antenna-to-target distance) is not crucial for many Δk radar applications, whereas this absolute phase information is more important for sonar applications. Additionally, in primarily-single-path line-of-sight-propagation environments (like in many radar applications), there is effectively little-to-no difference between an out-of-band field and an autoproduct-generated field. However, in multipath ocean acoustics environments, the differences between autoproducts and out-of-band fields may be non-trivial. For example, a multipath shallow ocean acoustic field well-described by rays at high frequencies were used to generate autoproducts at much lower frequencies that were found to correlate well with a low frequency acoustic field well-described by a modal decomposition. So the claim that autoproducts mimic out-of-band fields is more surprising in a field like ocean acoustics than it may be in a field like radar due to the non-trivial differences between high and low frequency propagation in ocean environments.

Time Domain Analogies: In the (Weissman 1973) paper, there is a discussion of the similarities between the Δk radar technique and impulse radar techniques, where phase differences in Δk radar can provide RMS ocean surface heights, whereas time delays in impulse radar can be used quite directly to estimate RMS ocean surface heights. As stated in that

paper, time delays and phase differences are simply Fourier conjugates of one another, and because the Δk radar regime doesnt appear to be subject to the difficulties of sonar regime (*i.e.* multipath leading to cross terms), the Fourier analysis comparing these two is straightforward. It is also stated in that paper that $R(\Delta k)$ is an inverse Fourier transform away from the sea level height probability distribution function, using Δk as the transform variable. This is similar to the discussion in Appendix A of this thesis covering how bandwidth averaged frequency-difference autoproducts, $\langle AP_{\Delta} \rangle (r, \Delta\omega)$, are Fourier conjugates with the magnitude squared of the complex analytic signal. In other words, the instantaneous power of the signal plus its harmonic conjugate (*i.e.* its Hilbert transform) added together is a Fourier transform away from the bandwidth averaged autoproduct. Or, mathematically, $F_{t \to \Delta\omega} \left[|P(r,t) + iH[P(r,t)]|^2 \right] = \langle AP_{\Delta} \rangle (r, \Delta\omega)$, where F is the Fourier transform, and H is the Hilbert transform.

Summary: Overall, the two-frequency correlation functions from Δk radar are similar to the autoproducts presented here, but with some key differences. Δk radar does not typically have the luxury of broadband signals or wide spatial sampling, whereas autoproduct-based sonar does not typically have the luxury of nearly-single-path wave propagation or a known broadcast waveform. It is possible, though, that Δk -like techniques could be applied to short range (high frequency) active sonar applications, particularly if the target were more distributed than localized. Its also possible that statistics of bathymetry variations, rough ocean surfaces, mesoscale eddies, or other pseudo-random oceanographic processes could be estimated with Δk -like active sonar (*i.e.* active inversion) techniques. However, these topics are beyond the scope of this thesis.

BIBLIOGRAPHY

Abadi, Shima, Haworth, Kevin J., Mercado, Karla P., & Dowling, David R. 2017. Using frequency-sum beamforming in passive cavitation imaging. *J. Acoust. Soc. Am.*, **141**(5), 3613–3613.

Abadi, Shima H., Song, H. C., & Dowling, David R. 2012. Broadband sparse-array blind deconvolution using frequency-difference beamforming. *J. Acoust. Soc. Am.*, **132**(5), 3018–3029.

Abraham, Douglas A., Gelb, James M., & Oldag, Andrew W. 2011. Background and clutter mixture distributions for active sonar statistics. *IEEE J. Ocean. Eng.*, **36**(2), 231–247.

Abramowitz, Milton, & Stegun, Irene. 1965. *Handbook of Mathematical Functions*. Courier Corporation.

Ammicht, E, & Stickler, D C. 1984. Uniform asymptotic evaluation of the continuous spectrum contribution for a stratified ocean. *J. Acoust. Soc. Am.*, **76**(1), 186–191.

Baggeroer, A. B., Kuperman, W. A., & Schmidt, Henrik. 1988. Matched field processing: Source localization in correlated noise as an optimum parameter estimation problem. *J. Acoust. Soc. Am.*, **83**(2), 571–587.

Baggeroer, A. B., Kuperman, W. A., & Mikhalevsky, P. N. 1993. An overview of matched field methods in ocean acoustics. *IEEE J. Ocean. Eng.*, **18**(4), 401–424.

Baldacci, Alberto, Haralabus, Georgios, Coraluppi, Stefano, & Prior, Mark. 2007. Adaptive sub-band processing in active detection and tracking. 25–29.

Bartberger, C L. 1977. Comparison of two normalmode solutions based on different branch cuts. *J. Acoust. Soc. Am.*, **61**(6), 1643–1643.

Beckers, Benoit, & Beckers, Pierre. 2012. A general rule for disk and hemisphere partition into equal-area cells. *Comput. Geom. Theory Appl.*, **45**(7), 275–283.

Beran, M J, & Parrent, G B. 1964. *Theory of Partial Coherence*. Prentice-Hall international series in physics. Prentice-Hall.

Bickel, Peter J., & Levina, Elizaveta. 2008. Regularized estimation of large covariance matrices. *Ann. Stat.*, **36**(1), 199–227.

Blacodon, Daniel. 2011. Spectral estimation method for noisy data using a noise reference. *Appl. Acoust.*, **72**(1), 11–21.

Bonomo, Anthony L., Chotiros, Nicholas P., & Isakson, Marcia J. 2015. On the validity of the effective density fluid model as an approximation of a poroelastic sediment layer. *J. Acoust. Soc. Am.*, **138**(2), 748–757.

Booth, N.O., Baxley, P.A., Rice, J.A., Schey, P.W., Hodgkiss, W.S., D'Spain, G.L., & Murray, J.J. 1996. Source localization with broad-band matched-field processing in shallow water. *IEEE J. Ocean. Eng.*, **21**(4), 402–412.

Borcea, Liliana, Papanicolaou, George, & Tsogka, Chrysoula. 2007. Asymptotics for the Space-Time Wigner Transform with Applications to Imaging. Interdisciplinary Mathematical Sciences, vol. 2, no. August 2016. World Scientific Publishing Co. Pte. Ltd.

Brekhovskikh, L. M., & Lysanov, Yu. P. 2003. *Fundamentals of Ocean Acoustics*. Springer.

Brumley, B H, Cabrera, R G, Deines, K L, & Terray, E A. 1991. Performance of a broad-band acoustic Doppler current profiler. *IEEE J. Ocean. Eng.*, **16**(4), 402–407.

Bucker, Homer P. 1976. Use of calculated sound fields and matchedfield detection to locate sound sources in shallow water. *J. Acoust. Soc. Am.*, **59**(2), 368–373.

Buckingham, Michael J. 1986. Theory of acoustic propagation around a conical seamount. *J. Acoust. Soc. Am.*, **80**(1), 265–277.

Buckingham, Michael J., & Giddens, Eric M. 2006. On the acoustic field in a Pekeris waveguide with attenuation in the bottom half-space. *J. Acoust. Soc. Am.*, **119**(1), 123–142.

Cerveny, V, Molotkov, Ivan Anatolévich, & Psencik, Ivan. 1977. *Ray method in seismology*. Univerzita Karlova.

Chapman, Chris H. 2004. *Fundamentals of Seismic Wave Propagation*. Cambridge: Cambridge University Press.

Cheng, Corey I, & Wakefield, Gregory H. 1999 (sep). Introduction to Head-Related Transfer Functions (HRTFs): Representations of HRTFs in Time, Frequency, and Space. *In: Audio Eng. Soc. Conv. 107*.

Chitre, Mandar, Shahabudeen, Shiraz, & Stojanovic, Milica. 2008. Underwater Acoustic Communications and Networking: Recent Advances and Future Challenges. *Mar. Technol. Soc. J.*, **42**(1), 103–116.

Chiu, Linus Y. S., Lin, Ying-Tsong, Chen, Chi-Fang, Duda, Timothy F., & Calder, Brian. 2011. Focused sound from three-dimensional sound propagation effects over a submarine canyon. *J. Acoust. Soc. Am.*, **129**(6), EL260–EL266.

Cohen, Leon. 1989. Time-frequency distributions-a review. *Proc. IEEE*, **77**(7), 941–981.

Cohen, Leon, & Posch, Theodore E. 1985. Positive Time-Frequency Distribution Functions. *IEEE Trans. Acoust.*, **33**(1), 31–38.

Collins, Michael D, & Kuperman, W a. 1991. Focalization: Environmental focusing and source localization. *J. Acoust. Soc. Am.*, **90**(3), 1410–1422.

Collins, Michael D., Cederberg, R. J., King, David B., & ChinBing, Stanley A. 1996. Comparison of algorithms for solving parabolic wave equations. *J. Acoust. Soc. Am.*, **100**(1), 178–182.

Cox, H, Zeskind, R, & Owen, M. 1987. Robust adaptive beamforming. *IEEE Trans. Acoust.*, **35**(10), 1365–1376.

Debever, Claire, & Kuperman, W. A. 2007. Robust matched-field processing using a coherent broadband white noise constraint processor. *J. Acoust. Soc. Am.*, **122**(4), 1979–1986.

Doolittle, R D, Tolstoy, A, & Sullivan, E J. 1993. *Special Issue on Detection and Estimation in Matched-Field Processing – Guest Editorial*.

Douglass, Alexander S., Song, H. C., & Dowling, David R. 2017. Performance comparisons of frequency-difference and conventional beamforming. *J. Acoust. Soc. Am.*, **142**(3), 1663–1673.

Dowling, David R., & Sabra, Karim G. 2015. Acoustic Remote Sensing. *Annu. Rev. Fluid Mech.*, **47**(1), 221–243.

Engen, Geir, Guneriussen, Tore, & Overrein, Øyvind. 2004. Delta-K interferometric SAR technique for snow water equivalent (SWE) retrieval. *IEEE Geosci. Remote Sens. Lett.*, **1**(2), 57–61.

Evans, R. B. 1983. A coupled mode solution for acoustic propagation in a waveguide with stepwise depth variations of a penetrable bottom. *J. Acoust. Soc. Am.*, **74**(1), 188–195.

Ewing, W. Maurice, Jardetzky, Wenceslas S., & Press, Frank. 1957. *Elastic Waves in Layered Media*. McGraw Hill.

Ferguson, Brian G. 1994. Application of the short-time Fourier transform and the WignerVille distribution to the acoustic localization of aircraft. *J. Acoust. Soc. Am.*, **96**(2), 821–827.

Fizell, R.G. 1987. Application of High-resolution Processing to Range and Depth Estimation Using Ambiguity Function Methods. *J. Acoust. Soc. Am.*, **82**(1987), 606—-613.

Foldy, Leslie L. 1945. The multiple scattering of waves. I. General theory of isotropic scattering by randomly distributed scatterers. *Phys. Rev.*, **67**(3-4), 107–119.

Fresnel, Augustin. 1866. *Œuvres completes d'Augustin Fresnel*.

Frisk, George V. 1994. *Ocean and Seabed Acoustics: A Theory of Wave Propagation*.

Geroski, David J., Dzieciuch, Matthew, & Dowling, David R. 2018. Explorations of in-situ passive source localization in the Philippine Sea using frequency-difference matched field processing. *J. Acoust. Soc. Am.*, **143**(3), 1760–1760.

Hamson, Rachel M. 1989. Environmental and system effects on source localization in shallow water by the matched-field processing of a vertical array. *J. Acoust. Soc. Am.*, **86**(5), 1950.

Hecht, Eugene. 2016. *Optics*. 5th edn. Pearson.

Hickman, Granger, & Krolik, Jeffrey L. 2004. Matched-field depth estimation for active sonar. *J. Acoust. Soc. Am.*, **115**(2), 620.

Hodgkiss, W. S., & Preisig, J. C. 2012. Kauai Acomms MURI 2011 (KAM11) experiment. *Proc. 11th Eur. Conf. Underw. Acoust. (ECUA 2012)*, **34**, 185.

Högbom, J. A. 1974. Aperture synthesis with a non-regular distribution of interferometer baselines. *Astron. Astrophys. Suppl. Ser.*, **15**, 417.

Hursky, Paul, Porter, Michael B., Siderius, Martin, & McDonald, Vincent K. 2004a. High-frequency (816 kHz) model-based source localization. *J. Acoust. Soc. Am.*, **115**(6), 3021–3032.

Hursky, Paul, Porter, Michael B., Siderius, Martin, & McDonald, Vincent K. 2004b. High-frequency (816 kHz) model-based source localization. *J. Acoust. Soc. Am.*, **115**(6), 3021–3032.

Hustedt, Bernhard, Operto, Stéphane, & Virieux, Jean. 2004. Mixed-grid and staggered-grid finite-difference methods for frequency-domain acoustic wave modelling. *Geophys. J. Int.*, **157**(3), 1269–1296.

Isakson, Marcia J., & Chotiros, Nicholas P. 2011. Finite element modeling of reverberation and transmission loss in shallow water waveguides with rough boundaries. *J. Acoust. Soc. Am.*, **129**(3), 1273–1279.

Jackson, Darrell R., & Richardson, Michael D. 2007. *High-Frequency Seafloor Acoustics*.

Jensen, Finn B., Kuperman, William A., Porter, Michael B., & Schmidt, Henrik. 2011. *Computational Ocean Acoustics*. Springer.

Johnson, D.H. 1982. The application of spectral estimation methods to bearing estimation problems. *Proc. IEEE*, **70**(9), 1018–1028.

Katsnelson, Boris, Petnikov, Valery, & Lynch, James. 2012. *Fundamentals of Shallow Water Acoustics*. Boston, MA: Springer US.

Kinsler, Lawrence E, Frey, Austin R, Coppens, Alan B, & Sanders, James V. 2006. *Fundamentals of Acoustics*. Vol. 1. London, UK: ISTE.

Kravtsov, Yu. A., & Orlov, Yu. I. 1993. *Caustics, Catastrophes and Wave Fields*. Springer Series on Wave Phenomena, vol. 15. Berlin, Heidelberg: Springer Berlin Heidelberg.

Kuperman, William A., & Roux, Phillipe. 2007. *Underwater Acoustics*. New York, NY: Springer-Verlag.

Labianca, Frank M. 1973. Normal modes, virtual modes, and alternative representations in the theory of surfaceduct sound propagation. *J. Acoust. Soc. Am.*, **53**(4), 1137–1147.

Lee, Kevin M., Ballard, Megan S., McNeese, Andrew R., & Wilson, Preston S. 2017. Sound speed and attenuation measurements within a seagrass meadow from the water column into the seabed. *J. Acoust. Soc. Am.*, **141**(4), EL402–EL406.

Leifer, Ira, & Tang, Dajun. 2007. The acoustic signature of marine seep bubbles. *J. Acoust. Soc. Am.*, **121**(1), EL35–EL40.

Lipa, Jessica E, Worthmann, Brian M, & Dowling, David R. 2018. Measurement of auto-product fields in a Lloyd's mirror environment. *J. Acoust. Soc. Am.*, **143**(4), 2419–2427.

Lopez-Sanchez, J.M., Fortuny-Guasch, J., Sieber, A.J., & Sarabandi, K. 1998. Validation of the backscattered frequency correlation function for the inversion of biophysical parameters from natural targets. *Pages 2390–2392 vol.5 of: IGARSS '98. Sens. Manag. Environ. 1998 IEEE Int. Geosci. Remote Sensing. Symp. Proceedings. (Cat. No.98CH36174)*, vol. 5. IEEE.

Love, Richard H. 1978. Resonant acoustic scattering by swimbladderbearing fish. *J. Acoust. Soc. Am.*, **64**(2), 571–580.

Lucke, Robert L. 2006. RayleighSommerfeld diffraction and Poisson's spot. *Eur. J. Phys.*, **27**(2), 193–204.

Ludwig, Donald. 1966. Uniform asymptotic expansions at a caustic. *Commun. Pure Appl. Math.*, **19**(2), 215–250.

Medwin, Herman. 1970. In situ acoustic measurements of bubble populations in coastal ocean waters. *J. Geophys. Res.*, **75**(3), 599–611.

Michalopoulou, Z.-H., & Porter, M.B. Focalization in the Gulf of Mexico. *Pages 3085–3088 of: 1996 IEEE Int. Conf. Acoust. Speech, Signal Process. Conf. Proc.*, vol. 6. IEEE.

Mori, Kazuyoshi, Miyazaki, Ayano, Ogasawara, Hanako, Yokoyama, Tomoki, & Nakamura, Toshiaki. 2006. Finite Difference Time Domain Analysis of Underwater Acoustic Lens System for Ambient Noise Imaging. *Jpn. J. Appl. Phys.*, **45**(5B), 4834–4841.

Morse, P. M., & Ingard, K. U. 1970. *Theoretical Acoustics*. McGraw Hill.

Morse, Phillip, & Feshbach, Herman. 1953. *Methods of Theoretical Physics*. McGraw Hill.

Mours, Alexis, Ioana, Cornel, Mars, Jerome, Josso, Nicolas, & Doisy, Yves. 2016. Target-depth estimation in active sonar: Cramer-Rao bounds for a bilinear sound-speed profile. *J. Acoust. Soc. Am.*, **140**(3), 1771–1782.

Nardin, Mark, Perger, W. F., & Bhalla, Atul. 1992. Numerical evaluation of the confluent hypergeometric function for complex arguments of large magnitudes. *J. Comput. Appl. Math.*, **39**(2), 193–200.

Nitzberg, Ramon. 1972. Constant-False-Alarm-Rate Signal Processors for Several Types of Interference. *IEEE Trans. Aerosp. Electron. Syst.*, **AES-8**(1), 27–34.

Pierce, Allan D. 1981. Acoustics: An Introduction to its Physical Principles and Applications. *J. Acoust. Soc. Am.*, **70**(5), 1548–1548.

Popstefanija, Ivan, McQueen, D.S., & McIntosh, R.E. 1993. A stepped-frequency delta-K microwave radar for oceanographic studies. *IEEE Trans. Geosci. Remote Sens.*, **31**(3), 681–691.

Porter, Michael, & Reiss, Edward L. 1984. A numerical method for oceanacoustic normal modes. *J. Acoust. Soc. Am.*, **76**(1), 244–252.

Porter, Michael B. 1993. Acoustic models and sonar systems. *IEEE J. Ocean. Eng.*, **18**(4), 425–437.

Porter, Michael B., & Bucker, Homer P. 1987. Gaussian beam tracing for computing ocean acoustic fields. *J. Acoust. Soc. Am.*, **82**(4), 1349–1359.

Primakoff, Henry, Klein, Martin J, Keller, Joseph B, & Carstensen, E L. 1947. Diffraction of Sound around a Circular Disk. *J. Acoust. Soc. Am.*, **19**(1), 132–142.

Riris, H, Carlisle, C B, McMillen, D F, & Cooper, D E. 1996. Explosives detection with a frequency modulation spectrometer. *Appl. Opt.*, **35**(24), 4694.

Sarabandi, K., & Nashashibi, A. 1999. Analysis and applications of backscattered frequency correlation function. *IEEE Trans. Geosci. Remote Sens.*, **37**(4), 1895–1906.

Sarabandi, K., Legault, S.R., & Sieber, A. 1999. Random media parameter estimation using the frequency covariance function of radar backscatter. *Pages 1832–1834 of: IEEE 1999 Int. Geosci. Remote Sens. Symp. IGARSS'99 (Cat. No.99CH36293)*, vol. 3. IEEE.

Sarabandi, Kamal. 1997. Δk-radar equivalent of interferometric SAR's: a theoretical study for determination of vegetation height. *IEEE Trans. Geosci. Remote Sens.*, **35**(5), 1267–1276.

Schmidt, Henrik, & Jensen, Finn B. 1985. A full wave solution for propagation in multilayered viscoelastic media with application to Gaussian beam reflection at fluidsolid interfaces. *J. Acoust. Soc. Am.*, **77**(3), 813–825.

Schmidt, Henrik, Baggeroer, A. B., Kuperman, W. A., & Scheer, E. K. 1990. Environmentally tolerant beamforming for highresolution matched field processing: Deterministic mismatch. *J. Acoust. Soc. Am.*, **88**(4), 1851–1862.

Schmidt, R. 1986. Multiple emitter location and signal parameter estimation. *IEEE Trans. Antennas Propag.*, **34**(3), 276–280.

Shang, E. C. 1985. Source depth estimation in waveguides. *J. Acoust. Soc. Am.*, **77**(4), 1413–1418.

Skudrzyk, Eugen. 1971. *The Foundations of Acoustics*. Vienna: Springer Vienna.

Soares, C. 2001. Matched-field processing: acoustic focalization with data taken in a shallow water area of the Strait of Sicily.

Sommerfeld, A. 1896. Mathematische Theorie der Diffraction. *Math. Ann.*, **47**(2-3), 317–374.

Song, H. C., de Rosny, J, & Kuperman, W. a. 2003. Improvement in matched field processing using the CLEAN algorithm. *J. Acoust. Soc. Am.*, **113**(3), 1379–1386.

Stanic, S, Briggs, K B, Fleischer, P, Sawyer, W B, & Ray, R I. 1989. High-frequency acoustic backscattering from a coarse shell ocean bottom. *J. Acoust. Soc. Am.*, **85**(1), 125–136.

Stein, Seymour. 1981. Algorithms for Ambiguity Function Processing. *IEEE Trans. Acoust.*, **29**(3), 588–599.

Stickler, D. C. 1975. Normalmode program with both the discrete and branch line contributions. *J. Acoust. Soc. Am.*, **57**(4), 856–861.

Stickler, D. C., & Ammicht, E. 1980. Uniform asymptotic evaluation of the continuous spectrum contribution for the Pekeris model. *J. Acoust. Soc. Am.*, **67**(6), 2018–2024.

Tappert, F. D. 1974. Parabolic equation method in underwater acoustics. *J. Acoust. Soc. Am.*, **55**(S1), S34–S34.

Thomson, D. J., & Chapman, N. R. 1983. A wide-angle split-step algorithm for the parabolic equation. *J. Acoust. Soc. Am.*, **74**(6), 1848.

Tindle, C T. 1979. Virtual modes and mode amplitudes near cutoff. *J. Acoust. Soc. Am.*, **65**(6), 1423–1428.

Tindle, C.T., Stamp, A.P., & Guthrie, K.M. 1976. Virtual modes and the surface boundary condition in underwater acoustics. *J. Sound Vib.*, **49**(2), 231–240.

Turin, George L. 1960. An Introduction to Matched Filters. *IRE Trans. Inf. Theory*, **6**(3), 311–329.

Urick, Robert J. 1975. *Principles of underwater sound / Robert J. Urick*. [rev. ed.] edn. McGraw-Hill New York.

Voitovich, N N, & Shatrov, A D. 1973. Normal-Mode Expansion of the field in an underwater sound channel. *Sov Phys Acoust*, **18**, 434–438.

Weissman, D. 1973. Two frequency radar interferometry applied to the measurement of ocean wave height. *IEEE Trans. Antennas Propag.*, **21**(5), 649–656.

Westervelt, Peter J. 1963. Parametric Acoustic Array. *J. Acoust. Soc. Am.*, **35**(4), 535–537.

Wigner, E. 1932. On the quantum correction for thermodynamic equilibrium. *Phys. Rev.*, **40**(5), 749–759.

Worthmann, Brian M, & Dowling, David R. 2016. Nonlinear signal processing techniques for active sonar localization in the shallow ocean with significant environmental uncertainty and reverberation. *Page 055003 of: Proc. Meet. Acoust.*

Worthmann, Brian M., & Dowling, David R. 2017. The frequency-difference and frequency-sum acoustic-field autoproducts. *J. Acoust. Soc. Am.*, **141**(6), 4579–4590.

Worthmann, Brian M., Song, H. C., & Dowling, David R. 2015. High frequency source localization in a shallow ocean sound channel using frequency difference matched field processing. *J. Acoust. Soc. Am.*, **138**(6), 3549–3562.

Worthmann, Brian M., Song, H. C., & Dowling, David R. 2017. Adaptive frequency-difference matched field processing for high frequency source localization in a noisy shallow ocean. *J. Acoust. Soc. Am.*, **141**(1), 543–556.

Yang, T. C. 1987. A method of range and depth estimation by modal decomposition. *J. Acoust. Soc. Am.*, **82**(5), 1736–1745.